Development of a Boron-10 based Multi-Grid Detector for Neutron Spectroscopy

Alexander Backis

Submitted in fulfilment of the requirements for the
Degree of Doctor of Philosophy

School of Physics & Astronomy
College of Science and Engineering
University of Glasgow

May 2023

To the creators of Star Trek, for inspiring children across the world to pursue a career in science. Me included.

Abstract

This work presents the continued development of the Multi-Grid, a boron-10-based cold to epithermal neutron detector technology. The Multi-Grid is a large area detector, tens of square meters, intended for time-of-flight neutron spectroscopy. The detector development started around 2010, and its first application is intended at the upcoming European Spallation Source, currently under construction in Lund, Sweden. This is to address the expected high flux at the upcoming facility, which is beyond the rate capabilities of current state-of-the-art detectors, and to substitute the large area helium-3 tube arrays commonly used for neutron spectroscopy, which have become prohibitively expensive at high He-3 gas pressures.

Here, the latest developments are shown, based on measurements with the most recent implementations of the Multi-Grid, which are the MG.SEQ and MG.LET prototypes. This includes the characterisation of different detector properties – such as neutron detection efficiency, signal-to-background ratio and energy resolution – as well as an investigation on how to properly select an internal shielding design. It also includes a detailed account of the effects of internal neutron scattering and how it can be reduced. This is a general step-by-step guide on how to compare and evaluate different neutron shielding candidates and it is relevant for all neutron detectors, not just the Multi-Grid.

The characterisation work is primarily based on data collected during two beamtimes: one at the ESS Test Beamline V20 at the Helmholtz-Zentrum Berlin, Germany, and one at the cold neutron spectrometer LET at the ISIS neutron and muon source, United Kingdom. For the internal shielding investigations, Geant4 was used together with the newly developed NCrystal library. Using these code packages, various shielding materials were modeled and simulations were performed of how neutrons interact with them.

From the results, a signal-to-background ratio of approximately 10^4 was shown together with an improvement in energy lineshape, which was broadly comparable to the LET helium-3 tubes and had a reduced energy smearing compared to that observed during a previous test at the CNCS instrument at the Spallation Neutron Source. Important information was obtained on how the effects on internal neutron scattering can be attenuated,

and a direct comparison was made with state-of-the-art helium-3 detectors in the LET instrument. The energy resolution was also studied in detail and the detection efficiency was re-confirmed. These contributions bring the development of the detector towards its finalisation and use at neutron scattering facilities.

Contents

List of Tables

List of Figures

Acknowledgements

During my three and a half years as a PhD student, I have received a huge amount of support from many individuals and organizations. Without this aid, this work would not be possible. Much of this help is acknowledged in the related publications produced during my studies, so here I will instead attempt a more personal approach.

First of all, I would like to thank my five supervisors – David, Kelly, Ken, Ramsey and Richard – for the collaboration we've had during this time and for everything you have taught me. Most importantly, I am grateful for the massive encouragement, support and calm atmosphere you have given during the intensely stressful times in the detector development. If I ever tutor a PhD student, I will do my utmost to follow your example and provide the same stable, positive and motivating environment.

Secondly, I would like to thank everyone at ESS whom I've had the privilege to work with. This includes in particular Kevin and Francesco for many invaluable conversations about neutron scattering and detectors. I would also like to thank Thomas for our discussions on simulations – which have always been extremely informative – and Anton for our work on the Multi-Grid detector before I started my PhD: thank you. A special thanks go out to Nicholai and Emil for many engaging conversations. I can only strive to create data visualisations in your league.

Thirdly, I would like to thank all my family and friends. This includes my mom, dad and brother – Annika, Kiriakos and Christopher – and of course their partners Paul, Malin and Jenny, but also my extended family in Sweden, Greece and Belgium, as well as my fiancée Sofie (I can never thank you enough for your solid support through the twists and turns of my PhD adventure) and her wonderful family. I would in particular like to thank my friends Johan, Henrik, Diego, Emil and Pablo – the movie nights, board games and Svedala Thai have been an honour – as well as Jonathan for all the delightful walks.

Finally, I am thankful for the brief but memorable time I spent living in Glasgow. You all made me feel warmly welcome and my stay in Scotland during this period will always have a fond home in my memory.

Declaration

The work presented in this thesis is based on research carried out at the Nuclear and Hadron Physics Group, School of Physics & Astronomy, University of Glasgow, UK, and the European Spallation Source, Sweden. No part of this thesis has been submitted elsewhere for any other degree or qualification and it is all my own work unless referenced to the contrary in the text. This work has been fully funded by the Neutron Scattering System Division at the European Spallation Source.

Overview

This work concerns the continued development of a novel neutron detector technology called the Multi-Grid [1–9]. The detector concept was invented at the Institut Laue–Langevin (ILL) [10] around the year 2010, and has since then been jointly developed with the European Spallation Source (ESS) [11–13] – an upcoming next-generation neutron scattering facility in Lund, Sweden – which is expected to start operation in 2027.

The detector development was prompted by the price uncertainty of helium-3-based detectors [14], as well as the high neutron flux expected at ESS, which is predicted to saturate traditional helium-3 detectors – due to charge pile-up effects – which limits their maximum rate capability. This pile-up effect is not as prominent in the Multi-Grid detector because it does not use charge-division for three-dimensional neutron hit reconstruction. Instead, the neutron hit location is reconstructed based on coincident signals from the cathodes and anodes in the active volume. This allows it to operate at around an order of magnitude lower gain, which lowers the charge released in each neutron event. Furthermore, because of the detectors segmented geometry – discussed in more detail in Chapter 2 – the charge released from consecutive events are spread over a larger region, which further suppresses pile-up effects.

The purpose of the development was to design a simple and scalable neutron detector at a low cost with a high performance and excellent count rate capabilities. This would allow the Multi-Grid to replace large-area helium-3-based detectors, which had become prohibitively expensive, in neutron spectroscopy instruments at future neutron sources and take full advantage of the high fluxes available there.

The full Multi-Grid detector requirements for a spectroscopy instrument at ESS are presented in table 2.1 in Chapter 2. These requirements include, among others, a momentum resolution of $\Delta Q/Q < 2\%$, an energy resolution of $\Delta\hbar\omega/E_\mathrm{i} < 1.5\%$ for wavelengths longer than 4 Å, a signal-to-background ratio of 10^4 at 5 Å, and a 50 times higher count rate capability compared to traditional helium-3 tubes. These requirements have been tailored to fit the scientific demands, which entails measuring neutron momentum and energy transfer with an excellent signal-to-background ratio at high counting speeds. The details on this

type of measurement are outlined in Chapter 1.

To develop the detector technology and prepare it for use at ESS, several prototypes have been built and tested. These prototypes have been characterised at neutron scattering facilities and laboratories, including the ILL, the Source Testing Facility (STF) [15], the Spallation Neutron Source (SNS) [16], the Helmholtz-Zentrum Berlin (HZB) [17], and the ISIS Neutron and Muon Source [18]. Here, work on selecting critical design parameters, such as internal shielding, is presented together with results gathered with the two most recent Multi-Grid detector prototypes: the MG.SEQ and the MG.LET. The outcome of these investigations are presented in Chapters 3, 4 and 5. In these chapters it is shown, for example, that by adding internal shielding in the active volume of the detector that the energy line shape reconstruction can be improved by at least a few tens of percent.

The scope of this thesis is to assess the detector's performance in terms of efficiency, internal scattering, energy resolution and signal-to-background ratio. To begin with, a presentation is given on why and how neutrons are used in neutron scattering facilities and what specific research will be done at ESS. After that, the general principles of neutron detection are shown and how they are implemented in Multi-Grid detectors and the prototypes investigated here. This is followed by the studies performed in this work, many of which were designed to be as general as possible. This is a novel approach in the neutron detector field and it makes the results relevant for many detector types, aiding in the research and development of future neutron detector technologies.

Chapter 1

Introduction

The Multi-Grid detector is intended for use in neutron scattering measurements and, therefore, has design parameters tailored to fit the requirements of such experiments. In this chapter, the general aspects of science with neutrons – as well as the specific details about ESS – are presented together with how the Multi-Grid fits into that context. It also outlines the detector principles the Multi-Grid is based on and the components needed for neutron detection in the energy range relevant to this work. This information is then used in the subsequent chapter to motivate the Multi-Grid detector design.

1.1 Neutrons

Neutrons are subatomic particles which together with protons constitute the vast majority of atomic nuclei. The focus of this work, however, is on free neutrons. These can be extracted from the nuclei via reactions such as fission or spallation, and, once released, can be used to probe the structure and dynamics of materials. This is generally done by aiming a beam of neutrons at a sample of interest and observing neutron state changes after the interaction, including momentum, energy and spin. This information is then used to understand the properties of the object under study. In this section, an overview is given of why neutrons are suitable for this type of measurement, how the measurements are performed, and what information can be obtained.

1.1.1 Properties

Neutrons are used as probes because they have a unique combination of properties [19]. These are shown in figure 1.1, where they are derived from four of the neutron's more basic attributes.

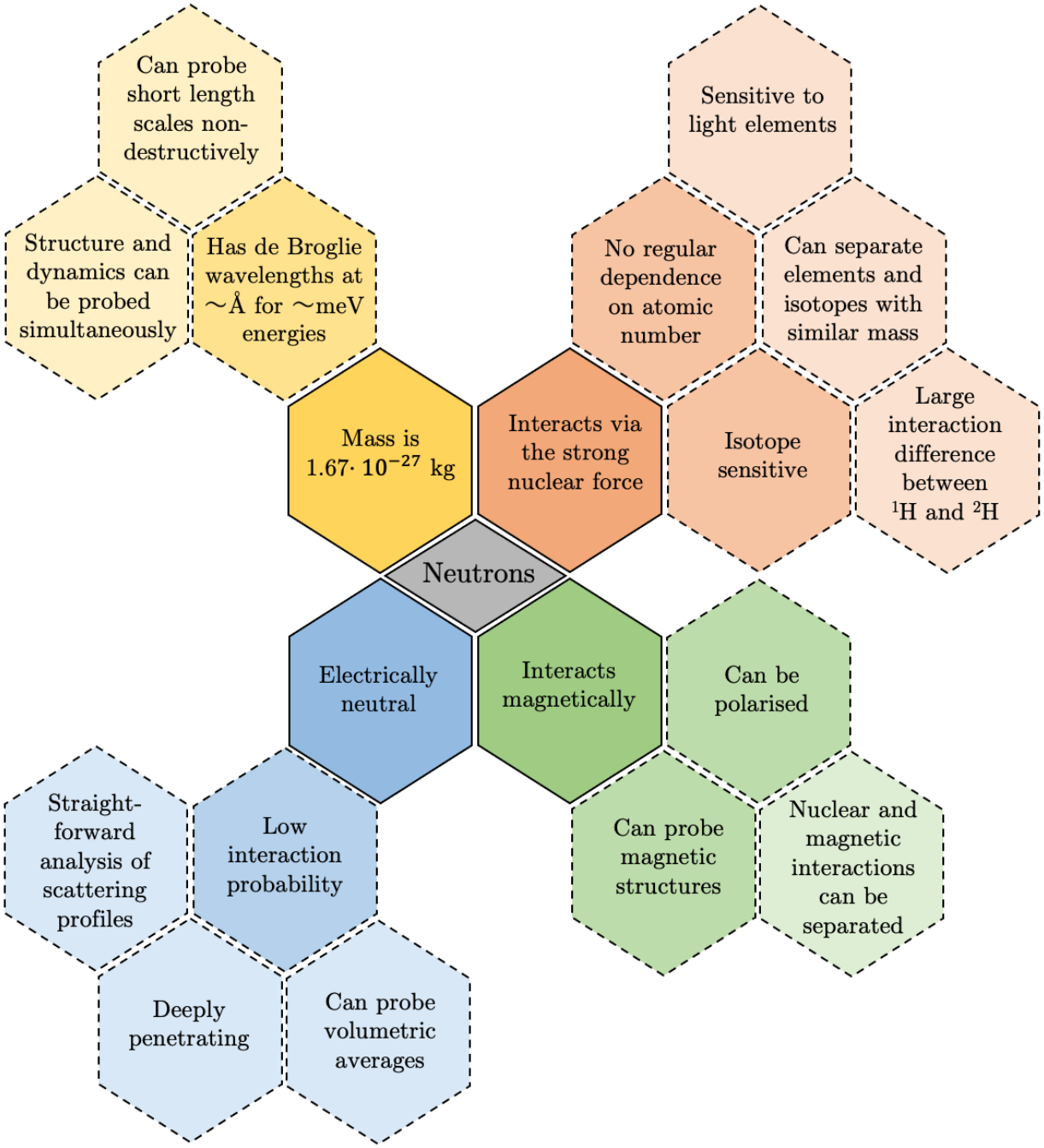

Figure 1.1: An overview of relevant neutron properties. In the centre, four neutron attributes are shown (solid hexagons). These are neutron mass, strong interaction, electrical neutrality and magnetic interaction. From these attributes, their useful consequences (dashed hexagons) are mapped out.

First of all, neutrons are electrically neutral, which leaves them unaffected by electric fields, such as those from the electrons and protons in atoms. They do, however, interact via the strong nuclear force, leading them to scatter off atomic nuclei. As the strong nuclear force has a small range ($\sim 10^{-15}$ m) compared to the size of an atom ($\sim 10^{-10}$ m) neutrons encounter almost no barriers when traversing through matter. They can therefore easily

reach deep into materials, probing bulk properties of the material instead of just surface effects. Furthermore, due to the low interaction probability, if a neutron interacts it usually only does so once. This leads to precise measurements, as few multiple-scattering events occur, making the uncomplicated scattering profiles straightforward to interpret.

As neutrons interact via the nuclear force, whose strength depends on the configuration of neutrons and protons inside the nuclei, neutrons interact differently with isotopes of the same element. The interaction strength is not dependent on nuclei size and can vary greatly between isotopes of similar mass. One example of this is the large difference in interaction cross-section between hydrogen and deuterium, which is heavily exploited in measurements involving biological matter, i.e. materials composed of large amounts of hydrogen. Neutrons are also sensitive to light elements – such as Li – making them a great complement to X-rays, which are more sensitive toward heavier elements. This is because, in contrast to neutrons, X-rays interacts with the electrons surrounding the nuclei and hence has an interaction probability that grows with the atomic number. It is therefore, for example, useful in imaging measurements to use X-rays when studying heavy element matter enclosed in light element matter (such as bones inside soft tissue) and neutrons when the opposite is true (such as water inside a metal kettle).

Neutrons also carry a spin and a magnetic moment, which makes them responsive to magnetic fields. Consequently, neutrons can be used to probe magnetic structures without being perturbed by electric fields, making them highly sensitive magnetic probes. Furthermore, because the magnetic moment has a direction, it is possible to polarise a beam of neutrons using an external magnetic field. This allows the direction of the magnetic fields in the materials to be probed. Polarised neutrons also have a corresponding spin precession around the direction of the external magnetic field, the Larmor precession, which can be used to get extremely fine timing resolution. This is done by analysing the phase shift of the spin precession after interacting with a material to extract timing information [20].

Another property is that, like all particles, neutrons follow the wave-particle duality of quantum mechanics and can be described as probability waves. When neutrons interact with matter, there is therefore the possibility of obtaining diffraction patterns from interfering neutron waves. Diffraction patterns carry information about the arrangement of atoms in the material and hence the material *structure*. This is because the patterns depend upon the distances between the scattering points, which reflects the internal geometry of the material.

Depending on the length scale of interest, the neutron wavelength λ can be adjusted to

an appropriate value according to the de Broglie relation for a free matter wave,

$$\lambda = \sqrt{\frac{h^2}{2Em_n}}, \tag{1.1}$$

where h is the Planck constant, E is the neutron kinetic energy and m_n is the neutron mass. The relation reveals that a larger mass results in a shorter wavelength for a given energy. Due to the specific mass of the neutron, wavelengths short enough to probe interatomic distances can be obtained at non-ionising energies ($\sim$meV). This makes the neutron a non-destructive probe[1].

At short wavelengths, neutrons have an associated energy comparable to the energy of molecular vibrations and kinetic energy of particles at room temperature. If a neutron exchanges energy with the material – such as gaining or losing energy from interaction with a moving particle – the fractional change in neutron energy is large, which makes it easily measurable. The change in neutron energy gives information about the *dynamics* of the material, such as rotation and translation of molecules of the probed material. Due to the neutron's sensitivity to magnetic fields, it can also probe dynamical magnetic behaviour. Finally, it is possible to *simultaneously* probe material structure and dynamics, as wavelengths of the order of Ångstroms (10^{-10} m) – typical atomic spacing – correspond to energies of the order of meV – typical vibrational and rotational excitation energies.

The appeal for using neutron as a probe, due to the reasons stated above, has led to many different measurement techniques being developed. These techniques can be grouped into *imaging* and *scattering* methods. These differ in their specific implementation and what material property they study: imaging measurements focus on the transmission of neutrons, while scattering measurements rely upon, as the name implies, the scattering of neutrons. That being said, the underlying theory for how neutrons interact with matter is the same. This theory is used to interpret the measurements and draw conclusions on how the material under study is structured and behaves. This is considered briefly in the next section, which is based on presentations found in [20–22].

1.1.2 Interactions

During a neutron imaging or scattering experiment there are two general processes in which neutrons interact with matter: absorption and scattering.[2] These two processes

[1]Note that this argument only holds for neutron scattering interactions and that for neutron capture reactions the subsequent released decay products – which can have energies in the order of MeV – can cause material damage.

[2]The possibility of a free neutron beta-decaying to a proton during the measurement is not included in the calculations due to the neutron lifetime, 886 s, being much larger than the total time needed of the free neutron in the measurement, usually below 1 s.

can be understood by studying figure 1.2, where a beam of neutrons with a flux per unit area ϕ (neutrons/unit time/unit area), is incident on a target. The target is a volume of general matter – such as a crystal, liquid or gas – and is composed of a collection of atoms.

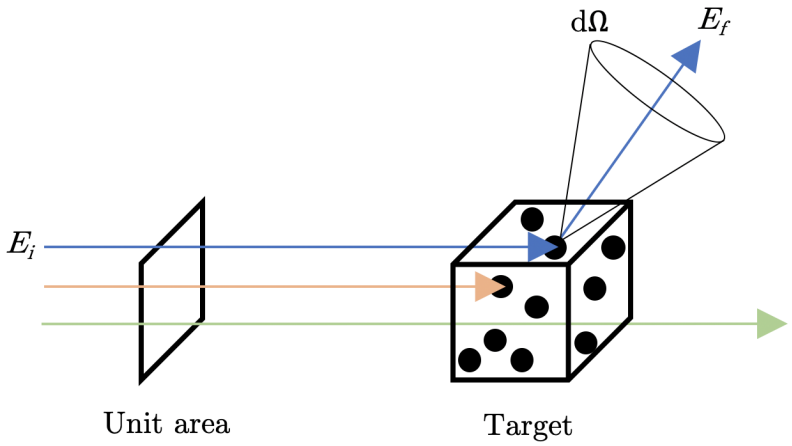

Figure 1.2: Neutrons incident on a target with a collection of atoms (black dots), illustrating scattering (blue), absorption (orange) and no interaction (green). The scattered neutron is seen changing direction and exiting into a solid angle dΩ with an energy E_f.

The probability of these processes occurring is expressed in *cross-sections*, which can be interpreted as sensitive areas in which the processes – absorption or scattering – occur. The larger the cross-section, the higher probability of interaction.

For the scattered neutrons, three different cross-sections are considered. These are known as the *partial differential scattering cross-section* $\mathrm{d}^2\sigma/\mathrm{d}\Omega\mathrm{d}E_\mathrm{f}$, the *differential scattering cross-section* $\mathrm{d}\sigma/\mathrm{d}\Omega$, and the *total scattering cross-section* σ. These are presented in equations (1.2a), (1.2b) and (1.2c), respectively,

$$\frac{\mathrm{d}^2\sigma}{\mathrm{d}\Omega\mathrm{d}E_\mathrm{f}} = \frac{1}{\phi}\cdot\frac{f_\Phi(E_\mathrm{f},\Omega)}{d\Omega dE_\mathrm{f}}, \tag{1.2a}$$

$$\frac{\mathrm{d}\sigma}{\mathrm{d}\Omega} = \frac{1}{\phi}\cdot\frac{F_\Phi(\Omega)}{d\Omega}, \tag{1.2b}$$

$$\sigma = \frac{1}{\phi}\cdot\Phi. \tag{1.2c}$$

In the equations, ϕ is the incident neutron flux per unit area, $f_\Phi(E_f,\Omega)$ is the number of scattered neutrons per second into a small solid angle dΩ with a final energy between E_f and $E_f + dE_f$, $F_\Phi(\Omega)$ is the number of neutrons scattered per second into a small solid angle dΩ, i.e. the integration over energy of $f_\Phi(E_f,\Omega)$, and Φ is the total number of neutrons scattered in all directions per second, i.e. the integration over solid angle of $F_\Phi(\Omega)$. Note that the units of Φ and ϕ are s^{-1} and $\mathrm{s}^{-1}\mathrm{m}^{-2}$, respectively, which gives

$[\sigma] = \mathrm{m}^2$.

The cross-sections stated in equations (1.2a), (1.2b) and (1.2c) correspond to quantities which can be measured in a neutron scattering experiment. This includes the neutron energy and the neutron scattering angle, as well as the combination of the two. The measured cross-sections can then be compared to the theoretical calculations, allowing hypotheses for the structure and dynamics of a material to be tested against experimental data. The initial and final neutron spin states are additional quantities that can be measured but are not included in the above expressions.

An in-depth derivation of the mathematical expressions for the cross-sections is beyond the scope of this work. However, to clarify which observables a neutron detector can be designed to detect, an overview of the formalism is given below to explain two types of neutron scattering. These include *coherent* and *incoherent* scattering, as well as *elastic* and *inelastic* scattering. These scatterings relates to, respectively, changes in neutron direction and energy, and it is these changes the detector is designed to measure.

Wave formulation

The cross-sections stated in the previous section are general: they encompass any type of scattering. This includes both nuclear and magnetic interactions. In the following, however, only nuclear cross-sections are considered as this is sufficient to understand the concept. It is also assumed the neutron energy does not change after scattering, i.e. elastic scattering is assumed.

Neutron wavelengths used in scattering experiments are in the order of Angstroms, which is five orders of magnitude larger than the width of a nucleus. Consequently, the interaction between a neutron and nucleus can be treated as a wave which scatters off a point source. This means that the scattering is isotropic, i.e. the neutron has an equal scattering probability in all directions.

If the wave function ψ_i of an incident neutron with a wavelength λ is stated as a plane wave traveling in the positive z-direction, as in equation (1.3),

$$\psi_i = e^{ikz}, \tag{1.3}$$

where $k = 2\pi/\lambda$ is the wavenumber, then the wave function ψ_f of a neutron scattered of an isolated nucleus can be expressed as the spherical wave

$$\psi_f = -b\frac{e^{ikz}}{r}, \tag{1.4}$$

where r is the distance from the nucleus and b is defined as the *scattering length* of the

nucleus. The scattering length is a complex number which relates to the likelihood of a certain reaction happening between the neutron and nucleus. The imaginary part is related to neutron absorption, while the real part is relevant to neutron scattering. The value of b is a parameter that has to be measured empirically for each nucleus.

Using the above formalism for treating neutrons as waves, it is possible to calculate the cross-sections in equations (1.2a), (1.2b) and (1.2c) more explicitly. By doing this, the phenomena of coherent, incoherent, elastic and inelastic reactions can be evaluated. This is considered next, starting with a study of the total scattering cross-section σ.

Total cross-section

Using the acquired wave functions for the incident and scattered neutrons, an explicit expression for σ can be found. As seen in equation (1.2c), this value depends on ϕ and Φ, which can be found using equations (1.3) and (1.4).

For particles, ϕ is acquired according to the following equation,

$$\phi = \frac{N}{A \cdot t}, \tag{1.5}$$

where A is the area the particles passed, t is the duration in which the particles passed the area A, and N is the total number of particles which passed the area A during the duration t. For wave functions, in contrast, the wave probability density $|\psi|^2$ – probability per unit volume – is used and the flux per unit area is calculated as

$$\phi = |\psi|^2 \cdot v \tag{1.6}$$

where v is the neutron velocity. By using this information together with equation (1.3), ϕ can be calculated via

$$\phi = |\psi_i|^2 \cdot v = v. \tag{1.7}$$

Next, Φ is calculated by determining the flux per unit area of the scattered neutrons scaled by the traversed area. Therefore,

$$\Phi = \phi_f \cdot A_s = |\psi_f|^2 \cdot v \cdot 4\pi r^2 = \frac{b^2}{r^2} \cdot v \cdot 4\pi r^2 = 4\pi b^2 v. \tag{1.8}$$

where A_s is the spherical surface area surrounding the nucleus, which all scattered neutrons traverse.

By inserting equations (1.7) and (1.8) into equation (1.2c), a relation between the total

scattering cross-section σ and scattering length b is acquired,

$$\sigma = \frac{\Phi}{\phi} = \frac{4\pi b^2 v}{v} = 4\pi b^2. \tag{1.9}$$

From the expression above, it is seen that the unit of b is in meter, which motivates the previously introduced name scattering *length*.

In the above expression only a single nucleus, one scattering point, is considered. Next, a system of multiple scattering centres is treated, illustrating how coherent and incoherent scattering arises from the combined contributions of the scattering locations.

Coherent and incoherent scattering

Coherent and incoherent scattering relates to the angular distribution in which particles scatter. Coherent scattering profiles have a structure – there is an angular dependence on the scattering distribution; while incoherent scattering has no pattern – the scattering profile is isotropic. The phenomenon arises from the interference of neutron waves scattering off many different nuclei and depends on how the atoms are structured and what scattering lengths they have. In this section, only stationary nuclei are considered.

The differential cross-section $\mathrm{d}\sigma/\mathrm{d}\Omega$ for a collection of nuclei is given by

$$\frac{\mathrm{d}\sigma}{\mathrm{d}\Omega} = \left| \sum_j b_j \cdot \exp(i\mathbf{Q} \cdot \mathbf{r}_j) \right|^2 \tag{1.10}$$

where b_j is the scattering length of the j:th nuclei, $\mathbf{Q} = \mathbf{k}_i - \mathbf{k}_f$ is the scattering vector and $\mathbf{r}_j$ is the location of the j:th nuclei. Note that the expression is a function of $\mathbf{Q}$, which depends on both the neutron wavelength and scattering direction.

To evaluate this expression, the relation $|A|^2 = AA^*$ is used, which gives

$$\frac{\mathrm{d}\sigma}{\mathrm{d}\Omega} = \sum_j \sum_{j'} b_j b_{j'} \exp[i\mathbf{Q} \cdot (\mathbf{r}_j - \mathbf{r}_{j'})]. \tag{1.11}$$

If the number of nuclei is assumed to be large and the value of b varies randomly across them, then the expression above can be simplified by using the average value of $b_j b_{j'}$ for each term in the summation. The average values of $b_j b_{j'}$, $\langle b_j b_{j'} \rangle$, are calculated as follows

$$\langle b_j b_{j'} \rangle = \langle b_j \rangle \langle b_{j'} \rangle = \langle b \rangle^2, \qquad j \neq j' \tag{1.12a}$$

$$\langle b_j b_{j'} \rangle = \left\langle b_j^2 \right\rangle = \left\langle b^2 \right\rangle, \qquad j = j' \tag{1.12b}$$

By substituting $b_j b_{j'}$ in equation (1.11) with the average values in equations (1.12a) and (1.12b), the expression for $\mathrm{d}\sigma/\mathrm{d}\Omega$ can be rewritten as

$$\frac{\mathrm{d}\sigma}{\mathrm{d}\Omega} = \langle b \rangle^2 \cdot \sum_{j,j'} \exp[i\mathbf{Q} \cdot (\mathbf{r}_j - \mathbf{r}_{j'})] + \left(\left\langle b^2 \right\rangle - \langle b \rangle^2 \right) \cdot N \tag{1.13}$$

where N is the total number of nuclei in the system.

The right-hand side of equation (1.13) consists of two terms. The first term represents coherent scattering, which depends on the relevant position of the nuclei in the system, as given by the double summation. The second term represents incoherent scattering and is independent of the arrangement of nuclei: it depends only on the total number of nuclei N.

The two terms are scaled differently with the scattering cross-sections in the system. The coherent term scales with $\langle b \rangle^2$, while the incoherent term scales with $\left(\langle b^2 \rangle - \langle b \rangle^2 \right)$, which is the variance of the scattering lengths. That is, the larger spread in scattering lengths the nuclei in a system have, the more incoherent scattering occurs in that system. It is from these two scaling terms that the coherent and incoherent scattering cross-sections of a system are defined, as seen in equations (1.14a) and (1.14b),

$$\sigma_{\mathrm{coh}} = 4\pi \langle b \rangle^2 \tag{1.14a}$$

$$\sigma_{\mathrm{incoh}} = 4\pi \left(\left\langle b^2 \right\rangle - \langle b \rangle^2 \right) \tag{1.14b}$$

where σ_{coh} is the coherent scattering cross-section and σ_{incoh} is the incoherent scattering cross-section.

It is worth considering where the differences in scattering length within a collection of nuclei come from. As mentioned in the introduction, isotopic differences are one factor which influences the neutron reaction probability. Another factor is the spin-state of the nuclei and the possible final combined spin-states between the neutron and the nuclei. In the following discussion, it will be assumed that the collection of nuclei are all of the same isotope to investigate the effect of the spin.

For a nucleus with spin I, two possible final spin-states can be constructed when the spin of the neutron and nuclei are combined: $I + 1/2$ if the neutron and nucleus spin are in parallel and $I - 1/2$ if the spins are anti-parallel. Due to spin degeneracy, these states are further subdivided. This is because the spin can only be measured in one perpendicular axis at a time (normally taken to be the z-direction), and the total spin can have different projections on that axis. For a particle with spin S, the number of projections, or degeneracy, is given by $2S + 1$. This means that if a nucleus with spin

$I = 1$ is considered, the first neutron-nuclei spin system – spins parallel – has a total spin of $S = I + 1/2 = 1 + 1/2 = 3/2$ (4 states), while the second neutron-nuclei spin-system – spins anti-parallel – have a total spin of $S = I - 1/2 = 1 - 1/2 = 1/2$ (2 states).

To account for the fact that the two configurations have a different number of final states, weighting factors are introduced:

$$w_+ = \frac{I+1}{2I+1} \tag{1.15a}$$

$$w_- = \frac{I}{2I+1} \tag{1.15b}$$

where w_+ is the fraction of states in the $I + 1/2$ configuration and w_- is the fraction of states in the $I - 1/2$ configuration.

In addition to the degeneracy, the final spin states have different interaction probabilities with neutrons. If the expressions for σ_{coh} and σ_{incoh} are modified to account for this, then equations (1.16a) and (1.16b) are obtained,

$$\sigma_{\text{coh}} = 4\pi(w_+ b_+ + w_- b_-)^2 \tag{1.16a}$$

$$\sigma_{\text{incoh}} = 4\pi\left[w_+ w_- (b_+ - b_-)^2\right] \tag{1.16b}$$

where b_+ is the scattering length for neutron-nuclei spins in parallel and b_- is the scattering length for neutron-nuclei spins anti-parallel. Using these equations together with experimentally determined values for b_+ and b_- [20] a few notable examples can be made. This is presented in table 1.1, where the nuclear spins I, scattering lengths b_+ and b_-, as well as cross-sections σ_{coh} and σ_{incoh} are shown for a selection of isotopes.

Table 1.1: Properties of a few isotopes, including spin I, scattering lengths b_+ and b_-, and cross-sections σ_{coh} and σ_{incoh}. Scattering lengths are in units of [fermi] $= 10^{-15}$ m and cross-sections are in units of [barn] $= 10^{-28}$ m^2. Data taken from [20].

	I	b_+	b_-	σ_{coh}	σ_{incoh}
^{1}H	1/2	10.82	-47.42	1.76	80.27
^{2}H	1	9.53	0.98	5.59	2.05
^{51}V	7/2	4.93	-7.58	0.02	5.07
^{232}Th	0	n.a.	n.a.	13.36	0

Here it has been assumed that the neutrons have the same energy before and after scattering. That is, only elastic scattering has been considered. This is now expanded, and both elastic and inelastic scattering is briefly discussed.

Elastic and inelastic scattering

Elastic and inelastic neutron scattering is related to energy transfer between the neutron and the nuclei. In elastic scattering, the neutron has the same energy before and after scattering, i.e. no energy transfer takes place. If an inelastic scattering occurs, in contrast, there is an energy transfer between the particles, which means that the neutron gained or lost a certain amount of energy.

In the previous section, the differential cross-section $\mathrm{d}\sigma/\mathrm{d}\Omega$ was covered. This gives information on the angular distribution of neutron scattering, but not energy exchange. That information is contained in the partial differential scattering cross-section $\mathrm{d}^2\sigma/\mathrm{d}\Omega\mathrm{d}E_\mathrm{f}$, which contains information about both scattering directions and energy changes. This is divided into a coherent and incoherent component, as given in equation (1.17),

$$\frac{\mathrm{d}^2\sigma}{\mathrm{d}\Omega\mathrm{d}E_\mathrm{f}} = \left(\frac{\mathrm{d}^2\sigma}{\mathrm{d}\Omega\mathrm{d}E_\mathrm{f}}\right)_\mathrm{coh} + \left(\frac{\mathrm{d}^2\sigma}{\mathrm{d}\Omega\mathrm{d}E_\mathrm{f}}\right)_\mathrm{incoh}. \tag{1.17}$$

If the scattering system is composed of a collection of identical nuclei, then the coherent and incoherent components of $\mathrm{d}^2\sigma/\mathrm{d}\Omega\mathrm{d}E_\mathrm{f}$ can then be expressed according to

$$\left(\frac{\mathrm{d}^2\sigma}{\mathrm{d}\Omega\mathrm{d}E_\mathrm{f}}\right)_\mathrm{coh} = \sigma_\mathrm{coh}\frac{k_\mathrm{f}}{k_\mathrm{i}}N\cdot S(\mathbf{Q},\omega) \tag{1.18a}$$

$$\left(\frac{\mathrm{d}^2\sigma}{\mathrm{d}\Omega\mathrm{d}E_\mathrm{f}}\right)_\mathrm{incoh} = \sigma_\mathrm{incoh}\frac{k_\mathrm{f}}{k_\mathrm{i}}N\cdot S_\mathrm{incoh}(\mathbf{Q},\omega) \tag{1.18b}$$

where k_i and k_f are the incident and final wave-vector, respectively, and N is the total number of nuclei. The function $S(\mathbf{Q},\omega)$ is the *scattering function* of the system, while $S_\mathrm{incoh}(\mathbf{Q},\omega)$ is the *incoherent scattering function*. The angular frequency ω is related to the energy transfer between the neutron and nuclei according to

$$\hbar\omega = E_\mathrm{i} - E_\mathrm{f} \tag{1.19}$$

where $\hbar$ is the reduced Planck constant, E_i is the incident neutron energy and E_f is the final neutron energy.

The expressions for $\mathrm{d}^2\sigma/\mathrm{d}\Omega\mathrm{d}E_\mathrm{f}$ in equations (1.18a) and (1.18b) can each be split into two factors. The first is a scalar factor, $\sigma_\mathrm{coh}\frac{k_\mathrm{f}}{k_\mathrm{i}}N$ and $\sigma_\mathrm{incoh}\frac{k_\mathrm{f}}{k_\mathrm{i}}N$, which determines how strong overall the scattering is for a specific wave-vector transfer. The second factor, $S(\mathbf{Q},\omega)$ and $S_\mathrm{inc}(\mathbf{Q},\omega)$, is a function that depends on both momentum transfer $\mathbf{Q}$ and neutron energy transfer $\hbar\omega$. It is this function that contains the structural and dynamic information of the system. One example of this is how nuclei are arranged (structure) and vibrate (dynamics).

In the next section, a brief overview is given of how these properties are measured and what methods are used to do so.

1.1.3 Methods

Depending on the cross-section of interest, $\mathrm{d}\sigma/\mathrm{d}\Omega$ or $\mathrm{d}\sigma^2/\mathrm{d}\Omega\mathrm{d}E_\mathrm{f}$, there are two broad categories of neutron scattering methods which are employed [21]. The differential scattering cross-section $\mathrm{d}\sigma/\mathrm{d}\Omega$ is measured using *Neutron diffraction*, while the partial differential scattering cross-section $\mathrm{d}\sigma^2/\mathrm{d}\Omega\mathrm{d}E_\mathrm{f}$ is measured using *Neutron spectroscopy*. In addition to this, there is *Neutron imaging*, which measures the neutron transmission cross-section σ_t[3]. These categories can be summarised as:

$$\begin{aligned} \sigma_\mathrm{t} &: \text{Neutron imaging} \\ \frac{\mathrm{d}\sigma}{\mathrm{d}\Omega} &: \text{Neutron diffraction} \\ \frac{\mathrm{d}^2\sigma}{\mathrm{d}\Omega\mathrm{d}E_\mathrm{f}} &: \text{Neutron spectroscopy.} \end{aligned}$$

In other words, neutron imaging measures neutron transmission and neutron diffraction measures changes in neutron momentum, while neutron spectroscopy simultaneously measures changes in both neutron momentum and energy. Three examples of measurement data, one for each of the categories, are presented in figure 1.3.

The measurements are performed over a wide spectrum of momentum and energy levels, and a variety of techniques within the three categories exist. This is presented in figure 1.4, where the different neutron measurement techniques are shown together with other probing methods, such as x-rays, optical microscope and Nuclear Magnetic Resonance (NMR). The Multi-Grid detector is designed for time-of-flight spectroscopy, which is covered by the blue hexagon.

Depending upon the application, specific neutron energies are used. These are classified into various energy regimes, where the most common ones include *cold*, *thermal* and *epithermal* energies. The approximate energy spans and corresponding wavelengths for these regimes are presented in table 1.2.

The motivation for choosing a specific range of neutron energies over another varies. For example, depending on the length scale of interest, the corresponding neutron wavelength can be tuned to match the requirements. If details on the atomic level are studied, then the neutron wavelength should be similar to that of atomic spacing, i.e. around 1 Å. A

[3]Due to the finite resolution of the instrumentation, scattering with angles smaller than the spatial resolution can be considered as transmitted [23].

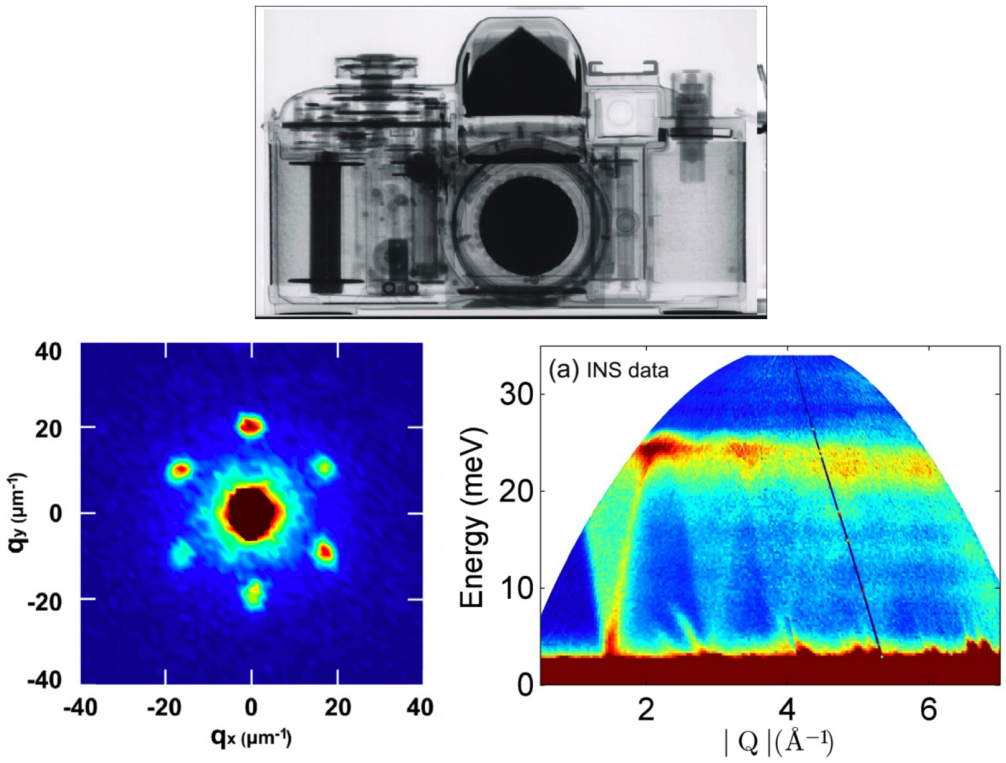

Figure 1.3: Example data collected using neutron imaging (top), diffraction (bottom left) and neutron spectroscopy (bottom right). The plots show, respectively, a neutron transmission distribution of a camera (information about external and internal macrostructure), a small-angle neutron diffraction pattern in momentum space collected from a crystal (information about atomic structure), as well as a momentum and energy transfer 2D heatmap distribution measured on the antiferromagnet $BaNi_2V_2O_8$ (information about atomic structure and dynamics). Figures taken from [24], [25] and [26], respectively.

Table 1.2: Energy regimes most commonly used in neutron scattering experiments [27].

	Energy (meV)			Wavelength (Å)		
Cold	0.05	→	5	40	→	4
Thermal	5	→	500	4	→	0.4
Epithermal	500	→	1 000 000	0.4	→	0.01

similar argument holds when studying molecular vibrations and particle diffusion: the energy of the property being investigated determines the appropriate neutron energy to use, which should be a close match. This ensures a large fractional energy change for the neutron, which increases the resolution.

In the following discussion, a few techniques of neutron diffraction and neutron spectroscopy are discussed together with how they are used to measure momentum and energy transfer. The focus will be on neutron spectroscopy, as this is the technique the Multi-Grid detector is designed for.

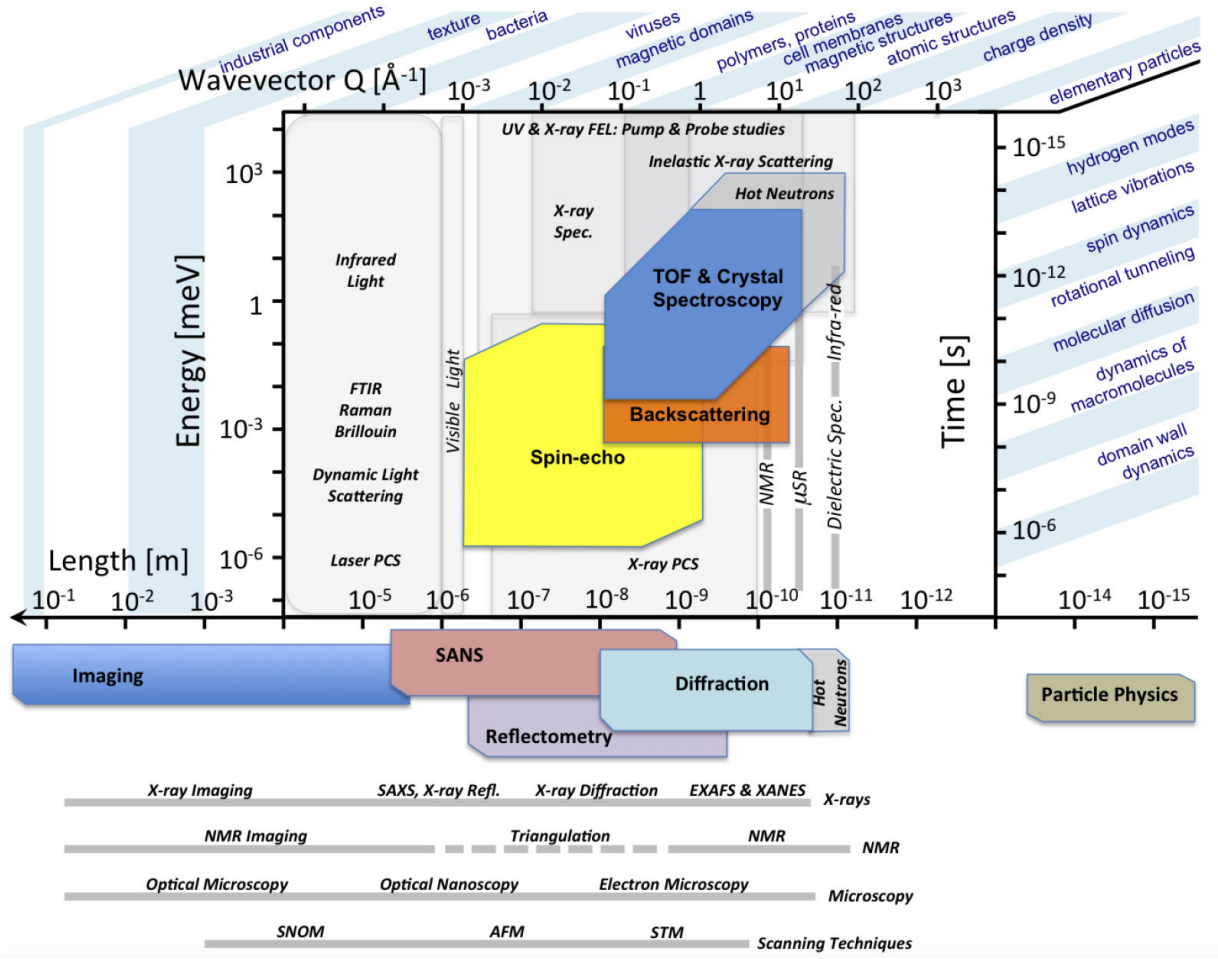

Figure 1.4: Overview of which domains different neutron techniques are relevant (coloured regions) together with other techniques (grey regions). The momentum transfer is seen on the top x-axis, which corresponds to the length scales seen on the bottom x-axis. The energy transfer is seen on the left y-axis, which corresponds to the time scales seen on the right y-axis. Application examples for the different length and time scales are seen at the peripheries of the diagram. Figure taken from [13].

Neutron diffraction

Neutron diffraction experiments investigate the material structure by studying the deflection angles of scattered neutrons. This is mainly done by exploiting Bragg reflections, which results in strong coherent scattering at certain angles. This is captured by Bragg's law,

$$n\lambda = 2d\sin(\theta) \tag{1.20}$$

where n is an integer, λ is the wavelength, d is the layer spacing and θ is the incident and scattering angle with respect to the reflective plane.

The angles for which Bragg reflections occur are dependent on the distances between the layers of scattering points in the sample, and hence the material structure. Therefore,

the material structure can be recreated by analysing the angular distributions of Bragg reflections.

The scattering angles obtained from the scattering profiles are commonly transformed into momentum space, where the main pattern analysis is made. To calculate momentum, the neutron energy is also required, which is either recorded before or after the scattering, depending upon the technique. That is, diffraction measurements assume that elastic scattering is the main mechanism and that no neutron energy transfer occurs.

There are different types of diffraction techniques, which specialise in different length scales and material types. A few of the most common ones include: *single crystal diffraction*, *powder diffraction*, *Small-Angle Neutron Scattering (SANS)* and *reflectometry*. Single crystal and powder diffraction study material structures down to the atomic level, while SANS and reflectometry study larger structures such as molecules, proteins and cell membranes.

For the last two techniques, the neutron scattering angles are especially narrow. This is because the techniques probe length scales that can be over two orders of magnitude larger than the wavelength of the neutrons used – corresponding to approximately $d = 1000$ Å and $\lambda = 10$ Å in equation (1.20) above – which gives small scattering angles θ. Hence, these instruments require an excellent position resolution to resolve the different narrow scattering angles of the neutrons. This is in contrast to the first two techniques where d and λ are comparable and the scattering angles are larger. For these techniques, the required position resolution is less stringent.

Neutron spectroscopy

Neutron spectroscopy experiments study the structure and dynamics of materials by measuring the scattering angles and energy transfer of neutrons. As seen in equation (1.17), this is made of two components: coherent inelastic scattering and incoherent inelastic scattering. The coherent component contains information such as crystal vibrations, while the incoherent component contains information on molecular vibration, rotation and diffusion.

The purpose of a spectroscopy measurement is to determine the scattering functions $S(\mathbf{Q}, \omega)$. However, the region of ($\mathbf{Q}$, ω)-space that can be probed is limited by the scattering angles neutrons can be detected in and the incident neutron energy. This region is defined according to equation (1.21), where the relationship between momentum transfer Q and energy transfer $\hbar\omega$ is given,

$$Q = \sqrt{\left[2E_{\mathrm{i}} - \hbar\omega - 2\sqrt{E_{\mathrm{i}}(E_{\mathrm{i}} - \hbar\omega)}\cos 2\theta\right] \cdot 2m_n\hbar^{-2}}, \tag{1.21}$$

where 2θ is the neutron scattering angle. This space is illustrated in figure 1.5 for an incident neutron energy E_i =100 meV and different scattering angles. It is seen that the incident neutron energy determines the rightmost region that can be probed, which is set by the maximum energy the neutron can transfer during a scattering event, namely all its energy.

If neutron scattering angles between 0° and 30° can be detected, then the region between the blue and orange lines can be probed. This emphasizes the importance of a spectroscopy experiment to have a large angular coverage, as to enable a wide region of ($\mathbf{Q}$, ω)-space to be probed. The energy transfer $\hbar\omega = E_\mathrm{i} - E_\mathrm{f}$ is defined from the point of view of the test sample the neutron interacts with. That is, a positive energy transfer – sample gained energy – implies that the neutron *lost* energy in the interaction, while a negative energy transfer – sample lost energy – means that the neutron *gained* energy.

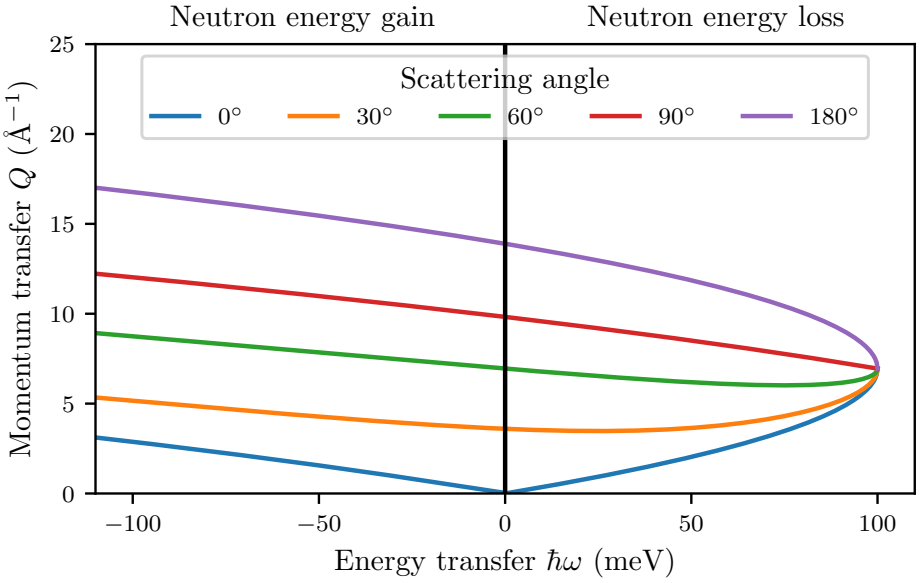

Figure 1.5: ($\mathbf{Q}, \hbar\omega$)-space available for different scattering angles (various colours) with the incident neutron energy E_i = 100 meV. The line where no energy transfer occurs is highlighted with a black vertical line. The left side of this line corresponds to neutron energy gain, while the right side corresponds to neutron energy loss. Figure adapted from [21].

There are two types of methods to measure the scattering functions, namely Inelastic Neutron Scattering (INS) and Quasielastic Neutron Scattering (QENS). The first type, INS, concerns neutron energy exchanges with the material under study in discrete steps. This includes exchanging vibrational energy quanta, *phonons*, and magnetic energy quanta, *magnons*, and is used to probe excitations in materials and molecules. The second type, QENS, is used to probe movements such as the diffusion of particles. The velocities of these particles can vary continuously and so can the neutron energy exchange with the par-

ticles. A one-dimensional schematic illustration of where these features appear, showing only the neutron energy transfer, is presented in figure 1.6.

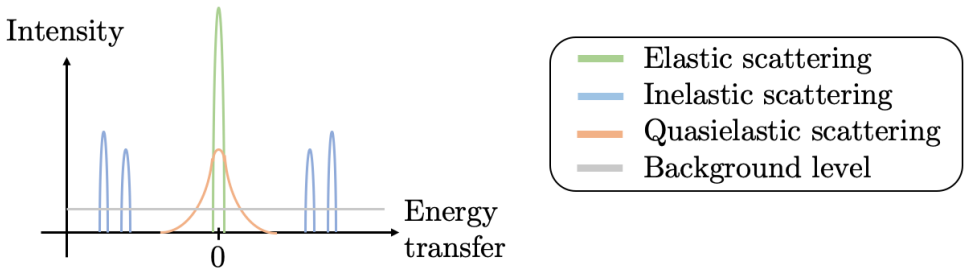

Figure 1.6: Schematic illustration of the differences between elastic (green), inelastic (blue) and quasielastic (orange) scattering in a neutron energy transfer spectrum. The background level (grey) is also included to highlight the importance of maintaining a low background rate. Figure adapted from [21].

It is essential for a neutron spectroscopy measurement, in contrast to neutron diffraction measurements, to extract the neutron energy both before and after the interaction. One way of doing this is by preparing a monochromatic beam of incident neutrons which are sent towards the sample. After the neutrons have scattered, the final neutron energy is measured. By comparing the incident and final neutron energy, the neutron energy transfer can be calculated.

This measurement scheme is called *direct geometry spectroscopy*[4] and is performed according to the setup shown in figure 1.7. The setup is presented in a Time-Distance diagram, where the neutron flight time is shown on the x-axis and the neutron travel distance on the y-axis. The measurement includes four main components: a neutron source, a chopper or crystal, a sample, and a neutron detector. As it is a requirement to know the neutron energy before reaching the sample, neutrons with only a specific energy are selected from the incident beam. This is usually done in one of two ways: by using a chopper or by using a crystal.

A chopper is a high-frequency rotating disc or cylinder with openings that the neutrons can pass through. The rest of the chopper is covered with an efficient neutron absorber, such as cadmium or gadolinium, which prevents neutrons from passing anywhere else. By placing the chopper in the path of the incident neutron beam, neutrons can only pass when the beam is aligned with the chopper opening. This chops the incident neutron beam into pulses. As the distance from the source to the chopper is known, the rotation frequency of the chopper can be tuned so that its opening aligns with neutrons with a specific velocity: all other neutrons are blocked. That is, a chopper uses the particle properties of neutrons

[4]When the conditions are flipped, i.e. when the incident neutron energy is allowed to vary and the final neutron energy is fixed, it is called *indirect* geometry spectroscopy.

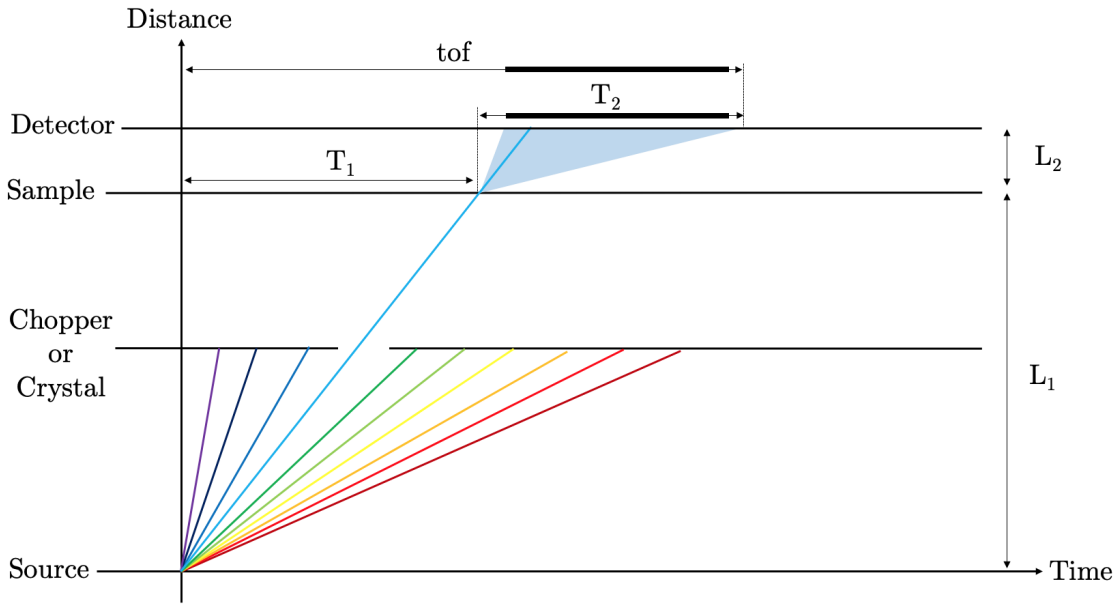

Figure 1.7: Time-Distance plot showing the general layout of a direct geometry spectroscopy measurement. This includes a polychromatic neutron source (different coloured lines), a chopper or a crystal which provides a monochromatic beam of neutrons (blue line), a sample and a detector to detect the scattered neutrons. The thick components of the arrows in T_2 and tof represent the possible lengths the arrows can have, which is governed by the specific energy transfer a neutron undergoes. Figure adapted from [20].

and selects a neutron energy E_n using the following equation,

$$E_n = \frac{m_n v_n^2}{2}, \tag{1.22}$$

where v_n is the neutron velocity.

A crystal, in contrast, uses the wave properties of neutrons to monochromise the beam. This is done by selecting an appropriate material with a crystalline structure, such as beryllium or copper, and placing the crystal in the neutron beam. By tuning the crystal inclination with respect to the incident beam, the crystal can be aligned such that the Bragg condition for a specific wavelength is fulfilled. This gives a strong reflection of neutrons with a specific wavelength, which are then sent towards the sample.

After the neutrons have scattered off the sample, they can either scatter elastically (continued blue line in figure 1.7) or inelastically (the light blue shaded region between sample and detector in figure 1.7). In inelastic scattering the neutron can either gain energy, which will increase its velocity, or lose energy, which will decrease its velocity. This makes some neutrons reach the detector earlier, and some later, than elastically scattered neutrons. It is this timing difference that is used to calculate the neutron energy transfer.

To calculate the energy transfer $\hbar\omega = E_\mathrm{i} - E_\mathrm{f}$, the quantities shown in in figure 1.7 is used. These include the source-to-sample distance L_1, the sample-to-detection distance L_2, and the full neutron time-of-flight tof, which is calculated as the time-difference between the start and stop reference times registered at the source and detector, respectively. Note that L_2 and tof is registered on an event-by-event basis for each detected neutron. The known incident energy E_i, corresponding to the blue line prepared by the chopper or crystal, is also needed. Using these quantities, the energy transfer can be calculated as follow,

$$\hbar\omega = E_\mathrm{i} - \frac{m_n}{2} \cdot \left(\frac{\mathrm{L}_2}{\mathrm{tof} - \mathrm{L}_1 \cdot v_\mathrm{i}^{-1}} \right)^2 \tag{1.23}$$

where v_i is the incident neutron velocity.

In the above discussion, it has been shown how neutrons are used to probe matter. However, extracting neutrons from atomic nuclei at the required rate to practically perform such measurements is challenging. To do this, large-scale research facilities are needed. These either use a nuclear reactor, such as at the ILL [10] in France, or a spallation source, like the SNS [16] in the United States, to produce neutrons. Of the two methods, spallation has seen the fastest increase in effective neutron flux (neutrons/s/cm^2/sr/Å) – i.e. flux usable for the experiment – during the last decades [28]. This is important, as neutron scattering is a signal-limited practice. The upcoming ESS is aiming to provide world-leading levels of neutron flux, with the ambition of enabling previously unattainable research findings to be discovered at the facility. The facility will enable neutrons in a large energy range, spanning from cold to epithermal energies.

1.2 The European Spallation Source

The European Spallation Source [11–13], or ESS, is a next-generation neutron scattering facility currently under construction in Lund, Sweden. In figure 1.8 an overview of the facility is given, where the major components have been highlighted. These include the accelerator, the target, the moderator and the instruments. The first three components are used to prepare neutrons with suitable energy for the measurement, while the last component – the instruments – is used to conduct science with the acquired neutrons. As seen in the figure, there is a wide selection of instruments, each specialised in a certain type of science. The completion date of ESS is set to be 2027.

Here, a brief description is given of ESS and how it is used to conduct science with neutrons. It starts by presenting how neutrons are generated, followed by an overview of the general layout of a neutron instrument. Finally, the two instruments the Multi-Grid detector is designed for, the CSPEC and T-REX instruments, are briefly introduced.

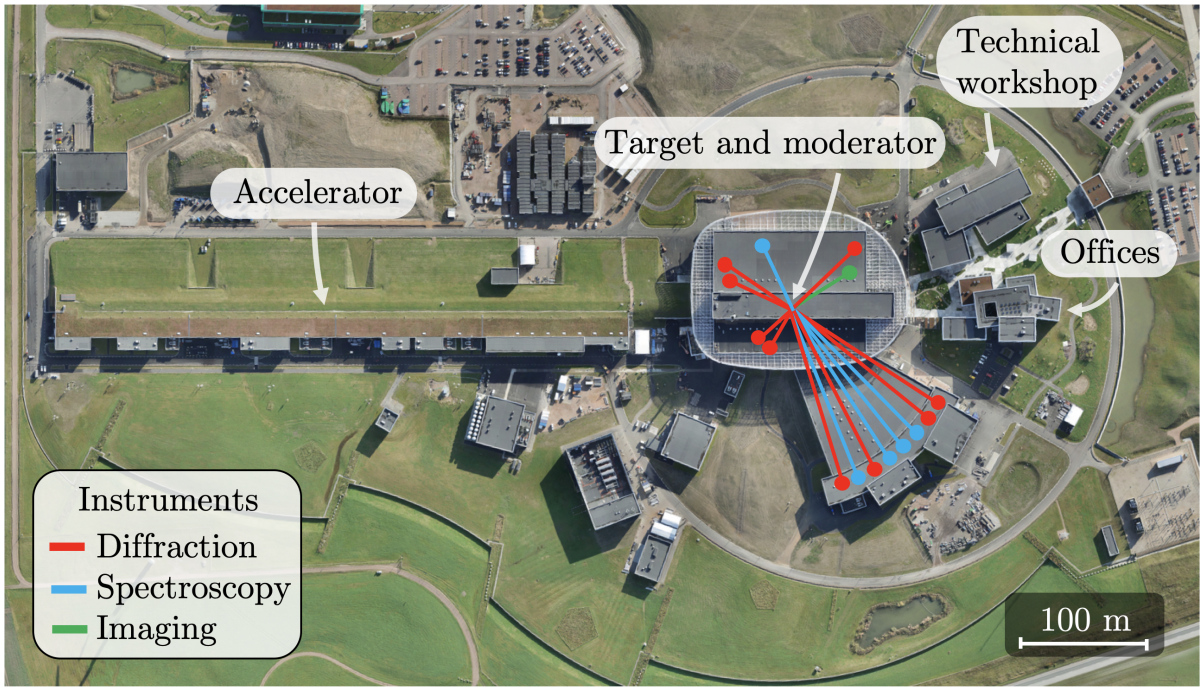

Figure 1.8: A photograph of ESS from above, highlighting the accelerator, moderator, target, technical workshop, offices and instruments. Figure adapted from [29].

1.2.1 Cold and thermal neutron generation

To generate neutrons, ESS uses the spallation process: a nuclear reaction consisting of bombarding a heavy nucleus with a highly energetic particle [11, 21]. After the incident particle has struck the target nucleus, it is initially absorbed and the nucleus is left in an excited state. This is followed by the ejection of highly energetic particles, including neutrons, which are absorbed by neighbouring nuclei, now leaving them in excited states. Finally, the neighbouring nuclei also de-excite, emitting a variety of particles including neutrons, protons, photons and neutrinos. Each spallation event results, on average, in 20-40 released neutrons. The released neutrons have a mean energy of around 50 MeV (the maximum energy is determined by the energy of the incident projectile) which is significantly higher than the energies desired for neutron scattering experiments.

For ESS, the spallation reaction takes place between a proton beam and a tungsten target. To achieve the reaction, the scheme presented in figure 1.9 is used, where a schematic illustration of the accelerator, target and moderator is shown. The first step in the process is to extract protons using an *ion source* that uses a rapidly varying magnetic field to heat hydrogen into a plasma, thus separating protons from electrons. The protons are then injected into the accelerator [30] where they are accelerated up to 2 GeV energy – 96 % the speed of light – before striking the tungsten target. This accelerator process is repeated at a rate of 14 Hz, where each proton pulse is 2.86 ms long.

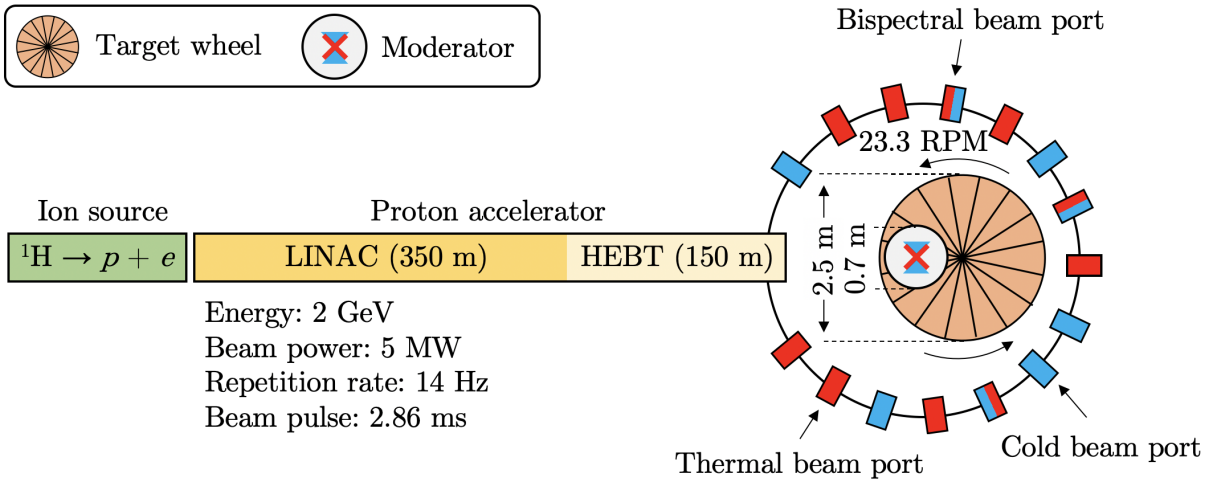

Figure 1.9: Schematic overview – not to scale – of how neutrons are produced for the ESS instruments, as seen from the top. Protons are extracted from an ion source and accelerated in a LINear ACcelerator (LINAC), after which they are transported in a High Energy Beam Transport (HEBT) section before striking the rotating tungsten target. Above and below the target, the moderator is located. The red and blue colours in the beam ports represent neutrons moderated in the cold moderator and thermal moderator, respectively.

The tungsten target is a large rotating wheel. It is 2.5 m in diameter, weighs 4 tonnes and rotates at a rate of 23.3 RPM. By doing that, the incident protons pulses are made to hit different parts of the 36 radial segments constituting the target, where they are stopped. This distributes the significant heat load induced by the spallation process, which can reach values up to around 30 kW [31].

Released neutrons from the spallation reactions reach the moderator placed above and below the rotating wheel. The moderator then slows down neutrons, by repeated inelastic collisions, to the energies required for the instruments. This is done either in the cold moderator (blue), containing cooled hydrogen, or the thermal moderator (red), containing ambient-temperature water. The moderation time – which can lie in the order of around tens to hundreds of microseconds [28] – is much smaller than the proton pulse width at ESS, 5 ms, and the angular distribution of the moderated neutron flux is approximately flat across the beam ports leading to the instruments [32]. The need for cold or thermal neutrons varies from instrument to instrument, and the instrument guides are either aligned with the cold or thermal moderator (or in some cases both). In total, there are 42 beam ports where neutrons can be extracted, allowing for future upgrades once the initial instrument suite has been completed. Moderated neutrons are guided out through the beam ports towards the instruments, which is the subject of the next subsection.

1.2.2 Instruments

Upon completion, ESS will host a large instrument suite, as shown in figure 1.8. The instrument suite is grouped into three categories, namely diffraction (red), spectroscopy (blue) and imaging (green). Using the strong neutron flux produced by the source and moderator ($\sim 10^{14}$ neutron/cm^2/s/sr/Å at 5 Å, a hundred times higher than that available at current facilities [11]), the ambition is to drive down measurement times – due to the increased rate of statistics – and to reach higher signal-to-background ratios – which is done by combining the high flux with an adequate shielding solution. This is useful, for example, in the case of biological research where many samples of interest can only be produced in mg quantities. At existing facilities, a measurement on such a sample would take around a full year, which is in practice unfeasible. At ESS, however, such a measurement could be done in 3-10 days [11].

Although the specific instrument setup varies, there are a few components that are common. These include,

- Neutron guide tubes
- Choppers
- Beam monitors
- Sample environment
- Detectors

As neutrons are electrically neutral and only carry a weak magnetic moment, they are guided using *neutron guide tubes* [33, 34]: hollow rectangular tubes where the inside is coated with materials highly reflective to neutrons. The guides exploit the fact that below a certain critical incident angle θ_c, neutrons experience total external reflection. This critical angle is material dependent, and by selecting appropriate materials – such as Ni – a sufficiently large critical angle can be obtained to allow efficient neutron transportation. The guides allow neutrons to be transported away from the spallation source to a region where the background is lower, improving the signal-to-background ratio. It is also possible to curve the neutron guides, which removes the instrument from the direct line of sight with the spallation source, further improving the performance.

Along the path of the neutrons, there are choppers [35] which define the wavelength or wavelength range desired for the experiment. There are also *beam monitors* [36] along the route which monitors the neutron flux. These are low-efficiency neutron detectors used for normalization purposes and for monitoring changes in the neutron flux changes between the choppers [37, 38].

At the end of the neutron guide, the neutrons reach the *sample environment*, where the sample under study is located. The purpose of the sample environment is to situate the sample under the desired conditions, such as pressure, temperature, and magnetic field strength. This could also be wet or biological environments. Materials used to enclose the sample are either those that scatter predominately incoherently, such as vanadium, or coherently, such as aluminum. Information on the scattering behaviour of the sample environment is then used for background subtraction.

Neutrons scattered from the sample are finally detected using a neutron detector, which registers the scattered neutrons on an event-by-event basis and assigns each event an energy and a scattering angle. There are different ways in which neutron detectors can be designed, and the parameters and requirements vary drastically between instruments. For example, diffraction measurements usually require an excellent position resolution as they are intended to study neutron scattering angles. Spectroscopy, on the other hand, has different priorities on how the detector should be optimized, as they are designed to measure both scattering angles and energy transfer. The detector under study in this work, the Multi-Grid detector, is intended for neutron spectroscopy measurements.

Out of the initial suite of instruments for ESS, there are five planned spectroscopy instruments, as seen in figure 1.8. Out of these, there are two instruments currently considering the Multi-Grid detector technology, namely the CSPEC and T-REX instruments. Both of these instruments are direct geometry time-of-flight chopper spectrometers. As such, they both use choppers to split the incident neutron beam into neutron bunches, where each bunch contains neutrons within a narrow energy band. The neutrons are sent towards a sample to scatter, whereafter the scattered neutrons are detected in an array of detectors. The exact details of the instrument setup, the neutron energies used and the aimed scientific research areas, are different between the two instruments. This is a crucial aspect, as it affects the design requirements of the detector.

The Cold Chopper Spectrometer CSPEC

CSPEC [39–41] is a cold neutron spectroscopy instrument, optimised for neutrons between 2 - 20 Å (20 - 0.2 meV). An overview of the instrument layout is presented in figure 1.10. The majority of the instrument, the first 160 meters, is designed to prepare a well-defined sequence of neutron pulses. These are then sent towards the object under study, the sample, which can be prepared in various conditions, such as high or low temperature, pressure or magnetic field. Finally, neutrons that scatter off the sample travel approximately 3.5 m to reach the detector, where their hit position and time-stamp are recorded.

The instrument is designed to receive neutrons from the hydrogen moderator, which moderates neutrons down to cold energies. The first part of the instrument is the shutter,

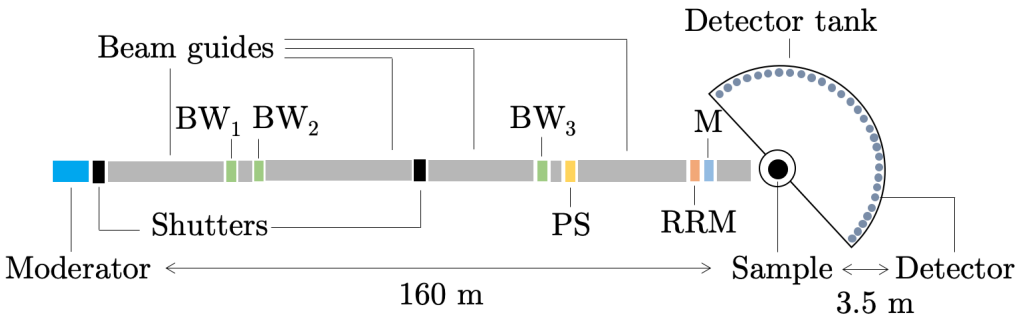

Figure 1.10: Schematic overview of the CSPEC instrument. Neutrons with a broad wavelength band are received from the moderator at the left and are then prepared into a sequence of approximately monochromatic pulses using a series of choppers (BW_1, BW_2, BW_3, PS, RRM and M) whereafter the neutrons scatter of the sample and are recorded in one of the detectors. Abbreviations are explained in the main text. Illustration based on instrument overview in [40].

which is a radiation blocker. This is used for personnel safety when maintenance of the instrument is required. This first shutter is a gamma blocker and is only intended to be used when the accelerator is off. This is for radioprotection from the highly activated target and surrounding shielding. There is also a second shutter, which is intended to block the neutron beam when maintenance is required further downstream.

After the first shutter comes the beam guide (grey), intended to guide the neutron beam towards the sample. The first part of the guide is curved, both in the vertical and horizontal directions. This is to remove highly energetic neutrons from the direct line of sight of the sample. By doing this, the background level of the instrument is decreased. The curved beam guide is followed by the chopper cascade, which is presented in figure 1.11. In the illustration, all of the CSPEC choppers are presented in a time-distance plot. The time-axis is split into segments of frames, where each frame corresponds to one repetition of the 14 Hz spallation source. The time-sequence of neutrons reaching the detector will dependent upon the chopper system and how the neutrons interact with the specific sample being studied. An example of a time-sequence is presented later in Chapter 5 in figure 5.24, where a spectrum corresponding to a $\sim$5 Å neutron pulse incident on vanadium in the LET instrument is shown.

The first choppers in the cascade consist of three Bandwidth choppers, BW_1, BW_2 and BW_3. The purpose of these is to cut the broad incident pulse from the moderator and to select the neutron wavelength band of interest. After that, the incident pulse is further modified by a Pulse Shape chopper (PS), a Repetition Rate Multiplication chopper (RRM) and a Monochromatic chopper (M). These choppers split the broad neutron pulse into a sequence of two or more narrow pulses. In this way, multiple approximately monochromatic

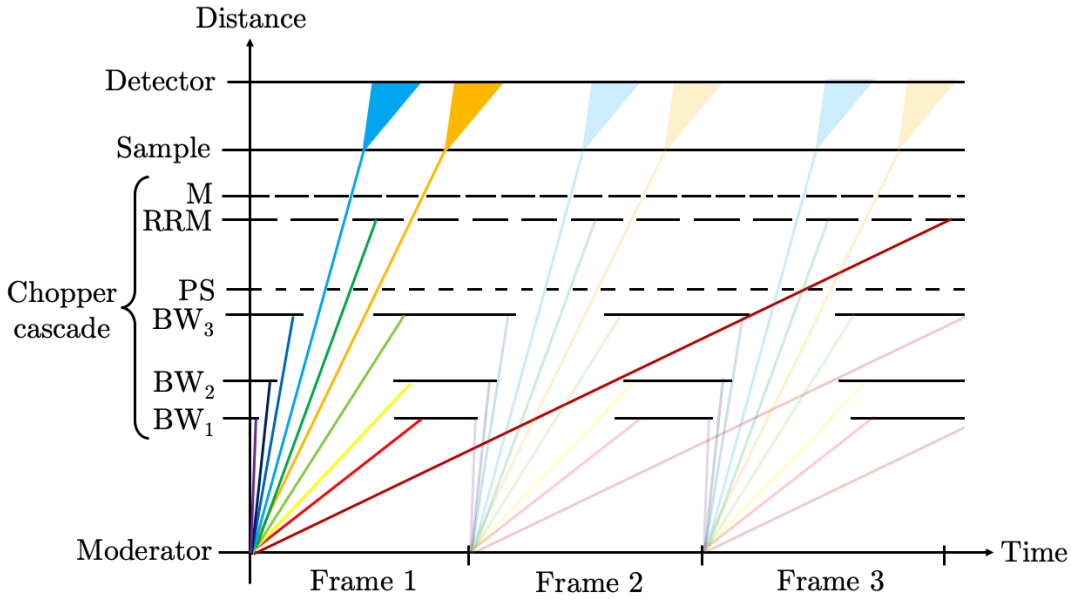

Figure 1.11: Simplified Time-Distance plot of the CSPEC chopper cascade, illustrating how several choppers are used together to prepare a sequence of monochromatic neutron pulses. When the neutron scatters of the sample its energy can change, as indicated by the filled triangles between the sample and detector. The start of each frame corresponds to a proton pulse from the accelerator striking the target. Illustration based on instrument overview in [40].

pulses are sent upon the sample in each frame.

Another function of these choppers is to prevent *frame overlap*, which is when fast neutrons from the following frame, or slow neutrons from the previous frame (dark red line in the figure 1.11), are inadvertently included in the current frame. As such, they would not have the energy intended by the chopper system and would therefore constitute background. Hence, removing these is desired to further increase the signal-to-background level.

After the chopper system has chopped the incident neutron beam into a series of monochromatic pulses, the neutrons hit the sample. The sample is placed within a sample environment, where it can be prepared in a wide range of different conditions. For the CSPEC instrument, this includes, a cryo-furnace, a 12 T magnet, a sample-rotation stage and a goniometer, among others. After the neutrons have scattered from the sample, they travel through the detector tank, which is put under a vacuum, whereafter the neutrons reach the detectors. The detectors are approximately 4 meters tall and are placed in a circumference around the sample.

The Bispectral Chopper Spectrometer T-REX

T-REX [41, 42] is a cold to epithermal neutron spectroscopy instrument, designed for neutrons of wavelengths between 0.7 - 6.4 Å (160 - 2 meV). A general overview of the instrument is shown in figure 1.12. The instrument design is similar to that of CSPEC, including a long section, 164 m, to prepare a sequence of monochromatic neutron pulses, followed by the sample, and finally, the detector tank, 10^{-6} mbar vacuum, where the neutrons can be detected in the detector array. Additionally, T-REX also has a wider energy span and the ability to polarise the neutron beam.

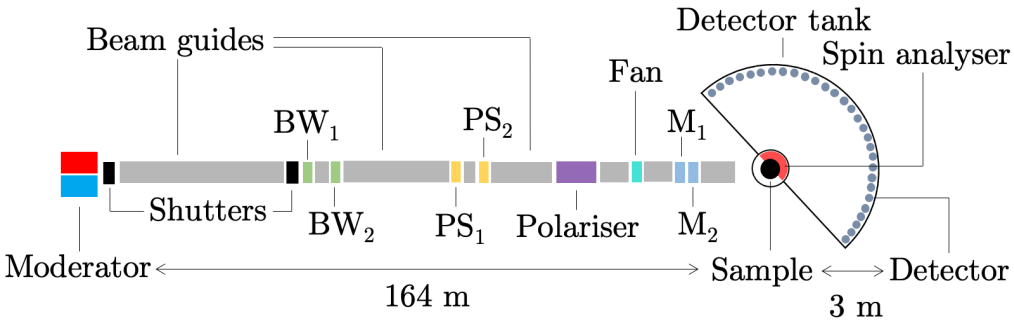

Figure 1.12: Schematic overview of the T-REX instrument. Illustration based on [41] and [43].

In contrast to CSPEC, T-REX can use neutrons from both the cold hydrogen moderator (blue) and the thermal water moderator (red), and it is referred to as a bispectral spectrometer. The instrument also has a different chopper cascade, including two BW choppers, two PS choppers, two M choppers and a *Fan* chopper. The purpose of the Fan chopper is to avoid frame overlap by suppressing neutrons from previous and following frames.

One of the main differences from CSPEC is that T-REX is equipped with a Polariser (purple) and Spin analyser (light red). As the name implies, the polariser can polarise the incident neutron beam, which is useful for experiments where the magnetic interactions should be separated from nuclear interactions. After the neutrons scatter of the sample, the "Magic-PASTIS"-setup [44], is used to analyse the spin of the scattered neutrons.

1.3 Neutron detection

One of the most important components of the T-REX and CSPEC instruments, as for all neutron scattering instruments, is the neutron detector. The neutron detector registers neutrons that are scattered from the sample as neutron events, where each event typically contains the neutron hit position on the detector and the associated timestamp. The aggregate of these events is then used to analyse the properties of the material under

study. The challenge is that one of the main advantages of using neutrons in scattering measurements, their weak interaction with matter, also complicates their detection.

Neutron detection is demanding because neutrons carry no electric charge. Additionally, because of the low neutron energies used in neutron scattering, it is not possible to use particle recoil techniques that are available for higher energy neutrons. Therefore, to detect low energy neutrons, a more indirect method is used. This is based on exploiting a strong neutron absorbing isotope – such as ^{6}Li, ^{10}B or ^{157}Gd – known as a *neutron converter*. A converter can capture a neutron, creating a new unstable nucleus, which then promptly decays into one or more charged particles. This process is shown in figure 1.13 where a neutron capture in ^{10}B is used as an example.

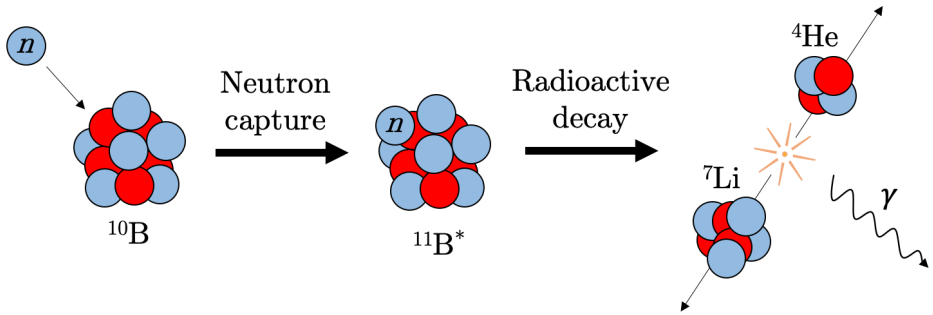

Figure 1.13: Illustration of a neutron capture reaction in ^{10}B. A neutron is seen approaching a ^{10}B-nucleus, whereafter the neutron is captured and an unstable ^{11}B*-nucleus is created. This nucleus then decays into a ^{4}He and a ^{7}Li nuclei, which are emitted back-to-back. In the main decay branch of this reaction, a gamma ray is also ejected.

The converter material is coupled with a charged particle detector system – such as a proportional counter, which is used as an example here – so the released charged particles from the neutron capture reaction can be registered. To do this, there are four general strategies, as seen in figure 1.14. To make the detection process as efficient as possible, two parameters are primarily optimised: the probability of neutron capture in the converter material and the probability of a conversion product reaching the proportional gas.

The first strategy entails using a single solid converter layer, placed perpendicular to the incident neutron beam. The second strategy, in contrast, is to tilt a converter layer with respect to the beam. This increases the neutron travel path through the material, increasing the absorption probability, while keeping the escape distance for the capture products as short as possible. The third strategy uses a sequence of thin layers perpendicular to the incident beam. This gives a large absorption probability, due to a long aggregate neutron travel path through all the layers, while at the same time keeping a high conversion product escape probability, as the escape path is kept short in each layer. The fourth and final method involves using a gaseous neutron converter, such as ^{3}He or ^{10}B in the chemical

form of BF_3, which can also function as a proportional gas.

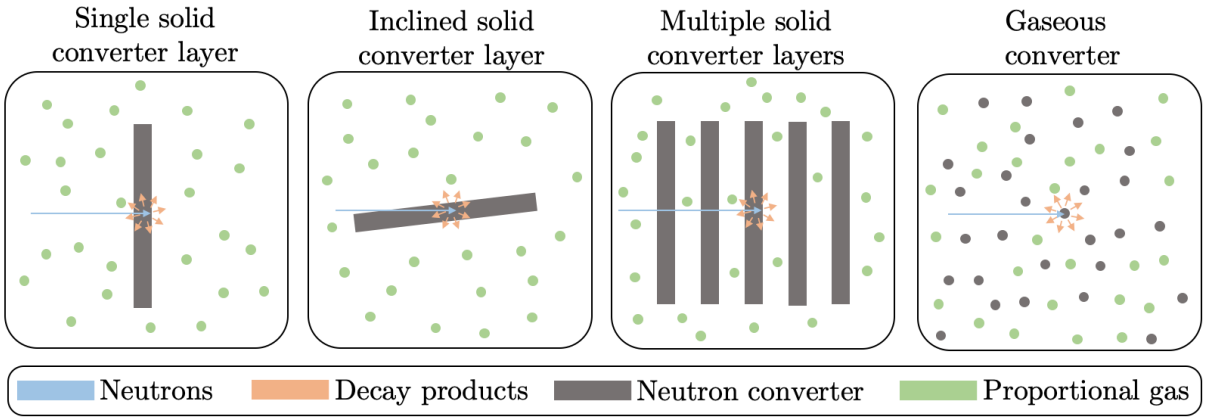

Figure 1.14: Summary of neutron converter usage. From left to right, the methods include: a single solid converter layer, an inclined solid converter layer, multiple solid converter layers and a converter in gaseous form. All methods involve the capture of a neutron (blue) in a converter (grey) and the detection of the capture products (orange) in a proportional gas (green).

In an indirect neutron detection measurement, all information about neutron energy and direction is lost after the conversion, and to extract those properties experimentally other means are necessary. This is done by using a timing system to keep track of when the neutrons are sent towards the sample – start time – and when the neutrons are collected in the detector – stop time – as illustrated in figure 1.7. The difference between these two times can then be used to reconstruct the neutron flight time. If this is combined with the neutron hit position in the detector, which gives the flight distance, then the neutron velocity can be inferred. From these quantities, it is then possible to calculate the neutron energy and momentum, as well as the direction (i.e. scattering angle) via the neutron hit position in the detector. In this method, a straight travel path from the scattering in the sample to the detection point in the detector is assumed.

Note that because of the relatively slow speed of thermal neutrons, ~ 0.2 cm/μs at 1.8 Å, the energy resolution of neutron detectors is limited by how accurately the location of the conversion reaction is known, as even a small uncertainty in location results in a relatively large uncertainty in time due to the slow speed of the neutrons (at 1.8 Å, the conversion events would be spread over 5 μs if the possible conversion distance is 1 cm). Hence, gaseous detector tubes should not be made too thick – a typical diameter is around 2.5 cm – and the distance between adjacent converter layers not too great – the Multi-Grid detector uses 1 cm spacing.

Furthermore, since neutrons are detected indirectly through charge deposited in the detector, any other charge resultant from non-neutron events – such as from cosmic background

radiation and intrinsic radioactivity in the detector – can induce false signals that are interpreted as neutrons. Such undesired background events can in principle degrade the instrument's overall signal-to-background ratio severely and therefore compromise the integrity of any given neutron scattering experiment.

To conclude, the energy resolution of the detector together with the signal-to-background ratio is vital to the performance of a neutron detector. This is especially true for detectors used in neutron spectroscopy and will therefore be of prime importance for the Multi-Grid throughout this work.

1.3.1 Signal generation

When a charged particle travels through matter it can lead to ionisation, creating electron-ion pairs. There are different ways to exploit this mechanism for radiation detection – such as using gaseous, scintillation or semiconductor diode detectors [45] – but the goal is always to extract the electrical signal out of the passing ionising particle. The focus in this section will be on gaseous radiation detectors.

Gaseous detectors use an electric field over a gas-filled volume to keep the released ions and electrons separated – which would otherwise recombine due to their charge attraction – and to drift them toward the detector cathode and anode for charge collection. Depending upon the mode of operation, the electric field may be set high enough to create secondary charges released from the accelerated primary electrons and ions. This is called a charge *avalanche*, also known as a Townsend avalanche, which can increase the signal produced by many orders of magnitudes. The movement of the charge in the electric field induces a measurable current which can be recorded and analysed.

The operational principle of a gaseous detector can be segmented into four parts: ionisation, the choice of gas, the choice of voltage, and current induction. These are discussed sequentially below, starting with ionisation.

Ionisation

For an incident particle to cause ionisation an energy exchange has to take place [46]. Here, the focus is on ionisation caused by charged particles and photons, which are of main concern to gaseous detectors.

A charged particle can interact with matter in different ways, including via strong and weak nuclear interactions, but the most probable interaction is electromagnetic interaction. For gaseous detectors, this mechanism predominately occurs through Coulomb interactions between the charged electrons and ions. This is captured by the Bethe-Bloch formula,

which models the energy loss per unit length, also known as the *stopping power*, of a charged particle traversing a medium. The formula is presented in equation (1.24),

$$\frac{\mathrm{d}E}{\mathrm{d}x} = -K \cdot \frac{Z}{A} \cdot \frac{\rho}{\beta^2} \left[\ln\left(\frac{2m_e c^2 \beta^2 E_M}{I^2(1-\beta^2)} \right) - 2\beta^2 \right], \tag{1.24}$$

where

$$K = \frac{2\pi N z^2 e^4}{m_e c^2}, \quad E_M = \frac{2m_e c^2 \beta^2}{1-\beta^2}, \quad \beta = \frac{v}{c}.$$

In the formula, Z, A, ρ and I refer to the medium the particle is traversing, and represents its atomic number, atomic mass, density and effective ionisation potential, respectively. The variables z and v refer to the traversing particle and represent its charge and velocity. The remainder of the formula is composed of constants, where N is the Avogadro constant, m_e is the electron mass, c is the speed of light, and e is the elementary charge. Note that the expression is independent of the mass of the incident particle.

Inspecting the formula, it is seen that stopping power increases with both the atomic number Z and density ρ of the medium, as well as the charge z of the incident particle. The dependence on particle velocity v, however, depends on two factors with opposite trends: β^{-2} and $(1-\beta^2)^{-1}$. Increasing the velocity from zero results in an initial steep decrease in stopping power, dominated by β^{-2}, followed by a slow rise from $(1-\beta^2)^{-1}$ inside the logarithm. In between these regions, the stopping power has a minimum value, and particles propagating at these velocities are known as *minimum ionising particles*. An important feature of this velocity dependence is that incident charged particles lose most of their energy at the end of their path. This is because that is where their velocity has been decreased the most and the stopping power is largest.

As with ionisation caused by photons, there are three primary processes involved: Photoelectric effect, Compton scattering and Pair production. The probability for these interactions to occur varies with the photon energy and atomic number Z of the medium the photon traverses, as shown in figure 1.15.

For low energies, the photoelectric effect is dominant. In this process, the photon is absorbed by a bound electron, transferring all its energy to the electron. The electron is then emitted with an energy $E_e = E_\gamma - E_b$, where E_γ is the energy of the photon and E_b is the binding energy of the electron. For medium energies, ranging from a few hundred keV to a few MeV, Compton scattering is the predominant process in this energy range. This process involves photons colliding with bound electrons, transferring part of their energies in inelastic collisions. This results in recoiling electrons, where each electron has an energy related to the photon-electron scattering angle. Finally, at even higher energies, pair production is dominant, which involves the creation of an electron-positron pair from

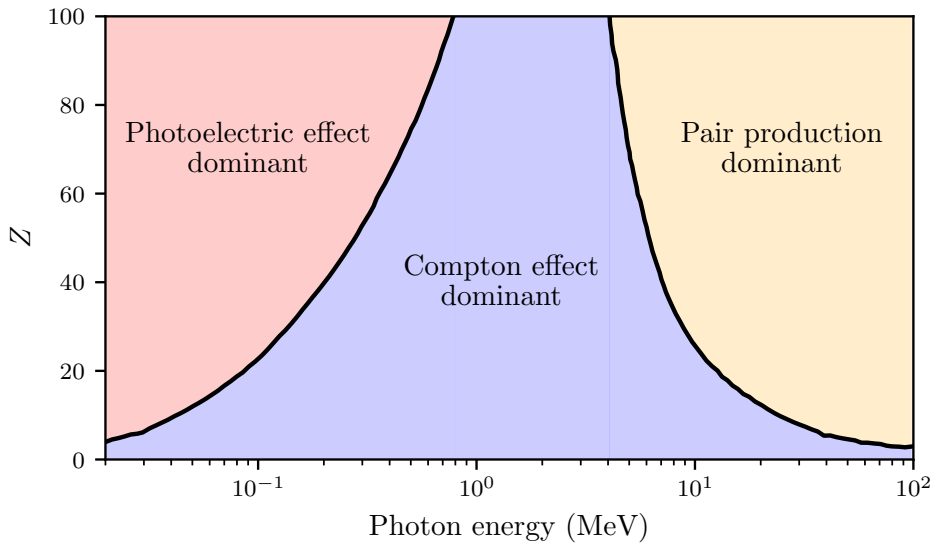

Figure 1.15: Overview of where the three photon-matter interactions – Photoelectric effect, Compton scattering and Pair production – are dominant as a function of photon energy and the atomic number Z of the medium the photon is traversing. The solid lines indicate where the probability is equal for two adjacent processes. Figure adapted from [45].

a photon. Note that all these processes involve the release or creation of charged particles, which then interact with matter in a similar way as that described in the Bethe-Bloch formula above.

When charged particles traverse a gas, they lose energy through charge collisions and cause ionisation. The total number of electron-ion pairs created from this ionisation, n_T, can be expressed according to,

$$n_T = \frac{\Delta E}{w_i} \tag{1.25}$$

where ΔE is the total energy loss in the gas volume and w_i is the average energy needed to produce one electron-ion pair. Therefore, gases with a low value for w_i give rise to more electron-ion pairs. This results in better statistics and the ability to detect lower energy particles. This aspect and a few others are explored next, where the appropriate choice of filling gas for the detector is discussed.

Gas

There are several factors to consider when selecting the gas for a radiation detector. First of all, the gas molecules should have low ionisation energy, enabling a large number of primary electron-ion pairs for a given energy loss in the gas volume. Having low ionisation energy also has the advantage that the detector can be operated at lower voltages and still enable charge avalanches, as even a small acceleration enables the initially released charge to induce secondary ionisation. This allows a high *gain* – a large increase in total released

charge compared to that initially released from the original ionising particle – even at low voltages. This is desirable from a practical operational point of view.

Low ionisation energy is a property found in noble gases. While more complex molecules – including CO_2 and C_4H_{10} – can dissipate energy in various non-ionising modes such as vibration and rotation, these options are not available to noble gases – He, Ne, Ar, Kr, Xe and Rn – which do not form molecules. Instead, the main mode of energy dissipation for noble gases is through ionisation. For this reason, using a noble gas as the main component in a gaseous detector is desirable. If cost is also taken into consideration, then the preferred choice is often Ar.

In addition to the noble gas, there are two other gases commonly added, namely *quenching gases* and *stopping gases*. The former is introduced to reduce the spread of avalanches, which can become continuously self-propagating in a volume where a noble gas is the only component. This is due to subsequent photon emissions, released in connection to the ionisation, which can induce further ionisations. Quenching gases include complex molecules, as the ones mentioned earlier, which attenuate the avalanches by non-ionising processes. This is done by absorbing the photon energy into vibrations and rotations. By mixing a quenching gas with a noble gas, higher gains can be achieved without continuous avalanches being released.

A stopping gas is added to increase the overall stopping power of the detector, which decreases the path length of the incident radiation before it is completely stopped. Because of the reduced path length inside the detector, the time and position resolution can be increased on when and where the particle was stopped in the detector volume.

In addition to the quenching and stopping gas, it is also possible to add small amounts of electronegative gases, such as O_2. These gases have a propensity to capture electrons and create long-lasting negative ions. Once electrons have been joined into ions, they can no longer cause further avalanches. It is therefore possible to use electronegative gases as an additional means to regulate the avalanches, which can further increase the gain of the detector. That being said, because the electronegative gases attenuate the avalanche processes they also compromise the detection efficiency of the detector, and only small quantities can be used.

Voltage

The response of a gaseous detector depends upon the voltage applied over the gas volume. This is categorised into different regions, as illustrated in figure 1.16[5]. In the first region,

[5]For detectors with an asymmetric electric field in the detection volume, such as the Multi-Grid detector, more detailed considerations than this general outline might be required. This is because, although detectors generally follow the trends outlined in the graph, different portions of the active

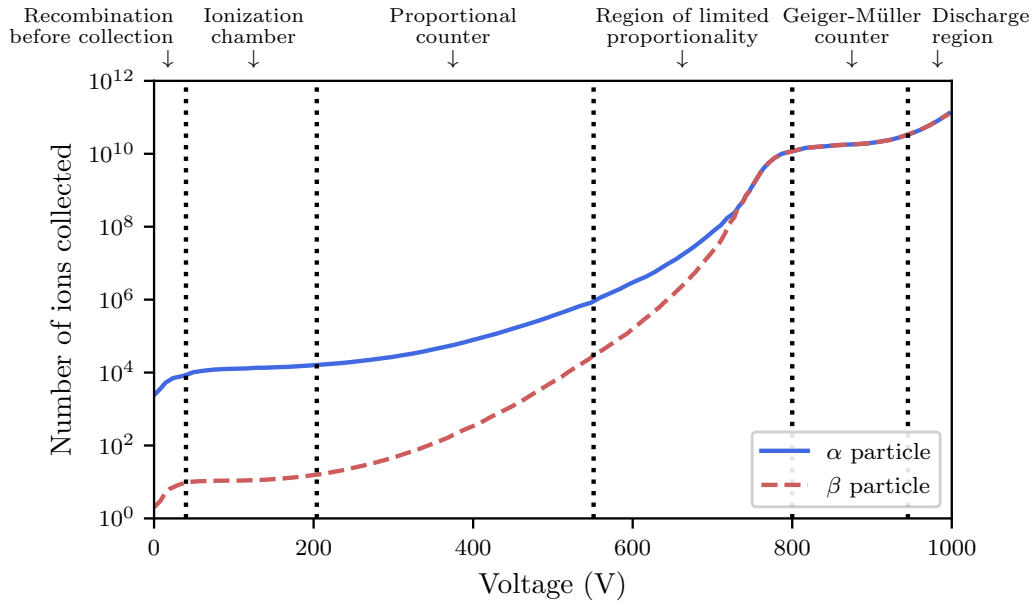

Figure 1.16: Typical dependence of the number of ions collected as a function of applied voltage, where the different regions have been annotated. In the diagram, the dependence for alpha and beta particles is shown. Note that the absolute number of collected ions depends on the detector specifications – such as gas, pressure and geometry – as well as the incident energy of the radiation. As such, the stated voltages for the different regions above does not, for example, correspond to the voltages needed to reach the same operational regions in the Multi-Grid detector. Figure adapted from [47].

there are a small number of ions collected due to the effect of electron-ion recombination. This changes when the voltage is increased to the second region, where *ionization chambers* operate. There the applied voltage is sufficient to prevent recombination and the number of collected ions is, ideally, equal to the number released by the ionising particle. If the voltage is further increased, the region of *proportional counters* is reached. In this region, the electric field is strong enough to accelerate the released electrons to energies where they can create more ion-electron pairs, resulting in charge avalanches. The total collected charge resulting from the avalanches is proportional to the energy of the original ionising particle. When the voltage is raised further, the region of *limited proportionality* is reached. Here the proportionality is partly lost, leading the way to the region of *Geiger-Müller counters* if the voltage is increased even higher. At this point, it is only possible to measure if a particle traversed the volume or not: there is no information on the energy of the original particle. The last step is when the voltage is so large that discharges start to occur between the cathode and anode. Starting from the Geiger-Müller region it is no longer possible to separate between the alpha and beta particles, as both particles induce avalanches that saturate the detector with charge.

volume could be operating in different modes due to differences in electric field strength across the active volume.

The focus in the following discussion is on proportional counters, as this is how the Multi-Grid detector is designed to operate. As a starting point, a detector with a cylindrical geometry is considered. This consists of a gas-filled conductive cylindrical tube with a metal wire running through the centre. The wire and cylinder shell are electrically insulated from each other and a potential difference is applied between them. The wire (anode) is set to be positive with respect to the cylinder (cathode). Between the anode and the cathode, there is now a radially symmetric electrical field, which depends inversely on the distance r from the centre of the wire according to $E(r) \propto r^{-1}$.

When an ionising particle traverses the gas-filled volume, the released electrons and ions will drift toward the wire and the cylinder respectively. Due to the asymmetry of the electric field, which is stronger close to the wire, only the electrons will induce charge avalanches. This occurs close to the wire, usually a few wire radii from the centre. A schematic illustration of this process is shown in figure 1.17.

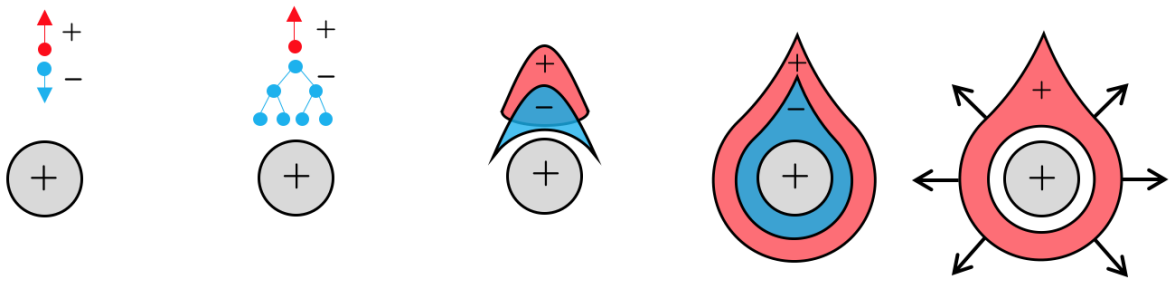

Figure 1.17: Schematic time sequence showing the avalanche growth along a thin wire (circle with a plus), as seen from the top. A released ion (red circle) and electron (blue circle) are seen in the leftmost frame. Figure adapted from [47].

In the first frame, the released electron and ion start to drift in opposite directions. In the second frame, the electrons are seen approaching close to the wire and avalanches are initiated. These avalanches are further propagated in the third and fourth frames, where the released electrons are seen enclosing the wire, covered by an outer shell of released positive ions. Finally, in the fifth frame, all the electrons have been collected, as they were released close to the anode, and only the positive ions remain. The positive ions drift towards the cylinder shell, and it is this movement which leads to the main signal generation in the detector.

In addition to the simple example mentioned above, it is possible to construct more complicated detector geometries. An example of this is the Multi-Wire Proportional Chamber (MWPC), which is constructed out of a plane of wires placed between conductive plates. The detection principle for this geometry is similar to that of the tube detector. That is, avalanches are created when the electrons reach the vicinity of the anode wires and the subsequent drift of the released positive ions then induce measurable currents in both

electrodes.

Current induction

When the released electrons and ions drift in the gas they induce a measurable current in the detector. This is a result of the released ions attracting – and electrons repelling – the electrons in the electrodes maintaining the electric field. A simple example of this can be seen in figure 1.18, where a positive charge is placed between two electrodes.

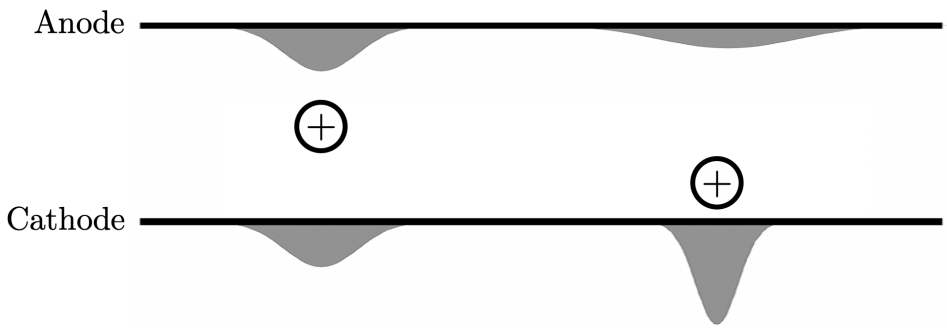

Figure 1.18: A positive charge placed between two electrodes, illustrating how electrons are accumulated on the cathode and anode by the attractive electric force of the positive charge. Two different positions of the charge are seen: one centred between the electrodes (left) and one closer to the cathode (right). Figure adapted from [47].

From the figure, it is seen that the electric field generated by the positive charge accumulates electrons on the anode and cathode. The ability of the positive charge to accumulate electrons on the electrodes depends on the electric field strength exerted by the charge, which depends on the distance between the charge and the electrodes. This is seen by comparing the charge profile in the left and right cases in the figure. If the positive charge is moving, there will be a change in the charge profiles on the electrodes over time. In other words, a moving charge induces a current.

The current induced on the electrodes depends on several factors – including the electric field strength between the electrodes, the detector geometry and the velocity of the moving charges – but most importantly the polarity of the charge and whether it is drifting with or against the electric field generated by the electrodes. To illustrate this, the situation in figure 1.18 is considered. As the positive charge moves from the centre towards the cathode, there is an outflow of electrons in the anode – which experiences a progressively weaker attraction from the positive charge due to the increasing distance between them – and an inflow in the cathode – where the opposite effect takes place. This means that a positive current is induced in the cathode and a negative current is induced on the anode. This effect is captured by the golden rule of induced signal formation, which uses a positive charge to explain the principle (for a negative charge, the signs are reversed):

> *A positive charge moving towards an electrode generates an induced positive signal; if it moves away from the electrode, the signal is negative.* [47]

The formalism for calculating induced currents on arbitrarily shaped conductors by a moving charge was developed by Ramo and Shockley [48, 49]. The basic relation is shown in equation (1.26) – modified to account for both positive and negative charges – where the induced instantaneous current in an electrode at unit potential by a moving charge is seen,

$$i = -qvE_v \tag{1.26}$$

where q is the particle charge, v is the particle velocity and E_v is the component of the electric field in relation to the direction of the particle. The equation assumes the field E_v which would be available if the charge was not present. It also assumes that all conductors except the electrode, which is at unit potential, are grounded.

In a wired detector, such as those presented previously, the induced current is mainly a consequence of the positive particle movement. This is seen in figure 1.17, where the created electrons are swiftly collected at the anode leaving only the ions to drift. This drifting of the positive ions then generates currents in both the anode and the cathode.

The quick collection of electrons is not only a consequence of their proximity to the wire but also due to their higher *mobility* than ions. Electrons drift in the gas with velocities of around 3 orders of magnitude faster than the ions, and it can take ions around milliseconds to reach the cathode to be neutralized. Due to demands on the count rate capabilities of the detector, the full current induced by the ions cannot be analysed and the processing is restricted to only parts of the signal. This is the topic of the next section, where signal processing is discussed.

1.3.2 Signal processing

Signals from the detector can be extracted in different ways depending upon the mode of operation, including current mode, mean square voltage mode and pulse mode [45]. The relevant mode for the detector under study in this work is pulse mode, which is the focus here. The basic scheme for the pulse mode is presented in the circuit diagram in figure 1.19.

When charges are moving in the gas volume, currents are induced on the electrodes of the detector. By connecting a capacitor and resistor to the circuit, this current can be made to charge a capacitor. After the capacitor has been charged, it will start to discharge via the resistor. This creates a voltage drop which can be measured as a function of time.

In this scheme there are two time constants to consider, namely the charge collection time

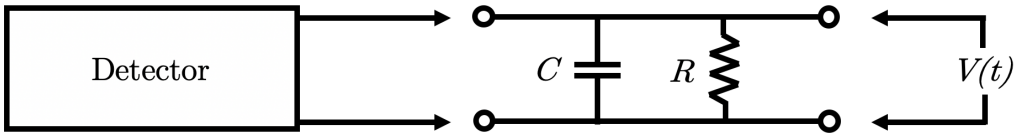

Figure 1.19: Simple circuit diagram illustrating how the induced current in the detector is used to charge a capacitor which then discharges via a resistor. The voltage is measured as a function of time over the resistor. Figure adapted from [45].

t_c, which is detector dependent, and the circuit time constant $\tau = RC$, which determines the discharge time of the circuit. Commonly, the circuit is designed so that $t_c << \tau$, which means that the trailing edge of the pulse is much longer than the leading edge. A benefit from this configuration is that the total charge Q collected from the current can be found through the simple relation in equation (1.27),

$$V_{\max} = \frac{Q}{C}, \tag{1.27}$$

where $V_{\max}$ is the maximum voltage recorded and C is the capacitance of the circuit.

The output of the circuit above is a succession of events – each with a fast rise time and long decay time – which have two important characteristics. Firstly, due to the relation given in equation (1.27), the important information of each event is in the peak maximum, which corresponds to the total charge collected in the capacitor. Secondly, due to the long tails of the events, there can be an off-shift in the peak maximum due to overlap between adjacent events.

To address event overlap, a *shaping circuit*[6] is introduced. The purpose of the circuit is to re-shape the long-tailed pulses received from the first circuit into a sequence of independent peaks. This is done using a sequence of CR-RC components, which are seen in the basic circuit diagram in figure 1.20. Depending upon the final shape desired, the number of CR and RC circuits in sequence can be adjusted. One way of doing this is by placing a first CR-circuit followed by n RC-circuits, CR-(RC)^n, all with equal values of $\tau = RC$. This gives Gaussian output pulses.

The output of a Gaussian shaping circuit can be expressed according to equation (1.28),

$$V_{out} = V_{in} \cdot \left(\frac{t}{\tau}\right)^n \cdot \exp\left(-\frac{t}{\tau}\right) \tag{1.28}$$

where V_{out} is the output-voltage, V_{in} is the input-voltage, t is the time and n is the number

[6]The circuit presented here corresponds to analogue pulse shaping. It is also possible to do – more expensive – digital pulse shaping, which requires a high sampling rate.

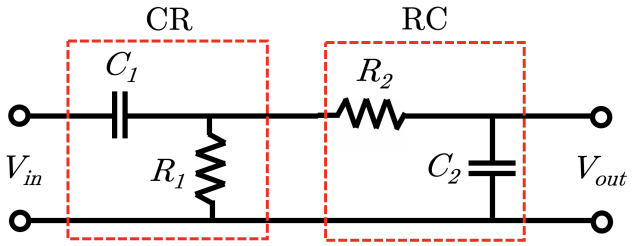

Figure 1.20: A diagram of a CR-RC shaping circuit. Figure adapted from [45].

of repetitions of the RC-circuit. The value of τ is also known as the *shaping time* and the value of $n\tau$ is known as the *peaking time*, which is the time needed for the output Gaussian pulse to reach its maximum. If a value of $n = 4$ is used, a good approximation of a Gaussian pulse is acquired. Note that the shaping time should be kept short enough to avoid overlap between adjacent events, but long enough to collect all the charge from the leading edge in the original pulse.

Using a Gaussian shaping circuit, the initial sequence of long-tailed pulses is transformed into a series of Gaussian pulses. The next step is to digitize these analogue pulses using Analog-to-Digital Converters (ADCs). Using ADCs, the timing and charge of each recorded event are stored in strings of data. From these values, it is then finally possible to extract all the neutron physics discussed previously: neutron scattering angles, neutron momentum transfers and neutron energy transfers.

Based on this neutron detection principle, the working of the Multi-Grid detector and its implementation is presented next.

Chapter 2

The Multi-Grid detector

The Multi-Grid is a large area (tens of square meters) cold to epithermal neutron detector concept, designed for time-of-flight neutron spectroscopy measurements. The detector has been designed to have equivalent, if not better, performance as conventional helium-3 tubes – as well as an equal price to the historic (before 2009) cost of helium-3-based detectors – and it is intended to be simple and scalable. The core principle of the detector is based on neutron absorption in multiple layers of $^{10}B_4C$ coupled with an MWPC, where neutrons are indirectly detected via the decay products from the ^{10}B neutron capture. The specific design details, such as detector dimensions and neutron wavelength optimisation, are tailored for the intended application. In this work, the focus is on the detector development for one of the ESS neutron spectroscopy instruments, CSPEC. This instrument has the detector requirements presented in table 2.1. Here, an introduction is given to the detection

Table 2.1: CSPEC detector requirements [40].

Specification	Requirement
Lineshape*	$\leq$ 2.5 times that of helium-3 detectors
Efficiency	$\geq$ 60 % at 4 Å
Count rate	$\geq$ 50 times that of helium-3 detectors
Intrinsic background level	< 0.35 Hz/m^2
Signal-to-Background†	$\geq 10^4$ at 5 Å
Gamma sensitivity	$\leq 10^{-6}$
Momentum resolution, $\Delta Q/Q$	< 2 %
Energy resolution, $\Delta\hbar\omega/E_\mathrm{i}$	< 1.5 % for wavelengths longer than 4 Å
Azimuthal angular coverage	$5^\circ \rightarrow 140^\circ$
Polar angular coverage	$90^\circ \pm 26.5^\circ$

* Based on tof spectra from an incoherent scatterer, measured at 2 K, in the region between $[3\sigma, 5\sigma]$ of the elastic peak.

† Based on tof spectra from an incoherent scatterer, where *signal* is the maximum value in the elastic peak and *background* is the time-independent background level.

principle and detector implementation, together with the current status of the detector

development.

2.1 Principle

The foundation of the Multi-Grid detector technology is based on neutron absorption in ^{10}B, recall figure 1.13, and is summarised in the reaction formula,

$$n + {}^{10}\mathrm{B} \rightarrow {}^{11}\mathrm{B}^* \rightarrow \begin{cases} {}^{7}\mathrm{Li}\,(0.83\,\mathrm{MeV}) + \alpha\,(1.47\,\mathrm{MeV}) + \gamma\,(0.480\,\mathrm{MeV}) & (94\,\%) \\ {}^{7}\mathrm{Li}\,(1.01\,\mathrm{MeV}) + \alpha\,(1.77\,\mathrm{MeV}) & (\ 6\,\%) \end{cases} \tag{2.1}$$

where the resulting excited ^{11}B nucleus promptly decays into two charged particles, a ^{7}Li-nuclei and an α-particle, and a 480 keV gamma-ray in the 94% decay branch. The Multi-Grid detector uses ^{10}B in the form of boron-carbide, $^{10}B_4C$, which is more mechanically and chemically stable than pure ^{10}B. In the design discussion presented below, the focus is on the dominant 94 % decay branch, and the kinematics are approximated as back-to-back for the charged particles, neglecting the momentum of the gamma-ray.

By placing $^{10}B_4C$ inside a proportional counter, captured neutrons can be inferred via the detection of any of the conversion products[1]. This is done by stacking several thin converter layers perpendicularly to the incident neutron beam, as shown in the third detection strategy presented in figure 1.14. The thickness of the converter layers is determined by the *effective range* of the ^{7}Li and α decay products, i.e. how far they can move in the $^{10}B_4C$ and still have sufficient energy to be detected in the proportional counter. The maximum effective ranges for the 1.77 MeV α-particle and the 0.83 MeV Li ions are 3.95 μm and 1.35 μm, respectively [3]. Having converter layers thicker than the maximum effective range is ineffective, as neutrons converted deep in the layer will result in decay products trapped in the converter. This needlessly lowers the probability of neutrons reaching the subsequent conversion layers, thus lowering the efficiency of layers located further downstream from the incident neutrons.

A few microns thick layers of $^{10}B_4C$ is not mechanically stable and are therefore deposited on thin substrates of aluminum. This is illustrated in figure 2.1, where incident neutrons are seen passing a sequence of $^{10}B_4C$+Substrate+$^{10}B_4C$ units, called *blades*. There are two $^{10}B_4C$ layers on each blade in which neutrons can be absorbed, as seen in the zoomed-in view to the right. The left case – decay products exiting in the same direction in which the neutron entered the layer – is called *forward-escape*, while the right case – decay products exiting in the opposite direction in which the neutron entered the layer – is called

[1]Detecting both conversion products simultaneously from a single capture reaction, although possible, is technically challenging. This is because the capture reactions are emitted back-to-back, which means that the free-standing $^{10}B_4C$ layer has to be sufficiently thin (around 1 μm) to allow both products to escape. This would make the converter layer fragile and sensitive to vibrations.

backward-escape[2]. In each case, only one of the two decay products can escape into the gas: the other is stopped in the substrate.

Between the blades, there are the anode wires. The wires are positively biased whereas the blades are set to ground, establishing a strong electric field between them. When a charged decay product escapes the $^{10}B_4C$ layer it ionises the gas molecules, leading to charge avalanches which free electrons and ions that then start drifting in opposite directions. The movement of the particles induces a current in both wires and blades, which is used to infer the absorption of the neutron. The details of this process are outlined in Chapter 1.3.1.

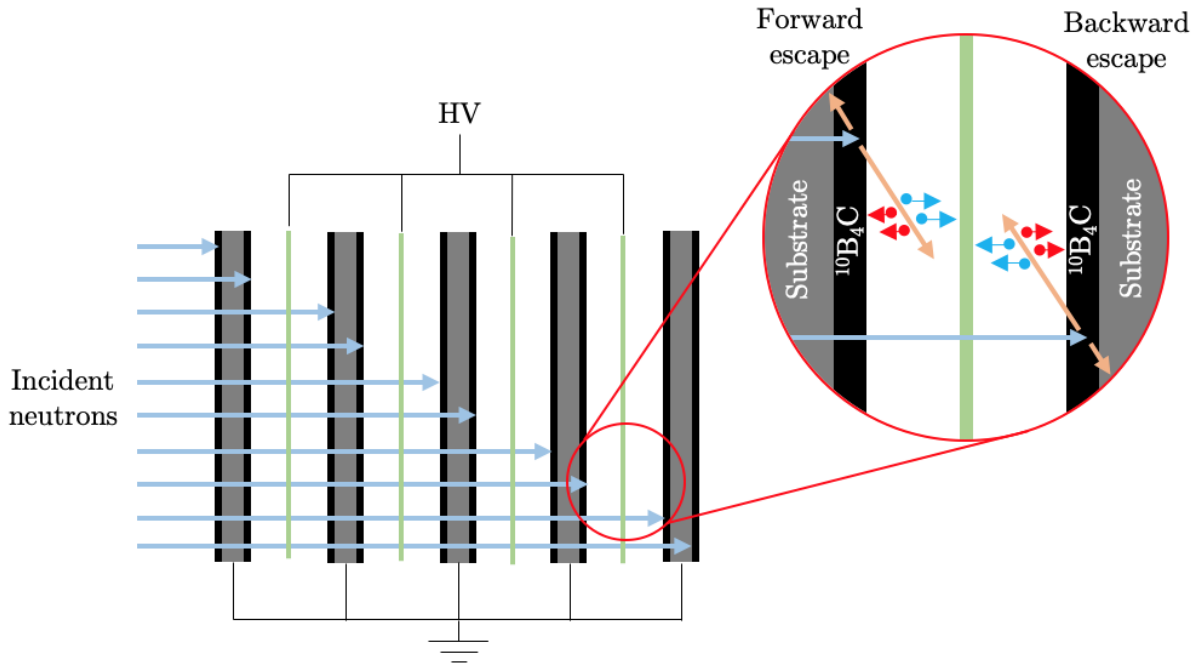

Figure 2.1: Illustration of neutron capture in the Multi-Grid detector, where the neutrons are detected in a sequence of $^{10}B_4C$+Substrate+$^{10}B_4C$ units. Incident neutrons (light blue) and capture products (orange) are shown in zoomed view to the right, together with released electrons (blue) and ions (red). The wires are shown in green and are connected to an HV supply, while the substrates and layers are connected to the ground. Note that only one capture product per reaction can escape the blade into the gas volume, the other is stopped in the substrate.

To extend the active surface area of the detector and to achieve three-dimensional position reconstruction – which is important for the neutron sample-to-detection flight length calculation, recall figure 1.7 – the arrangement presented in figure 2.2 is used. As can be seen, the active volume of the detector is composed of a stacked column of multiple identical *grids*. An example of a grid is highlighted at the bottom of the figure. Each grid

[2]In other publications the two modes are referred to as *transmission* and *back-scattering* mode, respectively. However, because of a similar nomenclature used here in the chapter on shielding, this was adjusted in this work to avoid confusion.

is composed of *normal blades* (aluminum substrates coated with $^{10}B_4C$) and *radial blades* (aluminum substrates either coated or non-coated with $^{10}B_4C$), which forms a grid array of cells. These cells are aligned with each other when the grids are stacked in a column, forming long rectangular tubes that go from the top to the bottom of the detector. The wires are then drawn within these tubes: one wire per stack of cells. This can be seen through the window at the front of the detector, which has been added for visualisation purposes. Each wire is positioned at the cell centres, while the grids are kept separated from each other using small spacers at the front (dark grey) and a larger insulator at the back (green). This segments the detection volume into a collection of rectangular *voxels*.

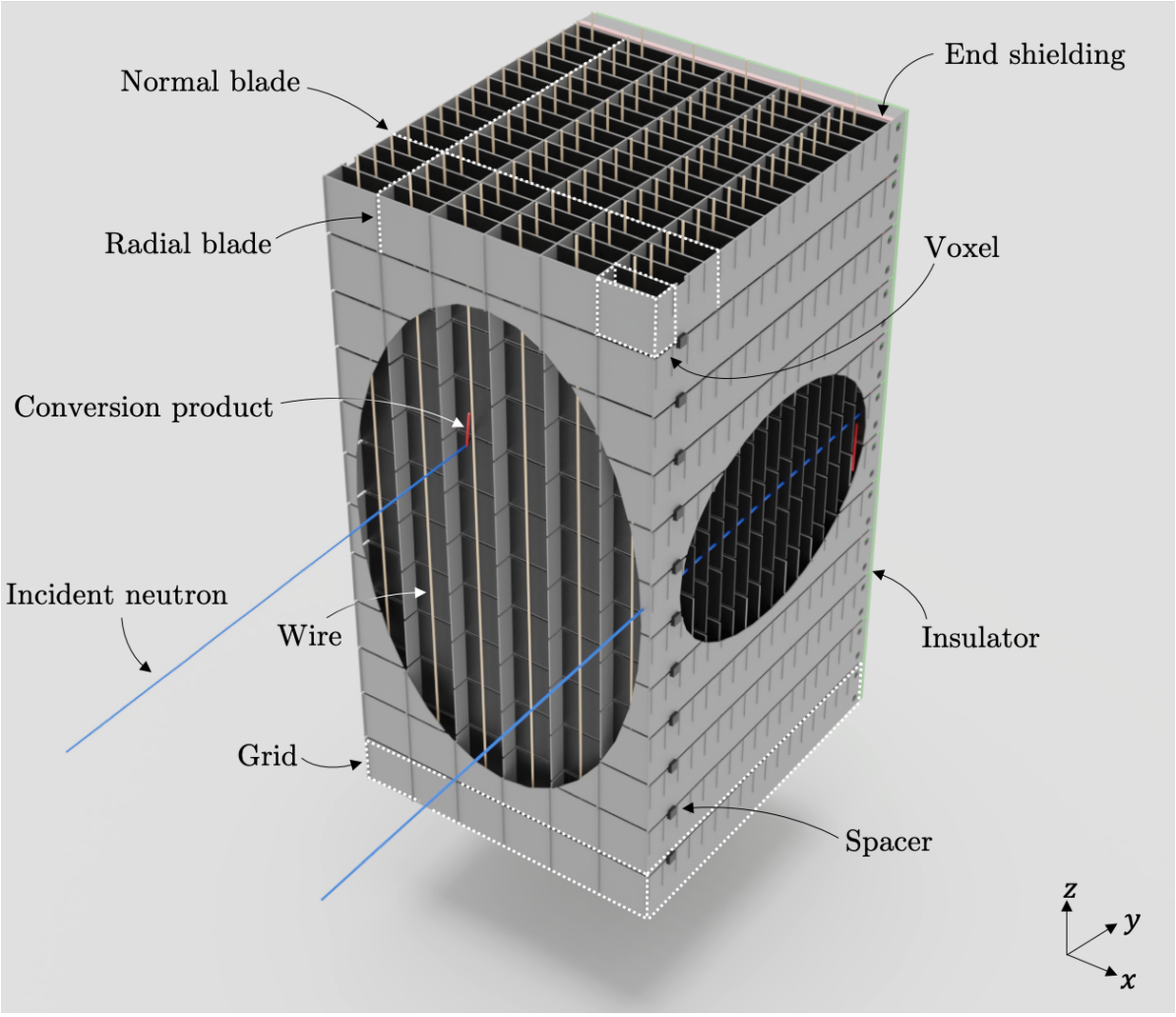

Figure 2.2: Overview of the Multi-Grid detector geometry, where the important components are annotated. To visualise parts of the internal structure, two elliptical viewing windows have been added: one at the front and one at the side. Note that each wire goes through all the grids in the column: one wire per stack of cells.

When incident neutrons (blue) arrive at the detector, they are absorbed in one of the layers and emit a conversion product (red) from the capture reaction. This unleashes

charge avalanches which induce localized currents in the detector. By studying which grids (z-position) and wires (x- and y-position) that the current was induced in, it is possible to locate in three dimensions where the neutron capture took place. In most cases, one wire and a few grids are involved in a single neutron event. This is because the released charge can spread more easily between grids than wires, as the wires are mostly separated from each other by the blades.

Note that at the back of each grid, there is neutron shielding (pink) and a block of material, called an *end blade*. The end blade provides mechanical support for the grid while the shielding prevents neutrons from scattering back to the detector. This is important, as that directly contributes to the intrinsic detector background. The reason for this is that the neutron travel path is always assumed to be a straight line from the sample position to the detection point in the detector. If a neutron takes other paths – such as traversing the whole detector depth, scattering at the back, and then returning in a random direction into the active volume – then the accuracy of the distance and scattering angle reconstructions, and consequently energy and momentum transfer calculations, is decreased. By adding a highly efficient neutron absorber at the back, neutrons that pass the whole depth can be stopped, preventing them from scattering back and being detected as background. The topic of shielding is studied in depth in Chapter 3.

Using the detection principle and geometry, the next step is to practically implement the Multi-Grid detector. This is the topic in the next sections, where the design parameters and operational details of the detector are presented.

2.2 Geometry

For the implementation of the Multi-Grid detector, there are several design parameters which are considered. These include the $^{10}B_4C$ layer thicknesses, the choice of substrate material, and the dimensions of the grids. When selecting these parameters, there are often competing constraints – such as performance, cost, simplicity and mechanical stability – which have to be considered simultaneously. In the following discussion, a brief overview of these parameters – and how they were selected – is presented, starting with the layout of the grid blades.

2.2.1 Blades

The purpose of the blades is to hold the multiple $^{10}B_4C$ layers, which capture neutrons and release charged capture products that can reach the gas volume. In the theoretical case, such as presented previously in figure 1.14, this process would be most efficient for an infinite number of layers (large neutron capture probability) where each layer is

infinitesimally thin (large decay product escape probability). Practically, only a finite number of layers can be used and the thicknesses of these layers have to be optimised to account for two conflicting restraints: neutron capture (thick layers favourable) and decay product escape (thin layers favourable).

This is further complicated by the fact that each layer has to be in the order of μm thick, which means that the layers are applied to substrates, forming the blades. This means that additional material is placed in the neutron flight path, introducing the probability of neutron scattering in the substrates. To reduce this probability, aluminum is chosen as a substrate, since it is mostly transparent to neutrons. Each aluminum substrate is then made as thin as possible without affecting the mechanical stability, which is around 0.5 mm. In addition to this, it is beneficial to keep the ratio of $^{10}B_4C$-to-aluminum as high as possible, thereby decreasing the relative effect of scattering. This is done by applying $^{10}B_4C$ on both sides of the aluminum substrates. This also allows the overall size to be smaller, as fewer aluminum substrates are needed to accommodate a given number of converter layers.

The next constraint concerns the total number of blades which can be used. This number is influenced by, among other factors, the minimum possible distance between adjacent blades and the maximum space available for the blades. If the distance between adjacent blades is small, then the gap to their encapsulated wire is also small. This affects the stability of the electromagnetic field, as even small mechanical deviations in wire and blade positions can have a proportionally large effect on the field. This influences the lower limit on how tight the blades can be packed. If this aspect is combined with the maximum depth available for the blades, which is affected by the space available in the detector tank of the instrument, as well as the required efficiency of the detector, then an appropriate number of blades is acquired. This is typically around 20 blades, which accounts for the diminishing return of adding additional blades after a certain number has been reached.

Thickness selection of the $^{10}B_4C$ layers to achieve the desired detection efficiency have been studied rigorously using both simulations and analytical calculations [3, 27, 50, 51]. This collected work covers many considerations involved in thickness selection, including optimisation for a single incident neutron wavelength and a spectrum of wavelengths. Here, a summary of this work is presented, illustrating some of the key findings.

Layer thicknesses

As a starting point, the scheme presented in figure 2.1 is studied. For each blade, there are two layers in which neutrons can be detected – one in backward-escape mode and one in forward-escape mode – and the neutron detection efficiency dependence on layer thickness

is different for the two cases. To calculate these efficiencies, two probabilities are needed: the probability of neutron capture and the probability of decay product escape. The first probability, neutron capture probability, is given by

$$P_{\text{abs}}(x, E) = 1 - \exp\left[-x \cdot n \cdot \sigma_{\text{abs}}(E)\right] \tag{2.2}$$

where P_{abs} is the cumulative neutron capture probability of a neutron with energy E after the neutron has traversed a depth x in a material. The variables n and $\sigma_{\text{abs}}(E)$ are materials properties, corresponding to the number density (nuclei/unit volume) and absorption cross-section per nuclei, respectively.

Next, the escape probability for a particle emitted in a random direction at depth x – with respect to the incident neutron direction – is considered. This can be approximated according to

$$\xi(x) = \begin{cases} \frac{1}{2} \cdot \left(1 - \frac{x}{R}\right), & x \leq R \\ 0, & x > R \end{cases} \tag{2.3}$$

where $\xi(x)$ is the escape probability at a depth x and R is the effective range of the particle.

If equations (2.2) and (2.3) are combined, it is then possible to calculate the efficiency in both backward-escape and forward-escape modes. This is presented in equations (2.4a) and (2.4b),

$$\epsilon_{\text{BE}}(d) = \int_0^d \xi(x) \cdot \frac{dP_{\text{abs}}}{dx}(x)dx \tag{2.4a}$$

$$\epsilon_{\text{FE}}(d) = \int_0^d \xi(d-x) \cdot \frac{dP_{\text{abs}}}{dx}(x)dx \tag{2.4b}$$

where $\epsilon_{\text{BE}}(d)$ and $\epsilon_{\text{FE}}(d)$ are the efficiencies in backward-escape mode and forward-escape mode, respectively, and d is the thickness of the layer. The forward-escape efficiency depends on $\xi(d-x)$ because, in that mode, the escape path of decay products is the longest if the neutron is absorbed in the start of the layer and the shortest if the absorption happens at the end of the layer. Note that $\frac{dP_{\text{abs}}}{dx}(x) \cdot dx$ is the probability of absorption within a small length dx at a depth around x.

The efficiency of a single layer is illustrated in figure 2.3, where both backward-escape efficiency (left) and forward-escape efficiency (right) is seen. For the back-scattering mode (recall zoomed view in figure 2.1, right case), the efficiency dependence on depth is seen to reach a maximum and then plateau. This is because, at a certain depth, the decay products created from neutron absorption cannot escape.

For the transmission mode (recall zoomed view in figure 2.1, left case), in contrast, the

efficiency is seen to reach a maximum at a certain thickness and then start to diminish. This follows from the fact that the decay products escape in the same direction as the neutron entered. When the thickness is increased beyond the effective range of the decay products, then the capture reactions at the start of the layer will result in decay products which can no longer escape. Hence, if the layer thickness is widened too much, the efficiency starts to diminish.

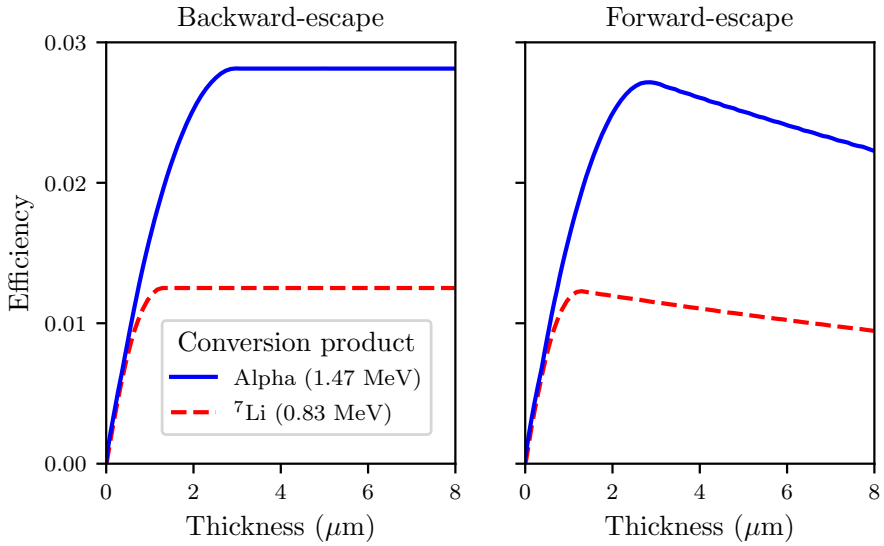

Figure 2.3: Detection efficiency calculation as a function of layer thickness for 1.8 Å (25 meV) neutrons incident perpendicularly on a single layer, showing both the backward-escape efficiency (left) and forward-escape efficiency (right), where the individual efficiencies of the two conversion products in the 94 % branch is shown. Figure adapted from [27].

Using the expressions for efficiency in backward-escape and forward-escape mode, the efficiency ϵ for a single blade is formulated according to

$$\epsilon(d_{\mathrm{BE}}, d_{\mathrm{FE}}, E) = \epsilon_{\mathrm{BE}}(d_{\mathrm{BE}}) + [1 - P_{\mathrm{abs}}(d_{\mathrm{BE}}, E)] \cdot \epsilon_{\mathrm{FE}}(d_{\mathrm{FE}}) \tag{2.5}$$

where d_{BS} and d_{T} are the thicknesses of the backward-escape and forward-escape layers, respectively. The factor $[1 - P_{\mathrm{abs}}(d_{\mathrm{BE}}, E)]$ is added because only the fraction of neutrons that are not absorbed in the backward-escape layer has the opportunity to be absorbed in the forward-escape layer.

The maximum efficiency for a single blade, as demonstrated in [27, 50], occurs when $d_{\mathrm{BE}} = d_{\mathrm{FE}}$, i.e. both the backward-escape and forward-escape layers have the same thickness, and this is true regardless of wavelength. In fact, having equal layer thicknesses on a blade can be demonstrated to hold even when multiple blades are used in sequence [27, 50], such as the case in the Multi-Grid detector design. That being said,

although the thicknesses within a blade are identical, the total efficiency of the collection of blades can still be increased by allowing the thicknesses to vary *between* blades.

The total efficiency of N blades with different thicknesses can be stated according to

$$\epsilon_{\text{tot}}(\mathbf{d},\, E) = \epsilon(d_1, E) + \sum_{k=2}^{N} \exp\left[-2 \cdot \left(\sum_{j=1}^{k-1} d_j\right) \cdot n \cdot \sigma(E)\right] \cdot \epsilon(d_k, E) \tag{2.6}$$

where $\mathbf{d}$ is a vector of length N containing the thicknesses of the blades, $\mathbf{d} = (d_1, d_2, ..., d_N)$, and $\epsilon(d_k, E)$ is the efficiency of a single blade with $d_{\text{BE}} = d_{\text{FE}} = d_k$ for neutrons with incident energy E. Note that for each blade considered in the summation, the probability of non-absorption in the preceding blades, $\exp\left[-2 \cdot \left(\sum_{j=1}^{k-1} d_j\right) \cdot n \cdot \sigma(E)\right]$, is used as a scaling factor for the blade efficiency $\epsilon(d_k, E)$. This means that the last blades in the sequence – furthest downstream from the incident flux – contribute the least to the total efficiency because they receive fewer neutrons.

Using this expression, it is now possible to determine the most appropriate layer thicknesses. This is shown in figure 2.4, where a 15-blade setup using monochromatic neutrons is presented. It is seen that the contribution of each blade in the overall detection efficiency drops as a function of blade number, as expected. Another observation is that the $^{10}B_4C$ thicknesses trend from thinner at the front to thicker at the back.

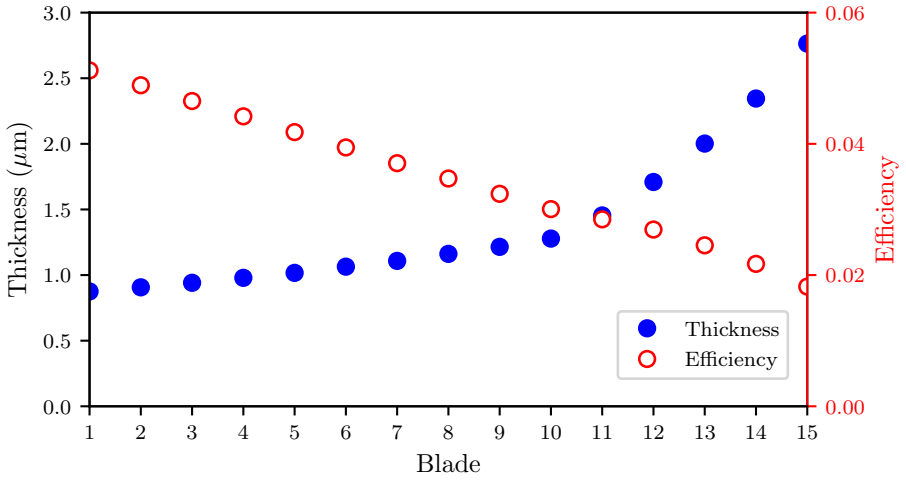

Figure 2.4: Distribution of layer thicknesses on blades (blue) and their contribution to efficiency (red) for a 15-blade configuration, optimised for 10 Å (0.9 meV) neutrons. The thickness and efficiency are shown separately on the left and right y-axis, respectively. Note that both the efficiency and thickness change monotonically as a function of blade number. Figure based on data from [27].

When considering monochromatic neutrons, the layer thicknesses are selected by starting from the last blade in the sequence, blade N, and iteratively adding the remaining blades

in front of it up to blade 1. The first step in this process is to tune the layer thickness on blade N with no constraints. Next, the layer thickness on blade $N-1$ is calculated. This calculation, however, also has to consider the flux loss incurred on blade N. Therefore, a trade-off between absorption in blade $N-1$ and absorption in blade N has to be made, optimizing for the total efficiency of the two blades. In other words, the efficiency *gain* of adding blade $N-1$ has to be weighed against the efficiency *loss* in blade N due to the flux deficit incurred by absorption in the new blade. This compromise results in a thinner layer thickness on blade $N-1$.

This process is then repeated for the rest of the blades, i.e. the efficiency gain of blade $N-2$ is weighted against the combined efficiency of blades $N-1$ and N, etc. For each added blade, the newly introduced efficiency has to be weighed against the efficiency of all the blades downstream from it. Therefore, the layer thickness of the newly introduced blade cannot be too thick, as it affects the flux reaching all the remaining blades. This results in progressively thinner blades towards the front.

For a polychromatic source of neutrons, this method of optimisation cannot be used. This is because – due to the varying neutron absorption probability of boron-10 as a function of energy – the neutron energy distribution changes as the neutrons pass through the blades. For example, if blade N is optimised for an energy distribution, then that distribution will be incorrect as soon as blade $N-1$ is added. This means that the layer thickness on blade N depends on all the previous blades and the iterative process no longer works: all blades have to be considered simultaneously. This is done by maximizing the efficiency in equation (2.7),

$$\epsilon^{w}_{tot}(\mathbf{d}) = \int_0^\infty w(E) \cdot \epsilon_{tot}(\mathbf{d}, E) dE \tag{2.7}$$

where $\epsilon^{w}_{tot}(\mathbf{d})$ is the optimised efficiency and $w(E)$ is the normalized weighting distribution containing the energy distribution that fulfils $\int_0^\infty w(E)dE = 1$. Using this relation, it is possible to optimise the $^{10}B_4C$ thicknesses in the Multi-Grid detector for a distribution of energies, such as those expected in the CSPEC or T-REX instrument. Just as in the case of monochromatic optimisation, polychromatic optimisation also results in thinner layers at the front and thicker layers at the back. However, due to practical considerations, there is an additional constraint added that it is not possible to use more than a few unique thicknesses. This is discussed next, where the method of applying the $^{10}B_4C$ layers on the substrates is covered.

Coating

$^{10}B_4C$ layers are applied to the aluminum substrates using physical vapour deposition DC magnetron sputtering [52], and it is performed by the ESS Detector Coatings Workshop in Linköping. This is done by bombarding a solid $^{10}B_4C$ target with highly energetic

ions, which results in individual $^{10}B_4C$ molecules being ejected. By placing the aluminum substrates close to the $^{10}B_4C$ target, as seen in figure 2.5, these $^{10}B_4C$ molecules can attach to the aluminum surface. If the procedure is continued for a sufficient amount of time, thin $^{10}B_4C$ coatings are grown on the aluminum substrates, forming the $^{10}B_4C$ films required for neutron detection.

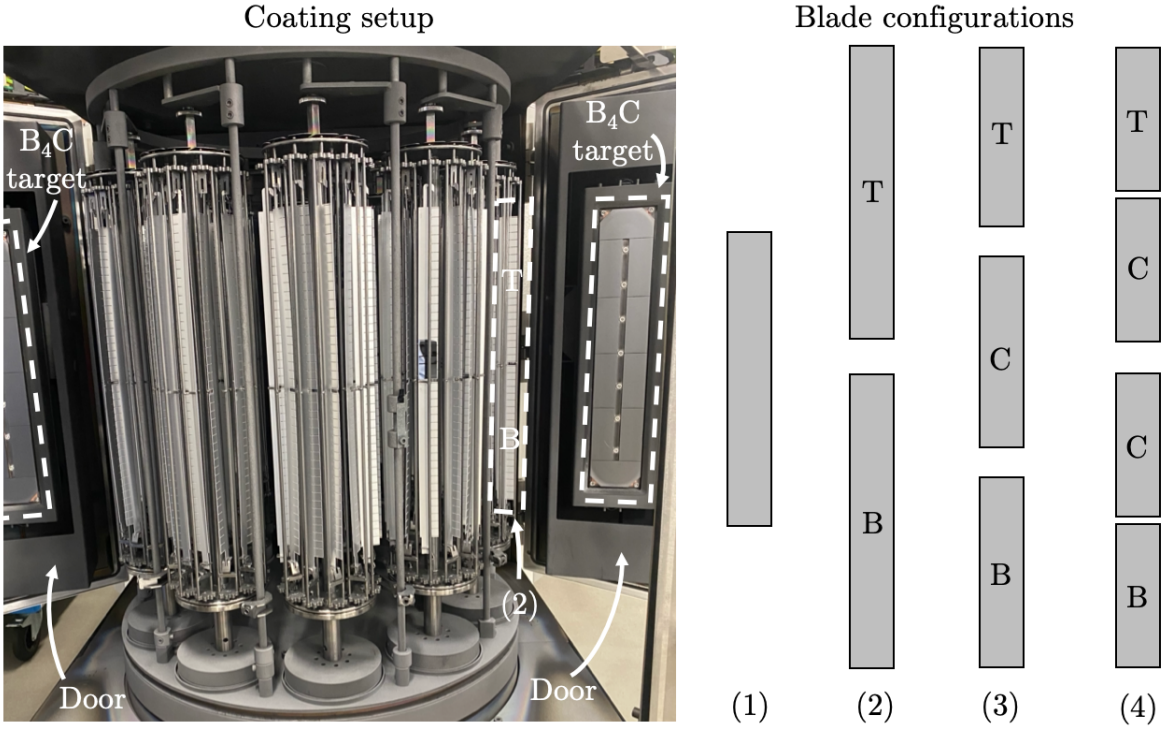

Figure 2.5: Illustration of how the blades are coated. On the left, a picture of blades, grouped in units of two in this example, is shown. To the right, other blade configurations are illustrated, ranging from units of one to four blades. The markings on the blade indicate the relative position of the blade: Bottom (B), Centre (C) and Top (T).

A picture of the substrates, as arranged during the coating procedure, is seen on the left in figure 2.5. The substrates are rotated in a planetary-like fashion: each substrate rotates around its centre, while simultaneously rotating around the centre of its group, and all groups of substrates rotate around their common centre. This ensures that both sides of each substrate receive an equal coating thickness. This is beneficial both from an efficiency perspective, as shown in the previous section, as well as a mechanical point of view: having an equal coating on both sides reduces stress on the aluminum substrates and keeps its surface flat.

During the coating process, the blades are grouped into units of one, two, three or four blades, as seen on the right in figure 2.5. Due to how these units and the $^{10}B_4C$-targets are positioned with respect to each other, an uneven distribution of coating is applied: the blades in the centre (close to the $^{10}B_4C$ target) obtain more coating than the ones at the top and bottom (further from the $^{10}B_4C$ target).

One example of this is coating configuration (3) which has three blades per unit, as illustrated in figure 2.5. The centre blades receive the maximum coating thickness, while the top and bottom blades receive a gradient from 100 % down to around 60 % of that maximum. To compensate for this, the T and B blades are always paired up when mounted in the grids, such that their thickness gradient go in opposite directions. The resulting average thickness of the two blades is about 80% of the aimed thickness. The centre blades, however, still receive almost 100% of the aimed thickness. This difference in thickness between C and the TB pairs is significant and has to be taken into consideration when mounting them into grids. An example of this is presented in table 2.2, where the blade configuration of a prototype is presented. As can be seen, the normal blades are arranged such that the TB pairs are at the front and the C blades are at the back for each target thickness. The coating thicknesses presented are based on measurement values obtained using a Scanning Electron Microscope (SEM).

Table 2.2: Coating configuration for the MG.LET Multi-Grid detector prototype, where $d_{targeted}$ and $d_{average}$ are the targeted and average thicknesses on the blades, respectively.

Blade #	1	2	3	4	5	6	7	8	9	10	11	12	13	14	15	16	17
Blade type	T	B	T	B	T	B	C	C	T	B	T	B	T	B	C	C	C
$d_{targeted}$ (μm)	0.65								1.15								
$d_{average}$ (μm)	0.53						0.64		0.93						1.13		

As shown earlier in this section, efficiency calculations for a series of uniform layers had been developed previously, and the optimal efficiency for the detector assuming uniform coating had been calculated. Part of this thesis work was to investigate how much the true efficiency deviates from the ideal case when a more realistic calculation is performed, which accounts for the thickness variation across the blades. Furthermore, it was to figure out if there is a way to compensate for this shift to bring it closer to the ideal case. Finally, due to a mismatch between the batch size of the coated blades and the number of blades required in a grid, it is not possible for all grids to have completely identical configurations without wasting blades. Therefore, to avoid waste, the task was to investigate the different possible grid permutations, see how much they differed from each other in terms of efficiency, and select a set of viable configurations. The efficiency of each grid permutation was approximated by averaging the efficiency across the thickness variations of the normal blades.

The result of this investigation is presented in figure 2.6, where each configuration is a small variation of the previously shown setup in table 2.2. As can be seen, all of the grid configurations have an acceptable efficiency difference – less than 2% absolute deviation from the previously optimised configuration over the full wavelength range for CSPEC – and a variation of less than 1 % between each other. Hence, all of the blades from the

coating can be used while still maintaining sufficient efficiency and uniformity between grids. These were the grid configurations implemented in the MG.LET, which is presented later in this chapter.

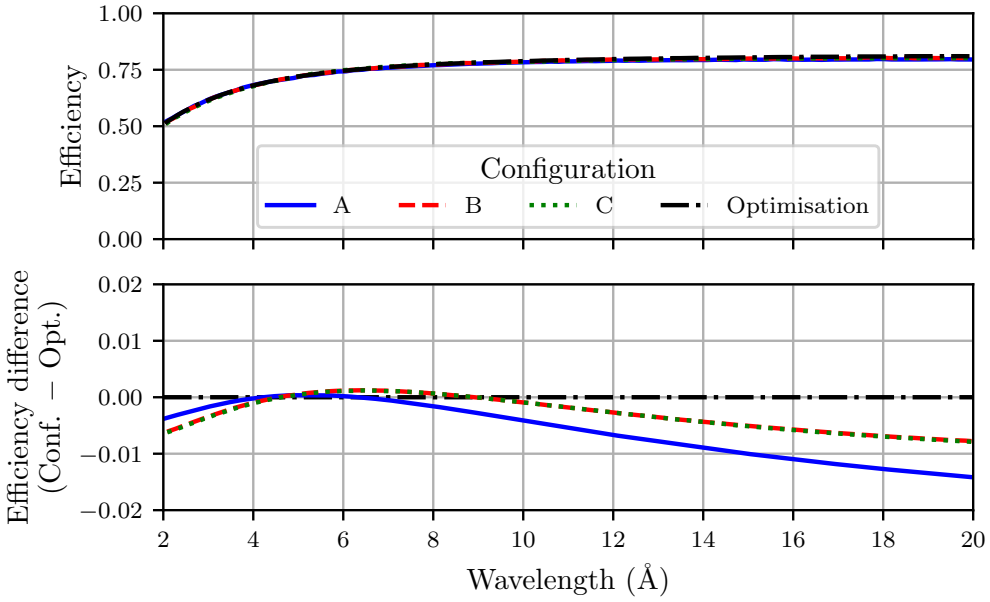

Figure 2.6: Grid efficiencies for different configurations (A, B and C) in the MG.LET grid design, showing both their absolute efficiency (top) and difference to the previously optimised configuration (bottom).

2.2.2 Grids

Once the blade configuration is set, the next step is to define the grid design. This is presented in figure 2.7, where an example grid is shown. The grid is composed of four components: normal blades (discussed in the previous section), radial blades, end shielding and an end blade. The specific details of how these parts are put together depend on cost, simplicity, scalability, mechanical stability and physics performance. A few of these considerations are presented below.

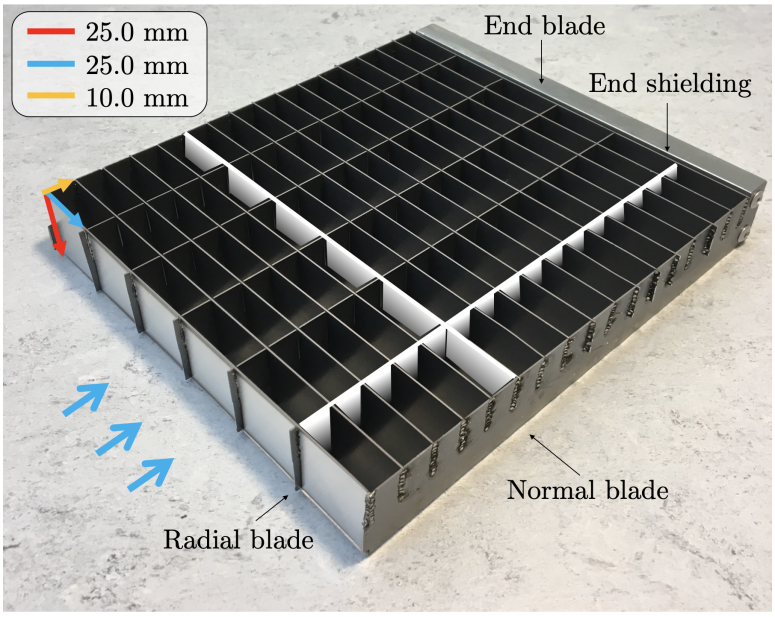

Figure 2.7: Example of a grid where the relevant components have been annotated together with the dimensions of the voxels. Incident neutrons are shown as blue arrows. In the picture, a representative normal and radial blade are highlighted with white.

Normal blades

As mentioned previously, the normal blades cannot be packed too tight as this affects the stability of the electric field and gives very tough requirements on mechanical precision. However, the spacing between them cannot be too large either, as this affects the time and position resolution of the detector, which in turn affects the neutron energy resolution. This is because each voxel has at least two $^{10}B_4C$-layers – four if the radial blades are coated – and incident neutrons can be converted in any of these. The information on which coating the conversion took place is not known, which means that each voxel has a fundamental conversion location uncertainty dependent on the distance between the layers. To fulfil the demands on energy and position resolution listen in table 2.1 – as well as to keep down any excessive costs incurred on the detector tank to host a detector with a large depth – the 1 cm spacing between the normal blades seen in the figure is chosen based on experimental results.

Radial blades

Concerning the spacing of radial blades and the height of the blades, this affects the scattering angle reconstruction. To satisfy demands on performance, mechanical simplicity and cost (a smaller spacing requires more radial blades and a greater number of channels to cover a specific area, which increases cost), these two dimensions are set to be around 2 cm, giving each voxel the dimensions of approximately $2 \times 2 \times 1$ cm^3.

Another feature to consider is if the radial blades should be coated or not. The purpose of the radial blade coating is to attenuate the effect of internal neutron scattering in the active detector volume – constituting a time-dependent background – by reducing the extra time and distance an internally scattered neutron travels before detection. The $^{10}B_4C$-coating on the radial blades absorbs the neutrons closer to their internal scattering point, thus reducing time and distance uncertainty. The coating thickness on the radial blades is set to around 1 μm, but the attenuation of internal scattering can be further increased by making this coating thickness thicker. This, however, comes with an increased cost that has to be weighted against the gain in performance.

Another possible option for reducing the energy smearing effect of internal scattering could be to coat the radial blades with a different converter than $^{10}B_4C$, such as Cd or Gd. These converters does not have heavy charge particles as conversion products and would hence have a different signature than that of the ^{10}B capture reaction. Hence, internally scattered neutrons that are absorbed on this type of radial coating could be cut in the analysis. However, care should be taken that the newly introduced radial coating does not introduce a significant shadowing effect of the incident neutrons and consequent decreased detection efficiency in the normal blades downstream.

End shielding

The purpose of the shielding at the back of the grid, similar to the radial blade coating, is to reduce the effect of internal neutron scattering by preventing neutrons from reaching the end blade. To work effectively, the end shielding should have two properties: a large neutron absorption probability and a small neutron scattering probability.

The choice of material is dependent on the incident neutron energies expected on the detector. Certain materials – such as cadmium and gadolinium – have a strong neutron absorption cross-section for cold neutron energies but also have a sharp drop in absorption when the neutron energies are increased towards the epithermal region. Boron, on the other hand, does not have a similar sharp drop in absorption for higher energies. This makes cadmium- and gadolinium-based shielding materials suitable for cold energies, while boron is more appropriate for epithermal energies.

For all shielding solutions, it is important to keep down the neutron scattering probability in the shielding materials. This is especially important when the shielding material contains hydrogenous binders, such as most epoxies. Consequently, if epoxy-Gd_2O_3 is used as an example, the weight ratio between epoxy and Gd_2O_3 is kept heavily in favour of Gd_2O_3, which increases the absorption-to-scattering ratio in the material.

Aluminum substrate

The final feature to consider is what type of aluminum should be used for the substrates, which influences the intrinsic background rate. The reason for this is related to the internal geometry of the Multi-Grid detector, which is large compared to the entry window due to the multi-layered structure. Due to this internal surface area, the intrinsic radioactivity of the blades must be kept low, as even low radioactivity can affect the background level.

Commercial aluminum naturally contains a small fraction – around 100 ppb – of alpha-emitting thorium and uranium isotopes [8]. The energy of these decay products ranges from around 4 MeV to 9 MeV, but due to the travel path through the aluminum, this is reduced when they reach the active volume. To mitigate the effect of this alpha contribution, there are two general approaches: either the alphas are stopped from exiting the aluminum – such as by coating the aluminum substrates with a few μm of nickel – or the concentration of the alpha emitters in the aluminum is reduced. For the detectors studied in this work, the second approach was selected and the substrate was chosen to be radiopure aluminum, which has less than 1 ppb of thorium and uranium. By switching from natural to radiopure aluminum, a reduction in background rate by around a factor of 50 has been observed [8]. This would reduce the observed background rate in the MG.IN6 [7] – 4.4 Hz over a 32×50 cm^2 active area – from 27.5 Hz/m^2 to 0.55 Hz/m^2. This is a significant reduction and would prevent the alpha contamination from being the dominant background source at neutron instruments such as the IN6 [8].

The reason the nickel-coating approach was not selected was because it was observed that – when applying $^{10}B_4C$ coating on top of the nickel coating – the nickel started to flake off after some time. This could also happen already during the coating process. The reasons for this were (1), the high stress the $^{10}B_4C$ incurred on the nickel and (2), the non-negligible mismatch in thermal expansion coefficients between nickel and aluminum. This results in stresses on the materials during the coating procedure when high temperatures are applied, which causes flaking. By using radiopure aluminum instead, these issues are avoided.

To confirm the expected low radioactivity of the radiopure aluminum acquired for the latest Multi-Grid detector prototype, the aluminum alpha activity per unit area was measured by iROC [53]. The measured rate was found to be $r_{\mathrm{Al}} = 0.00167 \pm 0.00167$ Hz/m^2, which was later corroborated by an independent measurement by the Boulby Underground Laboratory [54], United Kingdom, where similar results were obtained. Using this number, the intrinsic background level per unit active detector area of the Multi-Grid detector,

$r_{\mathrm{MG}}^{\text{active area}}$, can be calculated according,

$$r_{\mathrm{MG}}^{\text{active area}} = \frac{r_{\mathrm{MG}}^{\text{total}}}{A_{\mathrm{MG}}^{\text{active area}}} = \frac{r_{\mathrm{Al}} \cdot A_{\mathrm{MG}}^{\text{internal area}}}{A_{\mathrm{MG}}^{\text{active area}}} \tag{2.8}$$

where $A_{\mathrm{MG}}^{\text{active area}}$ and $A_{\mathrm{MG}}^{\text{internal area}}$ are the active and internal areas of the detector, respectively, and $r_{\mathrm{MG}}^{\text{total}}$ is the total rate on the aluminum surfaces facing the active volume of the detector. Using the grid in figure 2.7 as the basis for the calculation results in,

$$r_{\mathrm{MG}}^{\text{active area}} = \frac{r_{\mathrm{Al}} \cdot (2 \cdot 16 \cdot A^{\text{normal blade}} + 2 \cdot 6 \cdot A^{\text{radial blade}})}{A^{\text{normal blade}}} = 0.075 \pm 0.075 \text{ Hz/m}^2 \tag{2.9}$$

where $A^{\text{normal blade}}$ and $A^{\text{radial blade}}$ are the areas of normal and radial blades, respectively. The factor of 2 appears in the calculation above because most blades have two sides facing the active volume.

Based on these considerations, the background contribution of the internal aluminum should be low enough to fulfil the detector demands presented in table 2.1, which states that the intrinsic background level of the detector should not exceed 0.35 Hz/m^2.

2.2.3 Columns

An overview of how the grids are mounted into columns is presented in figure 2.8, where the MG.LET is used as an example. First, the grids are stacked in a sequence of grids – as shown in (a) – forming a column. The grids are kept electrically separated from each other by mounting each grid into a plastic insulator – as seen in (b) – which keeps a 0.5 mm spacing between adjacent grids. To also keep a reliable separation of the grids at the top, there are additional spacers. This is seen circled in (c), where B_4C-based spacers, selected to avoid adding additional scattering material in the detector, are shown.

At the two edges of the column, aluminum *end grids* are placed, as seen in (a) and (b). To reduce the alpha emission from the end grids, these are coated with a thin layer of nickel. The purpose of the end grids is to hold the wire PCBs – as seen in (d) – which support the wires that run through the cells in the grids. The wire PCBs transport the signals generated in the wires towards the readout system. For the grids, this is done via the grid PCB located underneath the insulator – as seen lying beside the insulator in (b) – which is connected via screws to the grids.

Once the column has been assembled, the next step is to insert it into the vacuum-proof vessel, as seen in (e). Within the vessel, the grid column is standing upright. The way neutrons are incident upon the grids has been highlighted with blue arrows in (a) and (e). At the back, there is an electronic box containing the Front-End Electronics (FEE).

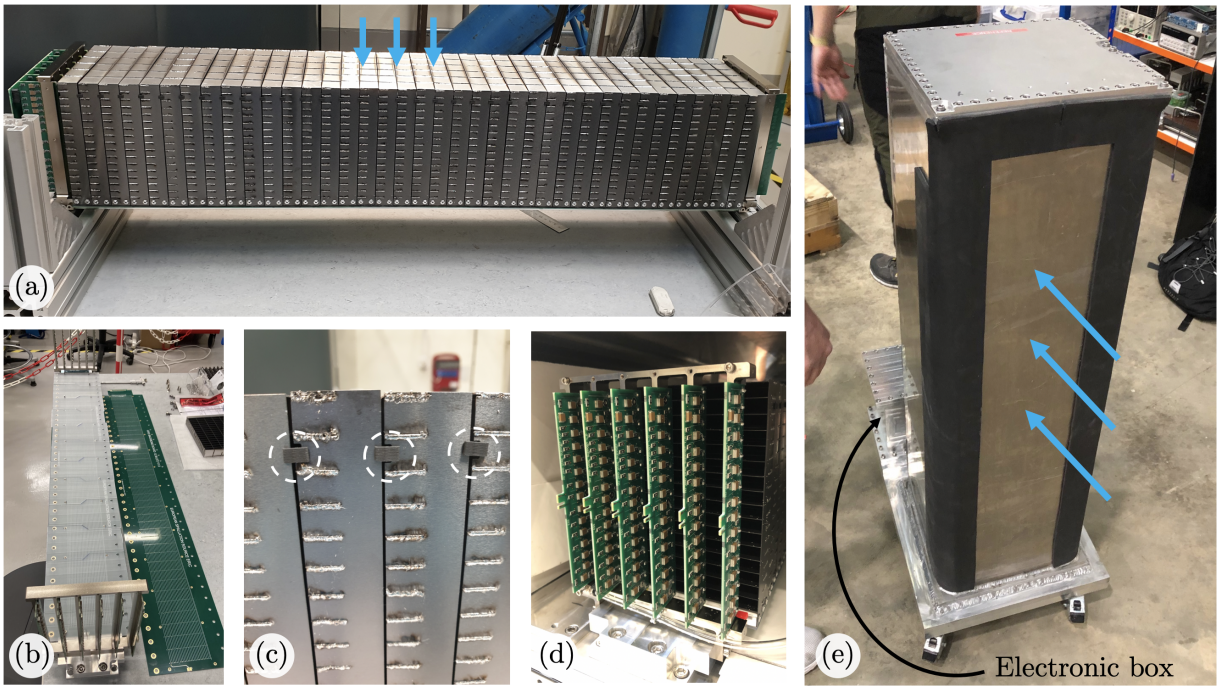

Figure 2.8: Overview of a column. Incident neutrons enter the detector from the side pointed at with blue arrows. The individual figures correspond to (a) column, (b) insulator, grid PCB and end grids, (c) spacers, (d) wire PCBs, and (e) vessel.

2.3 Operation

The detector operation can be split into aspects related to the MWPC, the readout chain and the data acquisition system (DAQ). These are discussed in turn, starting with how the MWPC component of the detector is configured.

2.3.1 MWPC

The settings of the MWPC are related to parameters like gas choice, voltage level and geometry. The choice of these, in turn, affects factors such as the movements of ions, charge multiplication and count rate, which are crucial for the detector operation.

To select an appropriate voltage level, the first step is to consider the Pulse Height Spectrum (PHS) of the detector. This is exemplified in figure 2.9, where the PHS for a helium-3 and a solid boron-10-based detector are shown. In these plots, there are two relevant features: a sharp rise in statistics for low charges – corresponding to gamma rays and electronic noise – and a structure spanning the rest of the spectra – corresponding to the charge released by the conversion products. The goal is to apply a voltage level on the detector so that all the features from the conversion products are spread over a large dynamical range of the ADC, while not accepting too much gammas and noise. To find this voltage level, a *plateau measurement* is performed.

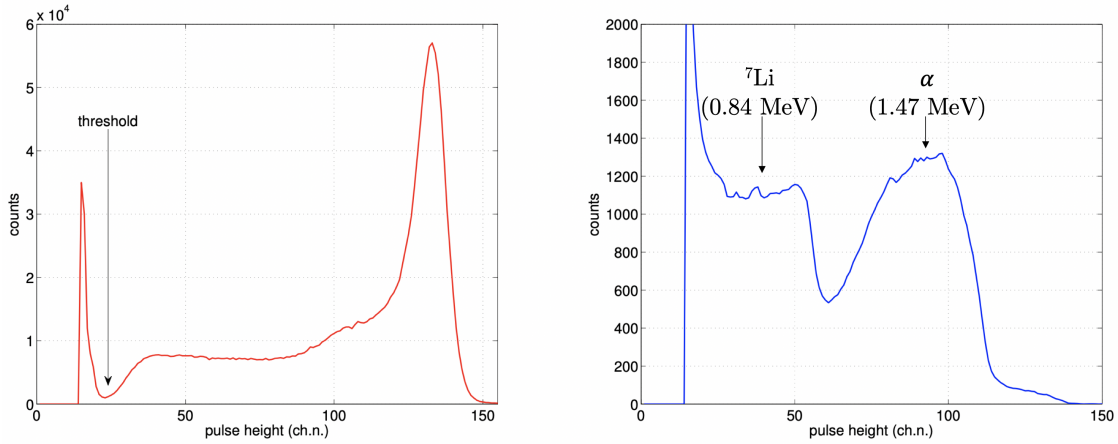

Figure 2.9: Comparison between the PHS obtained from a helium-3 based detector (left) and a solid boron-10 based detector (right). The x-axis is charge in ADC units. As can be seen, the clear valley between decay products and gamma events in the helium-3 spectrum (marked by the arrow) is absent in the boron-10 spectrum. Note that the exact details of the PHS will differ from detector to detector. The figure is taken from [27], with boron-10 decay products annotated by the author.

To perform a plateau measurement, the voltage is incrementally increased from zero upwards. This will take the detector through the first operation modes mentioned in the previous chapter – the region of recombination before collection and the region of ionization chamber – before reaching the region of proportionality. When increasing the voltage in this region, the gain of the detector increases with it. Eventually, the voltage level will allow sufficient charge release for the ADC to register the charge. By further increasing the voltage, more and more of the PHS falls within the dynamical range, and an increasing level of counts is seen as a function of voltage. If a helium-3 tube detector is used as an example, this continues until a valley in the spectrum emerges (see black arrow in figure 2.9). At this point, the number of counts temporarily stops increasing as a function of voltage: a plateau is reached.

For solid boron-10-based detectors, the plateau region is not as prominent as it is for the helium-3 tubes[3]. This is because the decay products in the former have a finite distance to travel in the converter layer before reaching the proportional gas. Consequently, the products will experience a charge loss before reaching the proportional gas, which can decrease the particle energies down to zero. Due to this, there is no valley in the PHS between gamma rays and charged products, as seen to the right in figure 2.9, and a plateau in a boron-10 based detector is more accurately described as a temporary decrease in slope as a function of applied voltage.

One example of such a scan is presented in figure 2.10. This was done by aiming a

[3]The exception to this is when the layers are very thin, $<< \mu$m [4].

collimated 1.5 mm × 1.5 mm neutron beam at a single grid, hitting the centre of a voxel [3]. The counts in that grid (blue), the grid plus nearest neighbours (red) and the grid plus all first and second neighbours (green) were measured as a function of applied voltage. By studying the plot, the location of the temporary decrease in counts as a function of voltage can be identified and a suitable operational voltage selected.

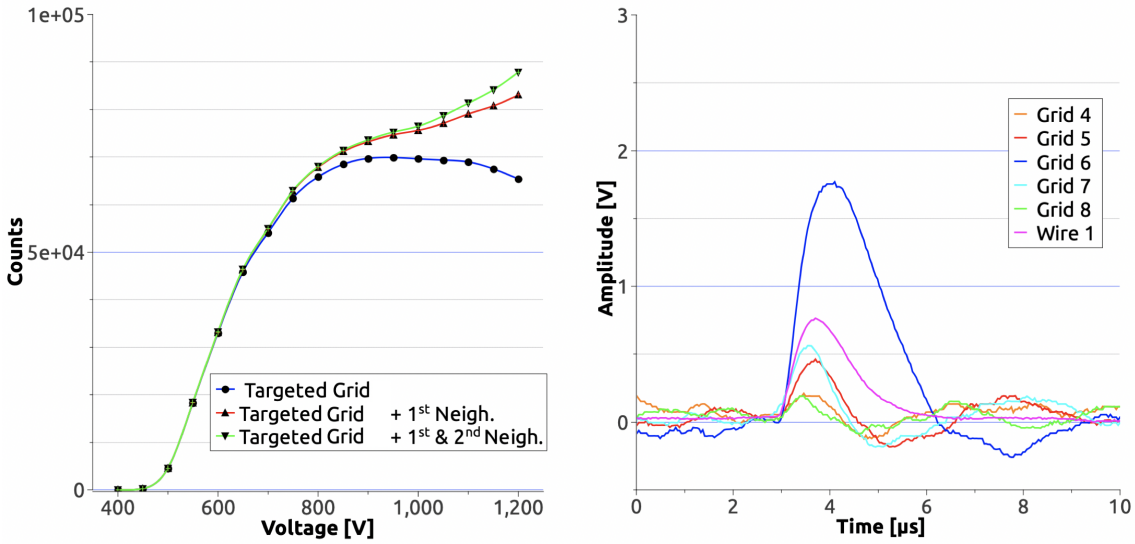

Figure 2.10: A plateau measurement using Ar-CO_2 (90:10) with the Multi-Grid detector (left) and an example of pulse shapes obtained from the shaping circuit (right). Note that the polarity of the wire signal has been inverted. Figures taken from [3], with a minor nomenclature change by the author in the left plot.

Another aspect observed in the plateau measurement is that even though a single grid is targeted, the neighbouring grids also register events. This is further highlighted to the right in figure 2.10, where an example of the recorded pulse shapes from the targeted grid (blue), the coincident wire (purple) and the neighbouring grids (remaining colours) are shown. One reason for this is that the decay products have a range of a few millimetres in the gas [3], which means that products emitted from one grid can be ejected in such a way that the released charge induces currents in the first neighbour. Another reason neighbouring grids can fire is that grids – due to their large charge storage capabilities and proximity to each other – behave as neighbouring capacitors. Hence, current induced in one grid can flow via capacitive coupling through its neighbours to the readout chain. In this way, multiple grids can fire even though only one was targeted. This gives the possibility to increase the position resolution by using Centre-of-Gravity (CoG) calculations on the charge collected in the multiple grids, as outlined in [3].

Other important considerations concern the choice of gas and operating pressure. By keeping the gas pressure low, the electrons and ions have higher mobility in the active volume. This increases the time resolution and the count rate capabilities – as the released

charge can be collected faster, thus minimizing space charge effects on subsequent events. These space charge effects are most important for ions – as they are slower – which may reduce the electric field strength between the wire and grid if they are in sufficient quantities, changing the behaviour of the proportional chamber. It is therefore desirable to remove this charge as quickly as possible.

The speed of this charge collection process is further aided by the segmented geometry of the Multi-Grid detector. That is, the neutron absorption is distributed along the many layers along the depth of the detector, which also distributes the released charge. This is split between the isolated tubes with one wire each, thus lowering the charge released around the individual wires. This further enhances the Multi-Grid detector's high count rate capability.

2.3.2 Readout chain

The purpose of the readout chain is to transport and process the signals generated in the detector. This can be divided into three components: signal transportation, analogue processing and digital processing in the electronics, and data handling. To transport the signals, PCBs are connected to the wires and grids, which connect each wire and grid to the analogue processing unit, as presented schematically to the left in figure 2.11. For each wire, there is a resistor separating it from the HV supply and a capacitor separating it from the analogue processing. The capacitors decouple the rest of the readout system from the HV applied to the wires and only transport the AC induced by the moving charge in the active volume. The grids do not have decoupling capacitors as they are kept at an approximate ground potential.

The next step in the readout chain is analogue processing in the FEE. For this, the MMR [55] FEE were used, which processes the signals as presented in figure 2.11. The purpose of this system is to prepare analogue pulses for the subsequent digital processing, but it is also to generate a trigger when an analogue pulse with an amplitude above a certain threshold, as specified from the digital readout, is obtained. For the shaper-integrator, a 500 ns shaping time was used, while for the TF-integrator it was 200 ns.

Digitization of the charge collected and the timing of when it happened are presented in figure 2.12, where the signal processing in the MMR is shown. The MMR is a self-triggering FEE card, meaning that every time an analogue channel outputs a charge with an amplitude above a certain discriminator threshold, a trigger is generated. Following the trigger, the charge from all channels is converted into ADC values. After that, a second threshold is applied, the so-called data threshold, which discards all channels with ADC values below this threshold. The information from the remaining channels – those with

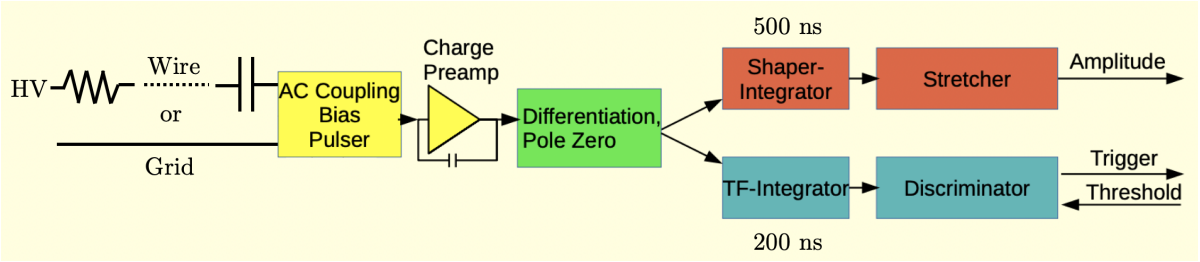

Figure 2.11: Schematic of the analogue signal processing unit. Figure taken from [55], with annotations by the author.

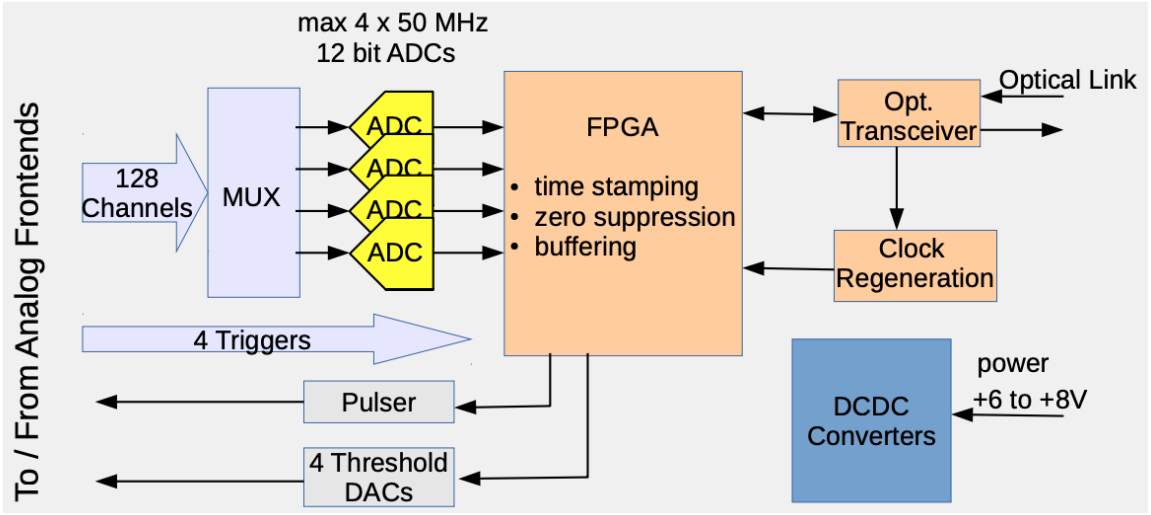

Figure 2.12: Schematic of the digital signal processing unit. Figure taken from [55].

ADC values above the data threshold – is then transmitted over the optical fibres to the VME receiver. Once the information has been received at the VME, it is grouped into discrete *events*. Each MMR card has 128 channels, can accept signals of both positive or negative polarity, and connects into one socket, *bus*, in the receiver.

Each of the recorded events contains a sequence of the channels which fired within a specified time window, where each channel has an associated ADC and bus, together with a common time of when the event took place. In this work, a 400 ns time window was used. The data is saved in a binary data format for offline data analysis. In the analysis, the charge is primarily used for background rejection and the channel number is used for hit location. The specifics of how this is done are detailed later in the data analysis chapter.

2.4 Prototypes

During the measurements done in this work, two different prototypes were used: one for HZB and one for ISIS. The first prototype was built in 2018 for characterization at the Fine-Resolution Fermi Chopper Spectrometer SEQUOIA [56] at the SNS. SEQUOIA is a thermal neutron instrument, similar to T-REX. The details presented in this work, however, concern the subsequent beamtime with this prototype, at the HZB. The second prototype studied in this work was built in 2022 for testing at the cold neutron spectrometer LET [57] at ISIS. In contrast to SEQUOIA, LET is similar to the upcoming CSPEC instrument. The two prototype names are, respectively, MG.SEQ and MG.LET. Their specifications are detailed in table 2.3 below.

Table 2.3: Differences between the MG.SEQ and MG.LET Multi-Grid detector prototypes. Note that there are two versions of the MG.SEQ: MG.SEQ.I (Ultra pure aluminum and no radial coating) and MG.SEQ.II (Al5754 and 1.25 μm radial coating).

	MG.SEQ	MG.LET
	Voxel dimensions	
x	22.5 mm	25 mm
y	22.5 mm	25 mm
z	10 mm	10 mm
	Grid configuration	
Aluminum alloy	Ultra-pure or Al5754	Ultra-Pure
Radial coating	None or 1.25 μm	2.00 μm
Normal coating	1.00 μm, 1.25 μm and 2.00 μm	0.65 μm and 1.15 μm
Normal blades	21	17
Radial blades	5	7
End shielding	MirroBor, 5 mm	Epoxy-Gd_2O_3, $\sim$1.5 mm
	Detector configuration	
Grids per column	40	37
Columns per vessel	3	1

The main difference between the two prototypes is that they are optimised for different incident energies: MG.SEQ is optimised for T-REX and MG.LET is optimised for CSPEC. Another important feature is that the MG.SEQ is divided into two versions – MG.SEQ.I and MG.SEQ.II – which differ in two aspects. This includes blade substrates made of radiopure aluminum, which the MG.SEQ.I have but not the MG.SEQ.II, and $^{10}B_4C$-coating on the radial blades, which in contrast the MG.SEQ.II has but not the MG.SEQ.I. The MG.LET detector has both these features incorporated: radiopure aluminum in the blades and coating on the radial blades. The final differences between the grid designs concern

voxel size and end shielding. For end shielding, the MG.SEQ grids use 5 mm MirroBor [58] while the MG.LET use ∼1.5 mm Epoxy-Gd_2O_3 (26 wt% Epoxy and 74 wt% Gd_2O_3). The MirroBor is a commercial product based on natural B_4C integrated into a rubber material, while the Epoxy-Gd_2O_3 is produced in-house at ESS.

The operational setup for the prototypes under study is presented in figure 2.13. Firstly, the detector operates with Ar-CO_2 (80:20) proportional gas. The gas supply is connected to a flow meter, from which the gas travels via the electronic box into the main detector volume. During operation, the flow meter is set so that a small over-pressure is maintained, circulating out the gas via an outlet tube. The circulation is set so that approximately one detector volume of gas is replaced each day.

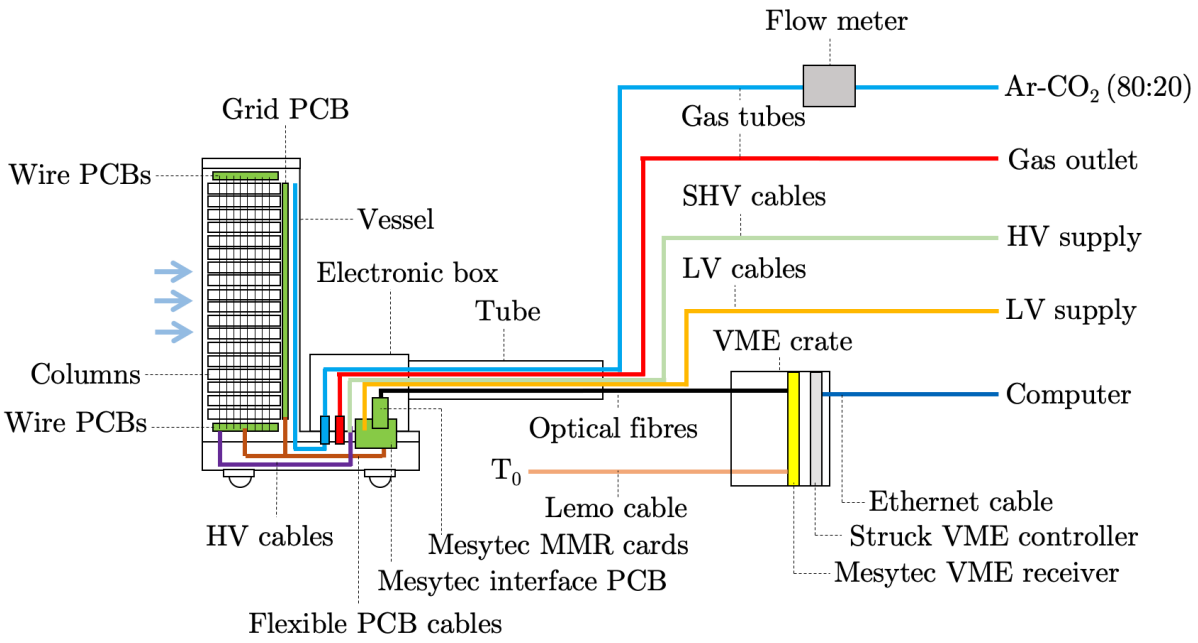

Figure 2.13: Overview of the connection scheme for the Multi-Grid detector. Incident neutrons are illustrated with blue arrows.

Secondly, the detector uses an HV supply to maintain a high potential difference between the wires and grids. The supply is applied to the detector using SHV cables, which are connected via an interface plate to the hollowed-out section in the bottom lid, where the HV is applied to the wires using HV cables. One SHV cable is used per column.

Thirdly, the detector uses a readout system to process the signals generated in the active volume. The main components of the readout system are PCBs, FEE, a VME receiver, and a computer. The PCBs are used to transport signals collected in the wires and grids, as well as to ground the grids and apply HV to the wires. Each column has one or two long PCBs for the grids and several smaller PCBs for the wires. The signals in the PCBs are read out at the bottom of the column, where they are transported via flexible PCB cables to a Mestytec interface PCB. This interface transfers the signals to the Mesytec MMR

FEE cards on the other side in the electronic box. At the MMR cards, the signals are digitized into ADC values, which are then sent via optical fibres to the Mesytec VMMR module [59] in a VME crate. At this point, the read-out events are created and forwarded to a computer via an ethernet cable. The readout chain is controlled via the Mesytec mvme software [60]. Note that the readout presented here is for the prototypes used in this work and not the final readout envisaged for the detector when installed at ESS [61], which is instead the RD51 Scalable Readout System [62].

2.5 Development

During the more than ten years of Multi-Grid detector development, much work has been carried out concerning the characterization of the detector performance. These aspects regard, among others, detection uniformity, gamma- and fast neutron sensitivity, energy resolution and neutron detection efficiency. During this evaluation, several prototypes were constructed and tested for that purpose. A brief overview of the research is presented below.

Coatings: To evaluate the suitability of the coatings, several investigations were made [2, 52, 63]. This included tests to ensure that the $^{10}B_4C$ layers contained low amounts of impurities, that they are radiation hard and that the film thicknesses are sufficiently uniform. The research also covers the coating process details, such as optimum coating temperature and the engineering required to enable mass production and to make the coating process reproducible. Recent work has focused on the understanding of surface effects on the coatings [64].

Uniformity: The efficiency uniformity was investigated by scanning the detector surface with a 1.5 mm $\times$ 1.5 mm collimated neutron beam [3–5]. Due to the narrow beam, it was also possible to scan the sub-voxel detector response and investigate how the efficiency and PHS vary with neutron hit location. From the investigation, it was concluded that a less than 1 % variation was found over the detection array.

Background: Several aspects of background reduction has been studied. This includes aspects of gamma sensitivity [6, 7], fast neutron sensitivity [9], internal alpha background reduction [8] and investigations on how the shielding design affects background from internal neutron scattering [23, 65, 66]. The investigations showed, for example, that by applying an appropriate threshold the gamma sensitivity of the Multi-Grid detector is equal to that of helium-3 detectors. This includes a gamma sensitivity in the order of 10^{-9} when a Cs-137 source was used. Additionally, a fast neutron sensitivity of around half that of helium-3 tubes was observed. Further investigations have later indicated two orders of magnitude lower fast neutron sensi-

tivity of boron-10-based detectors compared to helium-3 tubes [67]. Concerning the internal alpha background, it was seen that by switching from natural to radiopure aluminum substrates that the background rate could be reduced by a factor of 50.

Aging: The effect of aging [3] and neutron activation of detector components [68] – such as the Ar-CO_2 gas and aluminum – has been studied. It was found that the activity induced by the neutron flux when using a continuous flow of Ar-CO_2 gas is negligible. Furthermore, during a prototype test the detector was left in continuous use for 6 months without intervention and no deviations from steady state operation were observed [9].

Efficiency: Concerning the neutron detection efficiency, an analytical framework has been developed [27,50] and compared with simulations [3]. Additionally, neutron beam measurements have been performed for verification and validation, such as in [3, 7, 9]. The measurements showed a good match with the predicted efficiency. The code used to calculate the efficiency is available as public software and is also usable as an online tool [51].

Energy resolution: To compare the energy resolution, a vanadium sample was measured with both the Multi-Grid detector and helium-3 tubes [9,69]. As a metric, the Full Width at Half Maximum (FWHM) of the elastic peak was used. This examines the energy resolution of the full instrument – keeping variables such as choppers and guides constant – while only varying the detector. The measurement used incident energies between 0.76 meV and 80 meV, and for all peaks, a good match in energy resolution was observed between the two detector technologies.

Count rate: The count rate was probed by exposing the Multi-Grid detector and helium-3 tubes with a high neutron flux from a strong Bragg reflection [9]. During this measurement, the detector behaviour of the two technologies under high flux was compared. During the exposure, a loss of position resolution was found in the helium-3 tubes but not in the Multi-Grid detector. This indicates the high count rate capabilities of the Multi-Grid, which will need additional measurements to quantify it further.

Lineshape: To assess the energy lineshape, the Multi-Grid detector was been measured side-by-side with helium-3 tubes [7, 9]. This allowed a detailed comparison under normal operation conditions of how the two detectors resolve features from samples, such as vanadium. During the measurements, the Multi-Grid detector and helium-3 tubes were observed to resolve the same features. However, from the measurement data with the Multi-Grid detector, small differences were seen around the base of the elastic peak, which is an important region for QENS measurements. To

address and investigate this, simulations were performed [23, 65, 66] and coating on the radial blades was implemented for the next prototype.

2.6 Scope

The characterization in the previous section presents a broad summary of the many studies carried out before the start of this work to optimise and define many of the design parameters of the Multi-Grid detector. The purpose of the current study is to move forward from that point by examining the detector performance in terms of lineshape and signal-to-background ratio and to assess if it fulfils the criteria listed in table 2.1. The current work also includes experimentally quantifying the effect of coating the radial blades and investigating possible shielding configurations for the detector.

The studies done in this work to ensure and validate that the detector fulfils the requirements are divided into three parts: a shielding investigation, a beamtime at the ESS test beamline V20, and a measurement campaign at the cold neutron spectrometer LET. First, the shielding optimisation of the detector is presented with a framework created to quantitatively compare and narrow down a large collection of different shielding options for the final Multi-Grid detector. After that, the V20 studies are shown, which focus on quantifying the effect of radial coating on energy lineshape. The tests also present a re-confirmation of the neutron detection efficiency and a detailed comparison between the energy resolution of the Multi-Grid detector and a helium-3 tube. Finally, a summary of the LET measurements is given, which focuses on the energy lineshape and signal-to-background ratio of the detector during operation in a neutron spectrometer. The investigations are presented in one chapter each, starting with the shielding study.

Chapter 3

Detector shielding

Effective neutron shielding is an essential component for every detector, including the Multi-Grid. The shielding is used to reduce the flux of internally scattered neutrons and external background neutrons entering the active detector volume, thereby increasing the signal-to-background ratio. This is especially important for neutrons with energies the detector is optimised to detect: cold to epithermal neutrons. Therefore, the focus is on this energy range when searching for an appropriate shielding design for the Multi-Grid detector.

The task of finding an effective cold to epithermal neutron shielding design is not unique to the Multi-Grid detector. Indeed, it is relevant for many neutron detectors designed for neutron scattering instruments. Therefore, some effort went into defining a more generic step-by-step solution for a specific shielding requirement. This is not only valuable to the development of the Multi-Grid detector, but can potentially be used in other shielding applications as well.

Cold to epithermal neutron shielding for detector applications has been studied previously [23, 65, 66, 70]. In most of the investigations cited here, the focus was specifically on the Multi-Grid detector using a combination of measurement data and Geant4 [71–73] simulations. The aim was to investigate how background from internally scattered neutrons could be reduced by applying internal shielding.

In this work, however, a more generic method for examining the effectiveness of various shielding configurations is developed. The aim is to provide an easy-to-use guideline, based on analytical calculations, to identify potential shielding candidates. By following the guideline procedures, it should be possible to gain a fair idea of which shielding materials, and thicknesses, are necessary to reach a certain signal-to-background ratio (SBR). This is beneficial because it can be time-consuming to implement and run full-scale complex

simulations. Furthermore, the search space of possible shielding configurations depends on many parameters, which adds to the overall complexity. Therefore, it is desirable to have a method to narrow down the possible shielding candidates as much as possible at an early stage.

To quantitatively evaluate and compare different shielding configurations, an SBR metric, with reference to a generic detector geometry, is introduced to measure the amount of background neutrons entering the active detector volume. Each shielding configuration is divided into four components, one for external shielding and three for internal shielding, where each component is assigned a unique way of measuring its contribution to the overall background. This is because, depending on where the shielding is applied in the detector, it will serve different purposes, and will therefore require different ways to measure its performance. For example, the purpose of the external shielding is to keep out outside neutrons, so the only thing which should be considered here is neutron transmission. This is in contrast with internal shielding, where it is also necessary to consider how much of the incident neutrons scatter back into the active volume due to the shielding material.

The SBR metric depends on two attributes: (1), the amount of neutrons being transmitted through the shielding, *transmission*, and (2) the amount of back-scattered neutrons which re-emerge into the active volume, *albedo*. To analytically derive the value of these, it is assumed that the dominant factors are the neutron absorption and scattering probabilities in the shielding materials. To find these, the interaction cross-sections are first extracted from Geant4 (version 10.4.3) using the ESS Detector Group (DG) framework [74, 75], where the QGSP_BIC_HP_EMZ Geant4 physics list is used. The cross-sections are mainly extracted from materials which are modelled using NCrystal [76, 77], which is used to account for low energy neutron interactions – such as Bragg reflections – which is not treated in standard Geant4. After that, the corresponding interaction probabilities are then found using the mean free path approximation, which uses the cross-sections together with the average atomic density and material thickness. The derivation of the interaction probability formula is outlined in [27].

Using the obtained SBR for a specific set of shielding materials, such as Cd and Gd_2O_3, it is then possible to pinpoint which shielding materials would be appropriate to use. The final step is to have a procedure for navigating through the possible shielding candidates. This is provided at the end of the investigation as a flowchart that can be followed. Here, the full process – including the definition of performance metrics, the extraction of interaction cross-sections and the pinpointing of appropriate shielding materials – is presented. This investigation is a major part of the research work in this thesis and it has been published in a peer review journal [78] with the analysis framework uploaded to [79] for use by the wider community. Via the online repository, the code can be run directly in the browser.

3.1 Metric

To evaluate and compare different shielding configurations, a quantitative performance metric is needed. As the purpose of the shielding is to optimise SBR by reducing the background, this quantity is considered appropriate to quantify the shielding effectiveness. The SBR in this work, for a specific neutron energy E_n, is defined according to the following equation,

$$\mathrm{SBR}(E_n) = \left.\frac{\Phi^{signal} \cdot \epsilon^{detection}}{\Phi^{background} \cdot \epsilon^{detection}}\right|_{E_n} = \left.\frac{\Phi^{signal}}{\Phi^{background}}\right|_{E_n}, \tag{3.1}$$

where Φ^{signal} and $\Phi^{background}$ are the fluxes (neutrons/unit time) of signal and background neutrons, respectively, entering the active detector volume, while $\epsilon^{detection}$ is the neutron detection efficiency. Note that in the last step, the neutron detection efficiency is assumed to be identical for all neutrons, signal and background, with the same energy entering the active volume. This is not strictly correct as the neutron incident angle can affect detection efficiency. However, to keep the definition as general as possible, and to facilitate calculations, this is the approximation used.

The first step in determining the SBR is to define which background sources are considered. This is presented in figure 3.1, where the top view of a general detector shielding layout is shown. The background includes stray neutrons entering the active detector volume (1), albedo neutrons from the vessel walls and back (2), neutrons which are scattered inside the active detector volume (3), and albedo neutrons from the shielding materials themselves (4). Using the Multi-Grid detector as an example, each light grey region would approximately correspond to a column as seen from the top.

To attenuate these backgrounds, shielding is introduced externally and in all internal pathways leading to and from potential scattering locations, as shown in figure 3.1. The shielding configuration is divided into four generic components, namely external shielding (purple), end shielding (red), side shielding (blue) and interstack shielding (green). To evaluate the effectiveness of the shielding, it is useful to know – for each incident neutron hitting the shielding – how likely the neutron is of reaching the active volume as background (either through transmission or albedo). This will be referred to as the probability of the incident neutron "becoming background". This is a useful concept, as it is a general quantity which can be used to directly compare the different shielding components. A neutron can end up as background either through transmission, albedo or a combination of the two processes, where the exact details depend on the specific shielding component. For simplicity, neutrons are assumed to always hit the shielding perpendicularly and all scattering interactions are approximated to be elastic.

The purpose of the external shielding is to keep out outside neutrons, so the probability of

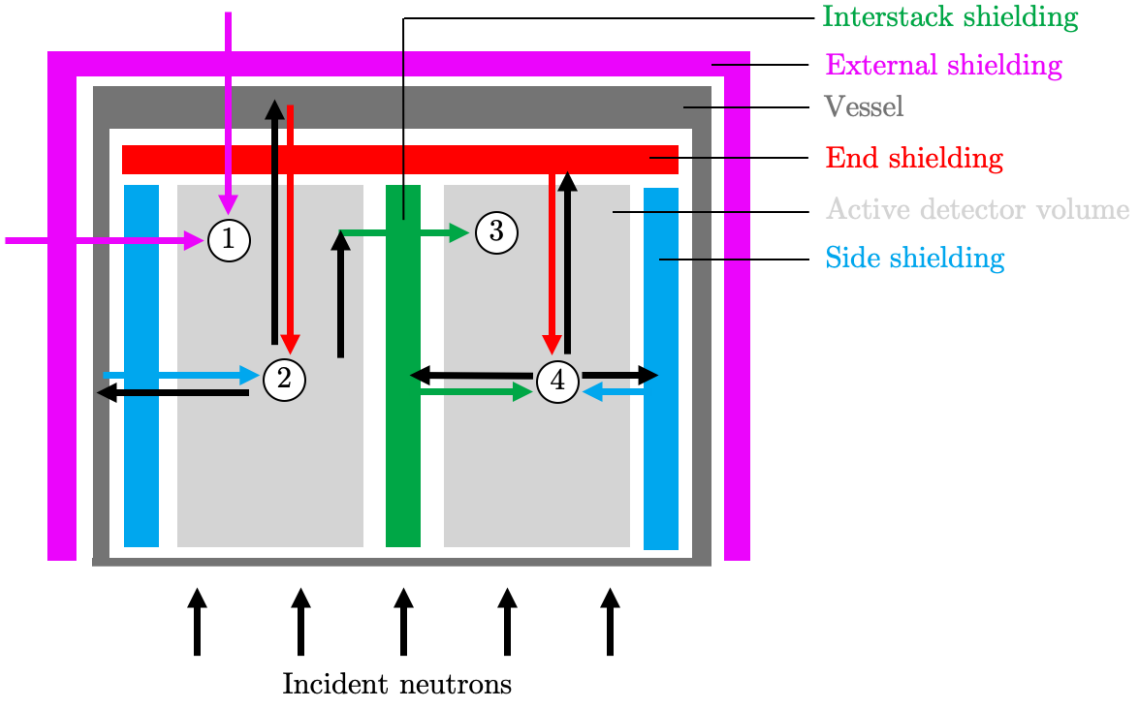

Figure 3.1: Top view of a generic neutron detector, displaying background neutrons together with the shielding configuration designed to attenuate them. In the figure, the vessel (dark grey) and active detector volume (light grey) are presented together with different categories of shielding (interstack, external, end and side shielding). The numbers associated with the arrows highlight the different types of backgrounds and include (1) external background, (2) scattering in the vessel, (3) scattering in the active volume and (4) scattering of the shielding materials.

an incident neutron upon the external shielding to become background, $P_{external}$, is simply the probability of the neutron to be transmitted through the shielding and reaching the active volume ($P_{transmission}$). This is in contrast with the interstack shielding, which serves two purposes: preventing scattered neutrons from reaching the adjacent active volume, while at the same time not scattering them back. Consequently, the probability of an incident neutron upon the interstack shielding to become background, $P_{interstack}$, depends on both the transmission and albedo probabilities ($P_{transmission} + P_{albedo}$).

For the side and end shielding, the probability for an incident neutron to become background, P_{side} and P_{end}, respectively, similarly depends on two terms. The first term represents the amount of neutrons which are transmitted through the shielding, back-scatters in the vessel, and are then transmitted back into the active volume ($P_{transmission} \cdot P_{vessel\,albedo} \cdot P_{transmission}$). The second term is the neutron albedo of the shielding itself (P_{albedo}). To be as general as possible, and to simplify the calculations, a worst-case scenario is applied: $P_{vessel\,albedo} = 1/2$. That is, if a neutron reaches the vessel, there is a 50 % probability that it will scatter back towards the active volume.

The probabilities, for each shielding component, of an incident neutron with an energy E_n upon the shielding to reach the active volume as background is summarised in the equations below,

$$P_{external}(E_n) = P_{transmission}|_{E_n} \tag{3.2a}$$

$$P_{side}(E_n) = P^2_{transmission} \cdot \frac{1}{2} + P_{albedo}\Big|_{E_n} \tag{3.2b}$$

$$P_{end}(E_n) = P^2_{transmission} \cdot \frac{1}{2} + P_{albedo}\Big|_{E_n} \tag{3.2c}$$

$$P_{interstack}(E_n) = P_{transmission} + P_{albedo}|_{E_n} \tag{3.2d}$$

where $P_{transmission}$ is squared for P_{side} and P_{end} because neutrons have to travel through the shielding twice during their round-trip.

The difference in the expected incident flux upon the separate shielding components is considered to get a clearer understanding of the relative importance of each component. The background flux due to the different shielding components is presented in equations (3.3a) to (3.3d), which show the relationship between incident neutron flux, $\Phi^{incident}$, and the background flux which escapes the shielding, $\Phi^{background}$, for neutrons with energy E_n,

$$\Phi^{background}_{external}(E_n) = \Phi^{incident}_{external} \cdot P_{external}\Big|_{E_n} \tag{3.3a}$$

$$\Phi^{background}_{side}(E_n) = \Phi^{incident}_{side} \cdot P_{side}\Big|_{E_n} \tag{3.3b}$$

$$\Phi^{background}_{end}(E_n) = \Phi^{incident}_{end} \cdot P_{end}\Big|_{E_n} \tag{3.3c}$$

$$\Phi^{background}_{interstack}(E_n) = \Phi^{incident}_{interstack} \cdot P_{interstack}\Big|_{E_n} \tag{3.3d}$$

where the subscript indicates which background component the flux refers to.

Using equations (3.3a) to (3.3d), the SBR definition in equation (3.1) can be expanded to,

$$\mathrm{SBR}(E_n) = \frac{\Phi^{signal}}{\Phi^{background}_{external} + \Phi^{background}_{side} + \Phi^{background}_{end} + \Phi^{background}_{interstack}}\Bigg|_{E_n}. \tag{3.4}$$

Note that each shielding component is treated independently. That is, in this simplified model, an increased thickness of the side and end shielding does not decrease the number of external neutrons entering the detector, which would be the case in a real-world application. Instead, this amount is completely determined by the thickness of the external shielding. The motivation for this is, again, to keep the model as simple as possible.

3.2 Calculations

To determine the shielding efficiency, it is necessary to evaluate equations (3.2a) to (3.2d), which contains the "incident neutron on shielding to background"-probabilities. As all of these probabilities depend upon $P_{transmission}$ and P_{albedo}, it is sufficient to determine these two quantities to evaluate the expression for all four shielding components. However, to do this analytically and in a general fashion, a few approximations and assumptions are made.

As a starting point, it is assumed that the transmission and albedo are determined by the neutron absorption and scattering probabilities in the material. These probabilities vary between materials and depend on the microscopic cross-sections – cross-section per nuclei – which influence the macroscopic cross-sections – microscopic cross-section scaled with atomic number density – that, in turn, determines the overall interaction likelihood. To calculate these probabilities, the interaction probability $P_{interaction}$ for a neutron with energy E_n travelling through a material of depth d is calculated according to

$$P_{interaction}(E_n,\, d) = 1 - \exp[-\Sigma(E_n) \cdot d], \tag{3.5}$$

where Σ is the macroscopic interaction cross-section, defined according to equation (3.6),

$$\Sigma(E_n) = \sigma(E_n) \cdot N, \tag{3.6}$$

where σ is the microscopic interaction cross-section and N is the atomic number density. The atomic number density N [cm^{-3}] relates to the weight density ρ [$\mathrm{g} \cdot \mathrm{cm}^{-3}$] according to equation (3.7),

$$N = \frac{\rho}{A} \cdot N_A \cdot N_{atoms\,per\,molecule}, \tag{3.7}$$

where A is the molecular weight [$\mathrm{g} \cdot \mathrm{mol}^{-1}$], N_A is Avogadro's number [6.022×10^{23} mol^{-1}], and $N_{atoms\,per\,molecule}$ is the number number of atoms per molecule. For molecules and composite materials, σ and N are calculated as atomic averages.

As the values of σ and N are material dependent, it is necessary to introduce a set of potential shielding materials to perform the calculations. These are presented in table 3.2, where a summary of all materials used in this work is shown with their corresponding average atomic densities $\bar{N}$ and chemical composition. The values of $\bar{N}$ were extracted using the ESS DG simulation framework.

An ideal shielding material absorbs all incident neutrons incident upon it without leading them to reflect or scatter. Therefore, most of the materials listed in table 3.2 were chosen for their large content of highly neutron-absorbing isotopes, such as ^{6}Li, ^{10}B, ^{113}Cd and ^{157}Gd. However, a few materials – namely aluminum and epoxy – were included in the

table not because of their shielding properties, but because they are commonly used in detectors and it is important to know their scattering yield. Finally, polyethylene is also investigated due to its large hydrogen content and consequent neutron scattering properties. This makes it a reference for what a worst-case scenario in terms of scattering might look like.

The investigated materials are implemented in two different categories, as highlighted by the asterisks and daggers in the table. Most of the materials are implemented as NCrystal materials (daggers), due to the extra information available concerning material structure. There are, however, a few exceptions, and these are implemented as standard Geant4 materials (asterisks). The first reason for this is that NCrystal does not model resonance frequencies in the cold to thermal energy range, which is why cadmium, Gd_2O_3 and the Epoxy-Gd_2O_3 mixtures are all implemented as standard Geant4 materials. In the Epoxy-Gd_2O_3 mixtures, both the Epoxy and Gd_2O_3 are implemented as standard Geant4 materials, as mixing standard Geant4 and NCrystal materials is currently not supported. Another reason for not using NCrystal materials, as in the case of MirroBor, is that the molecular structure formula of the material was not known at the time of writing this thesis.

For the compound materials in the table, approximations of the total weight densities are used for materials without table values, such as epoxy-Gd_2O_3 mixtures. This is done by first assuming that the weight density of each of the components does not change when they are part of a compound. After that, the volumetric fraction of each component needed to achieve a specific weight ratio, for example, 50 wt% epoxy and 50 wt% B_4C, is calculated. Using the obtained volumetric fractions for each component and scaling it with the corresponding densities, the resultant density of the compound is calculated.

The next step is to extract the average microscopic absorption and scattering cross-sections separately for these shielding materials. This is presented in figure 3.2, where the cross-sections were extracted from Geant4 using the ESS DG coding framework. The cross-sections presented are those resultant from both the data and algorithms (which account for effects such as Doppler broadening) that Geant4 uses to produce cross-sections. For the scattering cross-sections, this is the sum of cross-sections for all types of scattering, including those for coherent elastic, coherent inelastic, incoherent elastic and incoherent inelastic scattering. Using the microscopic cross-sections together with the corresponding atomic number densities, the macroscopic cross-sections of the materials are calculated, see figure 3.3.

Table 3.1: Summary of the materials used in this work, showing their molecular composition, weight distribution, enrichment level, and average atomic number densities $\bar{N}$. Materials implemented as standard Geant4 materials are marked with asterisks, while materials implemented using NCrystal are marked with daggers. Note that for their potential radiation hazard, the intensity of gamma rays produced from the neutron absorption reactions should not be ignored. MirroBor [58] and Boral [80] are commercially available products.

Material	**Composition**	**wt%**	**Enrich. [at%]**	$\bar{N}$ **[cm^{-3}]**
		Elements		
Cadmium*	Cd	100		$4.63401 \cdot 10^{22}$
Aluminum†	Al	100		$6.02325 \cdot 10^{22}$
		Molecules		
Gadolinium oxide*	$^{nat}Gd_2O_3$	100		$6.15251 \cdot 10^{22}$
Boron carbide (natural)†	$^{nat}B_4C$	100	^{10}B/B: 20	$1.36702 \cdot 10^{23}$
Boron carbide (enriched)†	B_4C	100	^{10}B/B: 99	$1.36712 \cdot 10^{23}$
Lithium fluoride (natural)†	^{nat}LiF	100	^{6}Li/Li: 8	$1.23396 \cdot 10^{23}$
Lithium fluoride (enriched)†	LiF	100	^{6}Li/Li: 99	$1.23392 \cdot 10^{23}$
Epoxy†	$C_{54}H_{60}O_9$	100		$1.02462 \cdot 10^{23}$
Polyethylene†	C_2H_4	100		$1.18497 \cdot 10^{23}$
		Compounds		
Epoxy - Gadolinium oxide* (50 - 50)	$C_{54}H_{60}O_9$ $^{nat}Gd_2O_3$	50 50		$9.68366 \cdot 10^{22}$
Epoxy - Gadolinium oxide* (35 - 65)	$C_{54}H_{60}O_9$ $^{nat}Gd_2O_3$	35 65		$9.30040 \cdot 10^{22}$
Epoxy - Boron carbide† (natural)	$C_{54}H_{60}O_9$ $^{nat}B_4C$	50 50	^{10}B/B: 20	$1.13422 \cdot 10^{23}$
Epoxy - Boron carbide† (enriched)	$C_{54}H_{60}O_9$ B_4C	50 50	^{10}B/B: 99	$1.13861 \cdot 10^{23}$
MirroBor*	$^{nat}B_4C$ C O H	80 14 5 1	^{10}B/B: 20	$7.95206 \cdot 10^{22}$
Boral† (90 - 10)	Al $^{nat}B_4C$	90 10	^{10}B/B: 20	$6.83984 \cdot 10^{22}$
Boral† (33 - 67)	Al $^{nat}B_4C$	33 67	^{10}B/B: 20	$1.12700 \cdot 10^{23}$

* Implemented as standard Geant4 material
† Implemented as NCrystal material

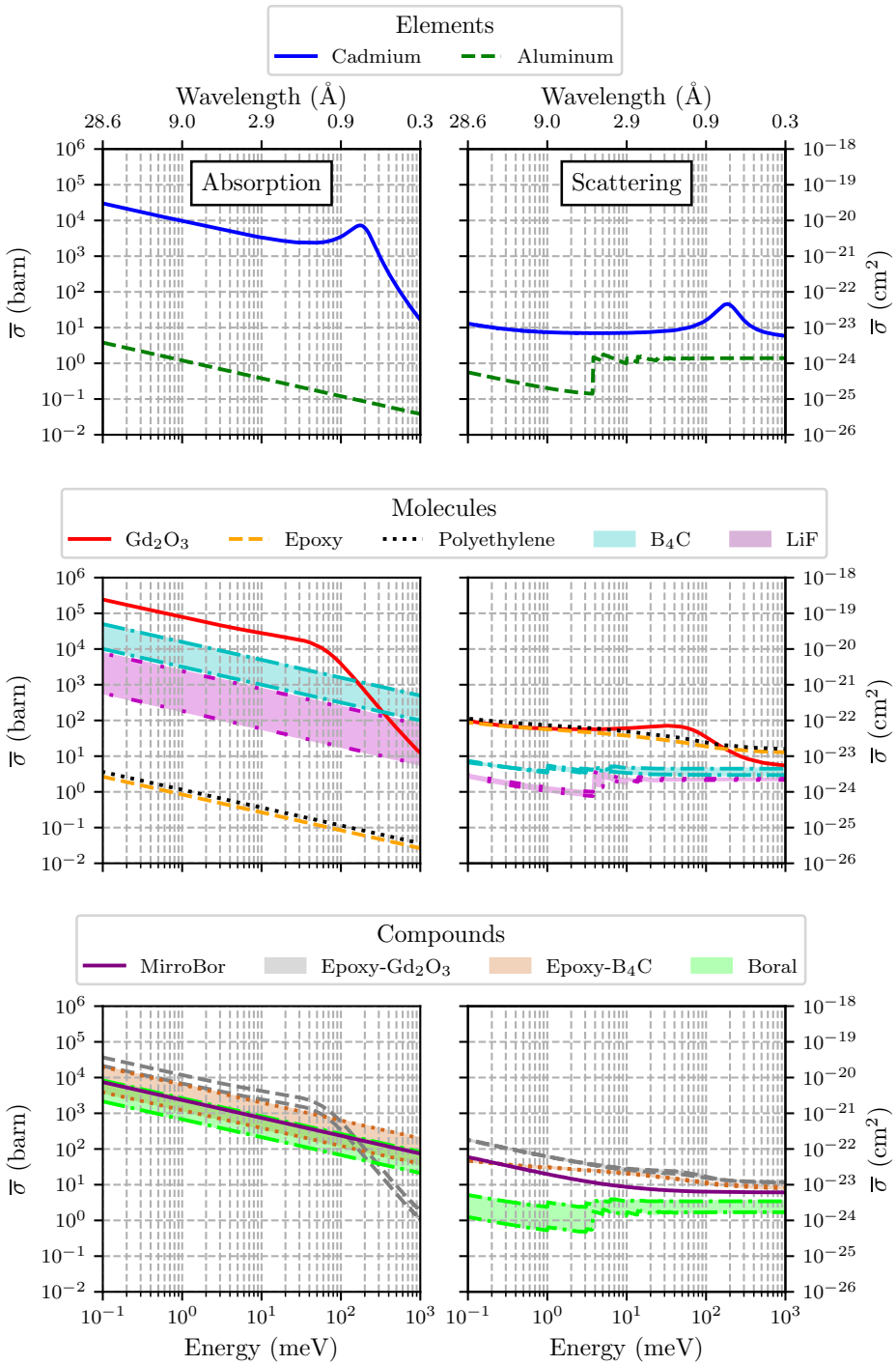

Figure 3.2: Average microscopic cross-sections $\bar{\sigma}$ for the materials under investigation. The width of the bands indicates the change in cross-section due to variation in material composition, as defined in table 1. The average atomic absorption and scattering cross-sections are presented in the left and right columns, respectively. For the scattering cross-sections, this is the sum of microscopic cross-sections for all types of scattering, including those for coherent elastic, coherent inelastic, incoherent elastic and incoherent inelastic scattering. Data extracted using the ESS DG framework [74, 75], as described in the text.

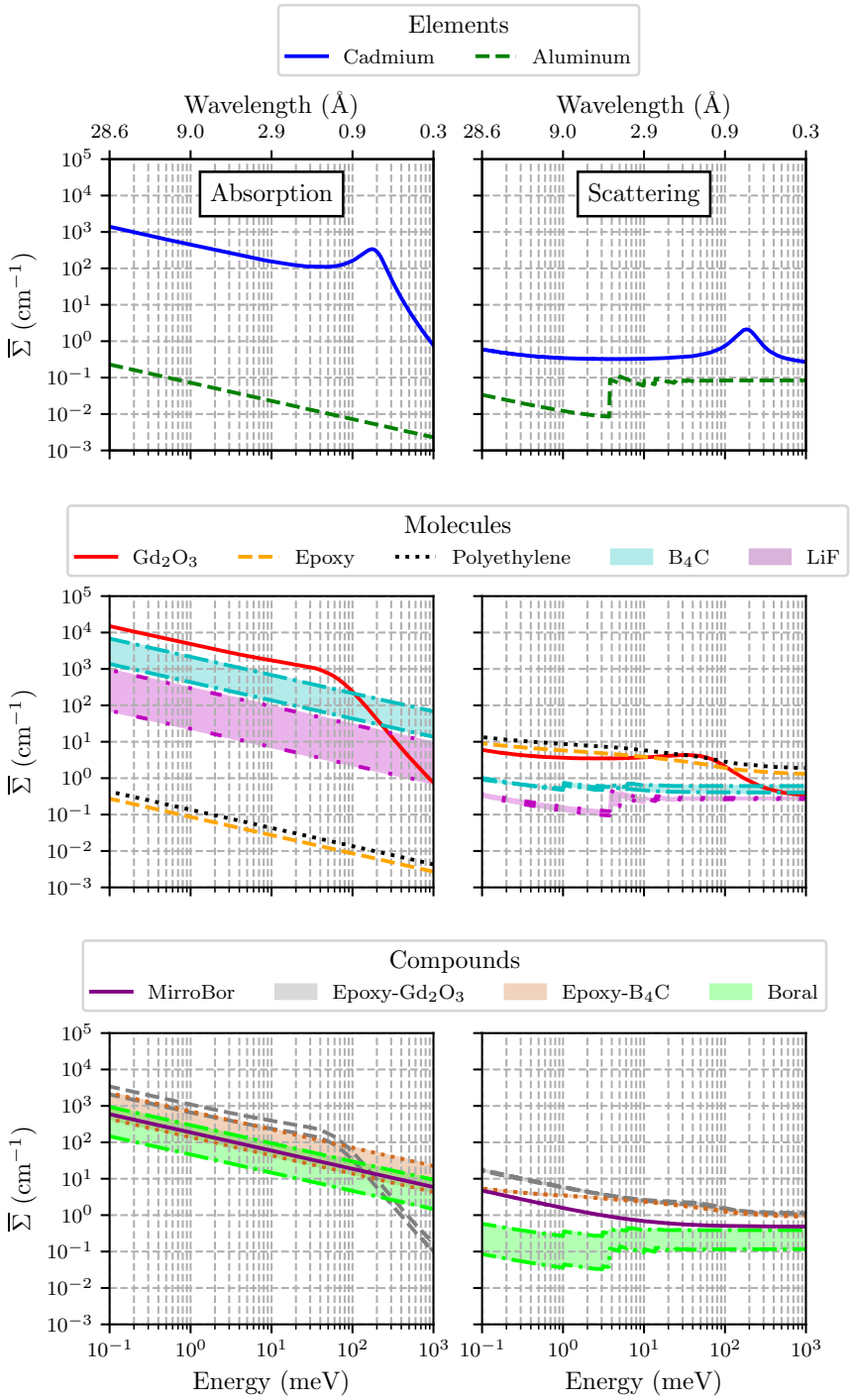

Figure 3.3: Average macroscopic cross-sections $\bar{\Sigma}$ for the materials under investigation. The width of the bands indicates the change in cross-section due to variation in material composition, as defined in table 1. The average macroscopic absorption and scattering cross-sections are presented in the left and right columns, respectively. For the scattering cross-sections, this is the sum of macroscopic cross-sections for all types of scattering, including coherent elastic, coherent inelastic, incoherent elastic and incoherent inelastic scattering.

Using the macroscopic absorption and scattering cross-sections together with equation (3.5), the absorption and scattering probabilities, $P_{absorption}$ and $P_{scattering}$, respectively, are calculated according to equations (3.8a) and (3.8b),

$$P_{absorption}(E_n,\, d) = 1 - \exp[-\Sigma_{absorption}(E_n) \cdot d] \tag{3.8a}$$

$$P_{scattering}(E_n,\, d) = 1 - \exp[-\Sigma_{scattering}(E_n) \cdot d] \tag{3.8b}$$

where $\Sigma_{absorption}$ and $\Sigma_{scattering}$ are the macroscopic absorption and scattering cross-sections, respectively.

Using the absorption and scattering probabilities, the next step is to estimate the transmission and albedo of the shielding materials. To simplify the calculations, a one-dimensional model representing the three-dimensional scattering problem is used. In the model, only single scattering interactions are considered[1] and all scattering is assumed to be isotropic and elastic. This means that half the neutrons are forward-scattered and half are back-scattered. This simplified one-dimensional model does not take into account any angular dependencies and therefore all neutrons are considered to be incident along the normal of the shielding material. Neutrons that scatter will be assumed to scatter along that same line, either forward or backwards.

For a neutron to be considered transmitted, it is required that it is not absorbed or back-scattered during its passage through the shielding medium, as illustrated in figure 3.4. Therefore, the probability of a neutron being transmitted can be expressed as the joint probability of both these conditions being fulfilled simultaneously.

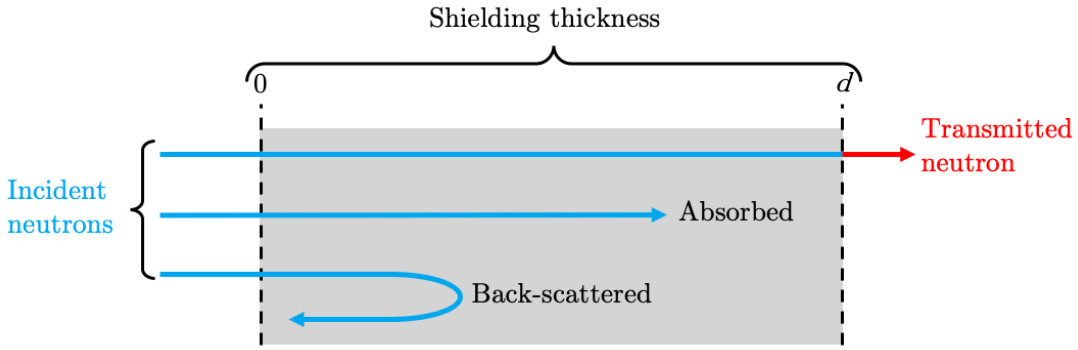

Figure 3.4: Visualisation of the one-dimensional transmission calculation for neutrons incident on a shielding with thickness d. For a neutron to be transmitted, it is required that the neutron is not absorbed or back-scattered in the shielding.

[1]The realism of this assumption varies with material and incident neutron energy, which affects the ratio between absorption and scattering cross-sections. For a 1 mm thick cadmium sheet with 25 meV (1.8 Å) incident neutrons, the probability of a single scattering can be approximated as $[1 - P_{absorption}(25, 0.1)] \cdot P_{scattering}(25, 0.1) \approx (1.0 \cdot 10^{-5}) \cdot (3.5 \cdot 10^{-2}) = 3.5 \cdot 10^{-7}$. Hence, the probability of multiple scatterings is negligible in this case.

As the probability of being absorbed is given by $P_{absorbed}$, it follows that the probability of not being absorbed is the inverse of this ($P_{not\,absorbed} = 1 - P_{absorbed}$). Furthermore, as the scattering is assumed to be isotropic, there is a 50 % probability that the neutron is back-scattered, i.e. $P_{back-scattered} = \frac{1}{2}P_{scattered}$. Hence, the probability of the neutron not back-scattering is given by the inverse of this, $(1-\frac{1}{2}P_{scattered})$. Therefore, the transmission probability, $P_{transmission}$, of a neutron with energy E_n incident on a shielding with thickness d is given by equation (3.9),

$$P_{transmission}(E_n,\, d) = (1 - P_{absorption}) \cdot (1 - \frac{1}{2}P_{scattering})\Big|_{E_n,\, d}. \tag{3.9}$$

For an incident neutron to become albedo, it is required that it is back-scattered at some point in the shielding material, that the neutron is not absorbed on the way to that point, and that it is not absorbed on the way back out from that point. This is visualized in figure 3.5. As the joint probability of these three conditions being fulfilled simultaneously is strongly dependent on where along the depth of the shielding the neutron is scattered, the shielding depth d is split into N segments which are considered individually. The total albedo probability is then calculated as the sum of the albedo contributions from all the segments. In the figure, the albedo contribution from the i:th segment is shown.

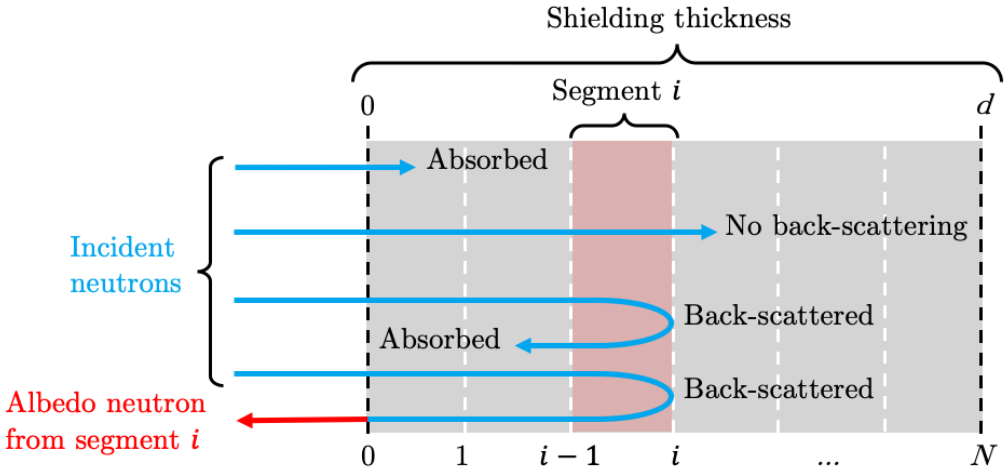

Figure 3.5: Visualisation of the one-dimensional albedo calculation for neutrons incident on a shielding with thickness d, illustrating how the shielding is divided into N segments. In the figure, the albedo contribution from the i:th segment is shown, which is highlighted in red. The segment thicknesses are assigned equal lengths on a one-dimensional logarithmic coordinate system. This is to facilitate calculations, which are needed over several orders of magnitude. Note that the neutrons are assumed to scatter from the deepest end of the segment.

For a neutron to become albedo in segment i, it must not be absorbed on the path leading up to the segment, nor in the segment itself. This probability is given by $(1 - P^i_{absorption})$,

where the superscript indicates the thickness, as seen in figure 3.5. Furthermore, it has to be back-scattered in the segment, which has a probability given by $\frac{1}{2}\left(P^{i}_{scattering} - P^{i-1}_{scattering}\right)$. Note that the probabilities are subtracted because they are accumulated probabilities, while the factor $\frac{1}{2}$ is due to the assumption of isotropic scattering. Finally, the neutron must not be absorbed on the way back, as it passes the same amount of shielding a second time. This probability is equal to the probability of not being absorbed on the way in, $(1 - P^{i}_{absorption})$, as it is the same path length.

Putting this together, gives the probability of albedo from a segment i, P^{i}_{albedo}, according to,

$$P^{i}_{albedo}(E_n) = (1 - P^{i}_{absorption})^2 \cdot \frac{1}{2}\left(P^{i}_{scattering} - P^{i-1}_{scattering}\right)\Big|_{E_n}, \tag{3.10}$$

where $(1 - P^{i}_{absorption})$ is squared because it appears twice. Using this expression, the total albedo probability, P_{albedo}, is in this work approximated according to equation (3.11),

$$P_{albedo}(E_n,\, d) = \sum_{i=1}^{N}(1 - P^{i}_{absorption})^2 \cdot \frac{1}{2}\left(P^{i}_{scattering} - P^{i-1}_{scattering}\right)\Big|_{E_n}, \tag{3.11}$$

where the summation is over all segments in the shielding layer.

Using the above approximations, the neutron transmission and albedo probabilities are calculated as a function of thickness for the shielding materials under consideration. This is presented in figure 3.6 for 25.25 meV (1.80 Å) incident neutrons. As can be seen, the transmission level *decreases* with increased material thickness, while the albedo level exhibits an almost opposite trend: it *increases* with shielding thickness, up to the saturation level where the curve plateaus. Using cadmium as an illustration, it is seen to have a 10^{-5} transmission and 10^{-3} albedo at a 1 mm thickness.

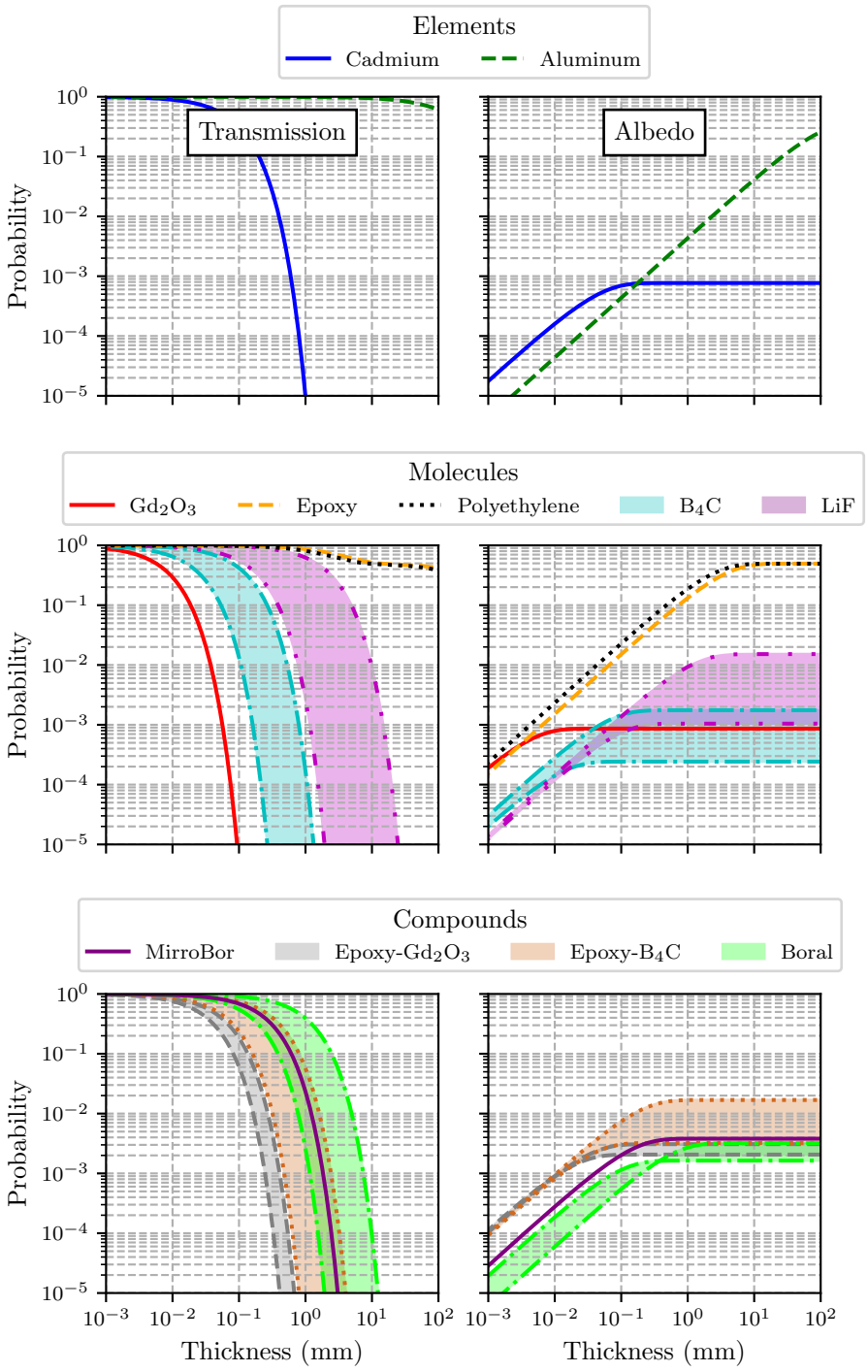

Figure 3.6: Transmission and albedo probability for a fixed incident neutron energy, 25.25 meV (1.80 Å), as a function of thickness for the materials under investigation. The width of the bands is due to variation in the material composition, as defined in table 3.2. The transmission is presented to the left and the albedo to the right.

3.3 Simulations

To validate the calculations and the simplifications assumed, a series of simulations are performed using Geant4 (GEometry ANd Tracking), a simulation platform developed by

an international collaboration initiated by CERN [81] for the studies of particles passing through matter [71–73]. Since its initial release, this simulation platform has been expanded to encompass a diverse range of applications, including cold and thermal neutron detector development. To facilitate the implementation and running of detector simulations, the ESS DG simulation framework [74, 75] has been developed to use within the context of Geant4. In this work, this framework is used together with the NCrystal package [76, 77], which models material interactions with low energy neutrons such as phonon interactions and Bragg scattering. In the following, a brief introduction to Geant4 and the ESS DG framework is given.

3.3.1 Geant4

Geant4 is, for research, a freely available simulation platform used in many different areas, including high energy physics, radiation protection, and medical applications [82]. The software simulates the passing of particles through matter using stochastical methods and can produce insights into highly complicated systems, such as the behaviour of an advanced particle detector system. It does this by iteratively calculating the movement of particles in the material in small consecutive steps, where a probabilistic action is performed at every step. These actions can be, for example, absorption, scattering or radioactive decay, and it creates a stochastic trajectory and interaction history for each generated particle initiated to travel through the material. The probability of the interaction processes is based on physics derived from empirical and theory-based models.

Some examples of the particles that can be tracked include fundamental particles – such as photons, electrons and muons – but also hadrons and nuclei, such as alpha particles. The behaviour of these particles can be simulated for a large energy range, spanning from a few hundred eV up to TeV [71], where the accuracy of the used models has been validated with experimental data. Depending upon the specific energy range of interest, different physics models can be used. This includes, for example, optical models for light propagation and transport through matter. These models can then be combined to select the physics of interest for the application being studied. This is called a *physics list*, which contains all particle information and physics interactions requested for the simulation.

In this work, a custom list is used, namely QGSP_BIC_HP_EMZ, which consists of QGS (Quark Gluon String model), BIC (BInary Cascade model), HP (High Precision neutron model) and EMZ (Electro Magnetic interactions, high resolution). The letter "P" means the model is used to treat de-excitations. Together with this physics list, the previously mentioned NCrystal package is used to model low energy neutron interactions with matter, which is important for this work. For these neutrons, parameters such as the lattice spacing between atoms, as well as phonon distributions, in materials is relevant.

This physics is not included in the standard Geant4 package – which focuses on higher energies – which is why NCrystal is used here to model neutron interactions.

To create and run a simulation, several steps need to be followed. These include defining geometries, material lists, particle interactions, tracking management, visualisation and a user interface. This is all included in Geant4, and it is implemented in a general fashion to allow a wide variety of applications. For the current work, the shielding investigation is closely tied to detector development and is specialized towards that specific topic. Therefore, the Geant4 simulations created for this work were made using the ESS DG framework, which is geared towards this type of research.

3.3.2 ESS DG framework

The ESS DG framework is an easy-to-use Geant4-based simulation framework that is publicly available [83]. The framework includes features such as geometry creation, particle instantiation, analysis tools and visualisation. Additionally, it includes high-level methods for running sequences of simulations using a parameter scan over different conditions, such as neutron energy and materials types. The simulations are controlled using a Python interface to change values such as the physics list, definition of particle instantiation, and parameter scans.

Using the framework, it is possible to quickly extract shielding material properties of interest, such as neutron transmission and neutron albedo, for a large selection of materials subjected to neutrons over a wide energy span. This is presented in the next section, where the simulations used in this work are shown.

3.4 Validation

The aim of the simulations is to investigate the validity of the transmission and albedo probabilities when a more realistic scattering and physics model is used and compare the results with those of the simplified analytical calculations. The simulation setup was designed to be as general as possible, with the aim to only probe two properties of the shielding materials: how many of the incident neutrons are transmitted and how many become albedo. The setup and geometry used for the simulations are shown in figure 3.7.

The simulation consists of three volumes and a particle generator. The volumes include a thin disc target and two semi-spheres, one for transmission and one for albedo, which together fully encapsulates both the particle generator and the target. The particle generator fires a pencil beam of monochromatic neutrons at a perpendicular angle towards the

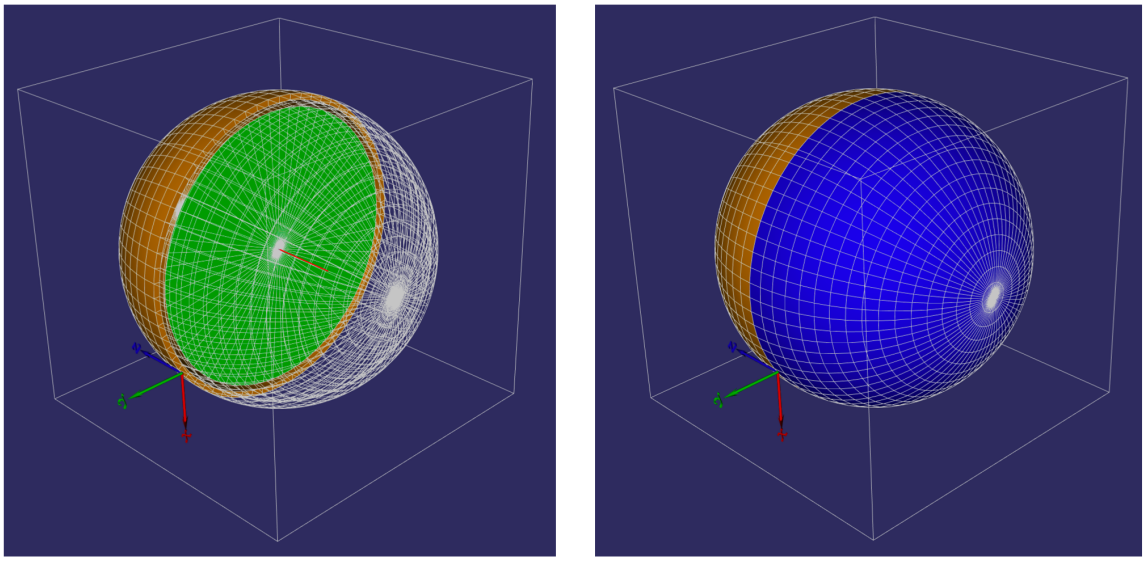

Figure 3.7: Geometry used for simulations, showing the shielding material (green thin disc), incident neutrons (red line), transmission detector (orange half sphere), and albedo detector (blue half sphere). In the left figure, the albedo detector is transparent to show the incident neutrons and shielding material, while in the right figure, both the albedo and transmission detectors are seen fully encapsulating the shielding material and incident neutrons.

centre of the target, whereafter the neutrons are either transmitted and detected, become albedo neutrons and are detected, or are absorbed in the target.

The varied parameters include the energy of incident neutrons, the thickness of the target, and the material of the target. A parameter scan was performed over all shielding materials, with 20 different neutron energies, logarithmically distributed between 0.1 meV and 1000 meV, and 20 different thicknesses, logarithmically distributed between 10^{-3} mm and 10^{2} mm. For each simulation run, 10^{6} incident neutrons were generated. The results from a representative material, cadmium, are presented in figures 3.8 and 3.9, where the results from the calculations and simulations are compared.

In figure 3.8, the transmission and albedo are presented as a function of thickness for three distinct neutron energies, as represented by the different colours. Calculated data are presented as lines while simulated data are highlighted by markers. In figure 3.9, each data point corresponds to a comparison between calculation and simulation output for a specific incident neutron energy (x-axis) and shielding thickness (y-axis). The colours correspond to the ratio between calculated and simulated data. For example, a green colour corresponds to a ratio between 1/2 and 2. Note that the limits are set between a factor of 1/5 and 5 and that values outside this range are projected on the maximum and minimum colours. Additionally, to retain adequate statistics, simulation values with a probability below 10^{-5} are not included in the analysis. The calculated iso-line for 10^{-5}

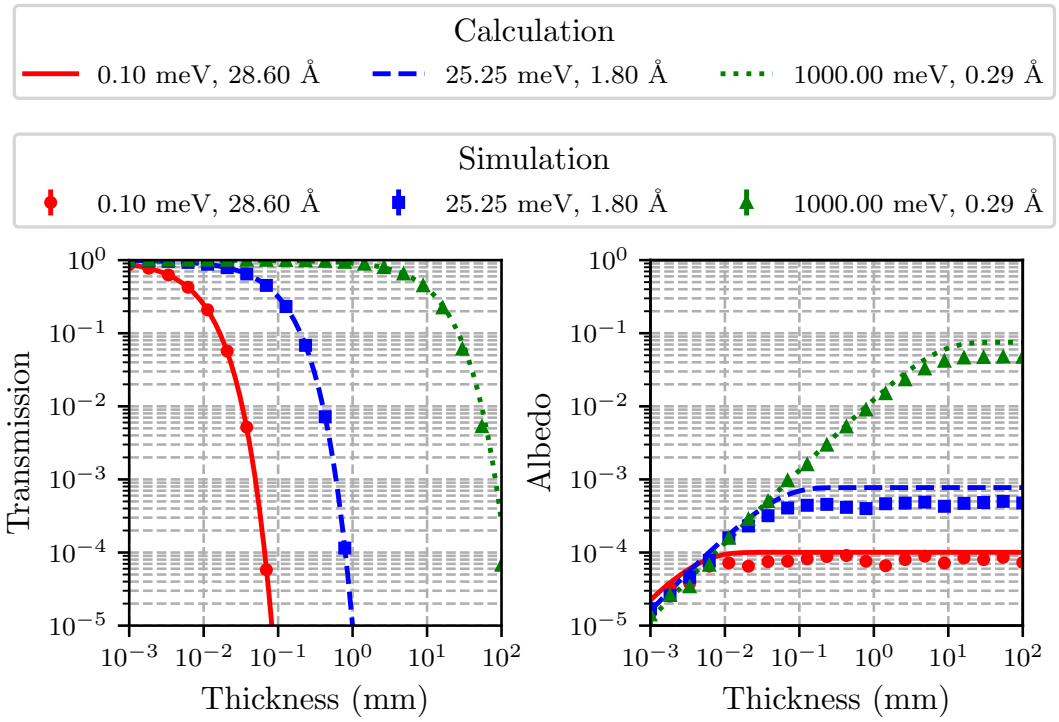

Figure 3.8: Cadmium, a one-dimensional comparison between calculation and simulation outputs, where the transmission and albedo comparisons are shown in the left and right plots, respectively. The comparison is done for three different energies, 0.10 meV (28.60 Å), 25.25 meV (1.80 Å) and 1000.00 meV (0.29 Å). Calculations are shown as lines while the simulation results are shown as markers, where each marker corresponds to a separate simulation. Error bars show statistical uncertainties, but are too small to be discernible.

transmission is shown as a black line, which is seen to closely follow where the simulation data drops below 10^{-5}.

From the results, shown for all materials in figures A.1 to A.16 in the Appendix, it is seen that for most materials the simulations and calculations are in agreement, within a factor of 2, over most energies and thicknesses. This deviation is not unexpected due to the simple model used in the calculations and is sufficiently accurate for the purposes of this investigation. The divergence is greatest for large thicknesses and high energies, where it exceeds a factor of 3 for some materials. There is also a strong transmission divergence for some materials, such as for the epoxy-Gd_2O_3 mixtures, for low energies when the transmission level drops below 10^{-5}. For these materials at this transmission level, the calculations underestimate the transmission level by more than a factor of 5. Nevertheless, as the calculations and simulations agree within a factor of 2 for the majority of the materials for most thicknesses and energies, the calculations are sufficiently accurate to be used to evaluate the degree of shielding needed for a detector.

One important contribution to the observed difference is that the analytical calculation

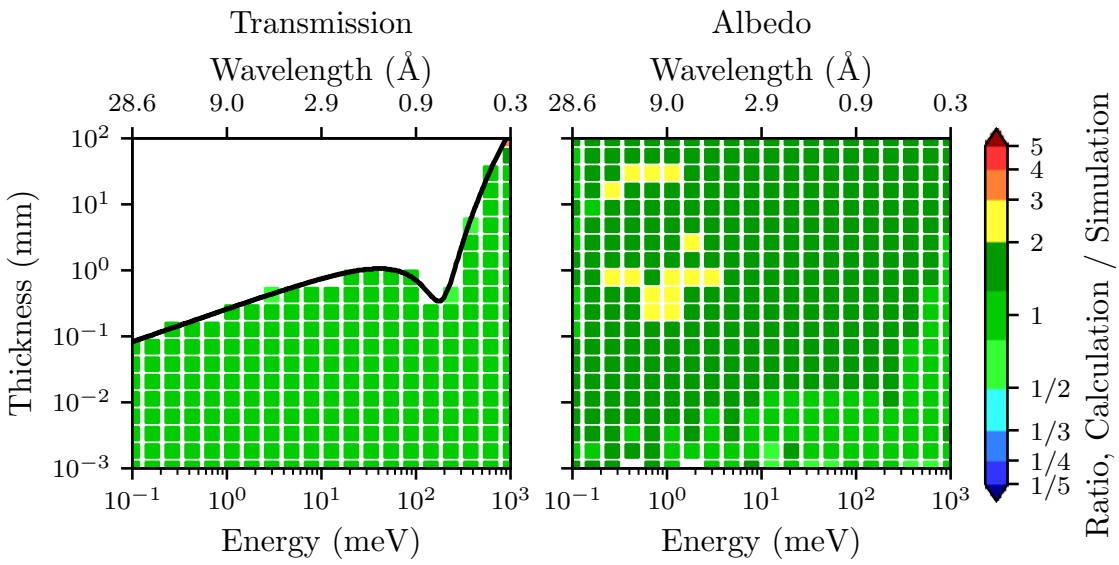

Figure 3.9: Cadmium, two-dimensional comparison between calculation and simulation results, where the transmission and albedo comparisons are shown in the left and right plots, respectively. The comparison is done for all combinations of 20 energies and 20 thicknesses evenly spread across the energy and thickness region under investigation. The colour shows the ratio between calculation and simulation data points. To only display data with a low statistical uncertainty, simulation values below 10^{-5} are not included in the analysis. The calculated iso-line for 10^{-5} transmission is presented in the left plot as a black line, which is seen to closely follow where the simulation data drops below 10^{-5}.

does not account for different scattering angles: it only considers travel paths perpendicular to the shielding material. This means that the calculation uses the shortest possible escape distance for albedo neutrons, as all other scattering angles will infer a longer escape path. This results in a higher absorption probability on the way back for a neutron scattered inside the shielding material with scattering angles divergent from 180°, and hence a lower albedo probability, as observed in the simulated data presented in figures 3.8 and 3.9. There are other effects not included in the analytic calculation which are also important – such as multiple scattering and neutron energy loss via inelastic collisions – and the influence of these vary depending on material and energy. The overall effect is seen for all materials and energies in the Appendix, which gives a wide overview of how the analytic calculation compares to the simulation.

Note that this investigation only probes how well the calculations compare to a more sophisticated simulation method, not real measurement data. Nevertheless, the comparison shows that a greatly simplified model is sufficient to replicate important features from the advanced Geant4 simulation. This is useful as it removes the need for simulations at the early stage of shielding material comparisons. To perform an experimental validation of the transmission and albedo levels for the materials presented here, further studies are

needed which are outside the scope of this work.

3.5 Procedure

Analytical approximations for neutron transmission and albedo have been shown to compare well to simulations, and it is now possible to quantify the performance of different shielding configurations according to the SBR metric presented earlier. However, to identify the most suitable shielding configuration for a specific application, a procedure to find the most appropriate configuration is needed.

The first step is to identify the constraints and requirements of the desired shielding. This includes information about how much space is available for the various shielding components and what the desired SBR is. Next, information is needed about which incident neutron energy the SBR should be fulfilled at. Finally, it is necessary to approximate the intensity of the incident flux on the different shielding components. This is to weigh the relative importance of shielding the different regions, as the amount of flux they are exposed to is generally not equal.

For simplification, and to make the discussion as general as possible, the signal and background fluxes are normalized to the signal flux. That is, the signal flux is set to 1 and the background fluxes are expressed in relation to the incident flux. This makes the SBR easy to grasp and can be deduced simply by looking at the background levels. Studying equation (3.4), it is seen that there are several ways of achieving a certain SBR, depending on the relative strength of the background levels from the various shielding components. Nevertheless, it is a requirement that the background from each of the components is below $\frac{1}{\mathrm{SBR}}$ to fulfil the SBR demand, and this is the criterion used here to ensure that the SBR requirement is fulfilled.

To find a suitable material, the desired SBR and background flux on the various shielding components are related to the more general quantity of "incident-neutron-to-background"-probability discussed earlier, which is material dependent. This gives the maximal acceptable probability, for each shielding component, to fulfil the SBR criterion. The conversion

expressions are presented in equations (3.12a) to (3.12d),

$$P_{external} = P_{transmission} = \frac{1}{\Phi_{external}^{incident}} \cdot \frac{1}{\mathrm{SBR}} \tag{3.12a}$$

$$P_{side} = P_{transmission}^2 \cdot \frac{1}{2} + P_{albedo} = \frac{1}{\Phi_{side}^{incident}} \cdot \frac{1}{\mathrm{SBR}} \tag{3.12b}$$

$$P_{end} = P_{transmission}^2 \cdot \frac{1}{2} + P_{albedo} = \frac{1}{\Phi_{end}^{incident}} \cdot \frac{1}{\mathrm{SBR}} \tag{3.12c}$$

$$P_{interstack} = P_{transmission} + P_{albedo} = \frac{1}{\Phi_{interstack}^{incident}} \cdot \frac{1}{\mathrm{SBR}} \tag{3.12d}$$

Using these equations, the search for suitable shielding materials can start by determining if the transmission or albedo probability is the limiting factor on the performance. Upon closer inspection, as shown in figure 3.10, it is found that at the thickness where the albedo level saturates – i.e. the thickness at which adding more material will not result in more neutrons being reflected back – the transmission level is larger or equal to the albedo level. This is true for all energies and materials investigated here, signifying that the upper performance limit of a shielding material is given by the albedo saturation level. This is an important result, as it simplifies the task of selecting the thickness which gives the best trade-off between transmission and albedo. This is because the only information necessary concerning the albedo probability is the saturation level, which determines the maximum performance level. Once this is known, the performance can be determined by adjusting the transmission level, which can be tuned to the desired level (limited, of course, by the albedo saturation level) by adjusting the shielding thickness. Note that the albedo saturation thickness is here defined as the thickness where the albedo probability has reached 95% of its maximum. This is due to the very slow increase in albedo as a function of thickness when the albedo probability is close to the saturation level.

By using equations (3.12a) to (3.12d) to calculate the required probabilities, figures B.1 to B.13 in the Appendix can be used to identify a shielding material which fulfils these requirements. Here, cadmium is used as an example, as seen in figure 3.11. In the figure, the probability iso-lines for $P_{transmission}$ (blue) and $P_{transmission}^2 \cdot \frac{1}{2}$ (red) are shown as a function of thickness and energy for three different values: 10^{-2}, 10^{-3} and 10^{-4}. Additionally, the albedo saturation thicknesses are shown as a function of energy, together with the corresponding albedo saturation level for each energy. Note that the albedo saturation level is colour coded according to the colour bar. By looking at the energy of interest and only up to the maximum thickness allowed for the shielding material, a suitable material can be identified with the thickness that achieves the desired performance. This procedure is outlined in figure 3.12 where a flowchart is presented, summarising all the steps discussed above. Note that the plots for all shielding materials under investigation are

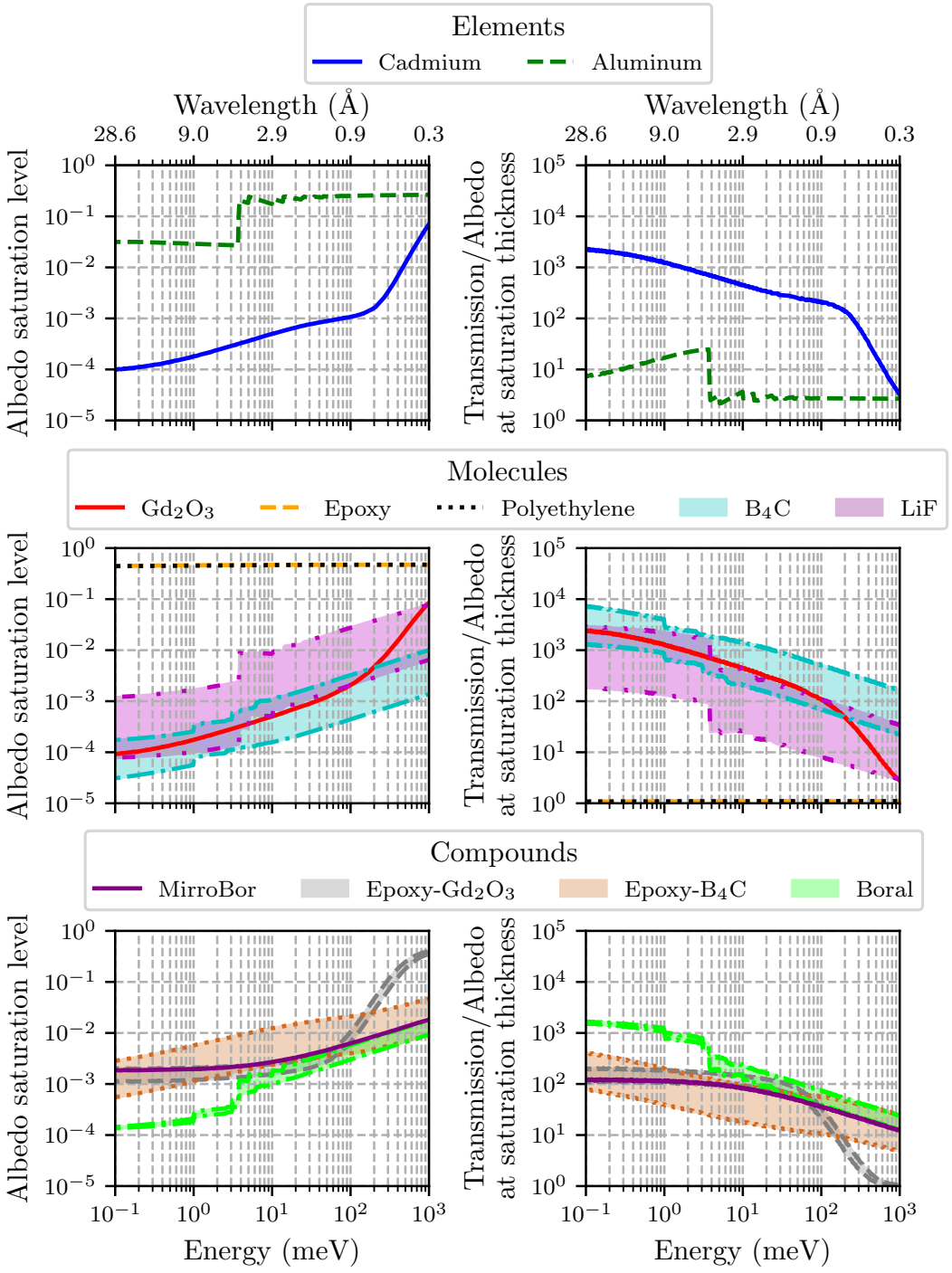

Figure 3.10: Albedo saturation level and a comparison with the transmission level at the saturation thickness. In the left plots, the albedo saturation level is seen, while in the right plots, the ratio between transmission and albedo at the albedo saturation thickness is shown. The width of the bands corresponds to the change in absorption and scattering cross-sections due to variation in material composition, as defined in table 1.

included in the Appendix.

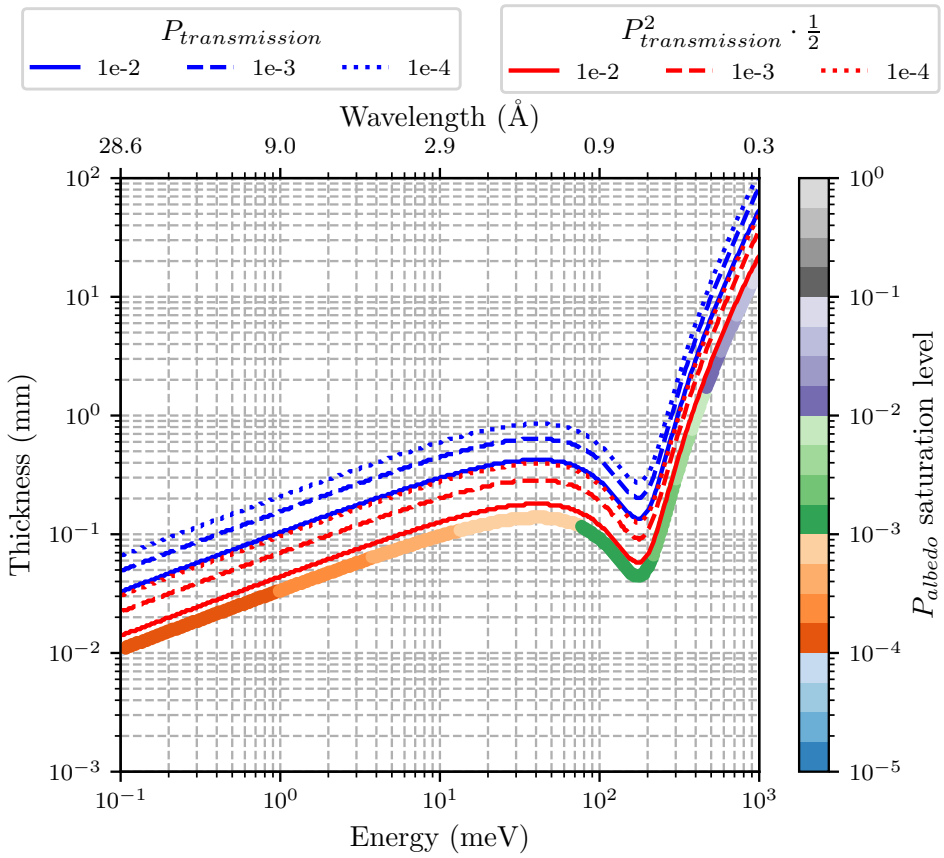

Figure 3.11: Cadmium, material properties needed for shielding investigation. The probability iso-lines for $P_{transmission}$ (blue) and $P^2_{transmission} \cdot \frac{1}{2}$ (red) are shown as a function of thickness and energy for three different values: 10^{-2}, 10^{-3} and 10^{-4}. Additionally, the albedo saturation thicknesses are shown as a function of energy, where the colour indicates the albedo saturation level.

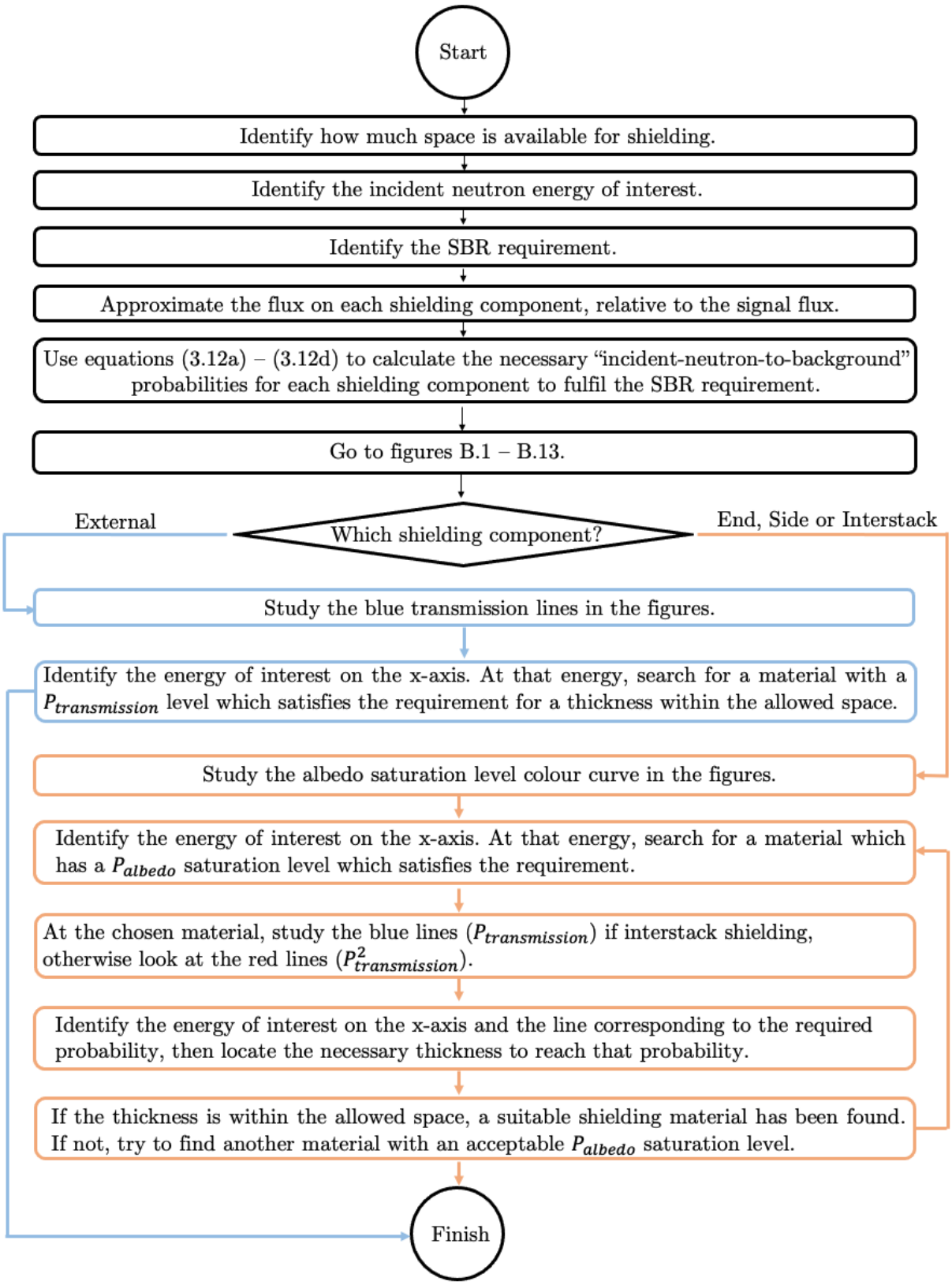

Figure 3.12: Flowchart outlining the procedure to select a suitable shielding material with an appropriate thickness for each shielding component.

3.6 Results

An easy-to-use calculation tool was devised to examine different neutron shielding materials for neutron scattering applications. The calculations were validated using Geant4-based simulations which consider both the real three-dimensional scattering paths in the materials, as well as more complicated physics, such as energy moderation through multiple scatterings. Comparing the calculations and simulations, it was seen that the one-dimensional model gives representative results on the transmission and albedo probabilities, as both the simulations and calculations agree within a factor of 2 for most materials and energies.

Based on the analytical calculations for transmission and albedo, the SBR for different shielding configurations could be calculated and used as a metric to quantitatively compare different shielding candidates. Each shielding configuration candidate was classified into four different components, including external, end, side and interstack shielding. For each shielding component, the probability of an incident neutron upon it to "become background" was calculated. This is a general quantity which can be used as a common unit to compare all shielding components simultaneously and to examine how they contribute to the overall background level.

Using the metric based on SBR, a brief guide was developed to identify an adequate shielding configuration that fulfils a specific requirement. It is based on the fact that the albedo probability, at the saturation level, is always smaller or equal to the transmission probability for all materials under consideration here. This simplifies the task of finding the thickness which gives the best trade-off between transmission and albedo, as the only information necessary is the albedo saturation level, which determines the upper performance. Once this is known, the performance can be determined by adjusting the transmission level, which can be tuned to the desired level by adjusting the shielding thickness.

Using the performance metric and the procedure outlined in this work, it was possible to find an initial shielding configuration candidate for a Multi-Grid detector for the CSPEC instrument, as outlined in [78]. There are of course additional parameters to consider than those discussed here, such as toxicity and machinability of the materials. However, the above analysis gives a fair idea of what materials are appropriate from the physics point of view, which is a crucial part of the shielding selection process.

The datasets generated and analysed in this work are publicly available in the *General considerations for effective thermal neutron shielding in detector applications - Analysis & Data* repository [79], which also contains all the analysis code.

Chapter 4

V20 measurements

The first set of measurements was performed at the ESS Test Beamline V20 [84, 85] at the BER II research reactor [86], part of HZB, which is located in Berlin, Germany. During these measurements the two MG.SEQ prototypes, MG.SEQ.I and MG.SEQ.II, were characterised, compared and benchmarked against a helium-3 detector. The purpose of the measurements was to characterise the detection efficiency, study the impact of radial blade coating on the energy lineshape, and investigate the time and energy resolution of the detector. Similar to the shielding investigation presented in the previous chapter, the results from the V20 measurements have been published in a peer-reviewed journal [87]. The data from the measurements are uploaded to [88] together with the metadata and instructions on how to read the files.

4.1 Method

The measurements were done by generating short neutron pulses in time and space using a tabletop Fermi-chopper and a series of slits. The neutron beam was directed towards one of the detectors under study – the MG.SEQ.I, the MG.SEQ.II or the helium-3 tube – while a beam monitor was used to characterise the incident flux. The details of the experimental method are presented in this section.

4.1.1 Gamma calibration

Before the V20 measurements began, a gamma calibration of the MG.SEQ was performed at the SEQUOIA instrument in a previous measurement campaign [69]. The gamma calibration was done by aiming a 70 meV neutron beam at a uranium-sulphide sample, which emits ∼MeV gamma rays following neutron absorption. This reaction has a time dependence related to incident thermal neutron pulses, and this can be used to isolate

the gamma contribution in the obtained time-of-flight spectra. Using that information, a discriminator threshold can be tuned to an appropriate value to reject unwanted gamma events.

This is illustrated in figure 4.1, where the tof spectrum (left) and threshold scan (right) are presented. In the left plot, the tof spectrum is plotted without a software threshold highlighting the different components: thermal neutrons, fast neutrons, gamma rays and background. In the small inset plot, a zoomed-in view shows the gamma and fast neutron peaks. In the right plot, the intensity of the components presented in the left plot is shown as a function of the software discriminator threshold. As can be seen, the gamma sensitivity has a sharp drop at around 100 ADC channels (the initial plateau is due to the hardware threshold being higher than the software threshold), which then levels out at 600 ADC channels. At this point, the rate of gamma contribution is comparable to the background level. The discriminator threshold selected for the SEQUOIA measurement is presented as a vertical grey line.

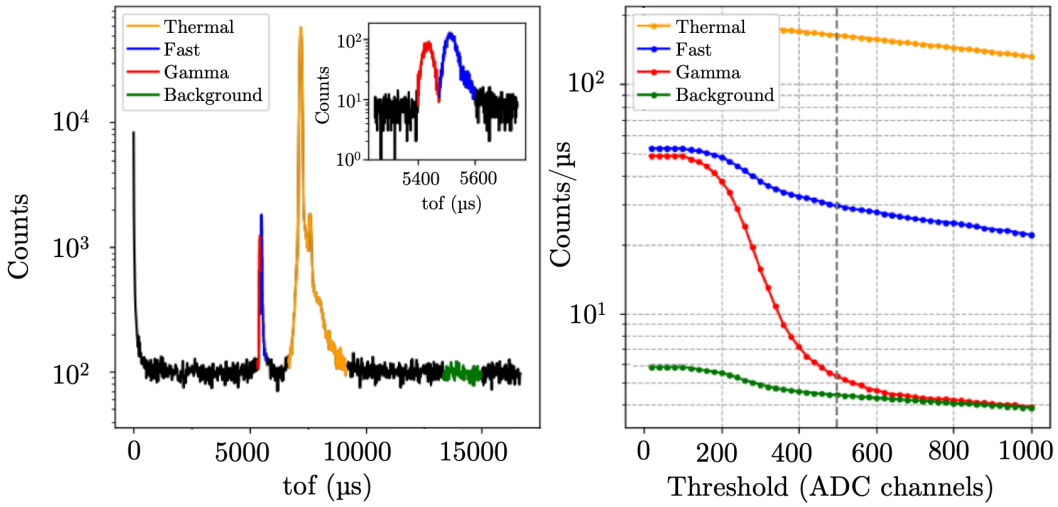

Figure 4.1: Gamma calibration for the MG.SEQ, measured at an earlier beamtime at the SEQUOIA instrument, SNS. On the left, the tof-spectrum obtained with 70 meV neutrons incident on a uranium-sulphide sample is shown – presented with no software threshold – where the different components in the spectra are colour-coded. On the right, the intensity of these components is plotted as a function of the software threshold. The vertical grey dotted line highlights the selected software threshold for the SEQUOIA measurements.

4.1.2 Setup

The V20 instrument was commissioned as a test beamline for ESS and it has a chopper system designed to mimic the long pulses to be obtained there. This is done using a pair of double-disc choppers: a source chopper and a BW chopper. Together, these deliver pulses at 14 Hz, each with a 60 ms pulse width, where the wavelengths in each pulse range

from approximately 1 to 10 Å. The beamline is also equipped with wavelength frame multiplication (WFM) choppers, which, together with a pair of frame overlap (FOL) choppers, cut the long pulse from the source chopper into smaller bunches. Additionally, it has an optional polariser at the end. This option was, however, not used during the measurement. Neither were the WFM and FOL choppers, which were parked in an open position. Instead, the basic 60 ms long pulses were used. A schematic overview of the V20 beamline is shown in figure 4.2. At the far right in the drawing, the optical benches are positioned, which is where the experiment-specific equipment is positioned, such as the experimental setup used in this work.

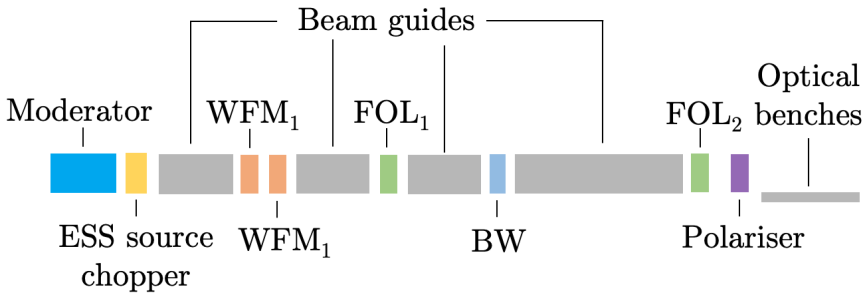

Figure 4.2: Overview of the V20 beamline. During the measurement, the ESS source chopper (yellow) and BW chopper (blue) were used to cut the incident neutron beam into wide pulses at a 14 Hz repetition rate. The WFM choppers (orange), FOL choppers (green) and polariser (purple) were disabled at this measurement. The optical benches are where the experimental setup was positioned.

The experimental setup placed in the optical benches section is shown in figure 4.3. The incident neutron beam is seen traversing downstream through the experimental setup towards the Multi-Grid detector. The beam is first collimated to 80 mm × 30 mm in size using a slit. The flux is then observed using a helium-3 based beam monitor [89], followed by an additional beam reduction using a second slit, which halves the beam width to 83 mm × 15 mm. A Fermi-chopper then cuts the long incident pulse into a series of short pulses, each a few tens of μs long. Finally, the beam is collimated to a 14 × 60 mm^2 rectangular beam before reaching either the helium-3 tube or the MG.SEQ.

During the direct beam measurements with the MG.SEQ, the helium-3 tube was removed from the path of the beam. During the background measurements, it was then re-installed such that it was blocking the direct beam from reaching the Multi-Grid detector. The helium-3 tube was covered with 5 mm thick Mirrobor shielding everywhere except for a small entry window for the incident neutron beam, which results in low transmission levels during the Multi-Grid background measurements. The MirroBor shielding, in combination with the high neutron absorption efficiency of the helium-3 tube in the measured wavelength range, resulted in transmission levels below the instrument background level for almost all data. The exception was for a data point at 1.2 Å, where the transmission

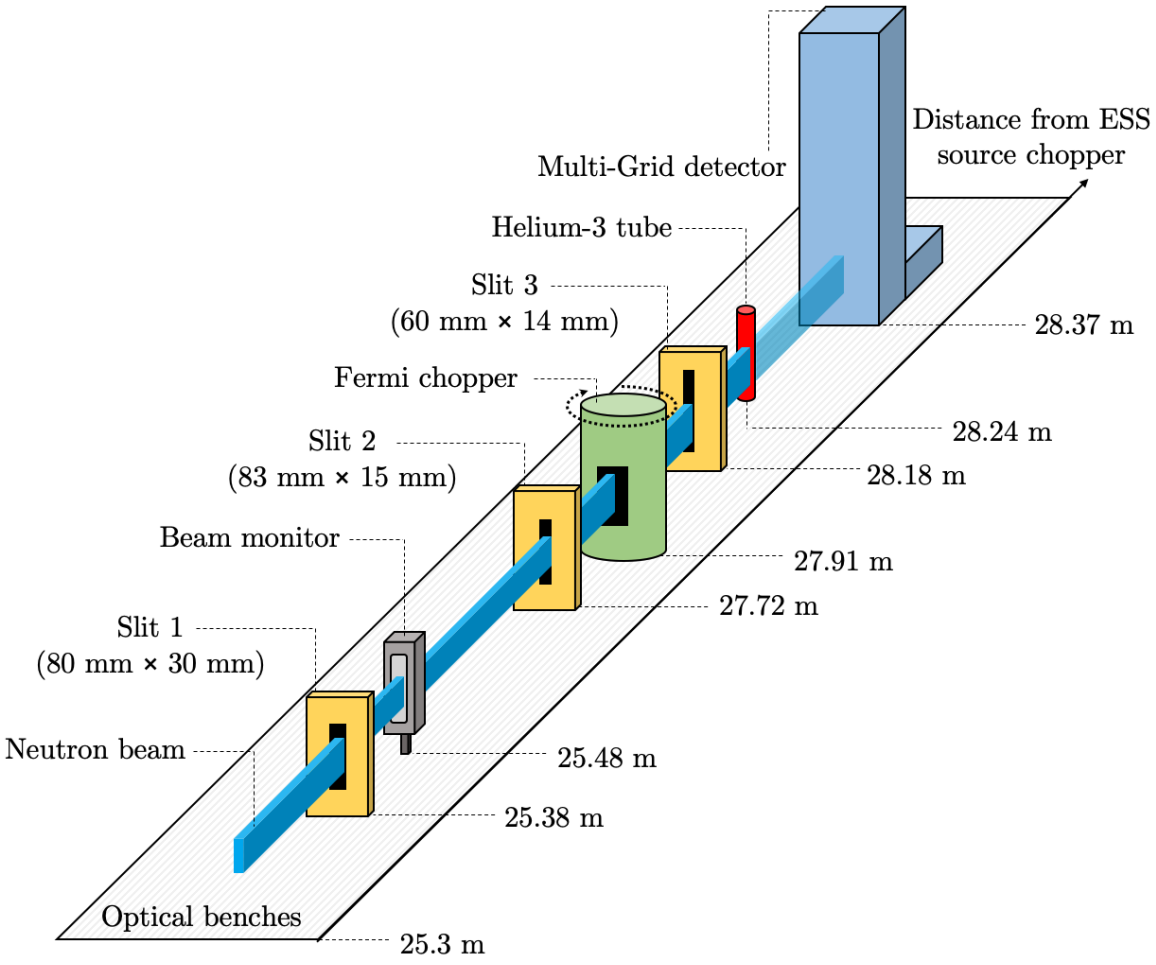

Figure 4.3: Overview of the experimental setup at the optical benches. On the side, the distance of the components to the ESS source chopper is shown. All numbers indicate the centre position of the components, except for the Multi-Grid detector, where the distance is taken from the front. The full setup includes – downstream from the source – the first slit (orange), the beam monitor (grey), the second slit (orange), the Fermi chopper (green), the third slit (orange), the helium-3 tube (red) and the Multi-Grid detector (blue). During measurements with the Multi-Grid detector, the helium-3 tube is removed from the beam. The numbers related to the slits indicate their openings: height × width.

was at the acceptable level of $< 5 \cdot 10^{-4}$.

Note that the MG.SEQ and the helium-3 tube are placed in a sequence and that the Multi-Grid detector is situated approximately an additional 50 % further downstream from the Fermi-chopper than the helium-3 tube. Furthermore, the signal-to-background ratio at the instrument is approximately 10^3 and is influenced by gamma radiation levels and stray neutrons in the vicinity of V20. Both of these facts are considered in the analysis.

4.1.3 Equipment

Concerning the equipment used during the measurements, both the beam monitor and helium-3 tube are commercially available products, while the Fermi-chopper is an experimental prototype developed by Jülich Forschungszentrum [90]. The characteristics and performance of this equipment are important for the interpretation of the results and are discussed below.

Beam monitor

The beam monitor used was a low-pressure helium-3 proportional counter [37,91,92] from Eurisys Mesures, currently Mirion Technologies [93]. The detector has an active area of 100×42 mm^2, with a 40 mm active depth. The thickness of the aluminum window in the neutron beam path is 4 mm, including 2 mm inlet + 2 mm outlet. The gas-filling is a 1.3 bar Ar-CH_4 (90:10 volume ratio) mixture, with a low pressure of helium-3. The neutron detection efficiency is $\sim 10^{-5}$ at 1.8 Å.

Fermi-chopper

For the measurements, an experimental 120 mm high and 27 mm in diameter lightweight Fermi-chopper was used to produce a series of $\sim$ 10 μs short pulses in time. The Fermi-chopper is synchronized to the 14 Hz source chopper frequency with a clock multiplier of 35, resulting in a 490 Hz rotation frequency. The chopper uses two rectangular chambers for neutron transmission and a gadolinium neutron absorber on the walls.

The resulting transmission of the Fermi-chopper is presented in figure 4.4. The top plot shows the pulse shape before the Fermi-chopper, collected using the beam monitor, while the bottom plot shows the sequence of short pulses after the Fermi-chopper, collected using the helium-3 tube.

The chopper system produces a series of sharp pulses. However, as can be seen in figure 4.5, there are additional features that have been introduced. First, odd and even peaks alternate in intensity. This is due to an asymmetry in the two rectangular Fermi-chambers, appearing every half rotation of the chopper blades. This is further discussed in [90]. Second, two distinctive side peaks are identified, suppressed by 1-2 orders of magnitude. Additionally, there are 2-3 orders of magnitude suppressed peaks appearing midway between the main peaks, coinciding with every quarter rotation of the chopper blades. This is caused by neutron leakage as the beam spot size was slightly larger than the width of the Fermi package, allowing neutrons to pass the side of the Fermi package every quarter rotation. These peaks do not cause a problem for the current analysis, as they are easily distinguishable from the main peaks.

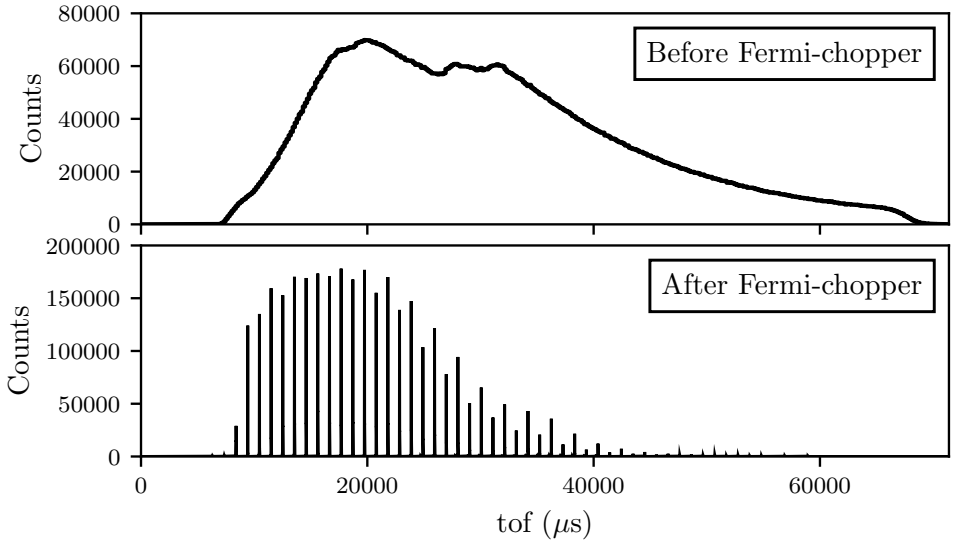

Figure 4.4: Time-of-flight spectra before and after the Fermi-chopper. On the top, a spectrum collected with the beam monitor is presented, showing the wide pulse from the source chopper. On the bottom, a spectrum from the helium-3 tube is shown, illustrating how the chopper splits the $\sim$ 60 ms long source pulse into a series of $\sim$ 10 μs short pulses.

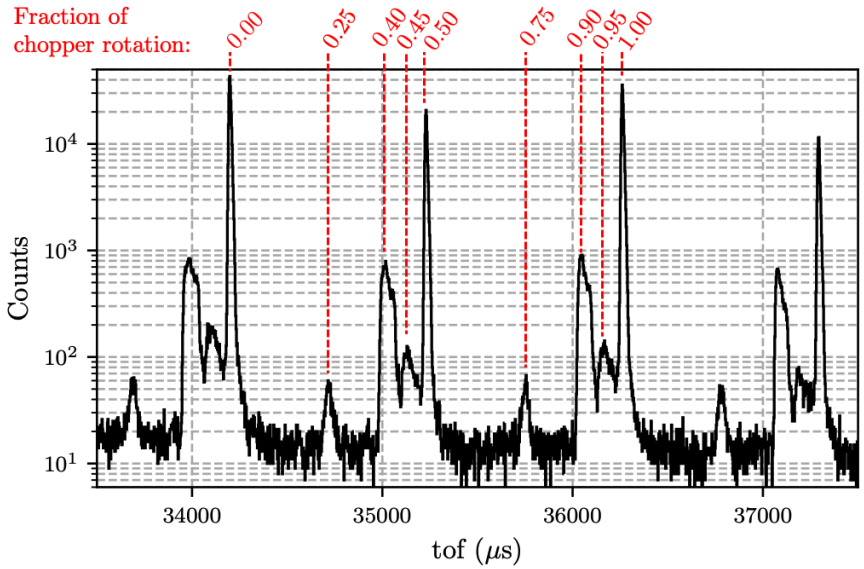

Figure 4.5: A magnified portion of the helium-3 tube tof-spectrum. Using a logarithmic scale on the y-axis, it is clear that there are side peaks which are 1-2 orders of magnitude smaller than the main peaks. The red text at the top indicates where the peaks occur in relation to the chopper rotation.

Helium-3 tube

The helium-3 filled proportional counter used in the measurements was supplied by Reuter-Stokes [94]. The tube has a total gas pressure of 10 bars, split between 9.85 bar helium-3 and 0.15 bar quenching gas. The active diameter of the tube is 25.4 mm, with a length

of 305 mm, enclosed in 0.51 mm thick stainless steel walls. During the measurements, the tube was wrapped in Mirrobor shielding, leaving a small window for incident neutrons.

The tube is not position sensitive and is operated at 1350 V. The read-out system consists of a multi-channel analyser, the FAST ComTeC MCA4 [95], which returns time-of-flight and collected charge for each neutron event. In case of a pile-up during the charge integration process, the event is also assigned a pile-up flag. Gamma events were rejected using a constant discriminator threshold on all events, applied at the software level. The shaping time was set to 1 μs.

The helium-3 tube detection efficiency is established using analytical calculations, which account for the absorption in the gas and the scattering in the stainless steel tube. The detection criterion is that if a neutron is absorbed, it is considered detected.

The neutron absorption probability is determined by using the helium-3 absorption cross-sections, gas pressure, and the propagation distance in the gas. The last factor varies depending on the location where the neutron hits the tube along the tube diameter. That is, the neutron has a longer travel distance if it hits the centre of the tube than at the edge, and the calculation accounts for this by using the average perpendicular tube depth as the neutron travel distance. The calculated absorption probability is then scaled by the fraction of the incident neutron flux lost due to scattering in the steel tube, which is estimated as the scattering probability scaled by the heuristic factor 0.5, as not all neutrons which scatter are lost. Corrections for factors such as wall effect and dead zones in the gas are not taken into account in this approximation.

In figure 4.6, the calculated efficiency is plotted as a function of hit position along the tube diameter, together with experimental data from a previous measurement [96, 97]. The data agree within a few percent, confirming the validity of the calculation. The offset is accounted for in later calculations as a systematic uncertainty. In figure 4.7, the average efficiency across the tube diameter is shown as a function of neutron wavelength. Two curves are presented, one with the beam centred on the tube and one with a 5 mm offset. This is to account for the systematic uncertainty of beam alignment.

The purpose of the helium-3 tube was to have a well-understood reference detector to benchmark the MG.SEQ and to use it as a flux normalization. The selected tube is an appropriate choice because it has a gas pressure representative of what is commonly used for helium-3 tubes in spectroscopy instruments.

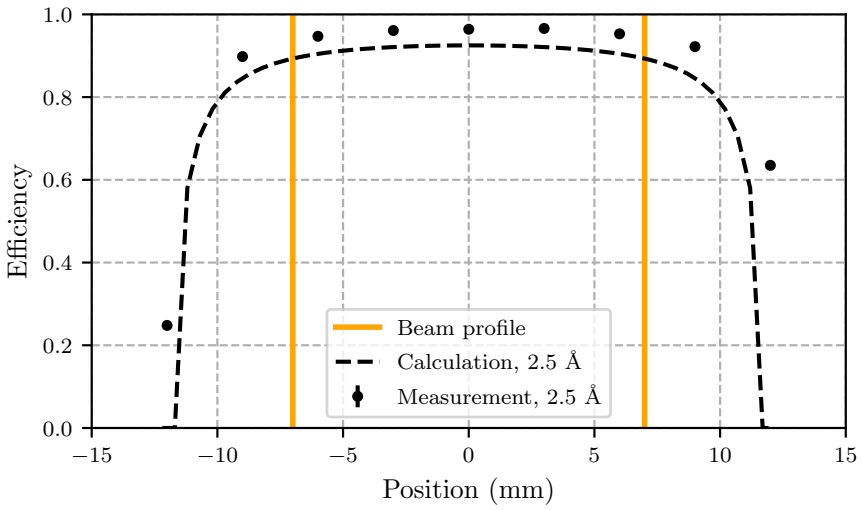

Figure 4.6: Neutron detection efficiency at 2.5 Å, shown as a function of displacement from the tube centre. The neutron beam width (orange lines) is shown together with the calculation (black dotted line) and experimental data (black dots). The data was gathered during a previous measurement at ILL.

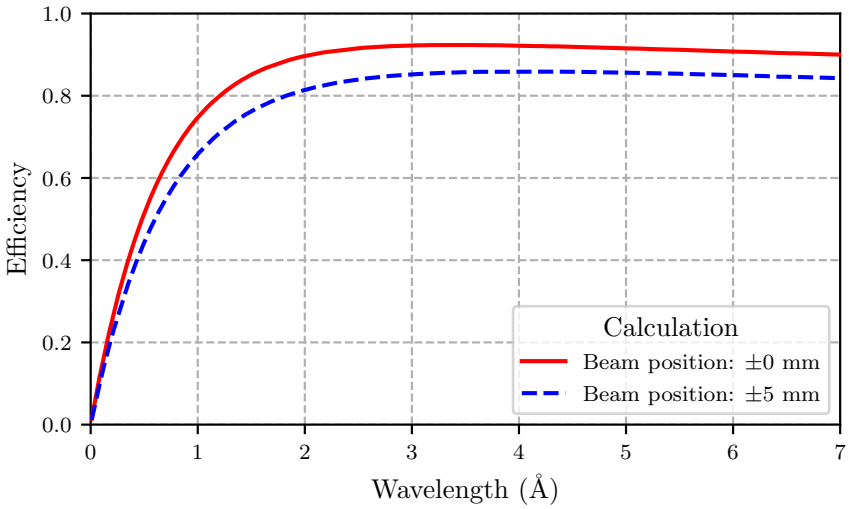

Figure 4.7: Calculated neutron detection efficiency as a function of neutron wavelength. Each value is averaged over the tube width hit by the beam, showing it centred (red) and at ±5 mm offset (blue).

4.2 Analysis & Results

Using the experimental setup described above, three direct beam measurements were conducted – one for each of the three detectors – leaving the remaining setup unchanged. In addition to this, background measurements were done for both MG.SEQ prototypes, one at a time, by blocking the incident beam with the helium-3 tube.

Three detector characteristics were investigated in the measurements: neutron detection

efficiency, internal scattering, and time and energy resolution. The MG.SEQ efficiency was inferred by comparing the count rates in the helium-3 tube – which has a well-understood efficiency – with the Multi-Grid detector. Internal scattering was examined by comparing data from the MG.SEQ.I, which did not have radial coating, with the MG.SEQ.II, which had radial coating. For each detector, the contribution of the internal scattering was identified by making a geometrical cut in the data by removing data from the direct beam, which was confined to a few grids, and only looking at data from the region where scattered neutrons were detected. Finally, the time and energy resolution of the detector was examined by closely investigating the lineshape of the Multi-Grid detector and comparing it to that of the helium-3 tube. In the following, the analysis, results and discussion are presented, starting with data extraction.

4.2.1 Data extraction

The first part of the analysis is data extraction, which is performed by deciding which content of the raw data to store, i.e. to perform a data reduction. Here, the values stored from each event include bus (corresponding to the FEE card which recorded the event), time and tof (the global time and time-of-flight of the event), wm and gm (number of wires and grids contributing to the event), wadc and gadc (total charge collected by all the wires and grids, respectively), as well as wch and gch (the one wire and one grid channel which collected the most charge among all the wires and grids that were coincident – registered together within a small time-window – in the event). Although the total number of wires and grids that constitute each event is noted – grid and wire multiplicity – only the wire and grid channel which collected the most charge is saved. These channels are then treated as hit location and used for position reconstruction. Likewise, only the sum of the collected charge is stored, which is saved separately for wires and grids. Hence, each neutron event has the information (bus, wadc, gadc, wch, gch, wm, gm, time, tof). Once this initial data reduction has been performed, the next step is to filter the data from the events that are unlikely to be due to neutrons. This is done based on multiplicity and ADC discriminator threshold.

Multiplicity

It is a requirement for a neutron event to have at least one wire and one grid in coincidence, otherwise, the neutron hit position cannot be reconstructed. Additionally, as the wires are physically separated from each other by the blades in the grids, it is not expected that charge will be collected by adjacent wires. Therefore, events with a wire multiplicity >1 are unlikely to originate from real neutron events. This is in contrast to the grids, which can have multiple channels firing from a single neutron event due to the long range of the

emitted conversion products, as well as the capacitive coupling between grids, which can cause neighbouring grids to generate signals as well. Based on this information, a filter is performed such that only events with wm=1 and $1 \leq \text{gm} \leq 5$ are accepted. This is shown by the black dotted lines in figure 4.8 (right), the rest of the data are rejected.

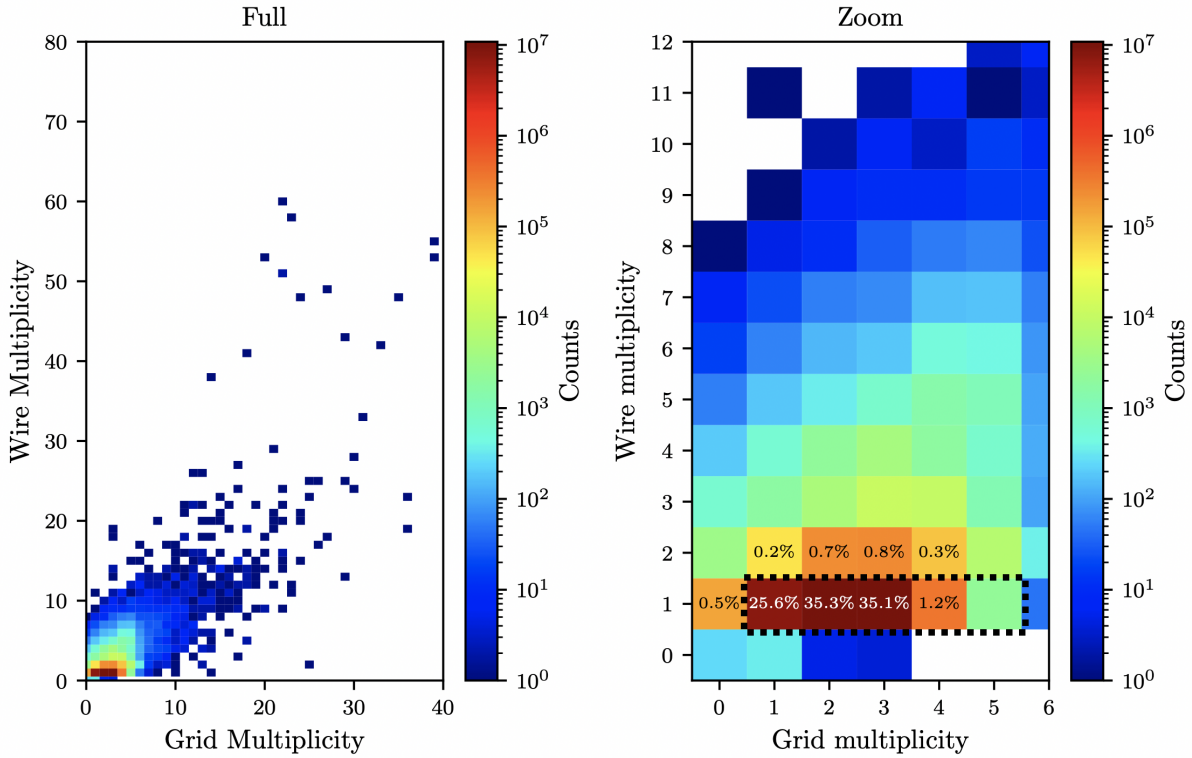

Figure 4.8: Multiplicity distribution, where a data file from the V20 measurements have been used as an example. Each square represents events with a specific combination of wire and grid multiplicity, while the colour code shows the number of events for that specific combination. The 2D histogram shown on the left is for all wire and grid multiplicities, while the histogram to the right shows a close-up of part of the graph. The cells with more than 0.1 % of the total events have been annotated with their respective percentage and the black dotted lines show which data is kept after the multiplicity cut has been applied.

Charge

A charge discrimination threshold is used to remove low ADC events, such as gamma rays and electronic noise. As there is an overlap in this region with real neutron events, some neutron events will be lost due to any effective cut. It is therefore important to set the threshold as low as possible without compromising the detector counting efficiency. This procedure is presented in figure 4.9.

In the plot, the y-axis is expressed in electronic channel numbers, where Grid 80 is the first at the bottom and Grid 119 is the last at the top (channels 0 to 79 are reserved for wires). The x-axis is expressed in 12-bit ADC channels, ranging from 0 to 4095. Gamma

events are seen concentrated in a distribution at the low ADC values, below the solid black line, while neutrons span the full range. Neutrons from the direct beam are seen hitting only three grids at the lower part of the detector, as shown by the three horizontal red stripes.

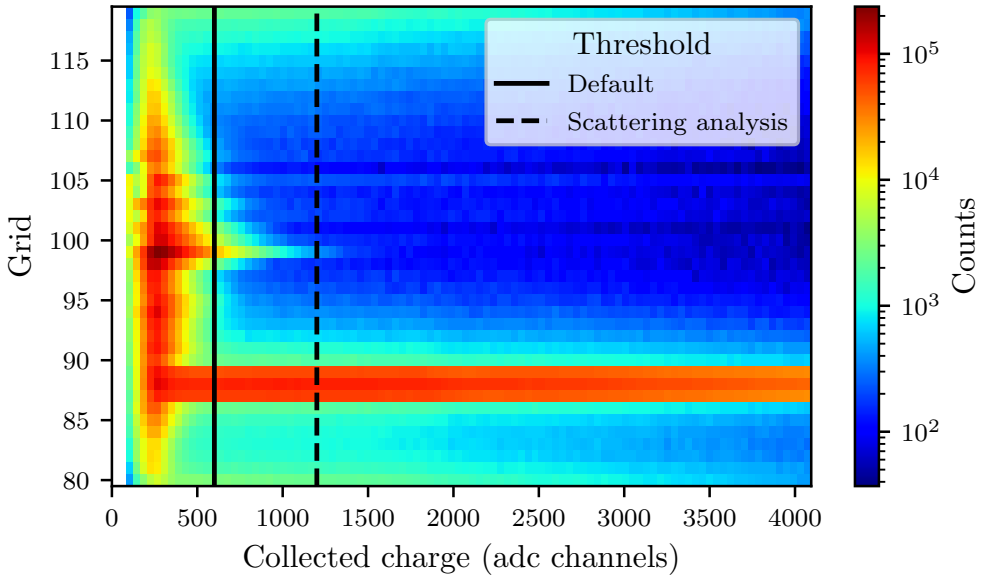

Figure 4.9: Charge threshold selection for the Multi-Grid detector at the V20 measurement, using data with the MG.SEQ.I as an example. In the figure, the grid PHS (x-axis) are shown for all individual grids (y-axis). The numbering refers to the electronic channel numbers related to the grids, where Grid 80 is the first grid at the bottom and Grid 119 is the last grid at the top. There are two separate thresholds: one for the internal scattering analysis (dotted black line) and one for the rest of the analysis (solid black line).

Here, a constant ADC software threshold at 600 ADC channels is applied, such that the gamma events are rejected. For the internal scattering analysis, however, a higher ADC cut is required to clean the data further. This is because the rate of scattered events is – in the middle region of the detector at parts of the lambda spectrum – comparable to the noise rate. These noise events are concentrated at the low ADC values, while the scattered neutron events span the full ADC range. Therefore, a cut at 1200 ADC channel is used for the scattering analysis, which removes the remainder of the noise present in the middle grid, while keeping a majority – around 80 % – of the events from scattered neutrons.

Note that this analysis procedure can be optimised in the future by applying individual ADC cuts on each channel to account for gain differences between them. By using this method, the apparent systematic gain increase observed in the detector – as seen by the increasing number of noise and gamma events from the edges (grid 80 and 119) towards the centre (grid 100) – could be accounted for and an increased number of neutron events

could be included in the analysis.

4.2.2 Neutron detection efficiency

Neutron detection efficiency is defined as the number of detected neutrons divided by the total number of incident neutrons,

$$\epsilon = \frac{S^{detected}}{S^{incident}}, \tag{4.1}$$

where ϵ is the neutron detection efficiency, $S^{detected}$ is the sum of detected neutrons and $S^{incident}$ is the sum of incident neutrons. For the Multi-Grid detector, the quantity $S_{MG}^{detected}$ is accessed from the number of counts in the data, while $S_{MG}^{incident}$ is estimated from a separate measurement with the helium-3 tube. Using these two measurements, the neutron detection efficiency for the Multi-Grid detector can be derived.

The incident neutrons on the Multi-Grid detector $S_{MG}^{incident}$, i.e. integrated absolute flux, is calculated as below,

$$S_{MG}^{incident} = S_{He-3}^{detected} \cdot \frac{1}{\epsilon_{He-3}} \cdot \frac{BM_{MG}}{BM_{He-3}}, \tag{4.2}$$

where $S_{He-3}^{detected}$ is the number of detected neutrons in the helium-3 tube, ϵ_{He-3} is the calculated efficiency of the helium-3 tube, and BM_{MG} and BM_{He-3} are the beam monitors counts from the Multi-Grid detector and helium-3 tube measurements, respectively. The fraction of the beam monitor counts accounts for the difference in flux during the two separate measurements.

Inserting equation (4.2) into (4.1), a formula for deriving the Multi-Grid efficiency as a function of the incident neutron wavelength λ_n is thus written according to equation (4.3),

$$\epsilon_{MG}(\lambda_n) = S_{MG}^{detected}(\lambda_n) \cdot \left(S_{He-3}^{detected}(\lambda_n) \cdot \frac{1}{\epsilon_{He-3}(\lambda_n)} \cdot \frac{BM_{MG}}{BM_{He-3}} \right)^{-1}, \tag{4.3}$$

where $\epsilon_{MG}(\lambda_n)$ is the derived Multi-Grid efficiency. Note that BM_{MG} and BM_{He-3} are the integrated beam monitor counts over the full wavelength spectrum taken during the measurements. This is because the variation in flux between the two measurements was wavelength independent, as is demonstrated below.

To check if using the accumulated beam monitor counts over the full wavelength spectrum is a valid approach, the beam monitor data for both the Multi-Grid detector and helium-3 tube measurements are plotted, see figure 4.10. It is seen that incident flux during the two measurements was similar, with the fraction between them being only a few percent below 1 and wavelength independent. The high uncertainty around 1 Å is due to poor

statistics. Hence, normalizing using the accumulated beam monitor counts, taken over the full wavelength spectrum, is deemed appropriate. The reason the fraction is below one is because a slightly lower flux was obtained during the Multi-Grid measurements.

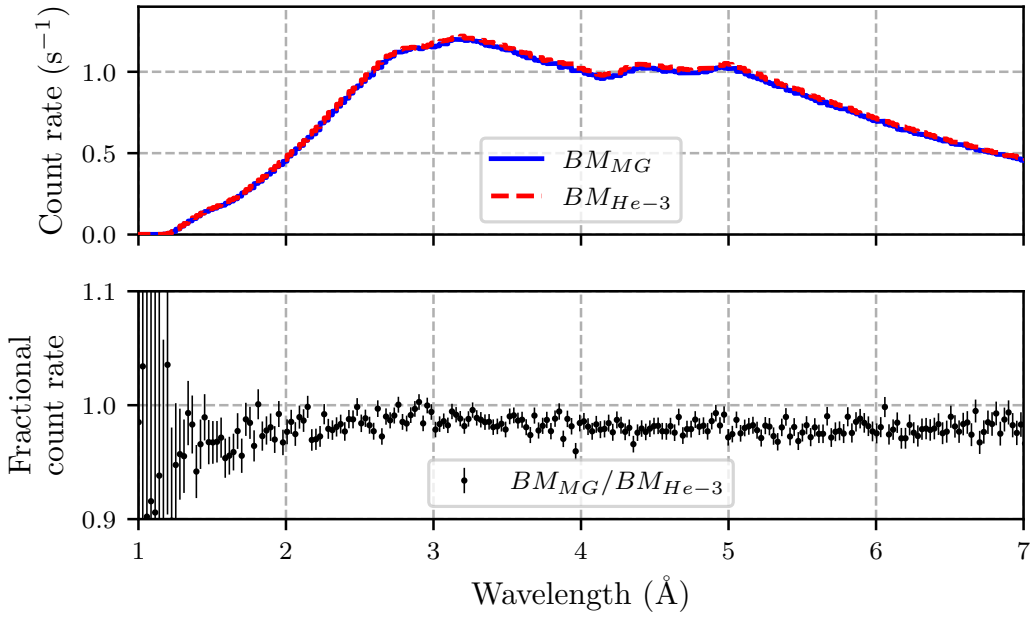

Figure 4.10: Beam monitor data taken during the measurements with the Multi-Grid detector (blue) and the helium-3 tube (red). At the top, the histogrammed beam monitor counts, normalized by measurement duration, are presented as a function of neutron wavelength. At the bottom, the fractional rates, BM_{MG}/BM_{He-3}, are shown.

The quantities $S_{MG}^{detected}(\lambda_n)$ and $S_{He-3}^{detected}(\lambda_n)$ are calculated by integrating counts above background for each peak received from the Fermi-chopper in the wavelength spectra. Due to the parasitic peaks shown in figure 4.5, there are systematic uncertainties when integrating the peak area. These uncertainties are accounted for by introducing two intervals: one very narrow, $\pm\sigma$, encompassing only the peak centre, and a wider one, encompassing the full peak, as well as any parasitic peaks. This is presented in figure 4.11. By using the narrow interval, effects from the parasitic peaks can be rejected, but it also means that any differences in peak shape between the Multi-Grid detector and helium-3 tube are not accounted for. Hence, by using the two intervals an estimate of the systematic uncertainty on the efficiency is obtained. Note that the parasitic distribution on the sides of the main peak is more smeared in the Multi-Grid data than in the helium-3 data. Again, this is because the Multi-Grid detector was located further away from the Fermi-chopper. This is also why the main peak is broader and the red and blue delimiters are located further from the peak centre.

Extracted peak areas – i.e. the number of detected neutrons for the Multi-Grid detector and helium-3 tube – are presented in figure 4.12 as a function of wavelength, where the

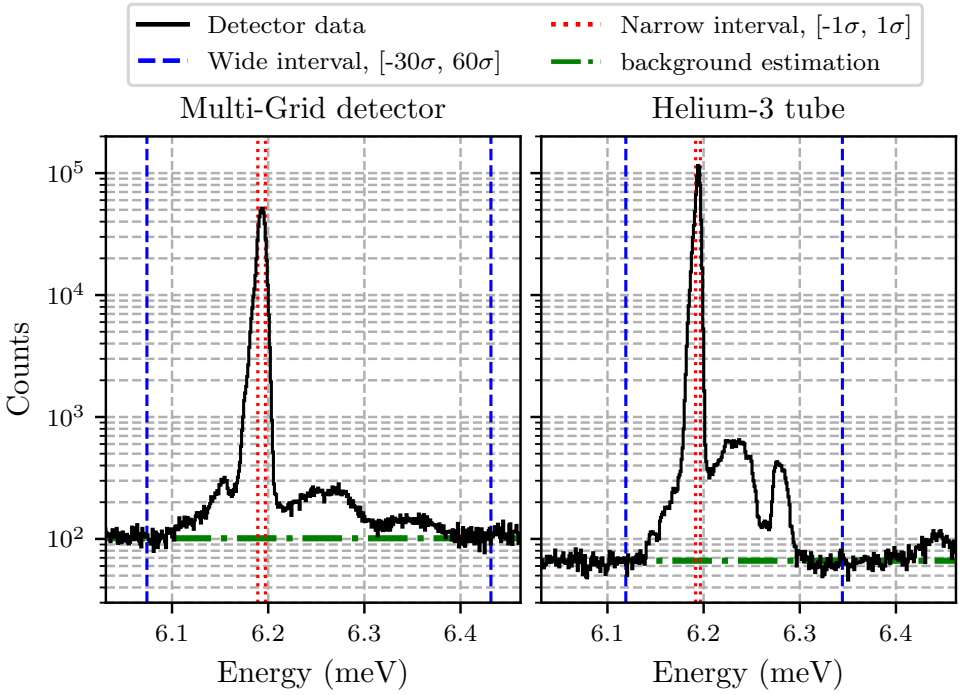

Figure 4.11: Peak area extraction. In the figure, an example of peaks at 3.6 Å is presented for the Multi-Grid detector (left) and helium-3 tube (right). In the plots, the wide (blue) and narrow (red) integration intervals are also presented, together with the background estimation (green).

areas from both the narrow and wide intervals are shown. The highest flux in the spectra, at around 2.5 Å, is approximately $2 \cdot 10^6$ s^{-1} cm^{-2}. The flux in the peak was estimated using data from the beam monitor, located a few meters upstream from the helium-3 tube. At this wavelength, the fraction of pile-up events in the helium-3 data (green squares) is seen to be substantial. This is discussed in more detail at the end of this sub-section.

With the measured number of detected neutrons for the Multi-Grid detector and helium-3 tube, together with the beam monitor data and theoretical helium-3 tube efficiency, it is now possible to derive the Multi-Grid detection efficiency using equation 4.3. This is presented in figure 4.13.

In the plot, the derived efficiency for the two integration intervals (red and blue) is compared to the analytical prediction (black), where the error bars show systematic uncertainties. The analytical calculation includes the attenuation of neutrons in aluminum, the absorption probability in the $^{10}B_4C$-coatings, as well as the escape probability of the conversion products to reach the active volume of the detector. Incident neutrons are assumed to hit the front of the detector at a perpendicular angle. All calculations are based on derivations presented in [27,51,98]. The width of the calculated efficiency indicates the systematic uncertainty, based on the uncertainty of the input parameters, as well as flux

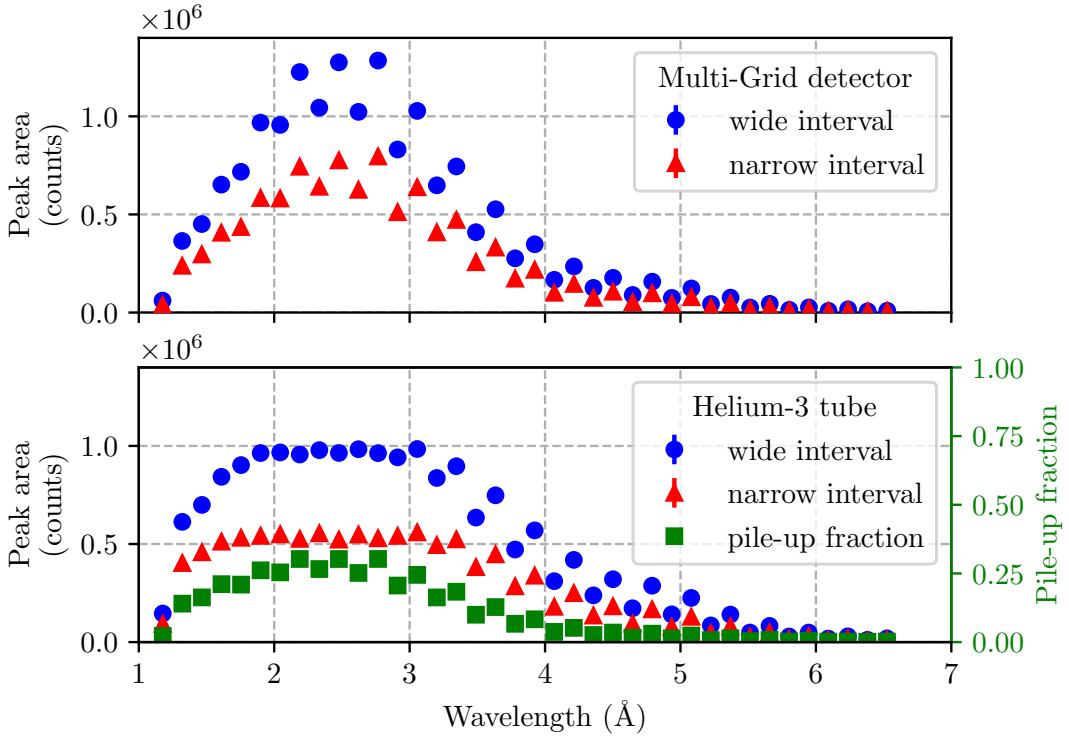

Figure 4.12: The measured number of detected neutrons used for efficiency calculation. In the figure, the integrated peak area is shown as a function of neutron wavelength for both the Multi-Grid detector (top) and the helium-3 tube (bottom). For both detectors, the peak areas are shown separately for the wide peak interval (blue) and the narrow peak interval (red). For the helium-3 data, the fraction of pile-up events encountered in the helium-3 read-out system (green) is plotted on a separate right-hand y-axis. Statistical uncertainties are shown in the error bars but are too small to be discernible.

loss due to scattering in the aluminum window.

For longer wavelengths, 4 to 6 Å, the derived and calculated efficiencies agree well within the uncertainties. For wavelengths shorter than 4 Å (highlighted by the grey area), a larger deviation from the calculation is evident. This is due to the saturation of the helium-3 detector system. The highest integrated flux rate in the spectra is high enough, $> 10^6$ s^{-1}, to cause multiple hits within the 1 μs shaping time of the read-out system. This is clear from the fraction of pile-up events in the tube (green), which follows the observed deviation. In addition, the data transfer speed limit per channel, $\approx 10^6$ events s^{-1}, is similar to the peak flux, which might cause a loss of data. This could have been prevented by using a lower incident flux. However, as the scattering analysis requires the best possible signal-to-noise ratio, a high neutron flux was essential.

An attempt was made to account for the saturation in the helium-3 tube using information on the incident flux and shaping time, as presented in [87]. However, the correction was not sufficient for the majority of data points within the saturated region. This could be

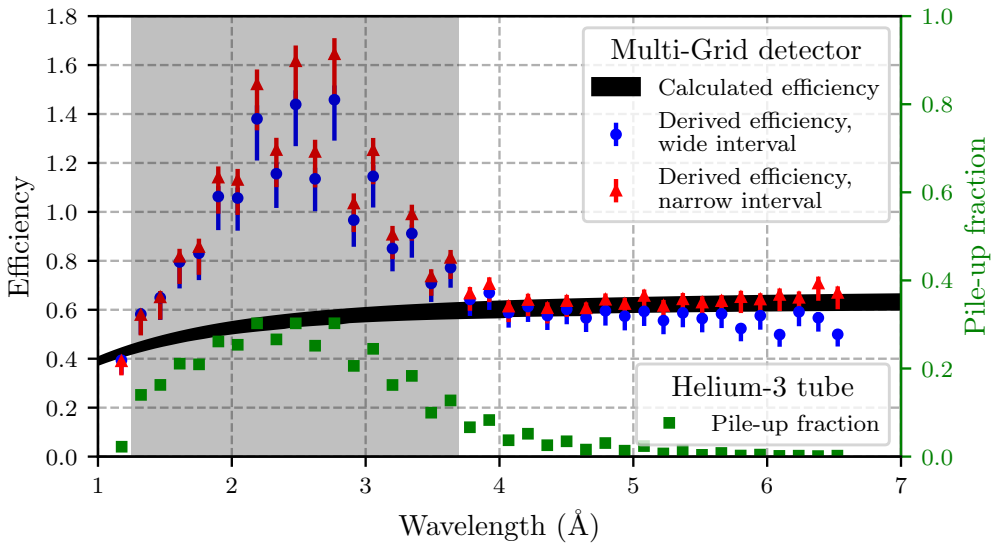

Figure 4.13: Derived Multi-Grid efficiency (blue circles and red triangles) plotted against the calculated efficiency (black band). The width of the black band shows the uncertainty range of the efficiency calculation. The fraction of pile-up events encountered in the helium-3 read-out system (green squares) is plotted on the separate right-hand y-axis. The grey region covers the unusable portion of the data, caused by saturation in the helium-3 detector system.

because the incident flux is intense enough to introduce additional effects in the helium-3 tube, such as space charge effects, which further decrease the efficiency. As these additional effects are not accounted for in the correction, a deviation is still seen.

The saturation process is the cause of the strong staggering effect between 2 and 3 Å. In figure 4.12, it is seen how the Multi-Grid detector follows the intensity from Fermi-chopper, i.e. every other pulse is more intense, even where the flux is at the highest level. This is not the case for the helium-3 tube, which does not record the alternating intensity equally well. As the oscillations between adjacent data points in the two detectors no longer match in this region, an inaccuracy in the efficiency calculation is obtained. The saturation effect seen in the helium-3 detector is absent in the Multi-Grid detector. This highlights the greater rate capability of the Multi-Grid detector, which is one of the main motivations for its development.

4.2.3 Effect of radial coating on energy lineshape

The purpose of the radial blade coating is to reduce the impact of internal neutron scattering, which is mainly caused by the presence of aluminum in the Multi-Grid detector [65]. The other elements in the neutron beam path, boron and carbon in $^{10}B_4C$, have a negligible effect. This is because $^{10}B_4C$, although having a 2-3 times higher scattering cross-section than aluminum in the measured energy range [20], have over two orders of magnitude thin-

ner total thickness compared to aluminum (60 μm and 14.5 mm, respectively, for neutrons incident perpendicular on the detector surface).

Aluminum has a periodic crystal structure, like any other crystalline solid, which allows for coherent scattering of atoms within the same crystal lattice, as well as incoherent scattering from the individual atomic nuclei. The neutron interaction cross-sections in aluminum are presented in figure 4.14. It is seen that for wavelengths between 1 and approximately 4.7 Å, coherent elastic scattering is dominant. The cut-off wavelength at 4.7 Å, where the coherent elastic scattering drops to zero, indicates the maximum wavelength where diffraction occurs in the crystal structure, i.e. the maximum wavelength where the Bragg condition can be fulfilled for the aluminum crystal lattice. For wavelengths longer than this, no coherent scattering occurs.

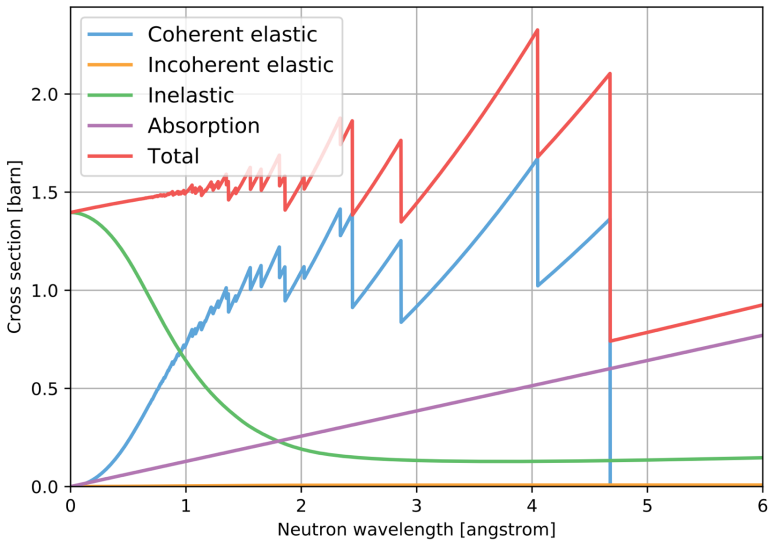

Figure 4.14: Neutron interaction cross-sections with aluminum, including elastic scattering (blue and orange), inelastic scattering (green), absorption (purple), and total cross-section (red). The figure was generated using NCrystal.

The impact of the scattered neutrons from the aluminum shows as an added time-dependent background in the detector, caused by an incorrect energy reconstruction of the scattered neutrons. To illustrate this, the expression for final neutron energy E_f – the neutron energy after interacting with the sample – in equation (4.4) is considered,

$$E_\mathrm{f} = \frac{m_n}{2} \cdot \left(\frac{\mathrm{L}_2}{\mathrm{tof} - \mathrm{L}_1 \cdot v_\mathrm{i}^{-1}} \right)^2 \tag{4.4}$$

where all the variables are the same as in equation 1.23. The important numbers in this context include the sample-to-detection distance L_2 and the total time-of-flight tof. As the distance L_2 is based on the assumed straight travel distance from the sample to the detection voxel, this distance will be incorrect if the neutron is scattered internally before

being detected. Moreover, as the total neutron time-of-flight will also change from the scattering, this further distorts the energy reconstruction. This effect is shown in equation (4.5), where the energy reconstruction of an internally scattered neutron is presented,

$$E'_{\mathrm{f}} = \frac{m_n}{2} \cdot \left(\frac{\mathrm{L}_2 \pm \Delta L_2}{(\mathrm{tof} \pm \Delta\mathrm{tof}) - \mathrm{L}_1 \cdot v_{\mathrm{i}}^{-1}} \right)^2 \tag{4.5}$$

where E'_{f} is the reconstructed neutron energy of an internally scattered neutron, $\pm\Delta$tof is the change in time-of-flight due to the internal scattering, and $\pm\Delta L_2$ is the change in assumed distance due to the incorrect voxel detection. As seen in figure 4.14, most scattering can be considered elastic within the energy range probed. Consequently, $\pm\Delta$tof will predominantly be positive, corresponding to the extra flight time between scattering and detection. This means that internally scattered neutrons will largely be reconstructed with an energy $E'_{\mathrm{f}} < E_{\mathrm{f}}$. The exception to this is when a neutron gains energy through inelastic scattering on the aluminum substrate and is scattered forward with a sufficiently small deviation, so that ΔL_2 is small. In this case, the neutron will be detected earlier than if it would not have been scattered, hence $\pm\Delta\mathrm{tof} < 0$ and $E'_{\mathrm{f}} > E_{\mathrm{f}}$.

To minimize the impact of scattered neutrons on the energy lineshape, the additional flight distance between scattering and detection should be kept as short as possible. This reduces ΔL_2 and Δtof in equation (4.5), closing in on the ideal case in equation (4.4). To facilitate this, $^{10}\mathrm{B}_4\mathrm{C}$-coating on the radial blades in the grids are used, which absorbs the neutrons closer to their internal scattering point.

To investigate the effect of the radial coating on the energy lineshape, data from MG.SEQ.I (non-coated radial blades) and MG.SEQ.II (coated radial blades) are compared. As the neutron beam is highly collimated, recorded events from scattered neutrons can be separated from those coming from the direct beam. This is achieved by performing a geometrical cut and removing all events in the direct beam, keeping only internally scattered neutron events. In other words, by looking at the area outside the direct beam, the only events seen there are those which have scattered internally. This is because direct neutrons cannot reach that area, so the neutrons recorded there must have undergone scattering to get there. The volume outside the direct beam region is defined as the *beam periphery*. Note that there are scattered neutrons in the beam region as well and that these are ignored in this approach. This is not an issue, however, as an absolute measure of scattering is not intended, only a comparison between MG.SEQ.I and MG.SEQ.II.

Background data is used to verify that the events seen in the beam periphery are indeed internally scattered neutrons. This is presented in figure 4.15, which shows data collected both with the direct beam and when the direct beam was blocked with the helium-3 tube. In the two left plots, 2D histograms are presented of grid vs tof (side view vs time), while

the two right plots show row vs tof (top view vs time). The helium-3 tube, 25 mm in diameter, is wide enough to stop the direct beam. However, it does not have sufficient solid angle coverage to make a prominent blocking of a potential halo effect. The long green lines in the top two figures are only seen when the helium-3 tube is removed from the direct beam, highlighting that they are due to internal neutron scattering.

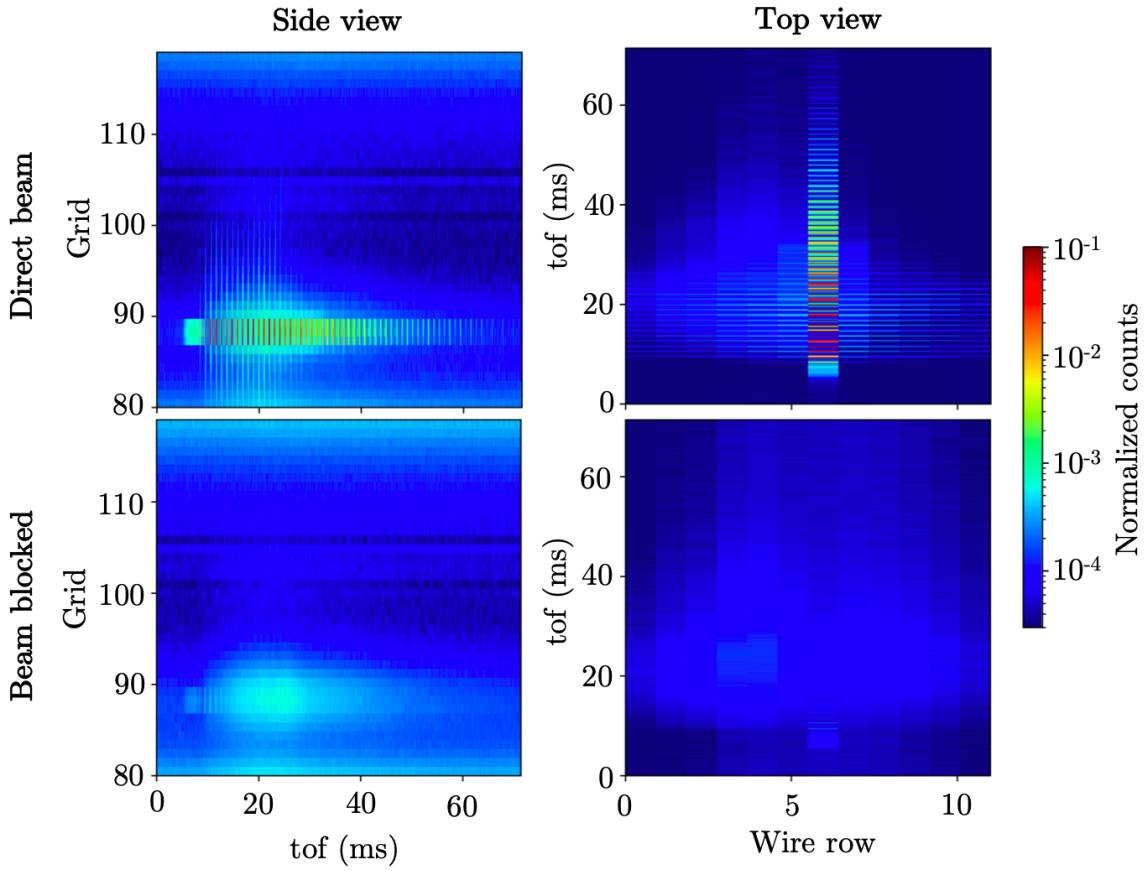

Figure 4.15: Histograms comparing data from the Multi-Grid detector when the beam was not blocked (top) and blocked (bottom). The two left plots show counts in grids vs. time-of-flight, while the two right plots show counts in wire rows vs. time-of-flight. The counts have been normalized to the accumulated beam monitor counts from the corresponding run. Data from MG.SEQ.I is used in this example.

By studying data with and without the cut on the direct beam, the wavelength distribution is acquired. This is presented in figure 4.16, where data from MG.SEQ.II is used as an example. The blue histogram is from the full data, while the red histogram is from data with a cut applied on the region of the direct beam. The green histogram is from the corresponding background measurement, which has an additional normalization based on the time-independent background level in the facility. This rate is seen in the flat region between 0 and 0.5 Å, which depends on the overall activity in the vicinity of V20 and cannot be accounted for by the beam monitor data alone. It is noted that the background data has no time correlation with the Fermi-chopper, i.e. an absence of sharp peaks.

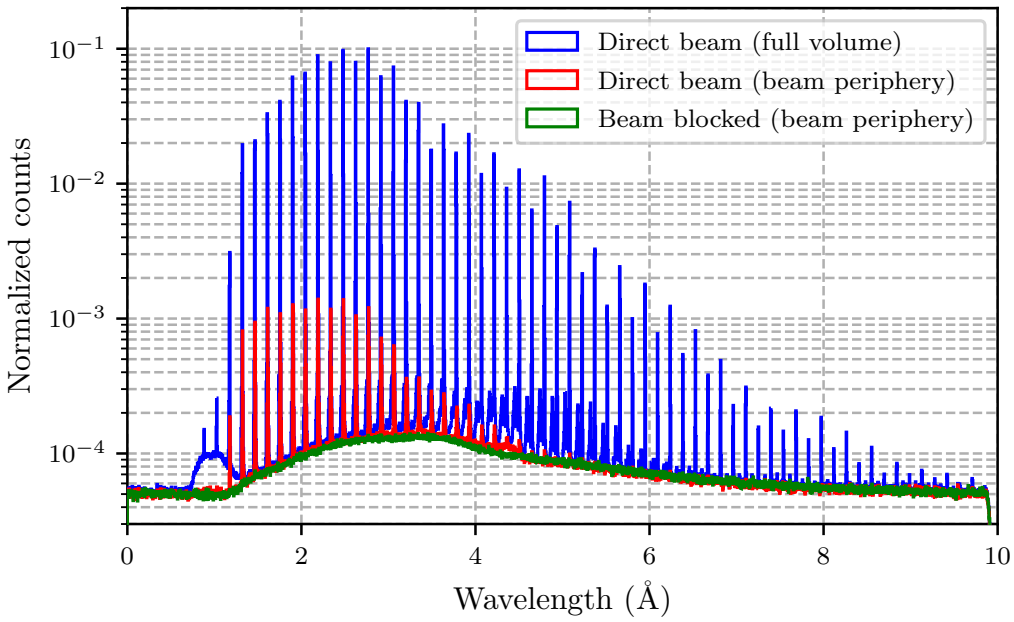

Figure 4.16: Wavelength histograms for the Multi-Grid detector, where data from the direct beam measurement is used to show two separate histograms: data from the full volume (blue) and beam periphery (red). The background data (green) is based on the beam periphery region. The plots are normalized by accumulated beam monitor counts, while the background data has an additional normalization based on the time-independent background level. Data from MG.SEQ.II is used in this example.

To study the energy lineshape in detail, data from a 1.47 Å measurement with the MG.SEQ.I is used as an example, as shown in figure 4.17. Again, the blue histogram is from the full volume, the red histogram is from the beam periphery, and the green histogram is from the background measurement. The majority of scattered neutrons are reconstructed with lower energy than the peak mean, resulting in a shoulder on the left side of the peak.

From the long green lines seen in figure 4.15, it is observed that the maximum distance the scattered neutron travel within the detector is approximately 15 grids, corresponding to about 30 cm. To estimate where these scattered neutrons are reconstructed in the energy spectra, equation (4.5) is used (modified for no energy transfer). This is done by using the peak mean as an approximation of the incident neutron energy, while assuming elastic scattering and that Δtof is the dominant factor in the distortion of the energy reconstruction. The coloured vertical lines in figure 4.17 show the result of this analysis, which overlaps well with the location of neutrons detected in the beam periphery (red).

A comparison in the energy lineshape with data from the helium-3 tube is presented in figure 4.18. Four histograms are shown, three from the Multi-Grid detector and one from the helium-3 tube. The separate histograms from the Multi-Grid detector correspond to

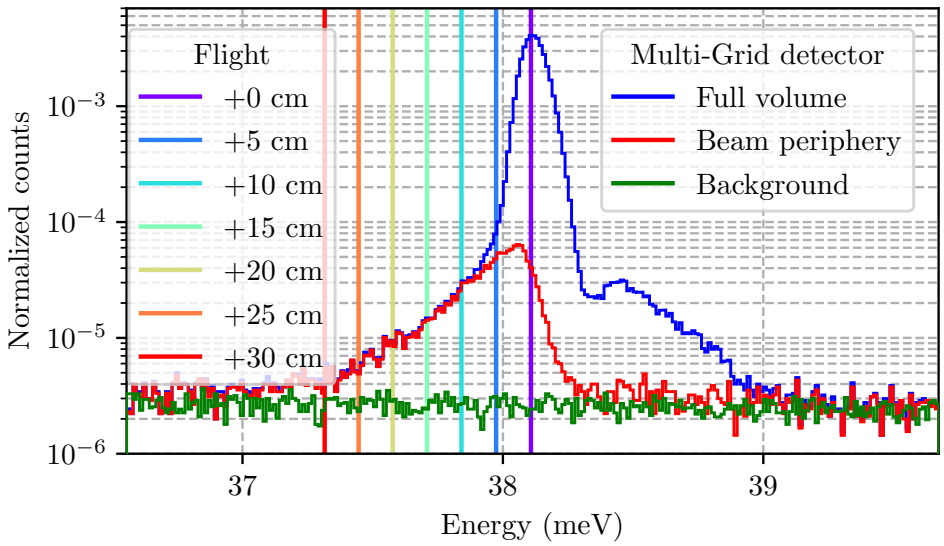

Figure 4.17: Effect on energy lineshape by internally scattered neutrons from a 1.47 Å measurement with the MG.SEQ.I. Histograms from the full volume in the Multi-Grid detector (blue), the beam periphery (red) and the background (green) are plotted together. The approximated location of scattered neutrons is shown as vertical lines, where each line corresponds to the energy reconstruction for scattered neutrons with a specific extra travel distance within the detector, as specified in the legend. The counts in the histograms are normalized to the accumulated beam monitor counts.

the full data, beam periphery, and beam centre. On the left side of the peak, the helium-3 data overlaps well with the data from the beam centre of the Multi-Grid detector (compare black and green). This further validates that the peak shoulder in the full data (blue) is due to scattered neutrons. Note that there is additional broadening in the Multi-Grid detector data, as it was further away from the Fermi-chopper than the helium-3 tube. This also affects the parasitic peak on the right side of the peak centre, which is present in both data sets but broader for the Multi-Grid detector.

To quantitatively compare the MG.SEQ.I and MG.SEQ.II in terms of time-dependent background suppression, a quantitative metric is introduced. As the purpose of the radial coating is to attenuate the magnitude of the shoulder on the left side of the peak – at different distances from the peak centre – the metric should assess how well this is achieved. To evaluate this, the ratio between the shoulder and peak area can be used: the Shoulder-to-Peak Ratio (SPR). This is defined as the number of counts above the background at a specified interval away from the peak centre, divided by the peak area. The background is estimated to be locally flat over the peak width and is calculated on a peak-by-peak basis, based on the rate at the side of the peak. The reason the background measurements are not used for background subtraction is because of non-negligible systematic offsets between the two MG.SEQ measurements.

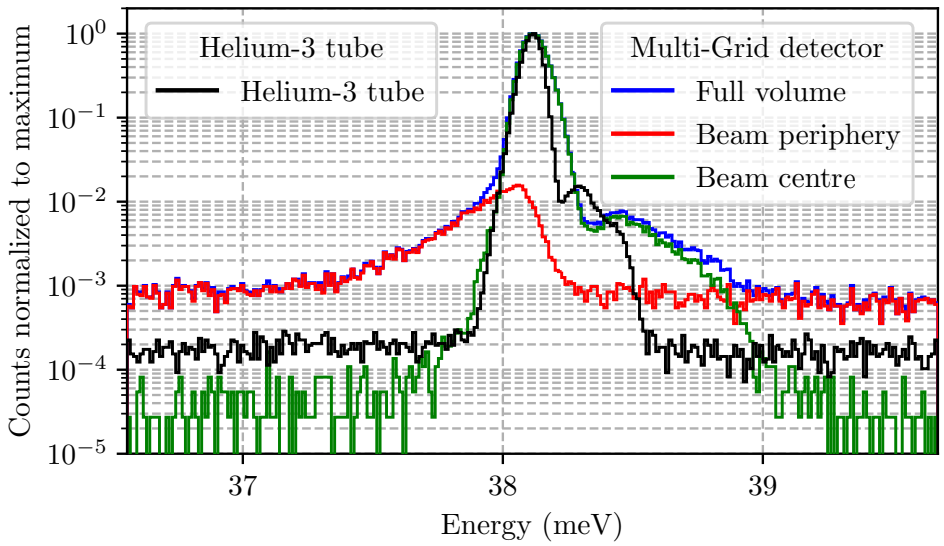

Figure 4.18: The effect of internally scattered neutrons on the energy lineshape by internally scattered neutrons at 1.47 Å in the MG.SEQ.I. Histograms from the full volume in the Multi-Grid detector (blue), the beam periphery (red) and the beam centre (green) are seen together with the helium-3 data (black). To facilitate peak comparison, the helium-3 data has been artificially shifted along the energy axis, such that it is aligned with the peak centre of the Multi-Grid detector. The counts are normalized to the peak maximum.

The chosen SPR metric is calculated according to,

$$\mathrm{SPR} = \frac{A_{\mathrm{shoulder}}^{E_1 \to E_2}}{A_{\mathrm{peak}}}, \tag{4.6}$$

where A_{peak} is the peak area within $\pm 5\sigma$ (using data from the full volume) and $A_{\mathrm{shoulder}}^{E_1 \to E_2}$ is the shoulder area within the energy interval E_1 to E_2 (using data from the beam periphery). In summary, the SPR captures the background-subtracted counts at a certain region $E_1 \to E_2$ at the edge of the peak, as a fraction of the full peak area. Consequently, a small SPR is desirable, as this implies a low amount of scattered neutrons in the specified energy range.

The limits E_1 and E_2 should be selected on a peak-by-peak basis, such that the same peak region is scanned for all peaks across the wavelength spectra. This is not a trivial task, as the peak shape changes with wavelength. This also complicates the comparison in SPR between different instruments, such as those done with the Multi-Grid detector at the CNCS [9], as the peak shape is heavily dependent on the resolution of the chopper system and the sample-to-detection lengths. Here, the peak shoulder is split into approximately three equally sized regions, where the region limits are based on the standard deviation σ around the peak centre. Each interval is 5σ wide, see vertical lines in figure 4.19.

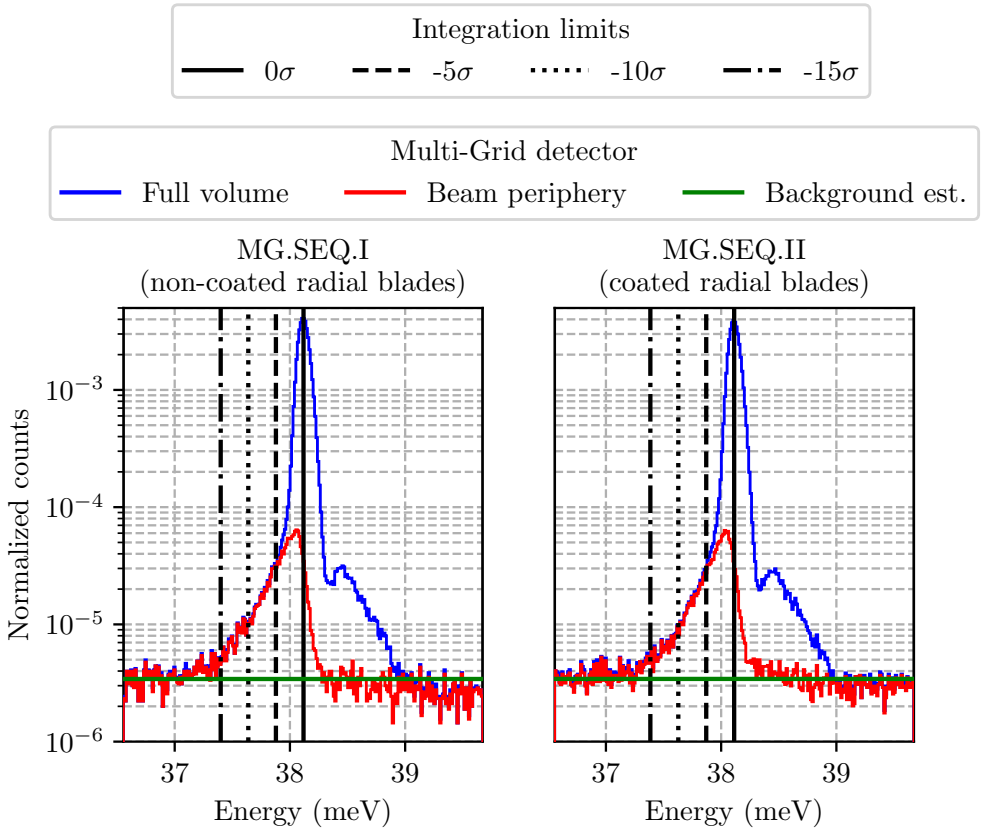

Figure 4.19: SPR extraction on a peak at 1.47 Å. Histograms from the full volume in MG.SEQ.I (left) and MG.SEQ.II (right) are compared to data where the direct beam is removed. The integration limits are presented as vertical lines. The standard deviation around the peak centre σ is calculated using a Gaussian fit. The estimated background is presented as a horizontal green line. The plots are normalized by accumulated beam monitor counts from the individual runs.

By repeating this analysis for each recorded peak in the data, a comparison between MG.SEQ.I and MG.SEQ.II as a function of wavelength is possible. This is presented in figure 4.20, where each data point corresponds to an incident neutron energy.

In the plot, the SPR is shown for the three different integration ranges: [-5σ, 0σ], [-10σ, -5σ], and [-15σ, -10σ]. These relative intervals vary in absolute range in energy from peak to peak. The absolute energy interval, ΔE, varies from approximately $\Delta E = 5 \cdot 10^{-1}$ meV at 1 Å, to $\Delta E = 5 \cdot 10^{-3}$ meV at 6 Å. It is observed that for wavelengths above the aluminum cut-off wavelength at 4.7 Å, the SPR is in most cases indistinguishable from zero. Furthermore, it is seen that for most wavelengths, MG.SEQ.I (non-coated radial blades) have a larger SPR than MG.SEQ.II (coated radial blades). This is visualised more clearly in figure 4.21, where the fractional SPR is shown: MG.SEQ.II divided by MG.SEQ.I. It is noted that the effect resulting from coating the radial blades increases with distance from the peak centre and that the scattered neutrons are attenuated more strongly

further away. Note that data is only shown up to 4 Å, as the statistical uncertainties for the remaining data points are too large for the fractions to contain meaningful information. The fractions from the full range can be seen in [87].

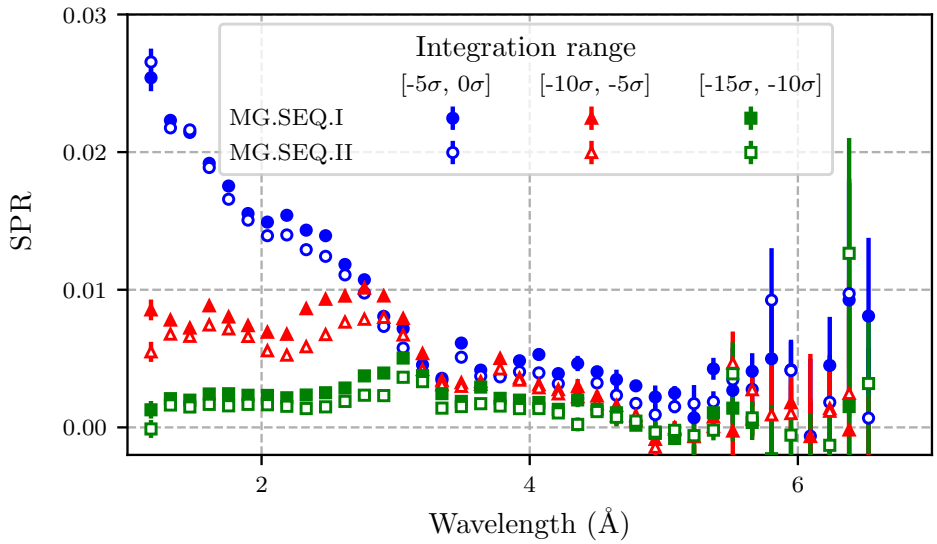

Figure 4.20: Comparison of SPR as a function of neutron wavelength, comparing MG.SEQ.I (non-coated radial blades) and MG.SEQ.II (coated radial blades). Three different integration ranges are used: [-5σ, 0σ] (blue), [-10σ, -5σ] (red), and [-15σ, -10σ] (green).

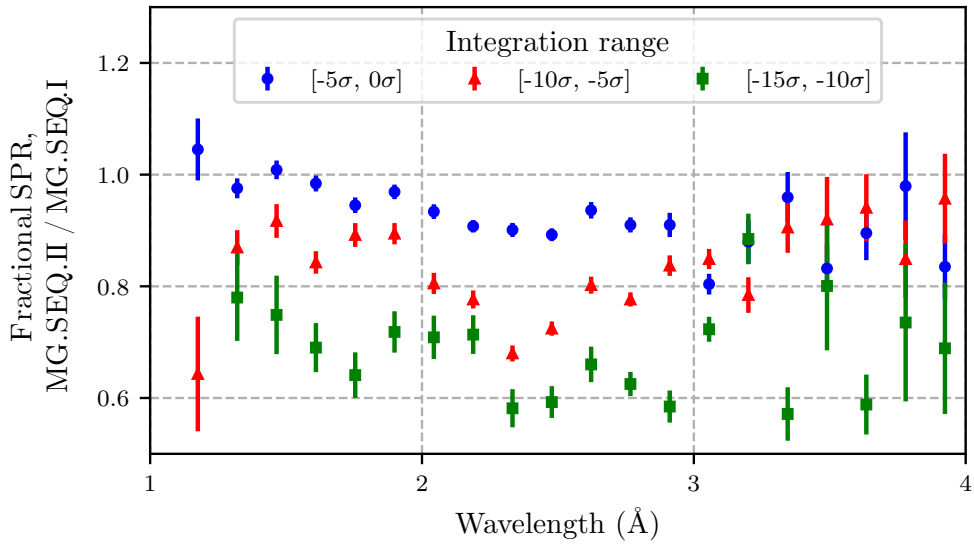

Figure 4.21: Comparison of fractional SPR as a function of neutron wavelength, comparing MG.SEQ.I (non-coated radial blades) and MG.SEQ.II (coated radial blades). Three different integration ranges are used: [-5σ, 0σ] (blue), [-10σ, -5σ] (red), and [-15σ, -10σ] (green).

The improvement of SPR by coating the radial blades is presented for the three shoulder regions in table 4.1. The results are based on data below 4 Å, where the statistical

uncertainties are acceptable. Note that these numbers are from a measurement with a collimated 14 × 60 mm^2 rectangular beam on the Multi-Grid detector, which is not generally the mode during normal operation. Furthermore, during normal operation, the aim is to calculate the final neutron energy based on the tof acquired from the approximately 3-5 meters flight path from the sample. This flight path is almost one order of magnitude shorter than the flight path used in the current experiment, which was around 28 meters. Consequently, in a standard measurement, the energy calculation is more sensitive to the extra tof acquired due to the internal scattering events, which give the radial blades a more important role. This is supported by preliminary results from the SEQUOIA measurements [69], where a greater effect of using the coated radial blades was seen.

Another effect to consider is that the direct beam used in the current measurement hits the detector close to 90°, in between radial blades. During normal operation, however, neutrons will in many cases hit a much larger portion of the detector surface area (with the important exception of Bragg diffraction from crystals, which can be a few cm^2 on the detector surface), and typically at angles with a small divergence around 90°. This will influence the effect of coating the radial blades, which will now also contribute to the efficiency of the detector due to the added converter material exposed to the incident neutrons. This will further lower the SPR, simply due to the increased height of the main peak.

Table 4.1: Average improvement of SPR between 1 and 4 Å by coating the radial blades. The results are presented separately for the three shoulder regions.

Shoulder region	Average improvement
[-5σ, 0σ]	7 ± 6 %
[-10σ, -5σ]	16 ± 8 %
[-15σ, -10σ]	31 ± 8 %

All presented percentage errors should be interpreted as variations around the mean, not statistical uncertainties. It is not expected that the radial blades will have a uniform effect across all wavelengths, so a mean with a low variance is not anticipated. This is because the effect of the radial blades depends on the number of blades crossed, which depends on the scattering angle of the neutrons. As the scattering angle is wavelength dependent, the effect varies as a function of wavelength, as was shown in figure 4.21. The stated standard deviations around the mean are meant to capture the magnitude of this variation over the measured wavelengths.

4.2.4 Time and energy resolution

The observed energy resolution depends on the resolution of the detector and the resolution of the chopper system. Therefore, the shape of the peak is a convolution of the chopper pulse shape and the detector response shape, which can be expressed conceptually according to

$$f_{\text{observed}} = f_{\text{chopper}} \otimes f_{\text{detector}}, \tag{4.7}$$

where f_{observed} is the observed energy distribution, f_{chopper} is the energy distribution from the chopper system, and f_{detector} is the detector energy response function.

The resolution of the chopper system f_{chopper} depends on all choppers in the setup, which in this case includes most importantly the source chopper and the Fermi-chopper. The initial pulse produced by the source chopper, which sends the T_0 (time zero) signal, travels 28 meters before reaching the Fermi-chopper. The long travel length allows neutrons with different energies to separate from each other in time, due to their different velocities. This pulse broadening is desired, as it increases the energy resolution when using the tof in relation to the T_0 signal to calculate neutron energy.

The purpose of the Fermi-chopper is to cut the wide incident pulse, with neutrons well separated in energy, into sharp well-defined pulses. These pulses, in contrast to the source pulse, should be kept as narrow as possible in time so that any broadening due to the full detector component f_{detector} is more easily observed. That is, by keeping the distance from the Fermi-chopper short, some information about the incident neutron energy is lost due to less separation in energy. However, because of the small separation in energy, any broadening due to the detector component will have a larger relative effect. Thus, keeping a small ΔT – and consequently ΔE – on the final pulse is important to study detector-related broadening.

The pulse width in time at the detector surface, $\Delta T_{\text{chopper}}$, is determined according to the following equation,

$$\Delta T_{\text{chopper}} = t_{\text{open}} + d(v_s^{-1} - v_f^{-1}), \tag{4.8}$$

where t_{open} is the Fermi-chopper window opening time, d the Fermi-chopper-to-detector distance, and v_s and v_f are the velocities of the slowest and fastest neutrons in the pulse, respectively. To reduce the broadening, it is important to have a short opening time and to keep the Fermi-chopper as close as possible to the detector. As the width of f_{chopper} grows as a function of $\Delta T_{\text{chopper}}$, the same conditions mentioned above are required to keep a sharp pulse in energy.

As the helium-3 tube and the Multi-Grid detector are at different distances from the Fermi-chopper, recall figure 4.3, the width in energy spectra from Multi-Grid data are

corrected to account for this offset. In the top plot in figure 4.22, the tof spectra are shown individually for each of the twenty wire layers in the Multi-Grid detector, together with the tof from the helium-3 tube. In the bottom plot, the energy spectra corresponding to these tof-values are presented. There, data from all twenty layers of the Multi-Grid detector are seen to be reconstructed at the same position, overlapping with the helium-3 data. However, there is an additional broadening on the Multi-Grid detector, caused by the additional distance from the Fermi-chopper.

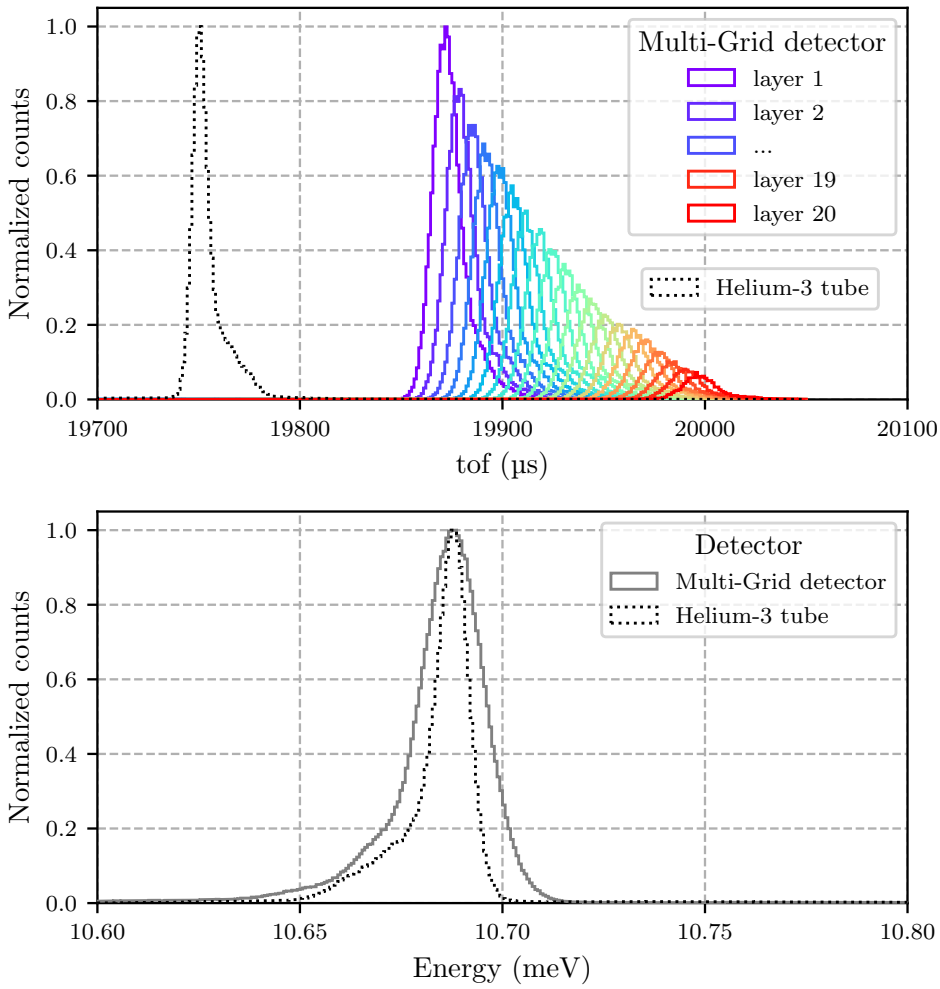

Figure 4.22: Time-of-flight and energy spectra at 2.8 Å. In the top plot, tof from the twenty individual layers in the Multi-Grid detector are presented from front to back (rainbow colours), together with the helium-3 tube (black). At the bottom, the corresponding energy spectra for the Multi-Grid detector (grey) and helium-3 tube (black) are shown. The histograms are normalized to peak maximum, to facilitate peak comparison.

The dominant contribution to the intrinsic tof resolution, and consequently energy resolution, is the tof variation due to differences in conversion location in the respective detectors. However, the seen distribution in tof is primarily determined by the pulse shape acquired, which is given by the chopper geometry and rotation frequency. Due to the symmetric

shape of Fermi-chambers in the chopper [90], this is the approximately Gaussian pulse observed.

To account for the extra pulse broadening in the Multi-Grid detector due to the additional distance from the chopper, the peak-width in energy is calculated using a Gaussian fit for each layer. This is presented in the top plot in figure 4.23[1], which shows how the peak width, defined as the FWHM, depends on the distance from the Fermi-chopper. In the bottom plot of the figure, the FWHM for each of the layers in the Multi-Grid detector – as well as the FWHM of the helium-3 tube – are plotted as a function of distance from the Fermi-chopper. A linear fit to the data points from the Multi-Grid detector is also shown, together with the fit uncertainties. The interpolation takes into account the widening of the pulse with distance and allows the Multi-Grid detector to be compared to the helium-3 tube. That is, the width of the Multi-Grid is interpolated to the value it would have had at the same distance from the Fermi-chopper as the helium-3 tube.

In the above example, the procedure is shown for a peak at 2.8 Å, but the same analysis is done for the rest of the peaks. This is shown in figure 4.24, where the FWHM of the two detectors are presented as a function of neutron wavelength. It can be seen that for the four data points corresponding to the shortest wavelengths measured, the Multi-Grid detector and the helium-3 tube have an equivalent energy resolution within the error bars. For the remaining wavelengths, the helium-3 tube has a finer energy resolution. However, the trend seems to indicate that for wavelengths shorter than those measured here, the Multi-Grid might have an advantage. The difference between the detectors is more prominent at longer wavelengths, where the chopper resolution is the finest.

One factor in the observed resolution difference is related to the conversion location uncertainties in the detectors. This effect has been approximated by the blue and red lines in figure 4.24, which show how the uncertainty in conversion location translates to a corresponding uncertainty in energy. This depends on the neutron absorption time distribution, which in turn depends on the conversion location uncertainty. This uncertainty can vary more in the helium-3 tube than in the Multi-Grid detector, as the absorption reaction can take place anywhere in the gas along the 2.5 cm depth of the helium-3 tube. For the Multi-Grid detector, in contrast, the absorption can only occur at discrete intervals of 0.95 cm (1 cm pitch $-$ 2 $\cdot$ 0.025 cm aluminum thickness), where the solid conversion layers are located. Note that the two calculated curves are always beneath the data points

[1]It is observed that the peak centre is at a lower energy for the front layer, ca 10.685 meV, compared to the back layer, ca 10.695 meV, with a gradual shift for in-between layers. This is because the $^{10}B_4C$-coating has a higher absorption cross-section at lower energies. Consequently, the low energy neutrons will be absorbed closer to the detector entrance than the high energy ones. That is, the peak centre will gradually shift to higher energies towards the back layers, as only the higher energy neutrons are likely to survive the full depth of the detector.

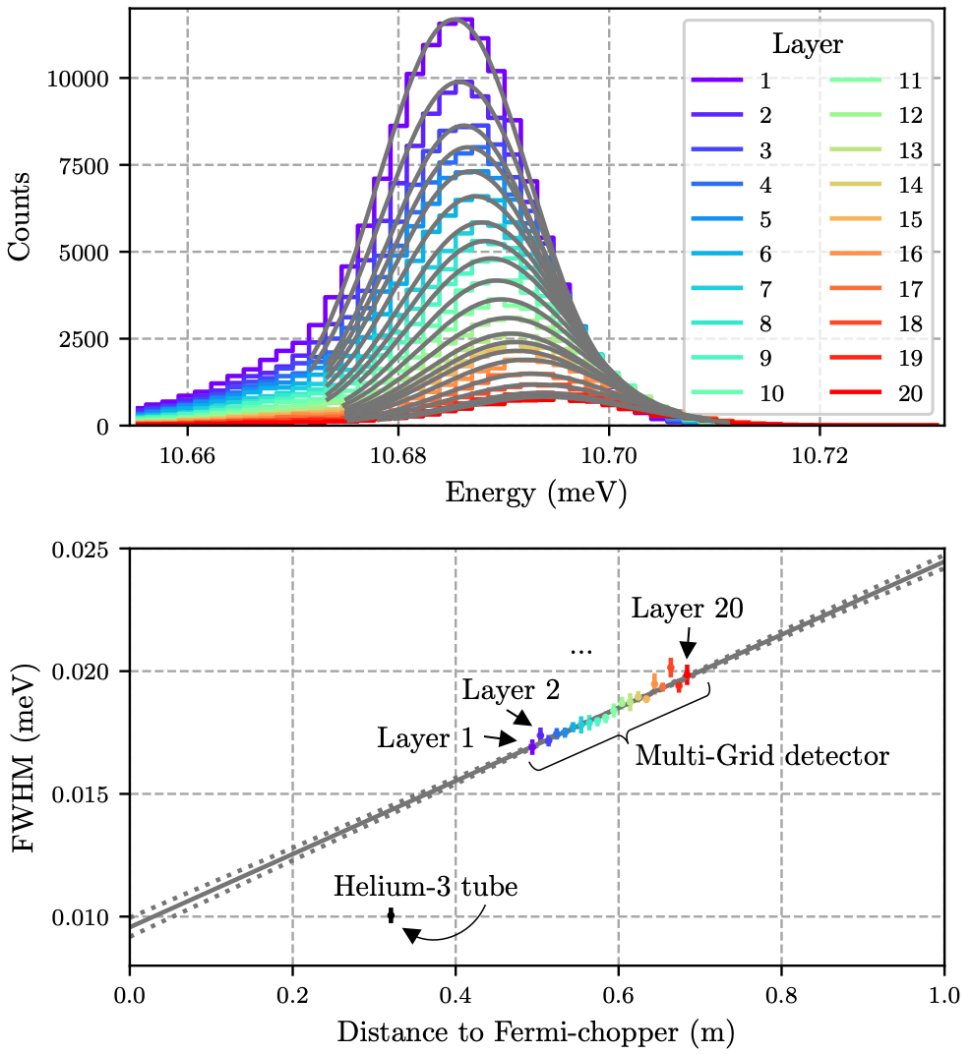

Figure 4.23: Correction for pulse broadening with distance, using 2.8 Å neutrons as an example. In the top plot, the widening in energy is presented for each layer. The distribution from each layer is fitted with a Gaussian (grey) and the FWHM is extracted from the fit parameters. In the bottom plot, the FWHM from each Multi-Grid layer (rainbow colours) is shown together with the FWHM of the helium-3 tube (black), as a function of distance from the Fermi-chopper. A linear fit (solid grey line) from the Multi-Grid points is also presented together with the fit uncertainties (two dotted grey lines), demonstrating how the chopper pulse widens with distance.

as they do not account for the remaining time uncertainties in the measurement, such as broadening from the electronics and charge collection times in the MWPC.

The calculated uncertainties are based on approximations shown in figure 4.25, where the conversion location uncertainties for the helium-3 tube and Multi-Grid detector are compared. The uncertainty in the helium-3 tube was acquired using a one-dimensional calculation of the neutron absorption as a function of depth, which was done for a series of different incident wavelengths. As an estimate of the detection location uncertainty,

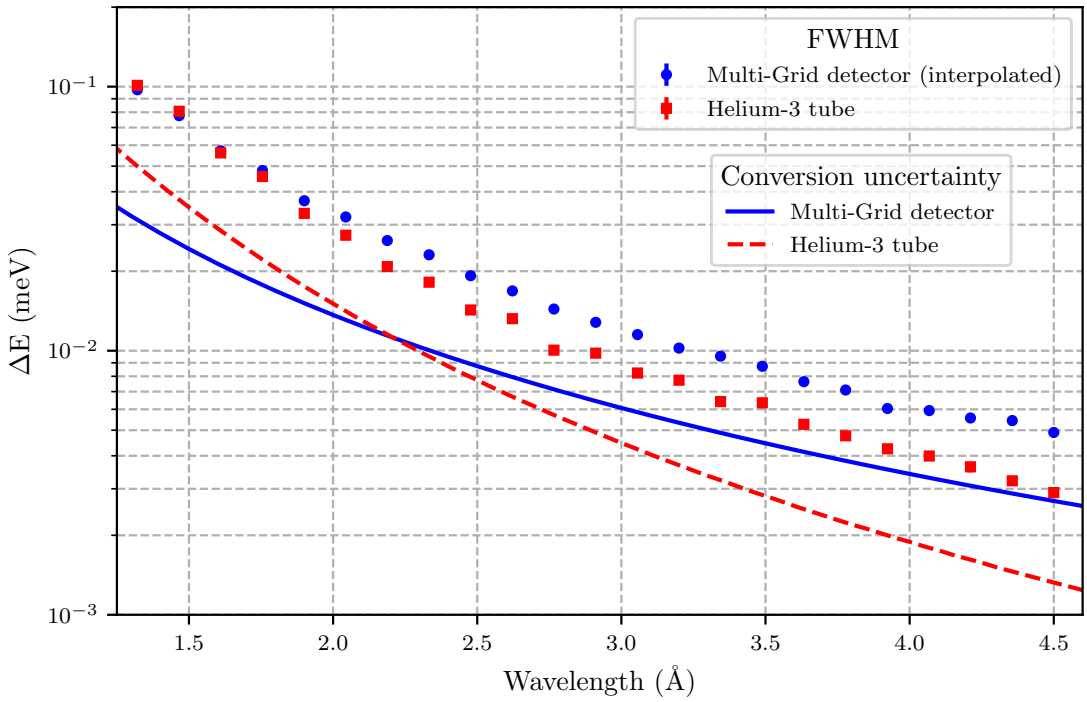

Figure 4.24: Comparison between the FWHM of the Multi-Grid detector (blue dots) and the helium-3 tube (red squares) as a function of neutron wavelength. The solid blue line shows the conversion location uncertainty in the Multi-Grid detector, while the dashed red lines present the conversion location uncertainty in the helium-3 tube, here considered as the range covered by 95% of the detected neutrons.

the depth where 95% of the detected neutrons are converted is used. Only the range is considered, as this is estimated to be the dominant factor of the neutron detection distribution. However, factors such as tube shape and conversion products ranges also contribute to the distribution. Using a high percentage, 95%, is an attempt to account for these missing factors.

The difference in conversion location resolution – and thus timing resolution – between the two technologies is further illustrated in figure 4.26, where the Multi-Grid tof distribution corresponding to a peak at 4.3 Å is plotted individually for each wire layer. This is plotted together with the related energy distribution. In the top plot, it is seen that each wire layer has a double peak in tof. This is because each wire layer is adjacent to two converter films, where neutrons can be absorbed in either one. If the two peaks corresponding to the first layer are fitted with one Gaussian each, then the distance between the fitted peak centres are 10.5 ± 0.4 μs. For 4.3 Å neutrons, which travels at approximately 0.09 cm/μs, this time difference translates to 0.97 ± 0.04 cm. This is within the expected 0.95 cm distance between adjacent converter films.

The double peak in time-of-flight results in a corresponding double peak in the energy

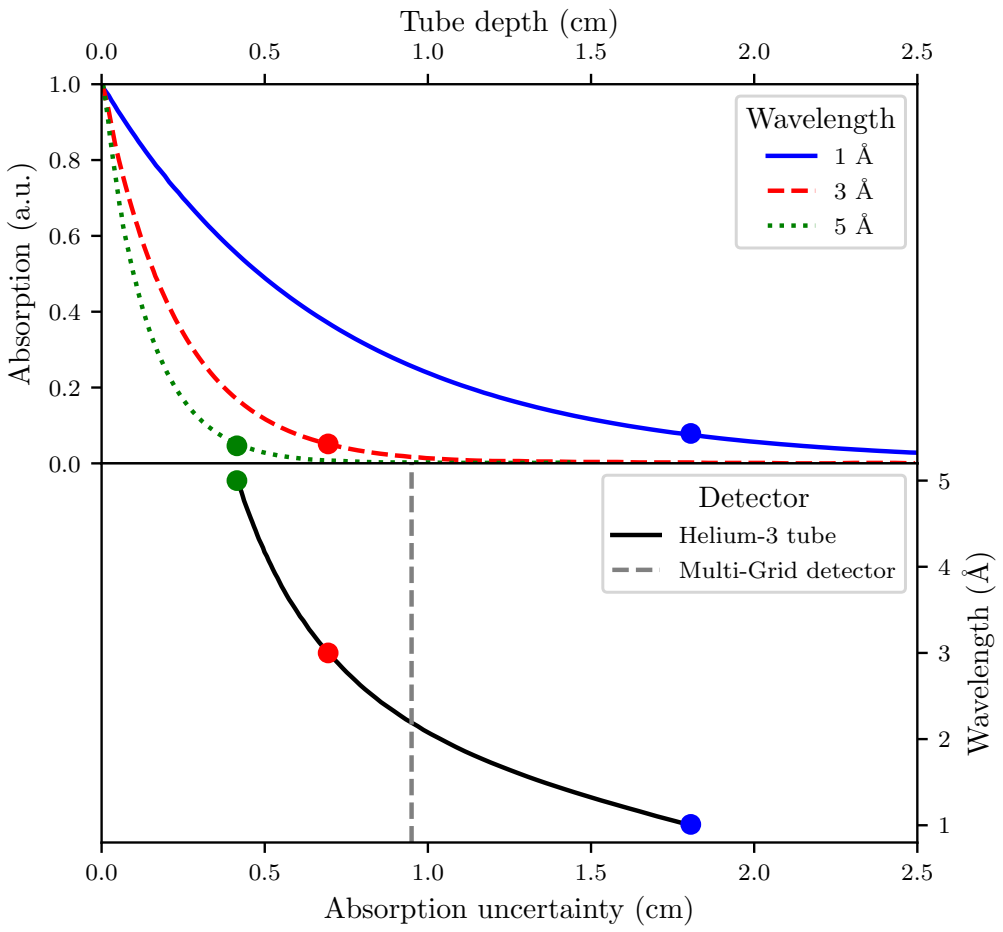

Figure 4.25: Conversion location uncertainty in the helium-3 tube and Multi-Grid detector. At the top, the distributions of the neutron converter locations in the helium-3 tube are presented for 1, 3 and 5 Å. The markers indicate the depth where 95 % of the detected neutrons have been absorbed for each distribution, which is treated as the conversion location uncertainty of the tube. At the bottom, the conversion location uncertainty of the helium-3 tube (black) is compared to the Multi-Grid detector (grey).

spectra as well, which is shown in the bottom plot where the Multi-Grid detector is compared to the helium-3 tube. It is worth noting, however, that the better the two Multi-Grid peaks are separated, the more information is gained concerning which coating surface the absorption took place. This could potentially be used to increase the spatial resolution of the Multi-Grid detector down to the specific surface the conversion took place, providing the peaks are sufficiently well separated.

From the analysis, a clear double peak is seen from the Multi-Grid detector for the longest wavelengths measured. However, in practical applications of the Multi-Grid detector at an instrument, such as at the CNCS and SEQUOIA instruments, this effect has not been observed due to the approximately one order of magnitude longer Fermi-chopper-to-detector distance in a typical instrument, which leads to additional pulse broadening. A compari-

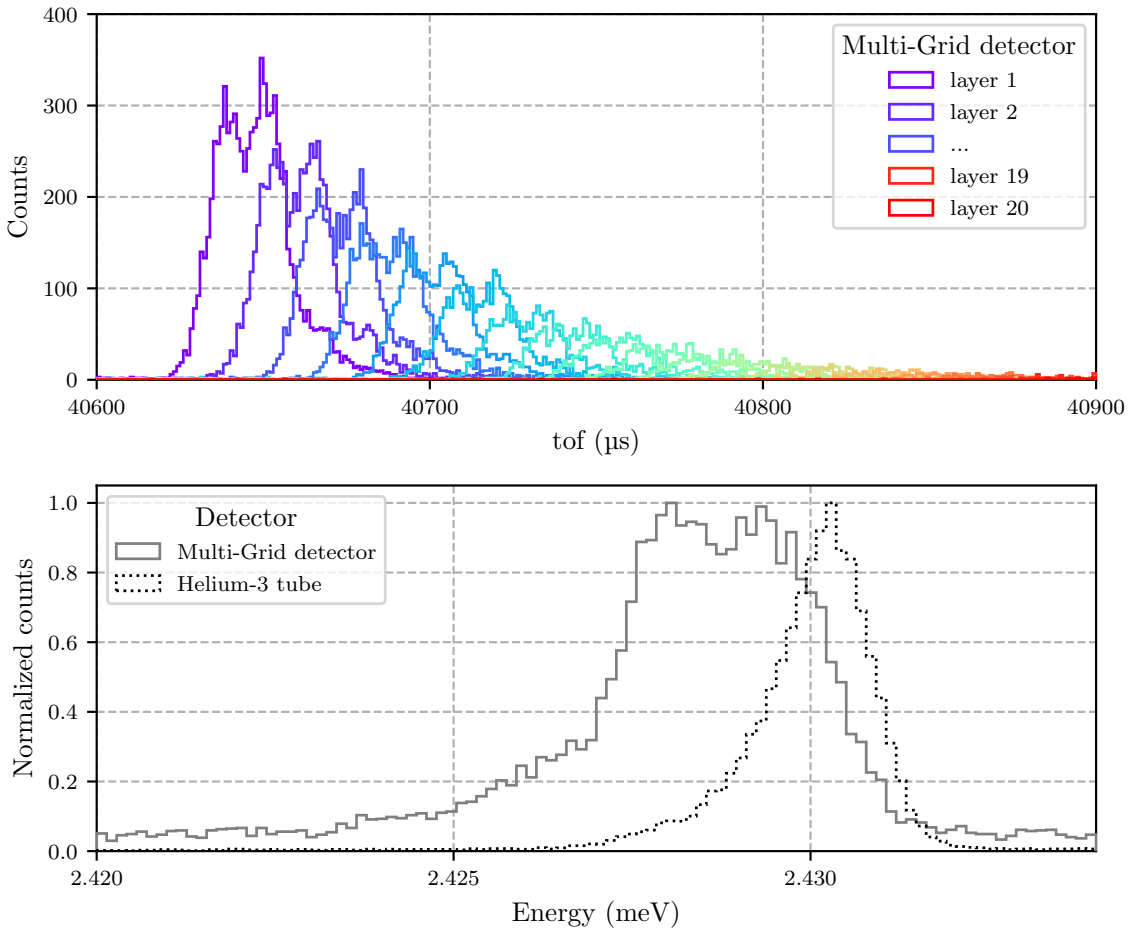

Figure 4.26: Demonstration of the neutron absorption timing difference between the Multi-Grid detector and the helium-3 tube. At the top, tof from each of the twenty layers in the Multi-Grid detector are histogrammed individually. This highlights the double peak present in each layer. At the bottom, the resulting energy distribution for the Multi-Grid detector (grey) is plotted together with the helium-3 tube (black). The histograms are normalized to the max values, to facilitate shape comparison. In this example, a peak at around 4.3 Å was used. The double peaks are only visible for the longest wavelengths used in the measurement.

son can be made between the current setup, which has a few tens of centimetres chopper-to-detector distance, with the CNCS and SEQUOIA instruments, where the equivalent distance is a few meters. As the pulse broadening is proportional to the distance, a corresponding one order of magnitude more broadening is seen at CNCS and SEQUOIA for the same wavelength range measured here [9, 69]. The effect of the double-sided coating is below the instrument resolution, and no difference in energy resolution is seen between the helium-3 tube and the Multi-Grid detector.

Note that the measured resolutions are a function of the detector specifications. The energy resolution of the helium-3 tube can be varied by choosing a different gas pressure in the tube and by changing the geometry. Conversely, the resolution of the Multi-Grid

detector can be adjusted by varying the distance between layers. It can also be changed by choosing a single-sided coating approach, whereupon the uncertainty concerning which coating the conversion took place would vanish. That is, the double peak observed for long wavelengths would disappear, as it is unambiguous in which conversion layer the reaction occurred. However, a consequence of this would be either to accept a reduced efficiency or a doubling of the detector depth. In both scenarios, the internal scattering would have a larger impact on the lineshape, as the ratio between converter material and aluminum within the detector would be smaller. Thus, there would be less converter material to absorb the scattered neutrons. This results in a design trade-off between energy resolution, background reduction, and efficiency.

Chapter 5

LET measurements

At the ISIS Neutron and Muon Source, the MG.LET was tested at the cold neutron spectrometer LET [57], see figure 5.1. The instrument has an operational neutron energy

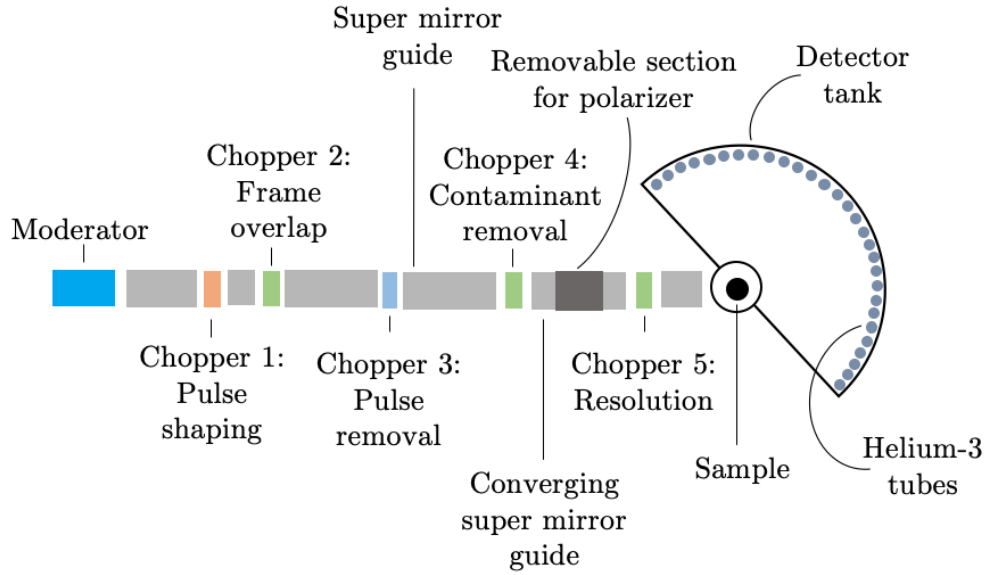

Figure 5.1: Schematic overview of the LET beamline. On the left, the incident neutron beam is received from the moderator. This beam is then split into a sequence of short pulses with precise energies using a series of five choppers. Before the last chopper, a converging super mirror guide is used to focus the neutrons into a smaller area. At the right, the sample and detector tank are seen. There is also a removable section which can be replaced with a neutron polarizer.

range spanning from 0.6 to 80 meV (11.7 Å to 1.0 Å) and it supports RRM, Repetition Rate Multiplication, which allows it to extract multiple energy peaks in each 100 ms time frame. The instrument is also equipped with an array of 4 m tall helium-3 tubes, arranged in a circumference 3.5 m from the sample, as seen from the top. This results in a large angular coverage: -40° to 140° in the horizontal plane and -30° to 30° in the vertical

plane. Additionally – as the upcoming CSPEC instrument is modelled on LET – the instrument has a similar neutron energy range, operational mode and angular coverage as that intended for CSPEC, which makes it an excellent environment for the Multi-Grid detector to be studied in. Additionally, the permanent helium-3 array in the instrument also serves as a good benchmark for the Multi-Grid detector performance.

5.1 Method

The purpose of the LET measurements was to characterise the energy transfer lineshape and the signal-to-background ratio of the Multi-Grid detector by comparing it to the helium-3 tubes, which operated in parallel during all the measurements. To make the data of the two detector systems as comparable as possible, a strong incoherent scatterer – vanadium – was used. This sample is often used in detector characterisation, as it facilitates the isolation of detector-dependent effects.

To cover a large energy range – thereby probing as much as possible of the CSPEC operational energy spectrum – the chopper system was operated in RRM mode. This was set so that five energies per 100 ms frame were obtained: 2.4 meV (5.8 Å), 3.7 meV (4.7 Å), 6.3 meV (3.6 Å), 13.4 meV (2.5 Å), and 44.9 meV (1.3 Å). The details of how the experimental setup was prepared to perform these measurements are presented below.

5.1.1 Gamma calibration

Before the MG.LET was shipped to ISIS, a thorough gamma threshold calibration investigation was performed at Lund University, Sweden, at the Source Testing Facility [15]. During the measurements, an uncollimated 16.64 MBq ^{60}Co source was placed directly in front of the detector. The ^{60}Co-source is a strong gamma emitter, which allowed a study of where gamma events are reconstructed in the PHS. This is presented in figure 5.2, where a comparison between a gamma and background measurement is shown for both wires and grids. The plot was extracted by subtracting the pulse height spectra obtained with and without the ^{60}Co-source present. As can be seen, the gamma events are heavily concentrated at low ADC values. The result of the investigation was that a 550 ADC software threshold is appropriate to remove the majority of gamma events. The full details of this investigation are found in [99].

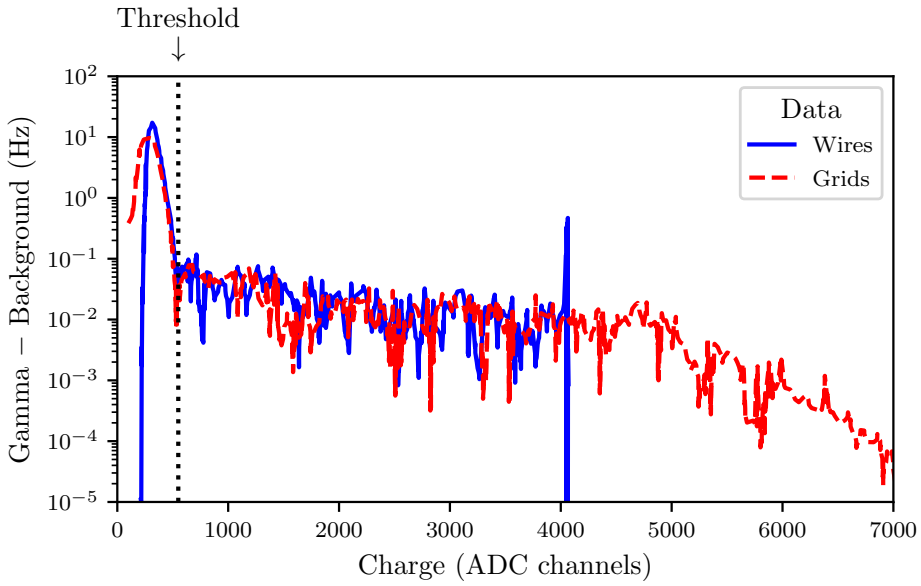

Figure 5.2: Gamma threshold investigation for the MG.LET performed at Lund University, where the difference between the PHS spectra collected with and without the gamma source is presented for both wires (blue) and grids (red). Figure adapted from [99].

5.1.2 Beamtime

The experimental setup used during the beamtime is presented in figure 5.3, where the MG.LET is seen installed inside the LET detector tank alongside 12 packs of 32 helium-3 tubes, each pack separated with cadmium vanes. The MG.LET detector is positioned in the front of the first of these helium-3 tube packs: placed between the tank opening door and the first cadmium vane. All of the cables required for the detector operation – including HV and LV cables, optical fibres, and gas inlet/outlet pipes – are led inside a flexi hose which is fed through the vacuum sealing at the top of the detector tank. Note that inside the detector tank, MirroBor sheets are used to shield the flexi hose closest to the MG.LET, while Cadmium is used to shield the hose closest to the sample. This is to minimize neutron scattering from the hose.

Inside the tank, the detector was covered with additional B_4C-based hard plastic external shielding on all sides except the front, as seen in figure 5.3. For the front, MirroBor is used to shield all areas around the active area. Furthermore, due to the gap between the external shielding and the top lid of the detector, additional cadmium shielding was added there to prevent neutrons from entering the active volume via that route.

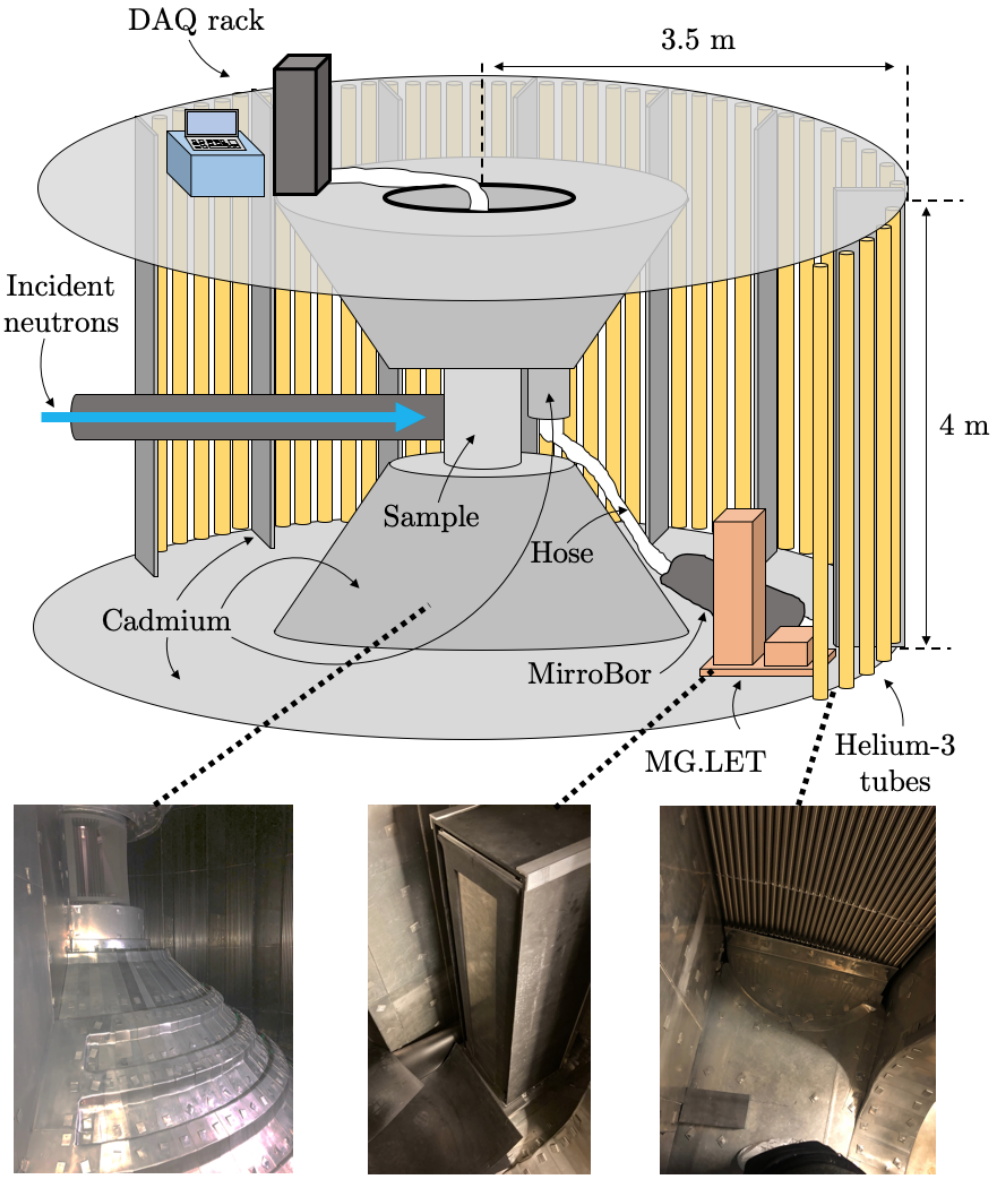

Figure 5.3: Schematic overview of the experimental setup in the LET detector tank. At the top, a schematic illustration of the inside of the detector tank is presented, highlighting the helium-3 tube array (yellow) and the position of MG.LET (orange). It is also seen how the MG.LET cables are guided in a hose (white), shielded by MirroBor (dark grey), and led up by the sample environment to the DAQ rack. At the bottom, pictures are seen corresponding to some components seen in the sketch.

Position reconstruction

Once the MG.LET had been installed inside the detector tank, the relative position of the detector with respect to the sample was established. To do this, the known positions of the permanent helium-3 tubes were measured in relation to the MG.LET detector, as seen in figure 5.4, which made it possible to calculate the position and rotation of the detector on the floor plane in the tank. To find the height, a previous data set of a vanadium

measurement was used where it was possible to see a sharp decline in statistics at the bottom of the tubes (right in figure 5.4). This drop corresponds to the location of the cadmium shielding close to the floor, which can be used to find the position of the floor in relation to the sample, and hence the relative height location of the MG.LET.

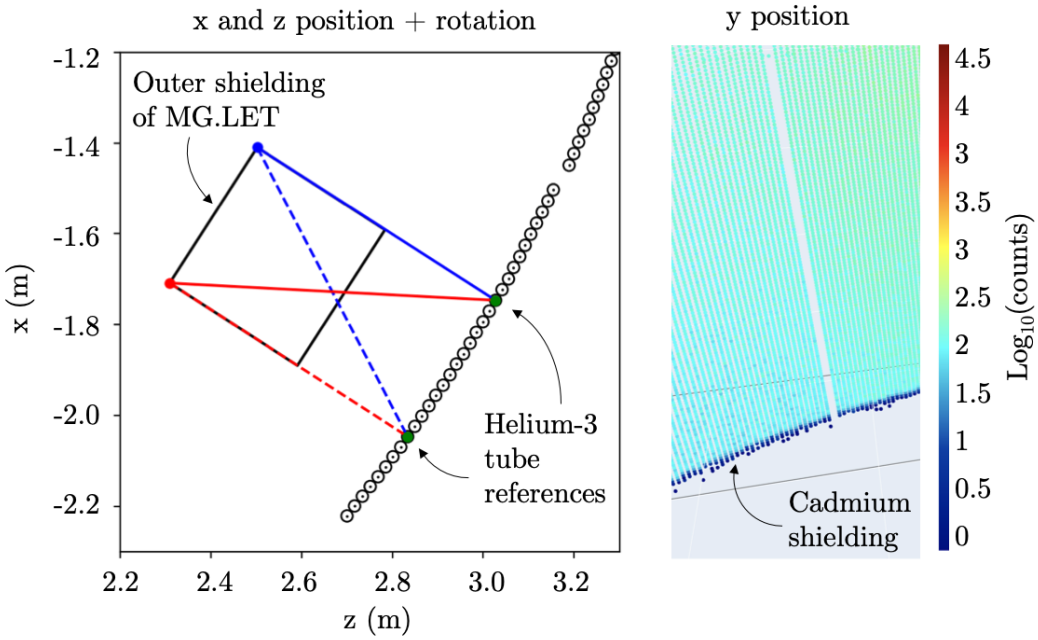

Figure 5.4: MG.LET position reconstruction. To the left, the measurements for position and rotation in the zx-plane are shown. This involved measuring the distance from two detector corners (blue and red) to two helium-3 tubes (green). To the right, the data used to establish the y-position is shown. The drop in statistics at the bottom corresponds to the location of the cadmium wall, which is used as a reference point to establish the height of the detector.

Once the external position of the Multi-Grid detector had been found, the next step was to calculate the positions of its voxels in relation to the sample position. To do this, a CAD model of the detector was used. In the model, the relative positions of all voxels in relation to an external corner of the vessel were included. Using this information together with the position of the external detector corners measured in relation to the sample, the voxel positions could then be inferred. This is presented in figure 5.5. From this, the secondary flight path of the scattered neutrons from sample to detection can be directly calculated for each voxel, based on their position relative to the sample.

The location of the external reference point – orange point in figure 5.5 – was determined

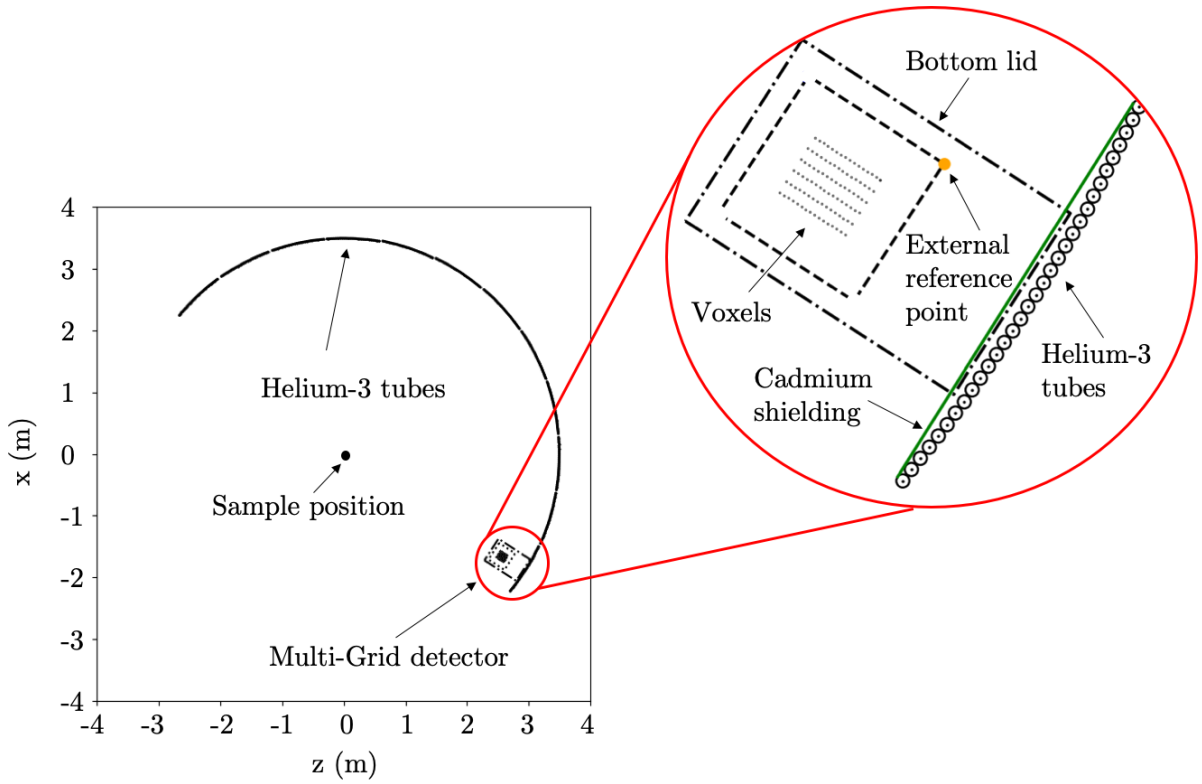

Figure 5.5: Position reconstruction in the zx-plane. To the left, the top view of the full detector tank is seen together with the location of the Multi-Grid detector. To the right, a zoomed part of the figure focusing on the detector and the important components is shown, including the external reference point, the voxels, the bottom lid and the cadmium shielding. As can be seen, there is only a slight overlap between the bottom lid and the cadmium shielding, which implies a good position reconstruction, as the bottom lid was close to the shielding when it was installed inside the tank.

to be:

$$x = -1.612 \text{ m} \pm 0.009 \text{ m}$$
$$y = -0.862 \text{ m} \pm 0.016 \text{ m}$$
$$z = \quad 2.779 \text{ m} \pm 0.010 \text{ m}$$

The uncertainty on the location of the reference point will affect the uncertainty on the energy resolution. This will vary from voxel to voxel and is proportional to σ_d/d, where d is the distance from the sample. For all voxels and energies under consideration in this work, the fractional energy uncertainty σ_E/E resulting from the position reconstruction is $< 1\%$. This is adequate for the current measurements, as the uncertainty will not manifest as a spread in reconstructed energies: it will be a constant off-shift. As seen later in figure 5.15, this off-shift is shown to be negligible.

C_{60} measurements

To validate the position reconstruction of neutron hits in the MG.LET detector, a white beam measurement was done on a C_{60} sample. This results in energy-dependent interference rings, where one example can be seen in figure 5.6. In the figure, 3D histograms of both the Multi-Grid detector and the helium-3 tubes have been performed for data within a short time window: 23.5 ms to 24.0 ms. From the alignment of the rings between the helium-3 array and the MG.LET, the neutron hit reconstructions in the detector voxels are confirmed to be accurate. This is further confirmed by the shadowed region on the helium-3 tubes located behind the detector. The vessel borders, including those for the bottom lid, are indicated with thin black lines.

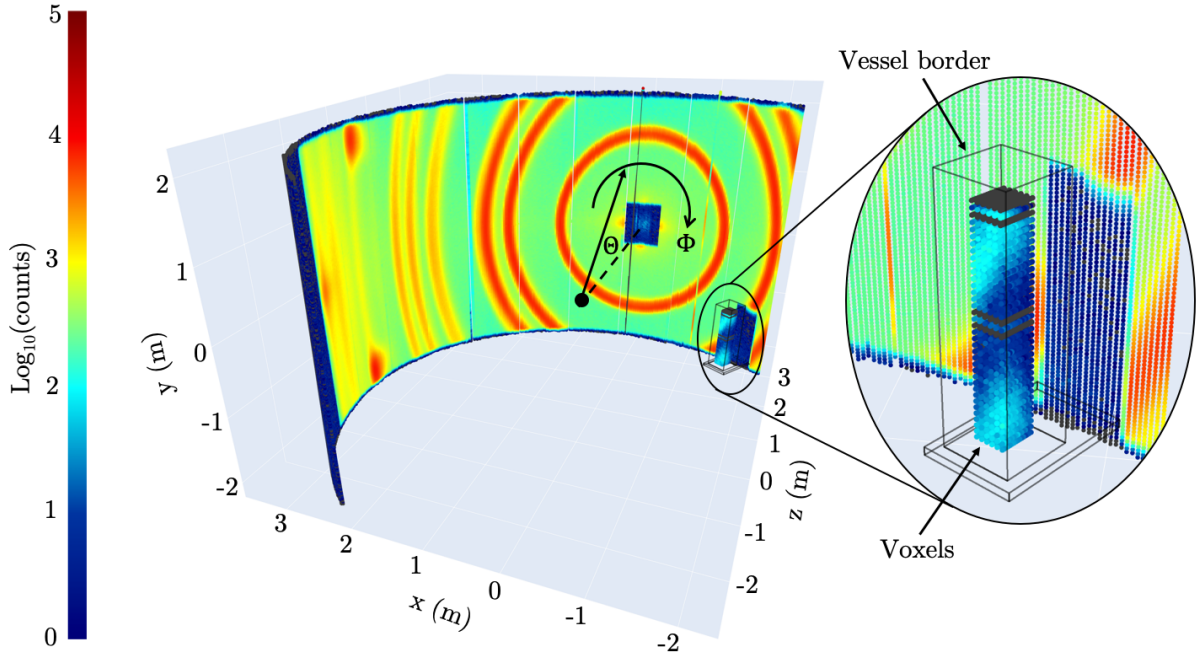

Figure 5.6: C_{60}, 3D histogram of helium-3 and the MG.LET data, showing the neutron hit positions relative to the sample (black dot). The definition of Θ, deviation angle from the positive z-axis, and Φ, rotation angle around the positive z-axis, is illustrated with black arrows. There is also a zoom of the Multi-Grid detector on the right-hand side, highlighting the vessel borders and the voxels. The histograms are produced for data with tof values between 23.5 ms and 24.0 ms.

Note that in figure 5.6, the ring counts in the Multi-Grid detector (light blue) are approximately two orders of magnitude lower than in the helium-3 tubes (red). One contribution to this is that the Multi-Grid detector, contrary to the helium-3 tubes, has a depth. For the MG.LET, this means that the detected neutrons are distributed over 16 layers, which means each voxel in the layers will receive around one order of magnitude fewer counts compared to the helium-3 tubes. To account for this, a 2D histogram of angular hit locations was produced, which sums the counts in all voxels oriented with the same angle as

the sample. This is shown in figure 5.7, where Φ and Θ are defined in the corresponding 3D visualisation of the data. Here, the difference in counts has been reduced between the two detectors, but it is still significantly lower than expected. Based on previous measurements and analytical calculations, the efficiency of the helium-3 tubes and the Multi-Grid detector should be comparable. This discrepancy in efficiency has been investigated in a post-beamtime study at the facility and later at the ESS lab Utgård [100].

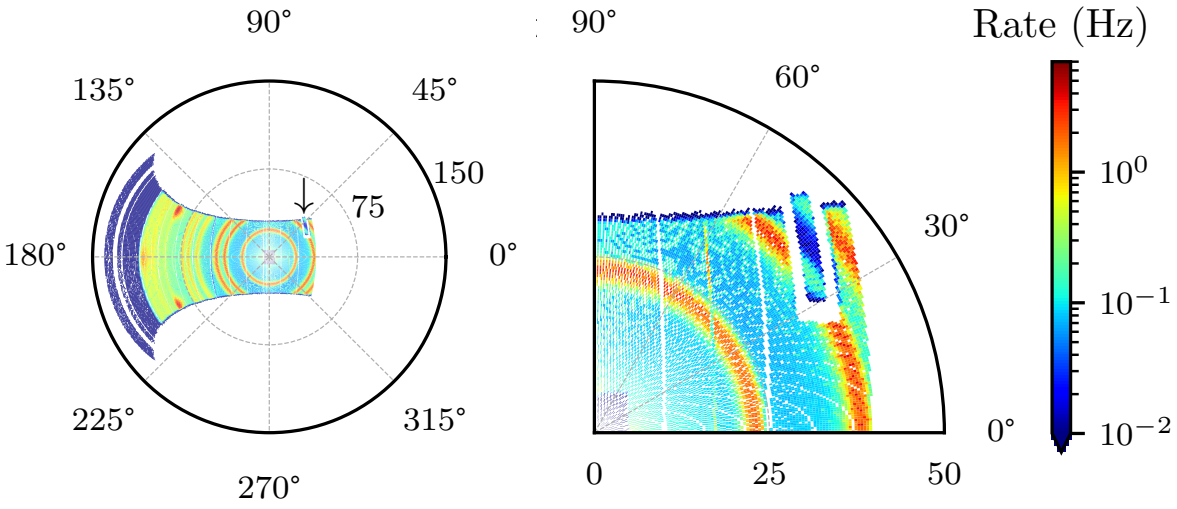

Figure 5.7: C_{60}, 2D histogram in a polar plot of helium-3 and the MG.LET data, showing the neutron hit positions in Φ (orientation around the centre in the plot) and Θ (distance from the centre in the plot). On the left, the full helium-3 array and Multi-Grid detector (highlighted with an arrow) are shown, while on the right a zoomed part is seen around the region where the Multi-Grid detector is located. The histograms are produced for data with tof values between 23.5 ms and 24.0 ms. The data from the helium-3 tubes located behind the MG.LET has been removed so the data in that region is not mixed.

Vanadium measurements

For the vanadium measurements, the chopper setting changed from white beam mode to monochromatic mode. The time-of-flight histograms produced by this setting on a vanadium sample are shown in figure 5.8. In the figure, the time-of-flight data corresponding to the five incident energies – 44.9 meV, 13.4 meV, 6.3 meV, 3.7 meV and 2.4 meV – is seen. The delimiters separating the peaks have been selected so that when the peaks are analyzed individually, only data related to the peak of interest is included.

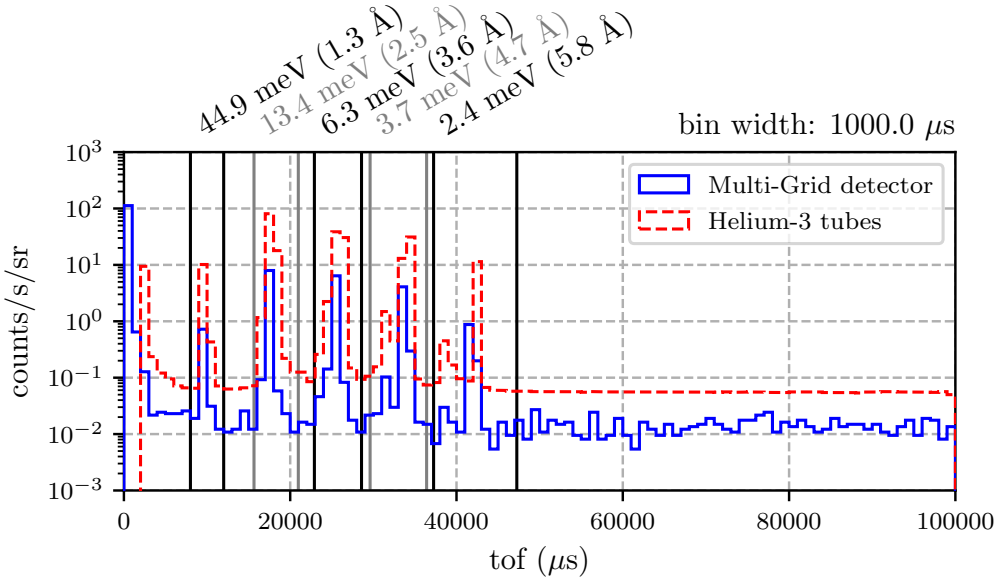

Figure 5.8: Time-of-flight histogram for the vanadium measurements, showing data from both the Multi-Grid detector (blue) and the helium-3 tubes (red). Data corresponding to the various incident neutron energies, shown on top, have been enclosed with multiple delimiters: each corresponding to a specific energy. The histograms are normalized to measurement duration and solid angle coverage for the respective detectors.

5.1.3 Inelastic scattering

To estimate the expected contribution from the inelastic scattering of vanadium – which constitutes a background in relation to the elastic peak in the current experiment – theoretical considerations are made. To estimate this contribution, it is first necessary to know which ($\mathbf{Q}$, $\hbar\omega$) range is used during the measurements, as this affects the scattering amplitudes. The relevant region is presented in 5.9, where the probed space is plotted for the different incident neutron energies used in this work. The reason MG.LET covers a smaller region than the helium-3 array is due to its smaller solid angle coverage, as seen in figure 5.7.

Next, it is noted that ^{51}V has less than 0.5% coherent scattering, as seen in table 1.1.2. This is because the b_+ and b_- cross-sections almost cancel out in the equation (1.16a), resulting in a very low coherent scattering cross-section. This effect counteracts the crystalline structure of vanadium, which would otherwise be beneficial for coherent scattering to occur. Hence, as natural vanadium is composed of 99.75 % ^{51}V, the metal can be approximated as a pure incoherent scatterer.

Based on this, the scattering profile of vanadium can be expressed as the incoherent partial

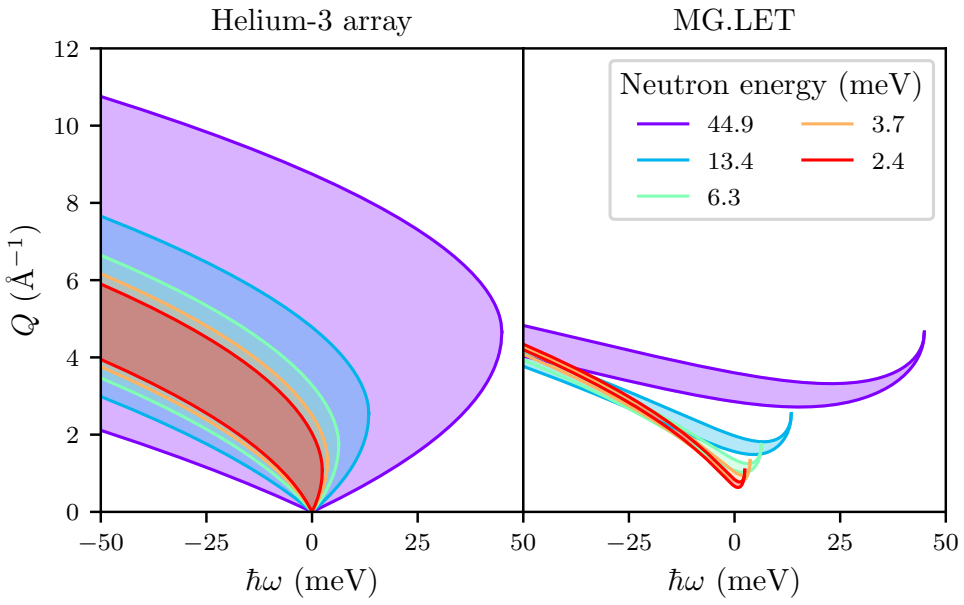

Figure 5.9: ($\mathbf{Q}$, $\hbar\omega$)-space covered by the helium-3 array (left) and the MG.LET (right) for the different incident neutron energies used during the measurements.

differential cross-section stated in equation (1.18b), namely

$$\left(\frac{\mathrm{d}^2\sigma}{\mathrm{d}\Omega\mathrm{d}E_\mathrm{f}}\right)_\mathrm{incoh} = \sigma_\mathrm{incoh}\frac{k_\mathrm{f}}{k_\mathrm{i}}N \cdot S_\mathrm{incoh}(\mathbf{Q},\omega). \tag{5.1}$$

To evaluate this expression, the first step is to approximate the incoherent scattering function $S_\mathrm{incoh}(\mathbf{Q},\omega)$. This is done by using the approximations outlined in [101], which states that the incoherent scattering function can be expressed as the summation below,

$$S_\mathrm{incoh}(\mathbf{Q},\omega) = \exp(-2W)\left[\delta(\omega) + 2W\frac{2\pi g(w)}{\gamma_0\omega[1-\exp(-\omega\hbar/k_bT)]} + \ldots\right] \tag{5.2}$$

where

$$2W = \frac{\hbar Q^2}{4\pi m_V}\gamma_0, \quad \gamma_0 = \int_0^\infty \coth\left(\frac{\omega\hbar}{2k_bT}\right)\frac{g(\omega)}{\omega}\,d\omega \tag{5.3}$$

and the parameters include the vanadium atomic mass m_V, the temperature T, the Boltzmann constant k_b and the vanadium phonon density distribution $g(\omega)$.

The first term in the summation corresponds to elastic scattering, while the second term and the dots relate to inelastic scattering. This is due to phonon interactions, where the second term corresponds to one-phonon interactions, and the dots represent the terms corresponding to two-phonon interactions and above. The higher phonon interactions are neglected here due to their low probability. Using this information, the incoherent scattering function can be separated into two components – one for elastic ($S^\mathrm{el}_\mathrm{incoh}$) and

one for inelastic scattering ($S^{\text{inel}}_{\text{incoh}}$) – according to

$$S^{\text{el}}_{\text{incoh}}(\mathbf{Q},\omega) = \exp(-2W)\cdot\delta(\omega) \tag{5.4a}$$

$$S^{\text{inel}}_{\text{incoh}}(\mathbf{Q},\omega) = \exp(-2W)\cdot 2W\frac{2\pi g(\omega)}{\gamma_0\omega[1-\exp(-\omega\hbar/k_bT)]} \tag{5.4b}$$

To obtain the inelastic intensity distribution, $I^{\text{inel}}_{\text{incoh}}(E_{\text{i}},2\theta,\hbar\omega)$, the last step is to insert equation (5.4b) into equation (5.1). However, to make the distribution more easily comparable to measurement data, a similar procedure as outlined in [102] is followed. This entails normalizing the inelastic intensity by the elastic intensity $I^{\text{el}}_{\text{incoh}}(E_{\text{i}},2\theta)$ – obtained by inserting equation (5.4a) into equation (5.1) and then integrating over E_{f} – according to,

$$\begin{aligned} R &= \frac{I^{\text{inel}}_{\text{incoh}}(E_{\text{i}},2\theta,\hbar\omega)}{I^{\text{el}}_{\text{incoh}}(E_{\text{i}},2\theta)} \\ &= \left(\frac{\mathrm{d}^2\sigma}{\mathrm{d}\Omega\mathrm{d}E_{\text{f}}}\right)^{\text{inel}}_{\text{incoh}}\cdot\left[\int_0^\infty\left(\frac{\mathrm{d}^2\sigma}{\mathrm{d}\Omega\mathrm{d}E_{\text{f}}}\right)^{\text{el}}_{\text{incoh}}dE_{\text{f}}\right]^{-1} \\ &= \frac{k_{\text{f}}}{k_{\text{i}}}\cdot\frac{\hbar Q^2}{m_V}\cdot\frac{g(\omega)}{\omega[1-\exp(-\omega\hbar/k_bT)]} \end{aligned} \tag{5.5}$$

where R is the ratio between inelastic and elastic scattering. Hence, the inelastic intensity can be calculated by multiplying R with the obtained elastic intensity in the data according to $I^{\text{inel}}_{\text{incoh}}(E_{\text{i}},2\theta,\hbar\omega) = R\cdot I^{\text{el}}_{\text{incoh}}(E_{\text{i}},2\theta)$. Note that this approximation assumes that the incident neutron pulse on the vanadium is monochromatic, which is not the case due to the finite resolution of real instruments and other background contributions. To account for the effect of elastic peak breadth, more calculations are needed to account for the consequent broadening in the inelastic features. Nevertheless, the expression estimates the magnitude of inelastic distribution surrounding the elastic peak, which is useful to know when evaluating the maximum signal-to-background level – i.e. elastic to inelastic ratio – expected in the data when all other instrumental sources of background have been removed.

At this point, the only remaining unknown is the phonon density distribution $g(\omega)$. This contains the information on what vibrational states are available as a function of energy – as exemplified in the introduction in figure 1.6 – and is approximated using data from [101], which is presented in figure 5.10. In the medium energy region, the data is used directly for the vanadium scattering calculations. However, for the low- and high-energy regions other considerations are made. At the low-energy region, the phonon density distribution behaves as $g = ax^2$ [101], and this is the approximation used here. For the high-energy region, the phonon density is set to 0. This is because there is an upper limit on the

frequency which the vanadium lattice can vibrate with, called the cut-off frequency. This corresponds to around 33 meV, and above that $g = 0$.

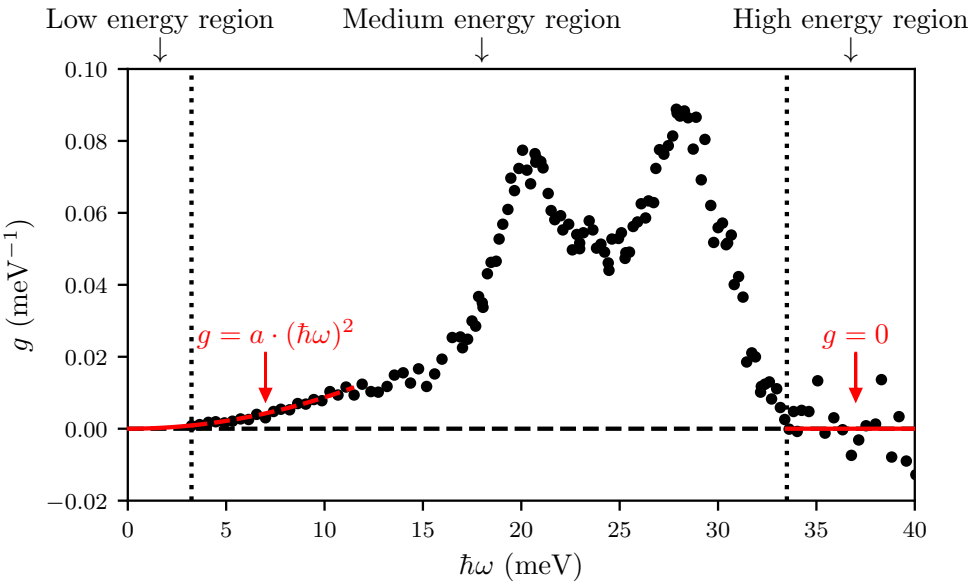

Figure 5.10: Vanadium phonon distribution, where the data is presented in black and the approximations at the high and low regions are shown in red. The data used for the fitted function is covered by the dotted red line. Data is taken from [101].

Using the phonon density distribution, it is now possible to extract the vanadium scattering distribution. This is presented in figure 5.11, where the normalized inelastic scattering is presented for different temperatures. On the left-hand side – neutron energy gain – the

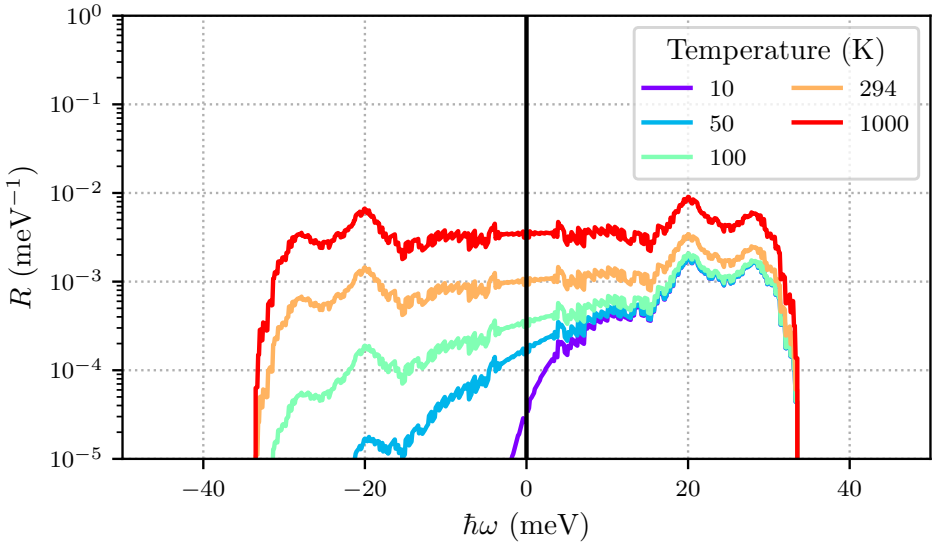

Figure 5.11: Calculated inelastic scattering normalized by elastic scattering, R, of vanadium for different temperatures. In this example, $E_i = 50$ meV and $2\theta = 40$ were used to generate the plots. The elastic scattering is illustrated as a black vertical line at $\hbar\omega = 0$.

interaction cross-section is seen to diminish with temperature. This is because, at low temperatures, there is less vibrational energy for the neutron to pick up, and hence a lower probability of this happening.

5.1.4 Intrinsic background

Another important aspect to consider when probing signal-to-background ratios is the effect of the intrinsic background, i.e. the rate of events registered in the detector when there is no external radiation present. To estimate this, it is first assumed that the background events are randomly distributed in time and across the detection volume. After that, it is examined – for each incident neutron energy received at LET – how this is recreated in energy transfer spectra. In figure 5.12, an example of 2.4 meV incident neutrons is shown for the full LET helium-3 array. To generate the plot 10^7 random events were produced, each with a random tof within 0 μs $\leq$ tof $\leq$ 10^5 μs and a random pixel hit position in the helium-3 tube array. This gives an estimate of the shape that the background contribution adds to the energy transfer spectra. In the plot, the resulting energy transfer spectra using only tof values within the delimiters for 2.4 Å, see figure 5.8, are presented in red. The reason for the drop in counts at high energy transfer values for the red data is because these events have been removed via the tof delimiters in the top left plot.

Using the above background estimation, β_{raw}, the next step is to make it comparable to measurement data. This is done by normalizing the distribution according to,

$$\beta_{\text{norm}}(\hbar\omega) = \beta_{\text{raw}}(\hbar\omega) \cdot \frac{1}{\text{sum}(\beta_{\text{raw}}(\hbar\omega))} \cdot f \cdot \frac{1}{bw}, \tag{5.6}$$

where $\text{sum}(\beta_{\text{raw}}(\hbar\omega))$ is the sum of the generated histogram, bw is the bin width in meV, and f is the fraction of all generated events that were reconstructed in the observable $\hbar\omega$-range. The first factor ensures that the total counts in the generated histogram are normalized to 1, which is then modified by the factor f because not all generated background events were reconstructed in the $\hbar\omega$ spectrum. Finally, the factor bw^{-1} takes into account binning effects and sets the unit of β_{norm} to meV^{-1}. Hence, to make the generated background curve comparable to measured data, the only remaining step is to scale it with the bin width used to generate the histogram which should be compared.

Using the acquired background estimation distribution, the impact of a specific detector background condition can be examined. This done according to equation (5.7),

$$\beta(\hbar\omega) = \beta_{\text{norm}}(\hbar\omega) \cdot r \cdot A \cdot t \cdot bw_{\text{hist}} \tag{5.7}$$

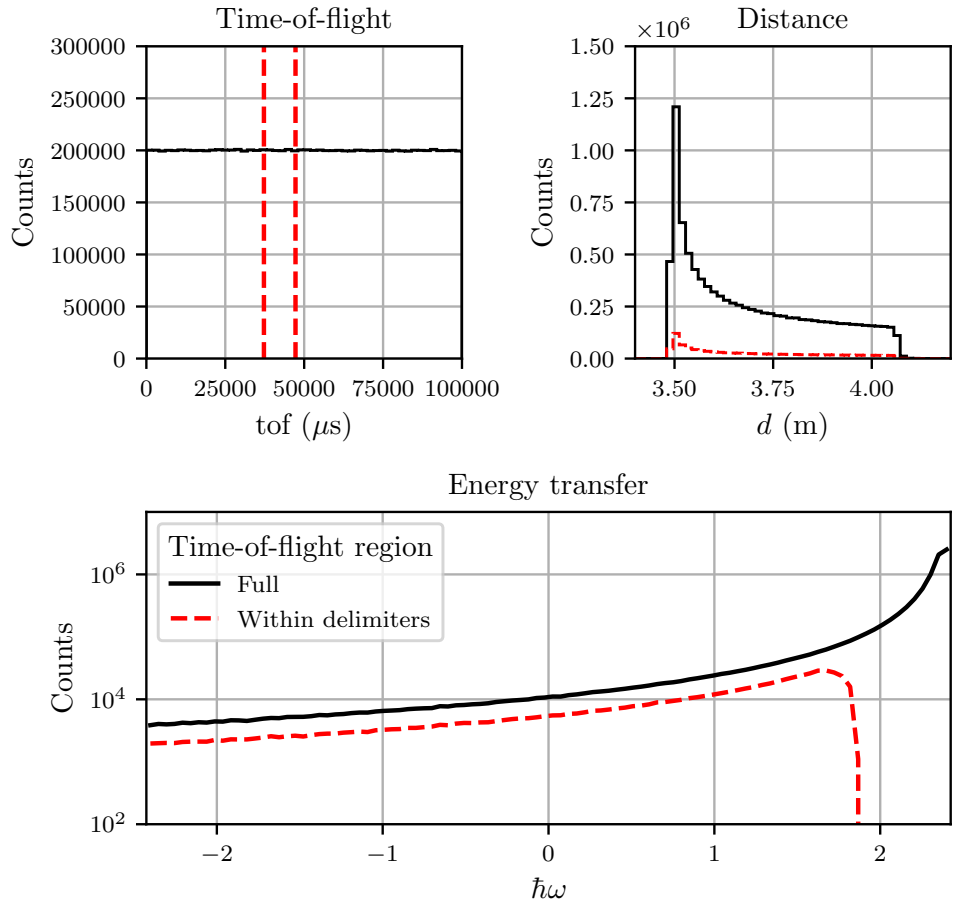

Figure 5.12: Estimated background distribution from full helium-3 array, using 2.4 meV incident neutrons as an example. In the top two plots, the generated tof values (left) and d values (right) are shown, while at the bottom the resulting energy transfer spectrum is presented. Data within tof delimiters used for 2.4 Å (see top left) are presented in red.

where $\beta(\hbar\omega)$ is the background estimation as a function of $\hbar\omega$, r is the background rate of the detector in Hz/m^2, A is the area of the detector in m^2, t is the measurement duration in s and bw_{hist} is the bin width in meV for which the intensity of the background is to be examined.

5.1.5 Signal-to-Background

Due to the low efficiency encountered in the MG.LET during the measurements, a relatively large bin width – comparable to the FWHM of the elastic peak – is necessary to get adequate statistics in each bin. This will affect the signal-to-background ratio seen in the data, due to an asymmetry in how the data is distributed in the elastic peak and the background. To quantify this effect, an ideal Gaussian distribution is plotted on top of a flat background, as shown in figure 5.13. In the left plot, the effect of using different bin widths is presented, while in the right plot the resulting signal-to-background ratios –

defined as the peak maximum over background level – as a function of bw/FWHM (bin width divided by the FWHM of the Gaussian). As can be seen in the plot, the signal-to-background ratio can drop by around 1 order of magnitude as a consequence of bin width choice.

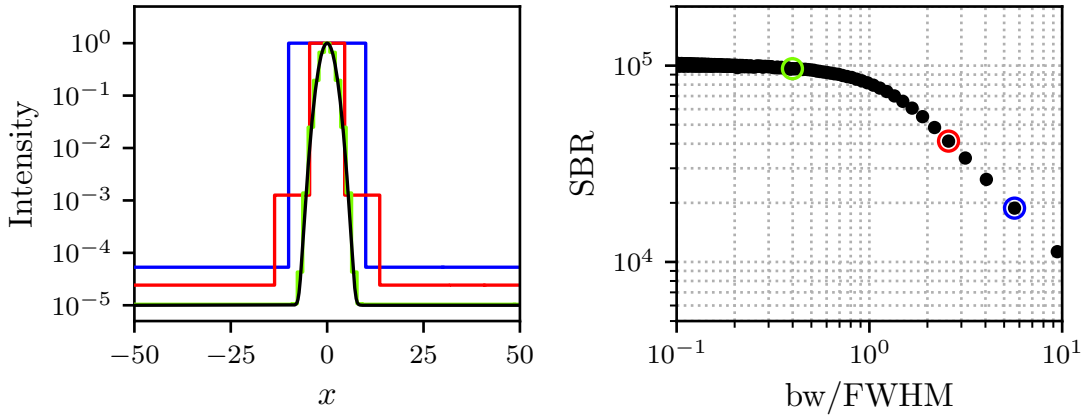

Figure 5.13: Relative SBR dependence on bin width. To the left, a Gaussian distribution over a flat background (black) is plotted together with the histograms of this distribution for different bin widths (various colours), all normalized to peak maximum. To the right, the SBR – peak maximum over background level – is seen as a function of bin width (bw) normalized by the FWHM of the Gaussian distribution. The total number of bins is always odd in this study, such that there is always a bin centred at the location of the Gaussian peak.

To examine how distributions with different SBR are affected by varying the bin width, the same analysis as above is done for three different distributions – ranging from SBR=10^3 to SBR=10^5 – as presented in figure 5.14. As can be seen, the relative SBR between the distributions does not change with bin width. Hence, conclusions about SBR comparisons between the MG.LET and helium-3 tubes can still be drawn, even though a wide bin width is used.

As might be expected, this means that the relative signal peak height in relation to the background is not an absolute measurement of detector quality and instrumentation. Rather, it is a function of bin width. The integral of the signal compared to the integral of the background, on the other hand, would indicate the quality of the measurement.

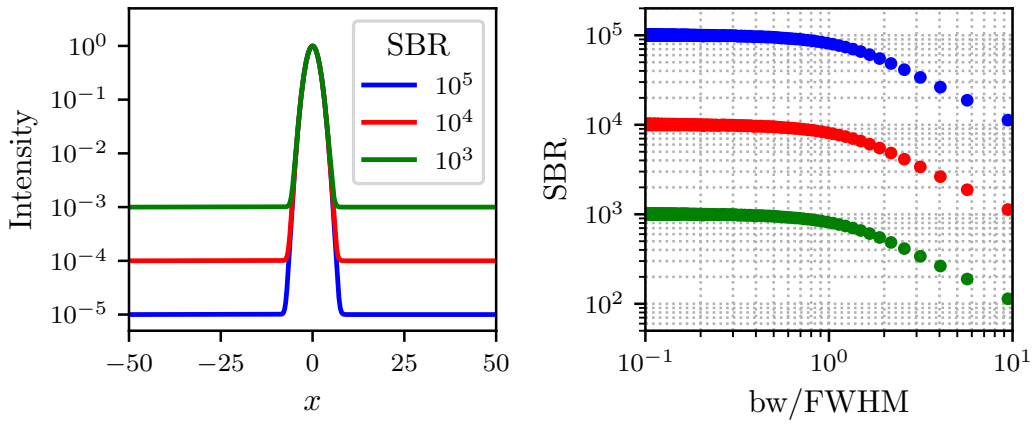

Figure 5.14: Relative SBR dependence on bin width for different distributions. To the left, three identical Gaussian distributions are seen over three different flat background levels (blue, red and green). To the right, the SBR – peak maximum over background level – for these distributions are seen as a function of bin width (bw) normalized by the FWHM of the Gaussian. The total number of bins is always odd in this study, such that there is always a bin centred at the location of the Gaussian peak.

5.2 Analysis & Results

The first step in the analysis is to determine the neutron energies in each of the neutron pulses produced by the chopper system. This is done by assuming elastic scattering and performing an energy calculation on the recorded neutron events, as seen in figure 5.15. For each acquired peak, the centre energy is approximated as the incident neutron energy. The difference in statistics is due to the lowered efficiency in the Multi-Grid detector during the measurements – which is discussed in more detail later – as well as the larger solid area coverage of the helium-3 tube array, previously shown in figure 5.6. Concerning the energy reconstruction, a good agreement is seen in the peak alignment for the two detectors, which are seen to overlap well when using the 0.05 meV bin width in figure 5.15.

Using incident neutron energies, the ($\mathbf{Q}$, $\hbar\omega$)-spectra can be plotted for each neutron pulse received. An example of this is shown in figure 5.16, where the spectra for 45 meV incident neutrons are plotted. However, as the focus of this work is to study the energy lineshape and signal-to-background ratio, only energy transfer spectra will be considered in the remainder of this work. The first part of this study is presented next, where the lineshape is investigated. The Multi-Grid data is extracted and reduced the same way as was done during the V20 measurements, the only difference is that a slightly lower discriminator threshold – 550 ADC channels – is used here.

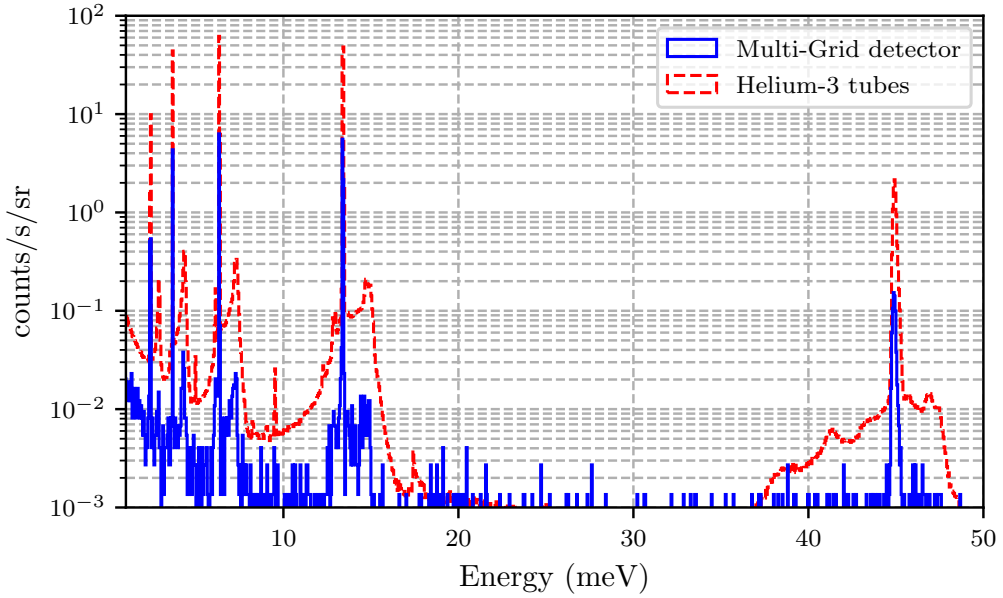

Figure 5.15: Vanadium measurement, energy spectra produced with the Multi-Grid detector (blue) and helium-3 tubes (red). The y-axis is normalized to measurement duration and solid angle coverage.

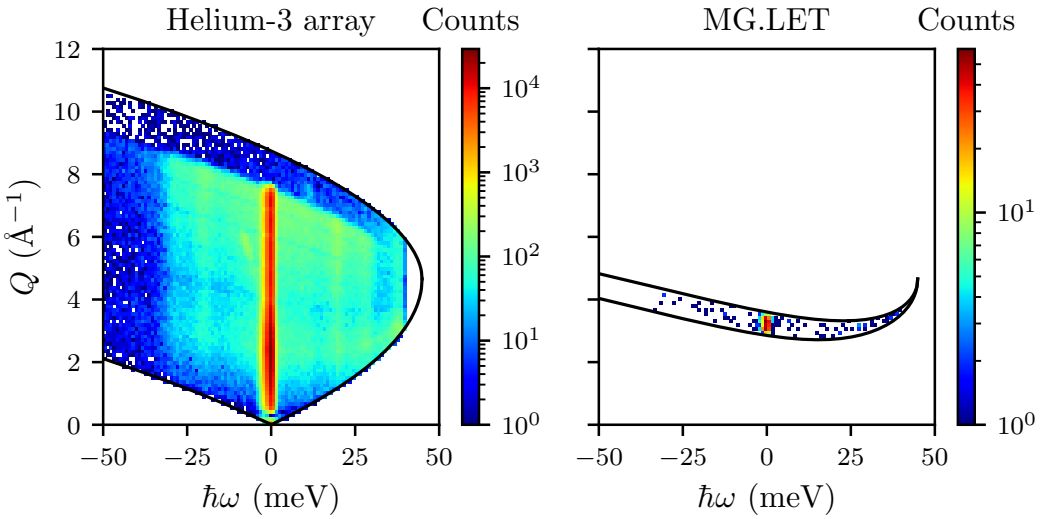

Figure 5.16: Vanadium ($\mathbf{Q}$, $\hbar\omega$)-spectra acquired with Helium-3 array (left) and MG.LET (right) for 44.9 meV (1.3 Å) incident neutrons. The solid black lines indicate the region which can be probed.

5.2.1 Lineshape

Using the incident neutron energies, the energy transfer for each of the five neutron pulses is calculated. This is presented in figure 5.17, where each row shows the energy transfer spectra for a specific incident neutron energy. To make the data as comparable as possible

between the MG.LET and helium-3 tubes, the histograms presented for the helium-3 tubes are based on data from an MG.LET-sized region of the helium-3 array located at the same polar angle as the MG.LET with respect to the sample.

As seen in the left column in the figure, the Multi-Grid detector and helium-3 tubes are seen to follow well around the top of elastic peaks. This is further emphasized by comparing the FWHM of the peaks, as presented in figure 5.18. Any comparison concerning lineshape at the base of the peak, the region of interest for QENS, is however inconclusive with this bin width due to insufficient statistics. If a wider bin width is used, averaging data over larger regions in the energy transfer spectra, then the area around the elastic peak is easier to compare between the detectors. This is presented in the right column, where the same data is presented as previously but with a wider binning and a larger energy range. As can be seen, the two detectors follow well within statistics.

In the right column of the figure, there are also theoretical predictions of inelastic vanadium scattering and the effect of intrinsic background in the helium-3 tubes. The calculations of these effects are not meant to follow the observed data precisely: only to estimate their respective contribution to the spectra. For example, for the two highest energies – 44.9 meV and 13.4 meV – significant inelastic scattering from vanadium is seen, which accounts for a large portion of the distribution around the elastic peak. This is an important effect to consider, as it limits the maximum signal-to-background which can be probed with vanadium at this incident neutron energy and sample temperature. This is in contrast to the lowest energy measured – 2.4 meV – where instead the intrinsic background level is predicted to limit the signal-to-background available. The calculated background level of the helium-3 array was based on the background rate of 0.04 Hz/m^2.

To investigate systematic uncertainties, the energy transfer was calculated based on data from three different regions of the LET helium-3 tube array and compared to the Multi-Grid detector, as presented in figure 5.19. This was to investigate if there were any important angle-dependent effects which should be accounted for. In the figure, the energy spectra are based on data from the full array (red), based on an MG.LET-sized region of the helium-3 array located at the same polar angle as the MG.LET (green) and a region of the helium-3 tubes in the close vicinity of the MG.LET (pink) was compared. The investigation showed a similar spectrum for all regions probed, confirming the expected incoherent scattering from the vanadium sample. As can also be seen, the energy line shape follows well between the helium-3 tubes and the MG.LET within statistics for most incident energies. The exception is the statistically significant deviation on the right-hand side of the peak at 13.4 meV, where a small bump in the MG.LET distribution is seen.

Another important observation concerns the line shape obtained with 3.7 meV incident neutrons in figure 5.19. This spectrum can be compared to a previous result with the earlier MG.CNCS prototype at SNS [9] – as presented in figure 5.20 – which were also collected using a vanadium sample with a similar incident neutron energy. Furthermore, because the sample-to-detection distances are comparable between the two measurements ($\sim$ 3.5 m), any impact on the energy lineshape due to internal scattering would be observable at the same location in the energy transfer spectra. Together with the similar width of the obtained energy peaks, this makes the data sets suitable for comparison. In the CNCS spectrum, clear shoulders on the elastic peak were seen in the Multi-Grid data which were absent in the helium-3 data. In the present spectrum, in contrast, no such shoulders are visible within statistics.

As the obtained peak width and shape is similar between the two measurements – and the signal-to-background ratio is sufficient in the current measurement to resolve the previously seen shoulders – a similar structure at the sides of the peak would have been observed with the MG.LET if it had a detector-dependent energy smearing similar to that previously seen. As this is not the case, however, we can conclude that the MG.LET does not have an intrinsic energy broadening as seen during the CNCS measurements. This can be stated even though the statistics are lower in the current study since the previously seen distribution (black) is significantly above the top of the statistical uncertainties (blue error bars) presented on a bin-by-bin basis on the LET data. Hence, an improvement in energy line shape reconstruction has been achieved with the MG.LET, and it is broadly consistent with that of the helium-3 detectors installed on LET.

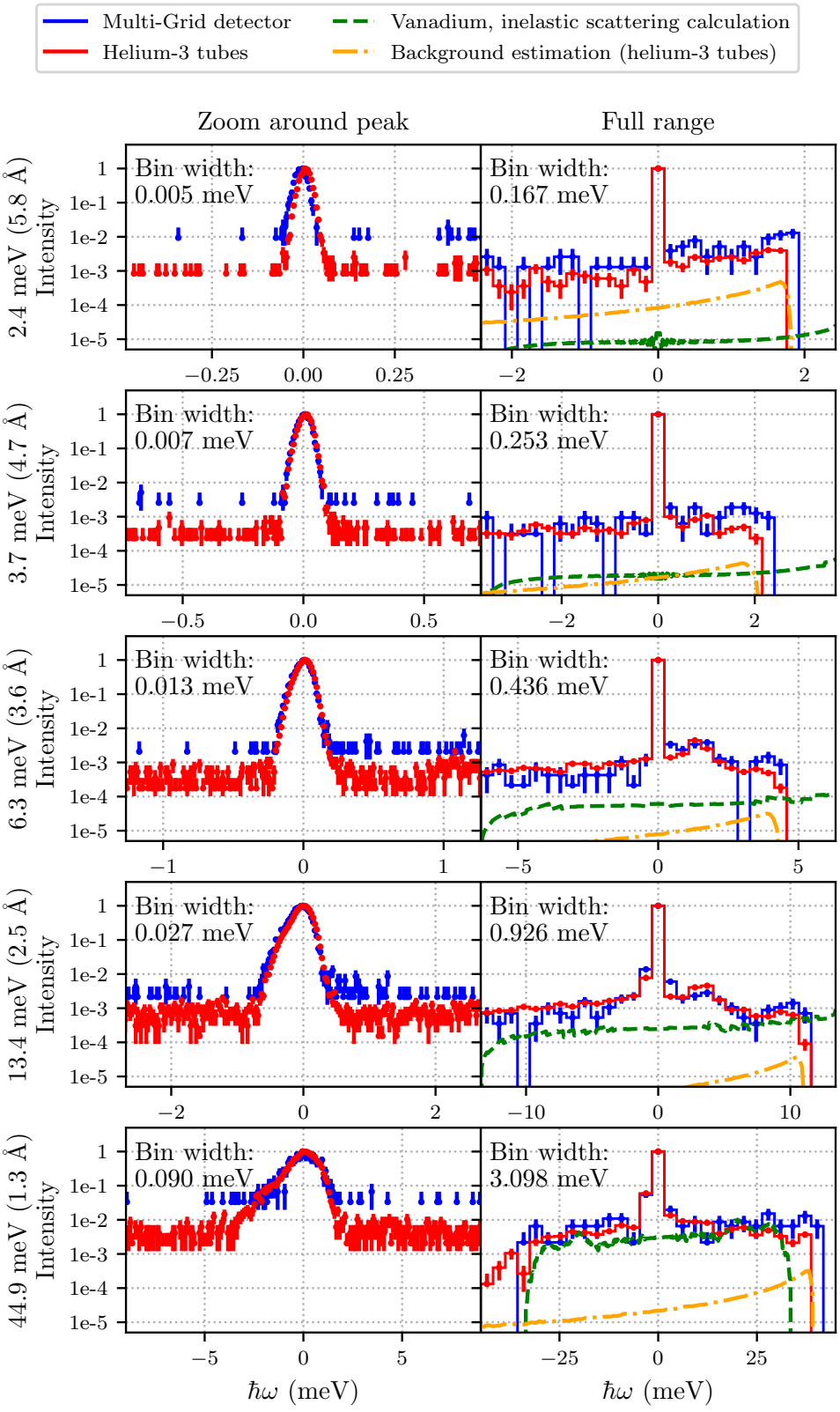

Figure 5.17: Vanadium, energy transfer plots comparing the Multi-Grid detector (blue) and helium-3 tubes (red). The left column shows a zoom around the peak and the right column shows the full range, while each row corresponds to a specific energy. In the right column, there are also estimations of the inelastic vanadium scattering and the background contribution for the helium-3 tube. The y-axis shows counts normalized to the peak maximum and statistical uncertainties are shown as error bars.

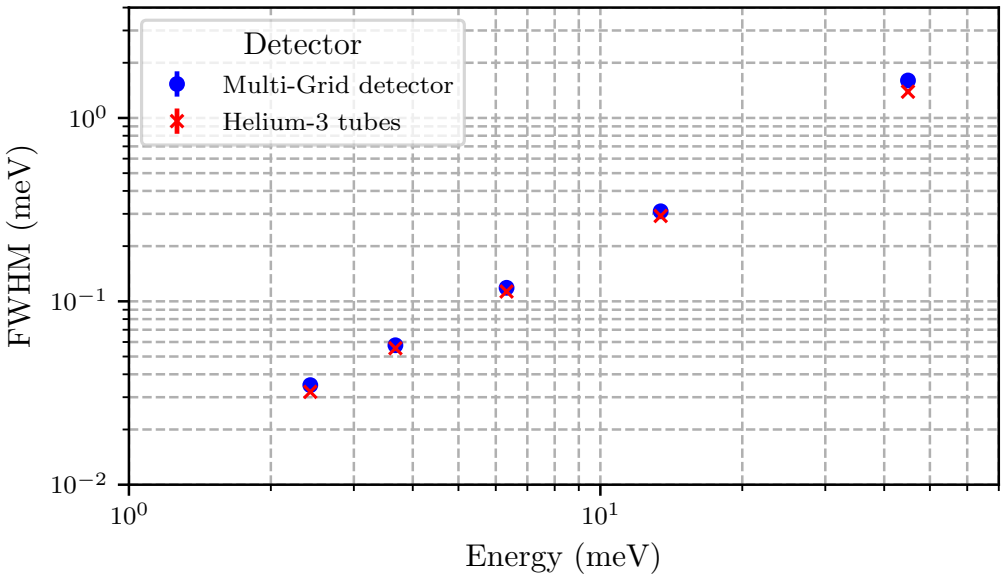

Figure 5.18: Energy resolution of the Multi-Grid detector (blue) and helium-3 tube array (red) during the LET measurements. The fit uncertainties are shown in the error bars but are too small to be discernible.

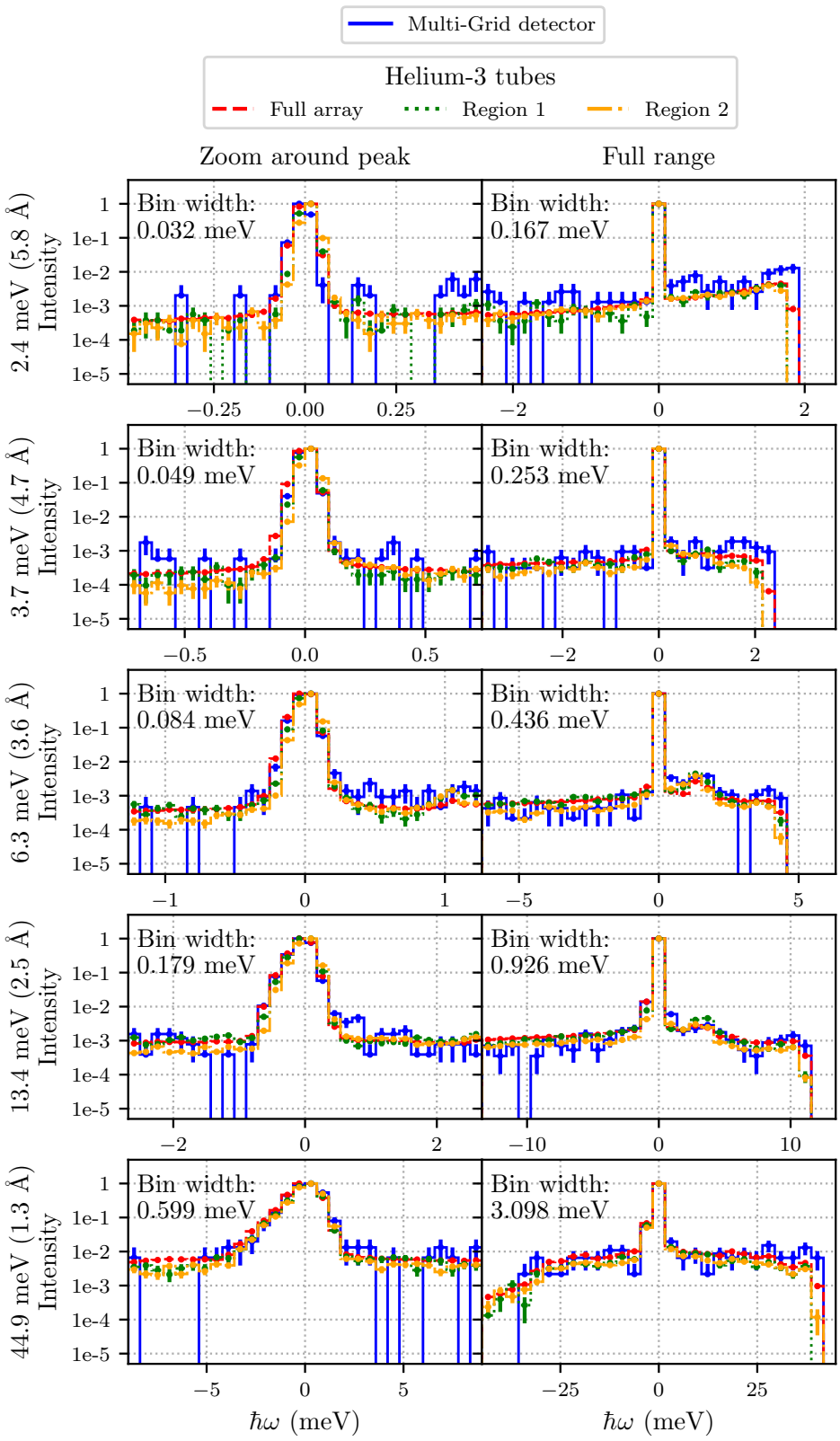

Figure 5.19: Vanadium, energy transfer plots comparing the Multi-Grid detector (blue) and three different regions of the helium-3 tube array. This includes the full array (red), an MG.LET-sized region of the helium-3 tubes at the same polar angle (green) and a region of the helium-3 tubes immediately surrounding the MG.LET (orange). The y-axis shows counts normalized to the peak maximum and statistical uncertainties are shown as error bars.

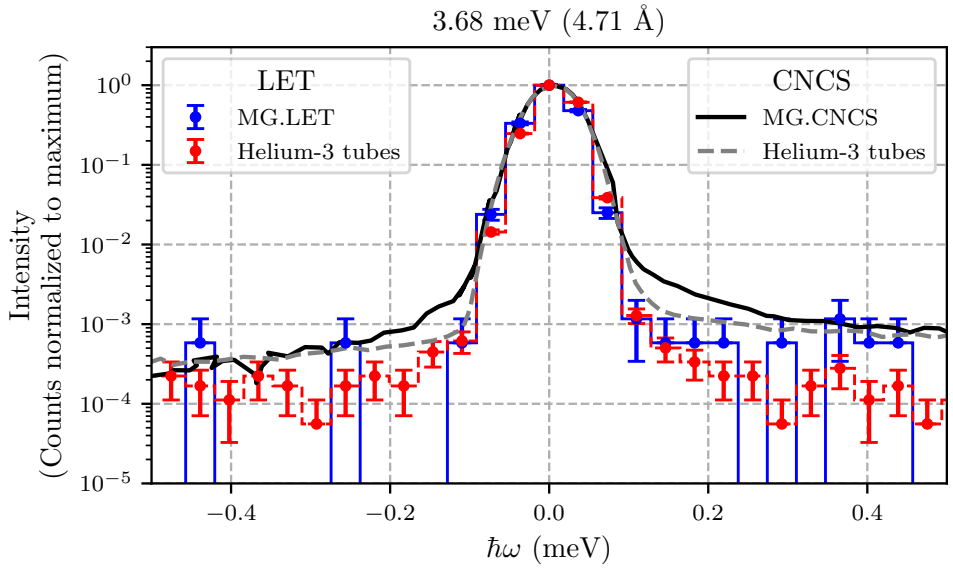

Figure 5.20: Vanadium scattering at 3.68 meV (4.71 Å), showing a comparison between data from the CNCS (black and grey) and LET (blue and red), where statistical uncertainties are shown as error bars. Note that the bin width is different between the two measurements. CNCS data taken from [9].

5.2.2 Detection efficiency

After the beamtime, a series of follow-up diagnostic measurements were conducted to understand the low counting efficiency in the MG.LET. First, a series of background measurements with the detector was performed outside the detector workshop area at ISIS with a short 10 cm long helium-3 tube running in parallel, acting as a reference. During the measurements, two different Ar-CO_2 gas bottles were used. The first was the bottle used during the measurements, bottle 1, while the second was a newly acquired Ar-CO_2 bottle, bottle 2. To perform the investigation, the detector was first flushed with gas from bottle 2, whereafter the gas supply was replaced with bottle 1. This measurement was then repeated with a weakly moderated ∼34 GBq ^{241}AmBe source, which gives better statistics. Again, the helium-3 tube was used as a reference and two measurements were conducted: one for each gas bottle. Bottle 2 was used at the start and then changed to bottle 1. The results of the two measurements are presented together in figure 5.21. The timing of the gas change is annotated in the figure.

As seen in figure 5.21, a strong dependence on the supplied gas was ascertained. When gas bottle 2 (the new supply) is replaced with gas bottle 1 (gas used during the measurements) the rate drops by more than a factor of 10 in the first measurement and a factor of 6 in the second measurement. To ensure this effect is not related to changes in the background environment at the facility, the rate in the helium-3 reference detector was examined. As can be seen, the rate in the helium-3 tube is constant over time – with the important exception of the accelerator-related background change highlighted in the plot – and does not follow the rate change seen in the Multi-Grid detector. Therefore, the changes seen can be attributed to the gas change.

To further investigate why this discrepancy in response occurred, a gas chromatography analysis was performed at ISIS. The results showed that the gas bottle used during the measurements contained 2.5 % oxygen, which was not present in the new gas bottle. Oxygen is an electronegative molecule, which means – as discussed in the introduction – that it can capture electrons. Once electrons have been captured, they cannot contribute to the avalanche production. Hence, having oxygen in the gas mixture reduces the strength of the avalanches, which can have a negative effect on the detector's effectiveness in registering the products of the neutron capture reaction, and thus the overall detection efficiency. It was therefore surmised the cause of the reduced detection efficiency was the oxygen.

To confirm that oxygen indeed had this effect on the Multi-Grid detector, a follow-up measurement was conducted at the ESS detector lab Utgård. This was done by conducting a background measurement with the Multi-Grid detector and a helium-3 tube – which, again, was used as a reference – side-by-side. During the measurement, two types of gases

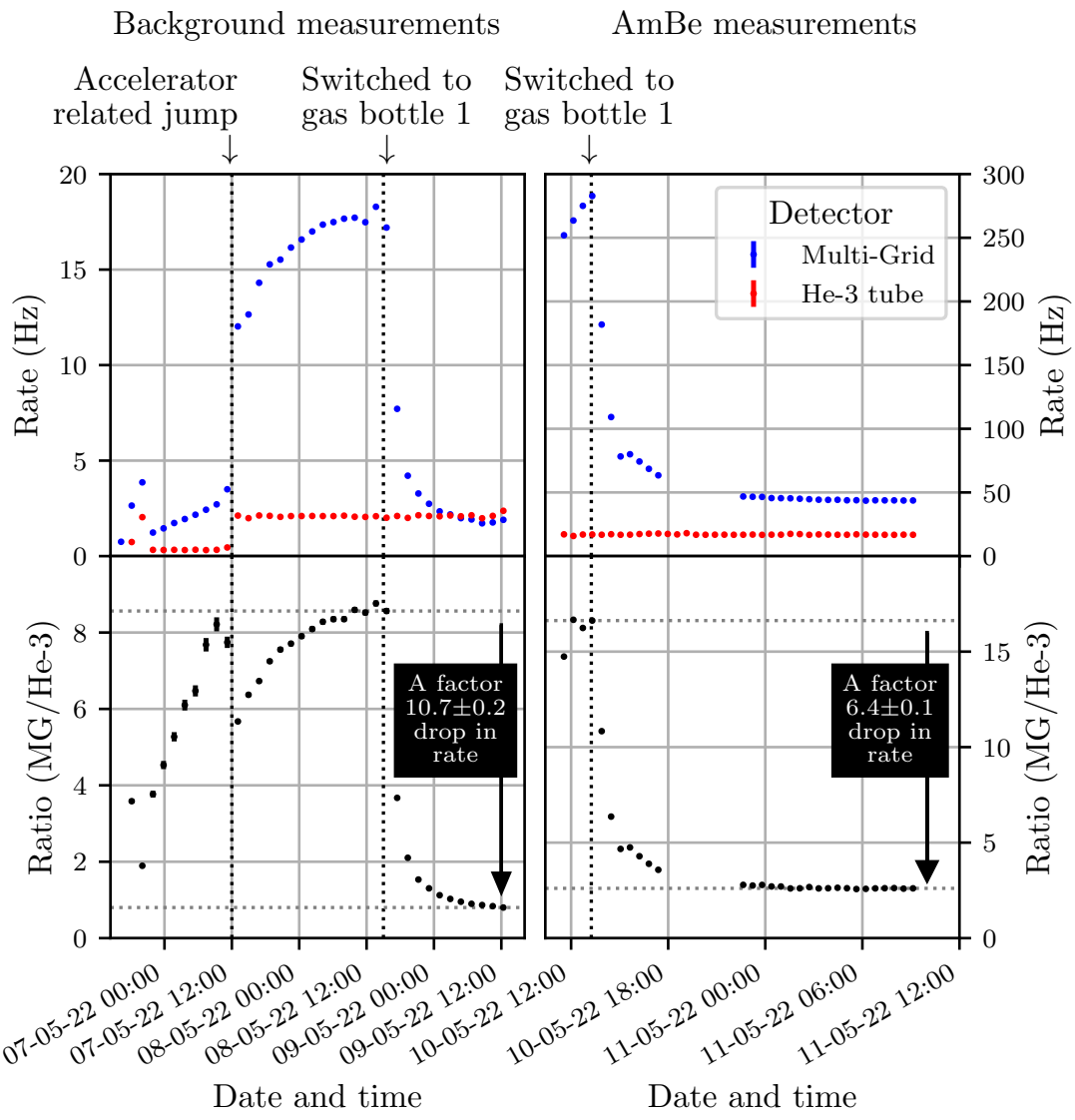

Figure 5.21: Background (left) and AmBe (right) measurements performed at ISIS, showing the recorded rate in the Multi-Grid detector (blue) and helium-3 tube (red), as well as the ratio (black). On the x-axis, the date and time are shown. The annotations highlight important events. Statistical uncertainties are shown as error bars.

were used: one with scientific grade Ar-CO_2 gas (82 % Ar + 18 % CO_2) and one with a custom-made gas mixture (74 % Ar + 24 % CO_2 + 2 % O_2). The results are presented in figure 5.22, where the strong dependence on gas supply was replicated. As can be seen, running with oxygen-contaminated gas reduces the efficiency by more than an order of magnitude. It can therefore be concluded that the low detection efficiency encountered during the measurements was due to the oxygen in the gas.

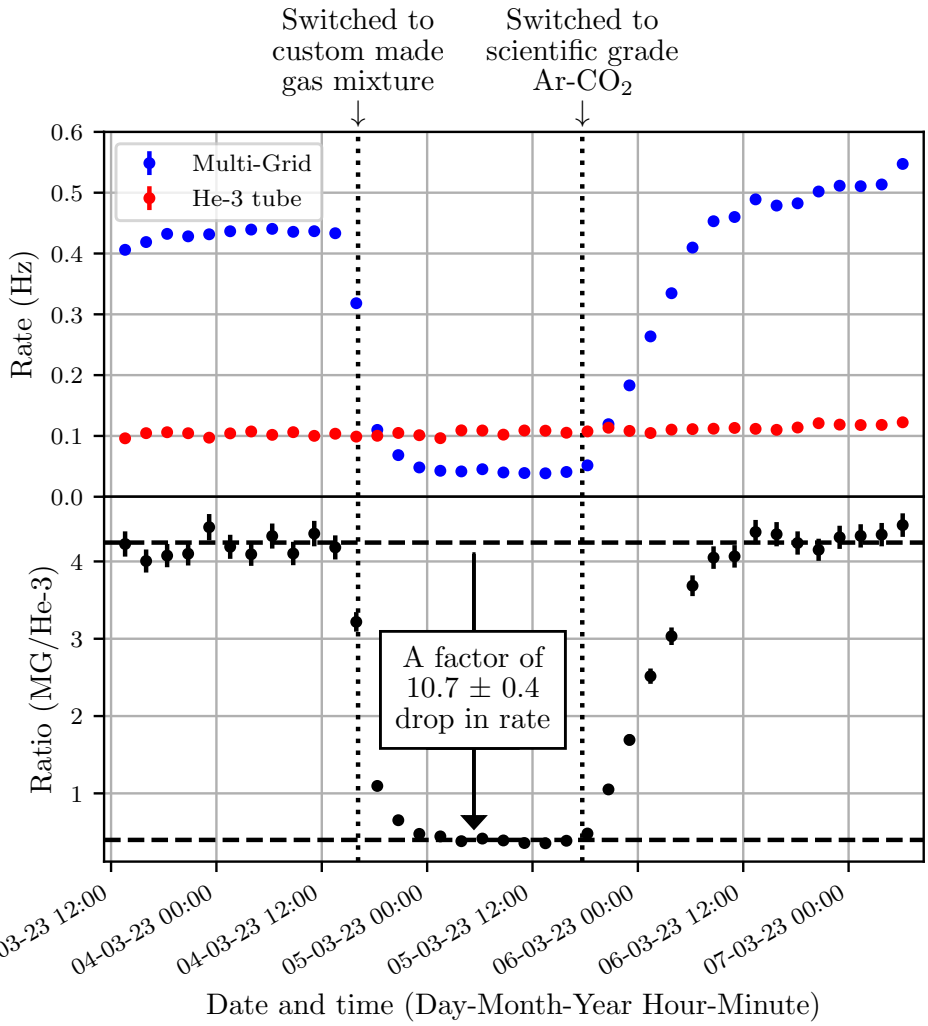

Figure 5.22: Background rate measurement in the ESS detector lab Utgård. At the top, the recorded rate in the Multi-Grid detector (blue) and helium-3 tube (red) is shown as a function of time. At the bottom, the fractional rate – Multi-Grid detector over helium-3 tube – is presented. The time of gas change is annotated and statistical uncertainties are shown as error bars.

5.2.3 Signal-to-Background

Using the obtained scaling factors from the previous section, the signal strengths of the Multi-Grid detector and helium-3 tubes can now be compared. To do this, data from an MG.LET-sized region of the helium-3 array – at the same polar angle as the Multi-Grid detector – is used for comparison. This is then normalized by measurement duration and solid angle coverage, as presented in figure 5.23. In the figure, both the default data from the MG.LET (blue) and the scaled data (light blue) are compared to the helium-3 tubes. For this comparison, the scaling factor of 10.7 was used. This is because – studying figure 5.21 – the MG.LET rate during the AmBe measurements (top right plot in the same figure) does not appear to have fully saturated at the time of gas change. This is further

validated by the measurements at Utgård, see figure 5.22, which also indicates a drop in rate of around a factor of 10.

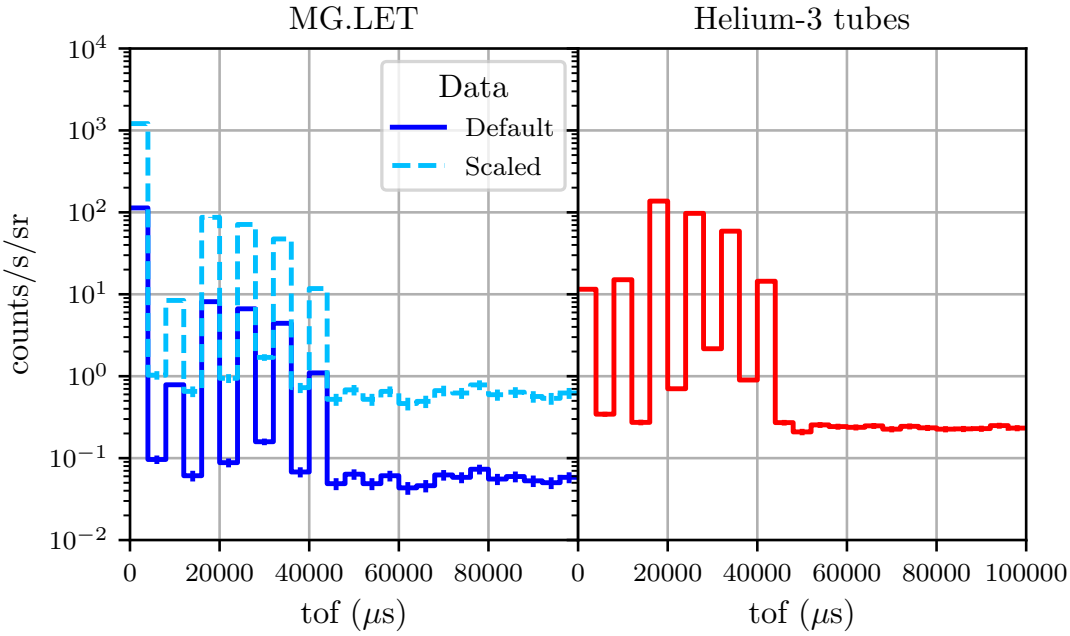

Figure 5.23: Time-of-flight spectra comparing the MG.LET (left) and the helium-3 tubes (right). In the left plot, the MG.LET data is presented as the default (blue) and scaled by a factor of 10.7 (light blue). Data in the helium-3 array is taken from an MG.LET-sized region at the same polar angle. Statistical uncertainties are shown as error bars but are in most cases too small to be discernible.

As can be seen in figure 5.23, when the scaling factor is applied the rate in the MG.LET is more comparable to the helium-3 array. However, to make a more detailed study of the neutron detection efficiency – such as was done during the V20 measurements – a more advanced analysis is necessary which is beyond the scope of this work. Furthermore, as the scaling factor was obtained from a measurement in a different radiation environment than that inside the LET instrument, there might be further effects which have to be accounted for to get a more accurate comparison.

To evaluate the signal-to-background criteria, as seen in table 2.1, a peak at around 5 Å is examined in tof spectra. This is presented in figure 5.24, which shows both the peak shape (top) and background level (bottom) for both the MG.LET and the helium-3 tubes as a function of tof. Note that the bin width is different between the top and bottom plots, which has been tuned to the difference in statistics in the signal and background parts of the spectra. To account for this effect both spectra are normalized with the bin width (bw). As seen in the figure, both the Multi-Grid detector and helium-3 tubes achieve in the order of 10^3 signal-to-background ratios: SBR = 849 ± 55 for the MG.LET and SBR = 3080 ± 84 for the helium-3 tubes.

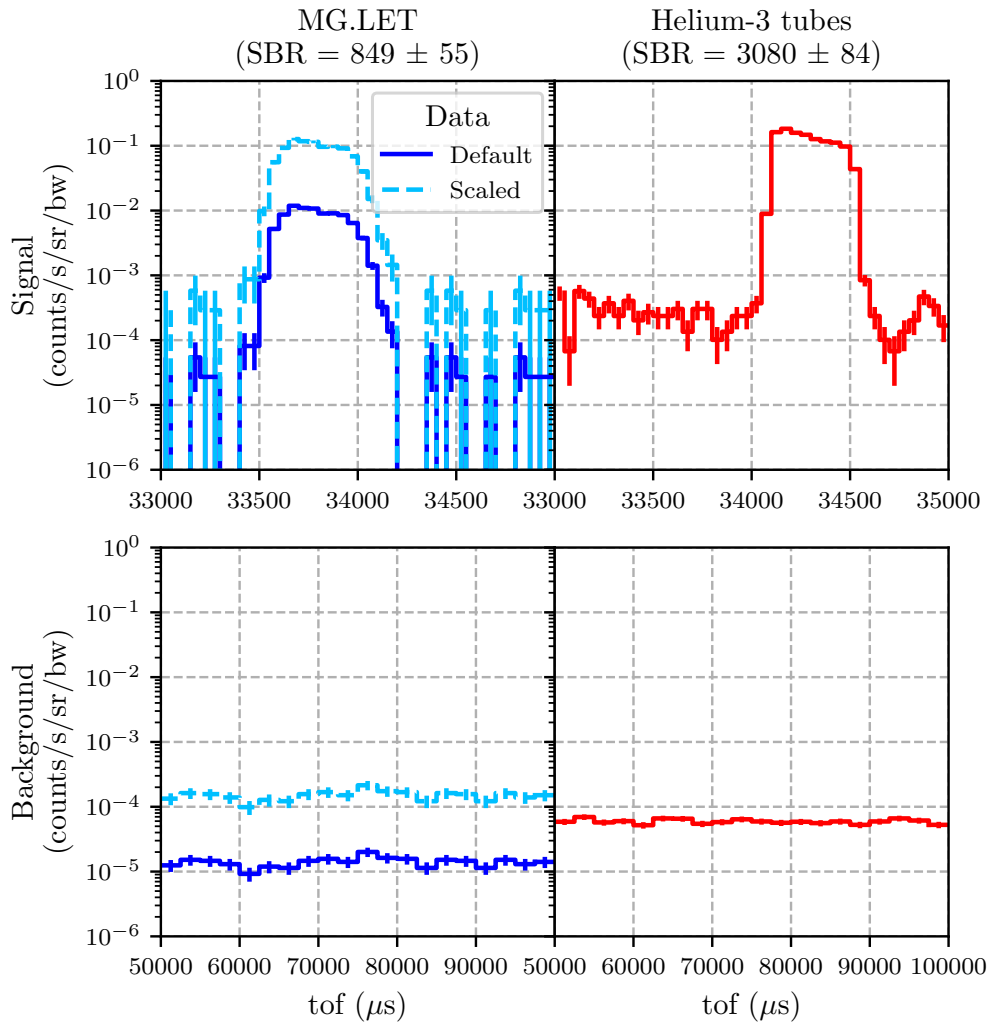

Figure 5.24: Signal-to-background comparison between the MG.LET (blue and light blue) and helium-3 tubes (red). At the top, the tof-spectra from the peak at 4.7 Å is shown, while at the bottom the flat background level is presented. All data has an additional normalization based on bin width (bw) to make the data comparable even though the bin width is smaller at the top plot. For both detectors, an SBR in the order of 1e3 is obtained. Statistical uncertainties are shown as error bars but are in most cases too small to be discernible.

One important difference between the two compared detector technologies is that the Multi-Grid detector has a depth dimension. This spreads the tof-distribution of the incident pulse along the layers, as previously shown in figure 4.22, which diminishes the peak intensity. To account for this effect, tof is combined with the sample-to-detection distance d to get either energy or wavelength. As the wavelength is proportional to tof for a given distance d, the flat tof background will be relatively flat in wavelength as well, which facilitates the signal-to-background considerations. Hence, wavelength is the quantity chosen for comparison. The result from this analysis is presented in figure 5.25, where the signal is presented at the top and the background at the bottom. In this case,

the signal-to-background ratios are around 10^4 for both detectors: SBR = 9368 ± 617 for the MG.LET and SBR = 26574 ± 778 for the helium-3 tubes.

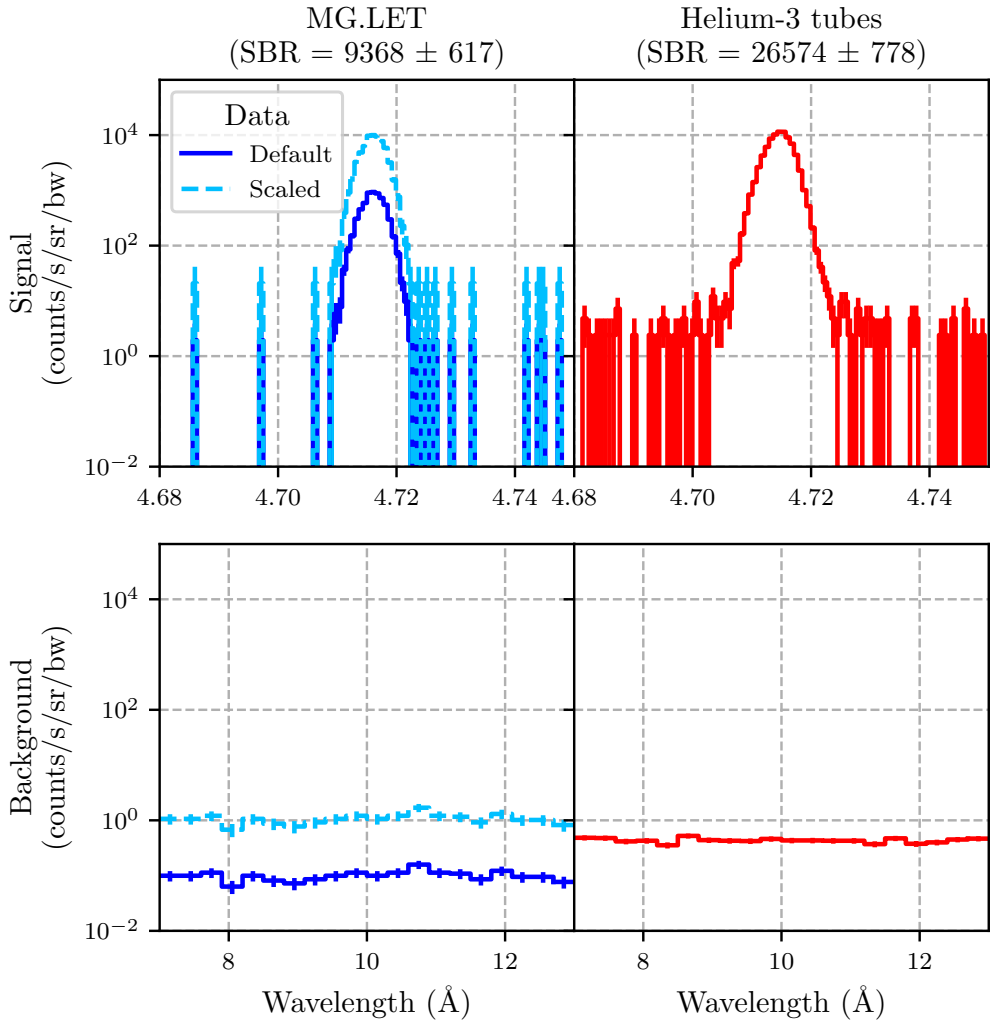

Figure 5.25: Signal-to-background comparison between the MG.LET (blue and light blue) and helium-3 tubes (red). At the top, the wavelength spectra from the peak at 4.7 Å are shown, while at the bottom the flat background level is presented. All data has an additional normalization based on bin width (bw) to make the data comparable even though the bin width is smaller at the top plot. For both detectors, an SBR in the order of 1e4 is obtained. Statistical uncertainties are shown as error bars but are in most cases too small to be discernible.

Chapter 6

Conclusions & Outlook

In this work, the development of the boron-10-based Multi-Grid detector has been presented. The first part of the work consisted of a general investigation of internal neutron shielding, while the second part focused on detector characterisation. The conclusions of these studies are presented below, followed by an outlook on the possible future steps in the detector development.

6.1 Conclusions

In the shielding investigation, an easy-to-use analytical procedure for finding an appropriate shielding configuration was presented. The procedure showed that by using a set of simplified calculations for neutron transmission and albedo, together with a set of performance metrics for the shielding materials, it is possible to gain a fair idea of which shielding materials, and with what thicknesses, are necessary to reach a certain signal-to-background ratio. Ideally, the final shielding configuration found should then be verified with a full detector simulation, and, if possible, also with measurement data. Nevertheless, using the analytical tools it is possible to explore a large parameter space of possible shielding configurations, which would be infeasible with full simulations, and identify shielding candidates. This greatly simplifies the effort of finding a suitable shielding and speeds up the design and implementation phase, which allows the engineering of a shielding configuration rather than retrofitting. This is not just applicable to the Multi-Grid but can be used for all types of neutron detectors.

From the V20 measurements, detector properties concerning efficiency, lineshape reconstruction and time and energy resolution were investigated. The derived efficiency of the MG.SEQ was observed to match the theoretical prediction for wavelengths above 4 Å and be close at 1.3 Å. For the remaining wavelengths, a strong discrepancy was seen, caused

by saturation in the helium-3 detector system which was unable to cope with the peak flux at these wavelengths. The MG.SEQ showed no sign of saturation, highlighting its higher count rate capabilities.

By studying data from MG.SEQ.I (non-coated radial blades) and MG.SEQ.II (coated radial blades), the net effect on the lineshape was compared. Between 1 and 4 Å, the average improvement induced by coating the radial blades was seen to increase with distance from the peak centre, starting at 7 ± 6 % between [-5σ, 0σ], and reaching 31 ± 8 % at [-15σ, -10σ]. It is important to note that these results were obtained in a direct beam measurement and that during normal operation the effect of the radial blades will be different. This is because – during standard operation – the energy resolution is more sensitive to the extra time-of-flight inflicted by internal scattering. This is due to the comparatively short secondary flight path – spanning from the sample to the detection point – that the final neutron energy is based on. Hence, coating the radial blades should have a larger effect during normal operation. These studies are useful for all neutron detectors in the context of internal scattering attenuation by using shielding inside the active volume.

The energy resolution of the MG.SEQ and helium-3 tube are observed to broadly match – within 5 μeV – over the measured wavelengths. For the shortest wavelengths, around 1.5 Å, the Multi-Grid detector and the helium-3 tube have equivalent resolutions. However, the trend implies that for shorter wavelengths than those measured here, the Multi-Grid detector might have the advantage. Above 1.5 Å, the helium-3 tube performs better in terms of energy resolution. One factor that contributes to this behaviour is that, for the helium-3 tube, neutrons can be converted anywhere in the gas along the 2.5 cm depth of the tube, while the absorption in the Multi-Grid detector only occurs at discrete intervals of 0.95 cm. This results in a difference in timing resolution. Due to this, at longer wavelengths, the obtained energy spectra from the Multi-Grid detector have a double peak, where each peak originates from one of the two conversion films adjacent to the same wire layer. This effect becomes more evident for longer wavelengths, as the additional path difference is more important for slow neutrons than for fast ones. However, in practical applications of the Multi-Grid detector at an instrument, such as at CNCS, SEQUOIA and LET, this effect has not been observable. This is due to the longer flight path and additional pulse broadening at these facilities, which causes the 0.95 cm timing difference to be far below instrument resolution. These results are not only relevant for the Multi-Grid detector but can be applied to other detector designs as well.

From the LET measurements, an energy lineshape comparison was made between the MG.LET and the permanent helium-3 tube array at the instrument. Although the low amount of data prevented a fine-detailed comparison at the base of the elastic peaks, the detectors did compare well within statistics for most energies when a broad bin width

was used. Additionally, a clear improvement in energy line shape reconstruction was seen for the MG.LET at 3.68 meV (4.71 Å) as compared to a previous measurement, and it is broadly consistent with that of the helium-3 detectors installed on the LET. The signal-to-background level – calculated for a peak at around 5 Å and compared to the flat background level in the spectra – was found to be around 10^3 in tof-spectra and 10^4 in lambda-spectra. The low efficiency of the MG.LET during the beamtime was investigated and shown to be due to the gas supply used, which contained a significant portion of oxygen.

6.2 Outlook

Based on the studies presented in this work, a better understanding of the detector behaviour has been obtained. Nevertheless, there are a few suggestions for the next steps that can be made. These mainly include further studies concerning background reduction and count rate capabilities, but there are also potential paths concerning data treatment and neutron energy determination as well.

First of all, to accurately investigate the intrinsic background level of the detector a quiet background environment is required. Such a location could be the Boulby Underground Laboratory [54], which is situated 1.1 km beneath the surface. At the laboratory, the natural background environment is exceptionally quiet due to the natural shielding of the rocks. This would allow for a careful study of the intrinsic background level in the Multi-Grid detector, as well as an opportunity to benchmark potential detector materials against each other in terms of activity. Before such a low-background test, however, it would be necessary to have a good understanding of the noise level contributed by the readout-system. This is so that a clear separation can be made on which backgrounds are related to the readout and which are intrinsic to the detector.

Next, the time-dependent background from internal neutron scattering can be further studied. One way of doing this would be to continue the work done here, which quantified the effect of coating the radial blades using a direct beam, and perform a similar study at a neutron spectroscopy instrument. This would probe the effect of the radial blades during normal detector operation and by using different samples – such as those with a low quasi-elastic scattering amplitude – it can be probed if the detector can reconstruct effects which might be blurred by internal scattering. This would also allow seeing if other data treatments – such as a potential background fitting of the shoulder of the elastic peak – can be used to accurately extract the quasi-elastic broadening.

Another path forward would be to perform further simulations and incorporate McStas [103], a neutron ray-tracing simulation package, into the current Geant4 detector

simulations. Using this package, it is possible to simulate all the instrument components in a neutron spectroscopy instrument before the neutrons reach the detector, which would allow an investigation of how the detector behaves under normal operation. Using the simulation package, it would be possible to try different samples and probe the detector response. This would allow, for example, studies on the impact on energy lineshape when only internal scattering is considered. It would also give a comparison with experimental data, which could help with the understanding of detector behaviour.

Finally, using statistical methods, it might be possible to increase the energy resolution of the detector. This is due to the multi-layered structure of the detector and the energy-dependent absorption probability of B-10, which results in different absorption profiles across the layers for different energies. Hence, by fitting the absorption profile, information about the incident neutron energy can be acquired. A few investigations of this effect have already been done in [104, 105], and it was concluded that by combining this information with tof a better signal-to-background ratio should be achievable. Hence, there might be potential in exploring this path.

Note that some of the studies suggested here would take significant amounts of instrumental time. This could detract from the user program and might therefore be unrealistic to perform, except during the instrumental commissioning. Additionally, due to the large size of the final detector, it is infeasible to perform final testing on an already existing instrument. Therefore, many of the here suggested future endeavours could be done during the commissioning of the detector at ESS. This would enable rigorous studies of the behaviour of the full detector array, including the effectiveness of the shielding and the optimisation of the signal-to-background ratio by tuning operational parameters. All of the results obtained with the full-scale detector could then be fed back to the next generation.

To conclude, during the ten years of development, most of the required detector properties – such as energy resolution, gamma sensitivity and efficiency – have been validated in the Multi-Grid technology. Part of the remaining work has been investigated in this thesis, together with a detailed account of general shielding considerations. Much of this work was designed to be relevant to many other neutron detector types and is thus a general development aid. The results presented here will provide vital input in the final development of Multi-Grid technology towards maturity and widespread implementation at neutron scattering facilities of the future. This will enable a scalable, low-cost and high-performance alternative to helium-3-based detectors, designed to accommodate the expected high flux at the next-generation neutron sources.

Appendix A

Comparison between simulation and calculation

Figures A.1 to A.16 shows the 2D comparison between calculation and simulation, as described in the main text. In the figures, each data point corresponds to a comparison between calculation and simulation for a specific incident neutron energy (x-axis) and shielding thickness (y-axis). The transmission and albedo are compared separately in the left and right subplots, respectively. The colours correspond to the ratio between the calculation and simulation probabilities for each data point, calculated via the Log_{10} difference between calculation and simulation. To retain adequate statistics, simulation values with a probability below 10^{-5} are not included in the analysis. The calculated iso-lines for 10^{-5} probability are presented in black lines.

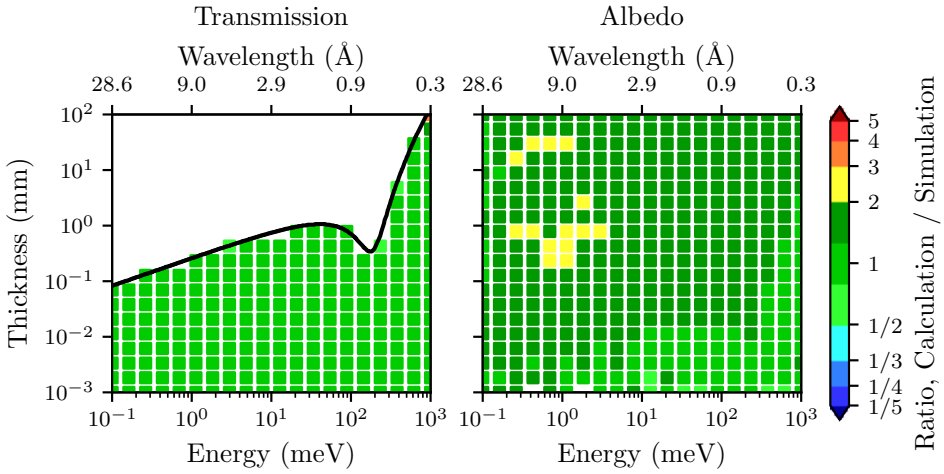

Figure A.1: Cadmium, a two-dimensional comparison between calculation and simulation. The transmission and albedo comparisons are shown in the left and right plots, respectively. The comparison is done for all combinations of 20 energies and 20 thicknesses evenly spread across the energy and thickness region under investigation. The colour shows the ratio between calculation and simulation. To only display data with a low statistical uncertainty, simulation values below 10^{-5} are not included in the analysis. The calculated iso-line for 10^{-5} transmission is presented in black in the left plot, which is seen to closely follow where the simulation data drops below 10^{-5}.

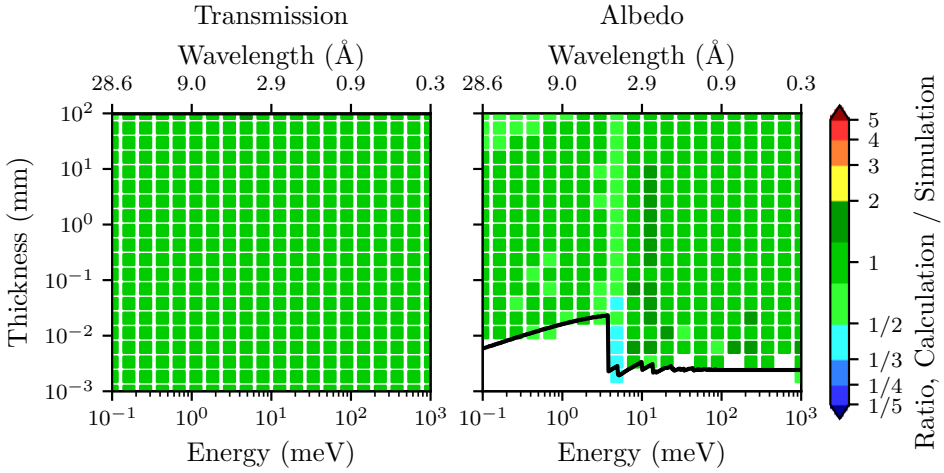

Figure A.2: Aluminum, a two-dimensional comparison between calculation and simulation. The transmission and albedo comparisons are shown in the left and right plots, respectively. The comparison is done for all combinations of 20 energies and 20 thicknesses evenly spread across the energy and thickness region under investigation. The colour shows the ratio between calculation and simulation. To only display data with a low statistical uncertainty, simulation values below 10^{-5} are not included in the analysis. The calculated iso-line for 10^{-5} albedo is presented in black in the right plot, which is seen to closely follow where the simulation data drops below 10^{-5}.

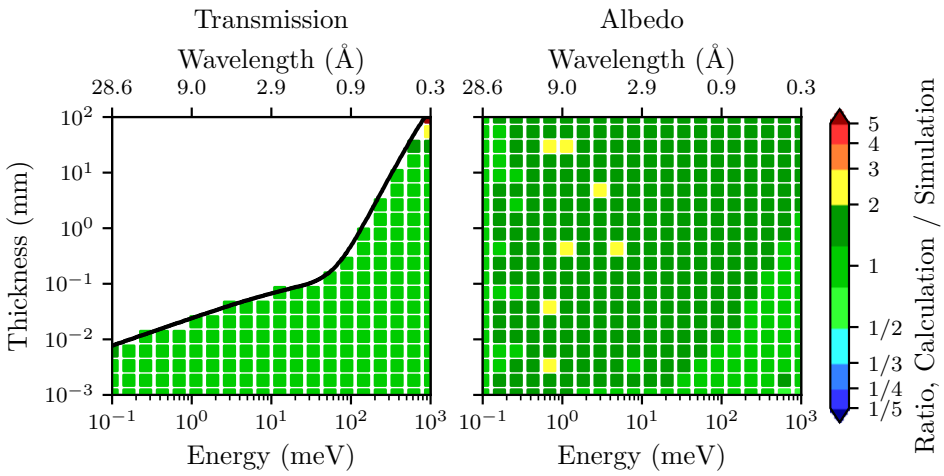

Figure A.3: Gd_2O_3, a two-dimensional comparison between calculation and simulation. The transmission and albedo comparisons are shown in the left and right plots, respectively. The comparison is done for all combinations of 20 energies and 20 thicknesses evenly spread across the energy and thickness region under investigation. The colour shows the ratio between calculation and simulation. To only display data with a low statistical uncertainty, simulation values below 10^{-5} are not included in the analysis. The calculated iso-line for 10^{-5} transmission is presented in black in the left plot, which is seen to closely follow where the simulation data drops below 10^{-5}.

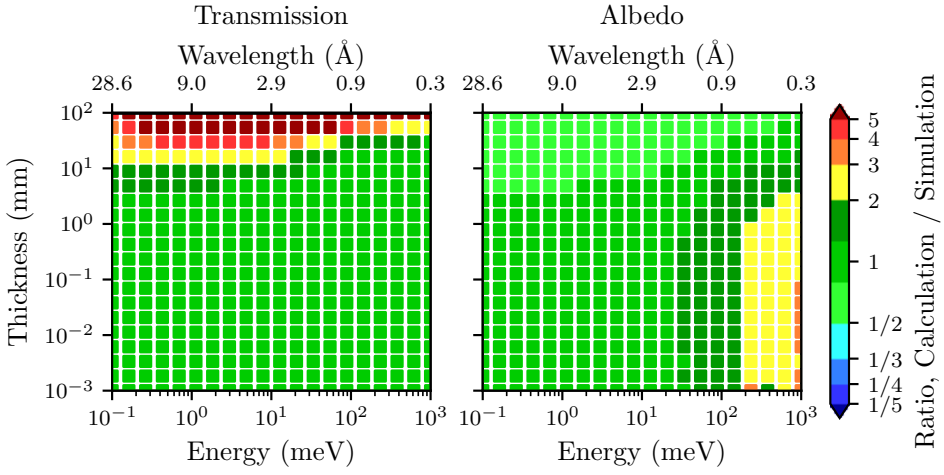

Figure A.4: Epoxy, a two-dimensional comparison between calculation and simulation. The transmission and albedo comparisons are shown in the left and right plots, respectively. The comparison is done for all combinations of 20 energies and 20 thicknesses evenly spread across the energy and thickness region under investigation. The colour shows the ratio between calculation and simulation. To only display data with a low statistical uncertainty, simulation values below 10^{-5} are not included in the analysis.

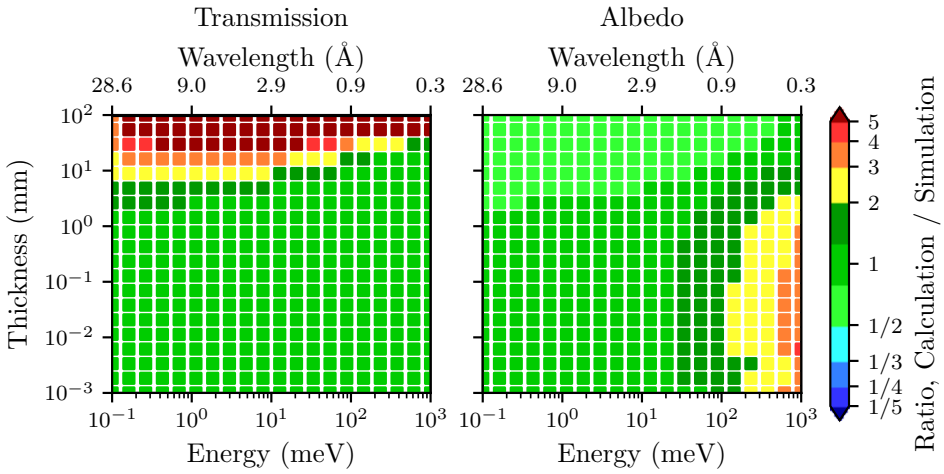

Figure A.5: Polyethylene, a two-dimensional comparison between calculation and simulation. The transmission and albedo comparisons are shown in the left and right plots, respectively. The comparison is done for all combinations of 20 energies and 20 thicknesses evenly spread across the energy and thickness region under investigation. The colour shows the ratio between calculation and simulation. To only display data with a low statistical uncertainty, simulation values below 10^{-5} are not included in the analysis.

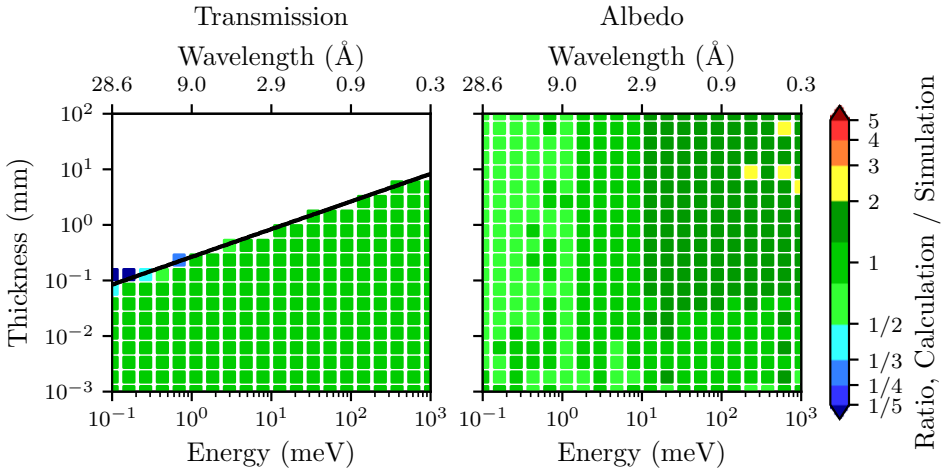

Figure A.6: $^{\text{nat}}B_4C$, a two-dimensional comparison between calculation and simulation. The transmission and albedo comparisons are shown in the left and right plots, respectively. The comparison is done for all combinations of 20 energies and 20 thicknesses evenly spread across the energy and thickness region under investigation. The colour shows the ratio between calculation and simulation. To only display data with a low statistical uncertainty, simulation values below 10^{-5} are not included in the analysis. The calculated iso-line for 10^{-5} transmission is presented in black in the left plot, which is seen to closely follow where the simulation data drops below 10^{-5}.

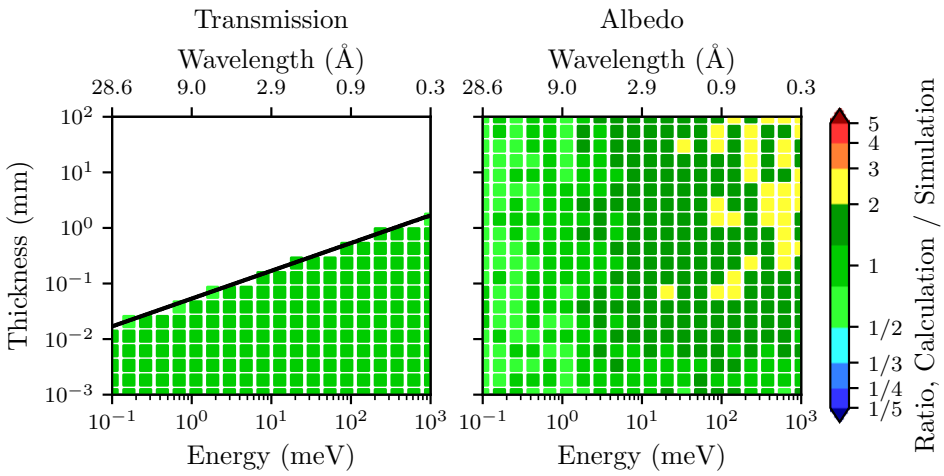

Figure A.7: B_4C ($^{10}B/B$: 99 at%), a two-dimensional comparison between calculation and simulation. The transmission and albedo comparisons are shown in the left and right plots, respectively. The comparison is done for all combinations of 20 energies and 20 thicknesses evenly spread across the energy and thickness region under investigation. The colour shows the ratio between calculation and simulation. To only display data with a low statistical uncertainty, simulation values below 10^{-5} are not included in the analysis. The calculated iso-line for 10^{-5} transmission is presented in black in the left plot, which is seen to closely follow where the simulation data drops below 10^{-5}.

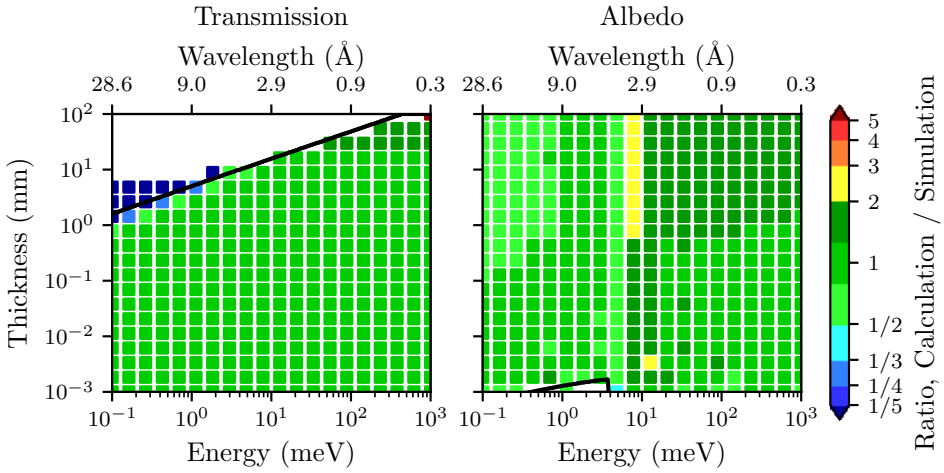

Figure A.8: ^{nat}LiF, a two-dimensional comparison between calculation and simulation. The transmission and albedo comparisons are shown in the left and right plots, respectively. The comparison is done for all combinations of 20 energies and 20 thicknesses evenly spread across the energy and thickness region under investigation. The colour shows the ratio between calculation and simulation. To only display data with a low statistical uncertainty, simulation values below 10^{-5} are not included in the analysis. The calculated iso-lines for 10^{-5} probability is presented in black for transmission and albedo in the left and right plot, respectively.

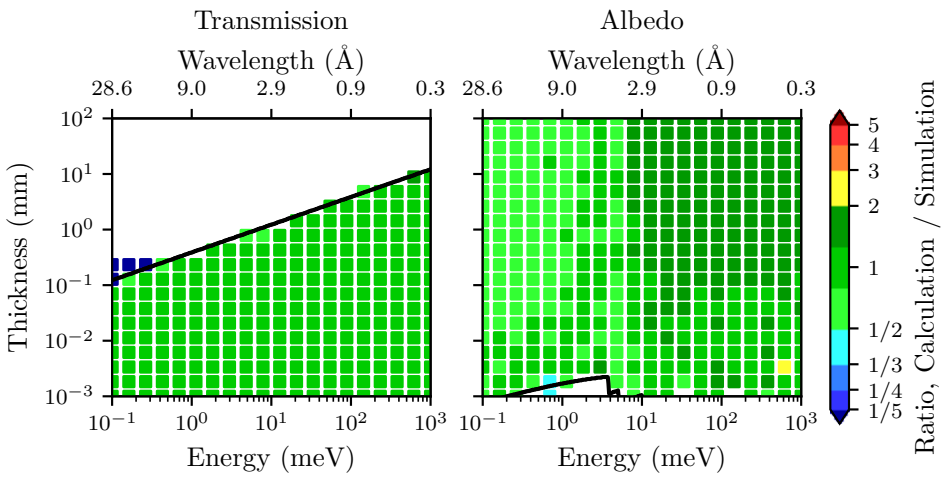

Figure A.9: LiF (^{6}Li/Li: 99 at%), a two-dimensional comparison between calculation and simulation. The transmission and albedo comparisons are shown in the left and right plots, respectively. The comparison is done for all combinations of 20 energies and 20 thicknesses evenly spread across the energy and thickness region under investigation. The colour shows the ratio between calculation and simulation. To only display data with a low statistical uncertainty, simulation values below 10^{-5} are not included in the analysis. The calculated iso-lines for 10^{-5} probability is presented in black for transmission and albedo in the left and right plot, respectively.

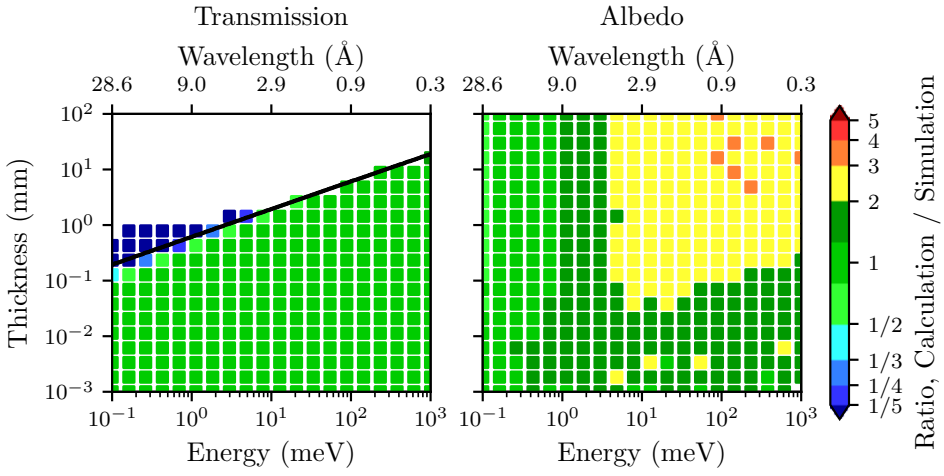

Figure A.10: MirroBor, a two-dimensional comparison between calculation and simulation. The transmission and albedo comparisons are shown in the left and right plots, respectively. The comparison is done for all combinations of 20 energies and 20 thicknesses evenly spread across the energy and thickness region under investigation. The colour shows the ratio between calculation and simulation. To only display data with a low statistical uncertainty, simulation values below 10^{-5} are not included in the analysis. The calculated iso-line for 10^{-5} transmission is presented in the left plot in black.

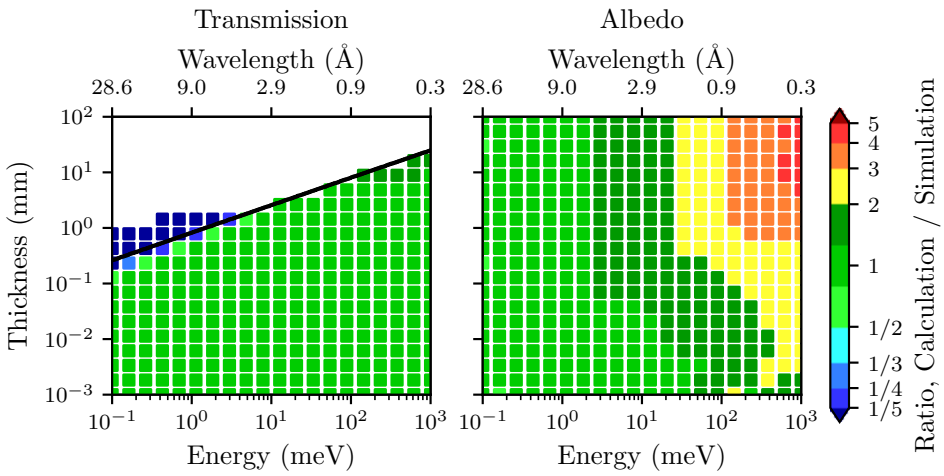

Figure A.11: Epoxy-$^{nat}B_4C$ (50 wt% epoxy + 50 wt% $^{nat}B_4C$), a two-dimensional comparison between calculation and simulation. The transmission and albedo comparisons are shown in the left and right plots, respectively. The comparison is done for all combinations of 20 energies and 20 thicknesses evenly spread across the energy and thickness region under investigation. The colour shows the ratio between calculation and simulation. To only display data with a low statistical uncertainty, simulation values below 10^{-5} are not included in the analysis. The calculated iso-line for 10^{-5} transmission is presented in black in the left plot.

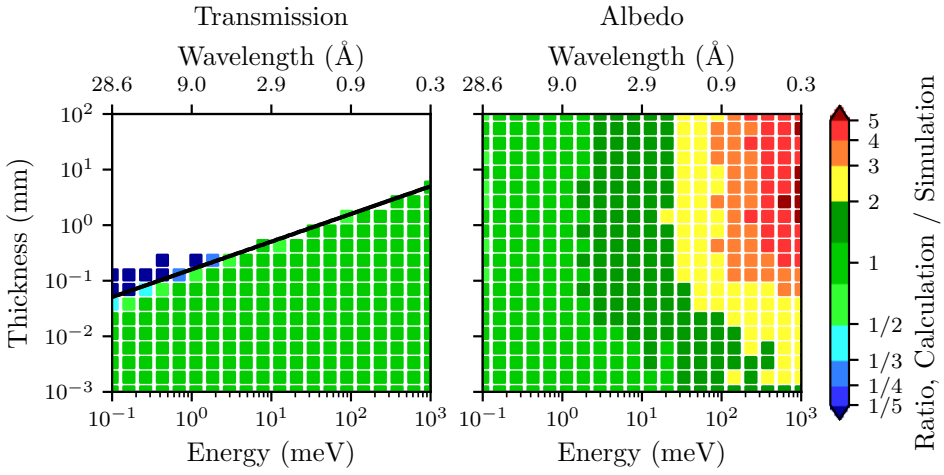

Figure A.12: Epoxy-B_4C, $^{10}B/B$: 99 at% (50 wt% epoxy + 50 wt% B_4C), a two-dimensional comparison between calculation and simulation. The transmission and albedo comparisons are shown in the left and right plots, respectively. The comparison is done for all combinations of 20 energies and 20 thicknesses evenly spread across the energy and thickness region under investigation. The colour shows the ratio between calculation and simulation. To only display data with a low statistical uncertainty, simulation values below 10^{-5} are not included in the analysis. The calculated iso-line for 10^{-5} transmission is presented in black in the left plot.

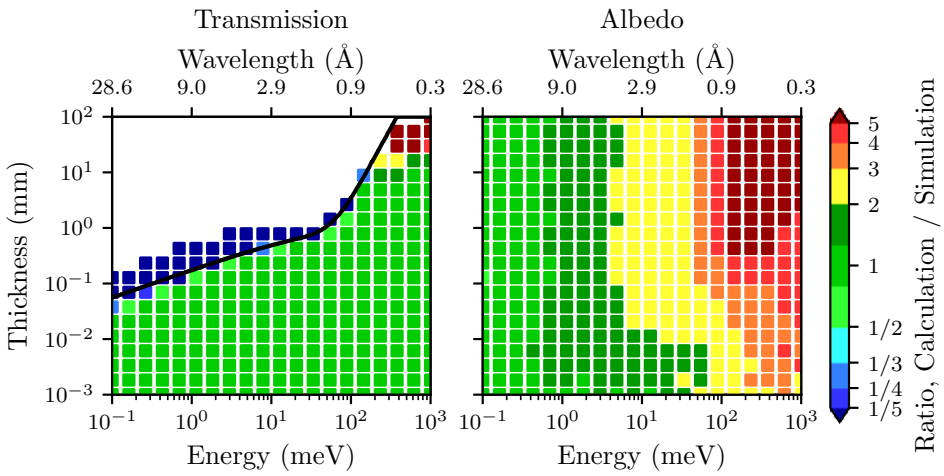

Figure A.13: Epoxy-Gd_2O_3 (50 wt% epoxy + 50 wt% Gd_2O_3), a two-dimensional comparison between calculation and simulation. The transmission and albedo comparisons are shown in the left and right plots, respectively. The comparison is done for all combinations of 20 energies and 20 thicknesses evenly spread across the energy and thickness region under investigation. The colour shows the ratio between calculation and simulation. To only display data with a low statistical uncertainty, simulation values below 10^{-5} are not included in the analysis. The calculated iso-line for 10^{-5} transmission is presented in black in the left plot.

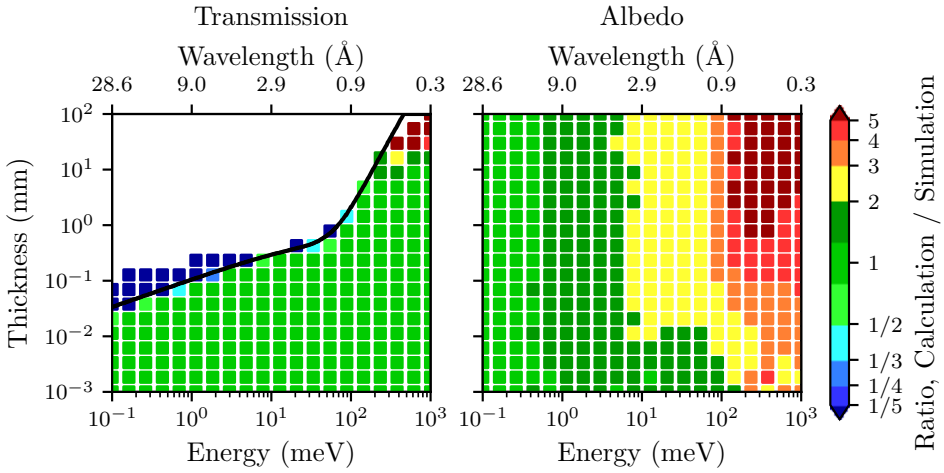

Figure A.14: Epoxy-Gd_2O_3 (35 wt% epoxy + 65 wt% Gd_2O_3), a two-dimensional comparison between calculation and simulation. The transmission and albedo comparisons are shown in the left and right plots, respectively. The comparison is done for all combinations of 20 energies and 20 thicknesses evenly spread across the energy and thickness region under investigation. The colour shows the ratio between calculation and simulation. To only display data with a low statistical uncertainty, simulation values below 10^{-5} are not included in the analysis. The calculated iso-line for 10^{-5} transmission is presented in black in the left plot.

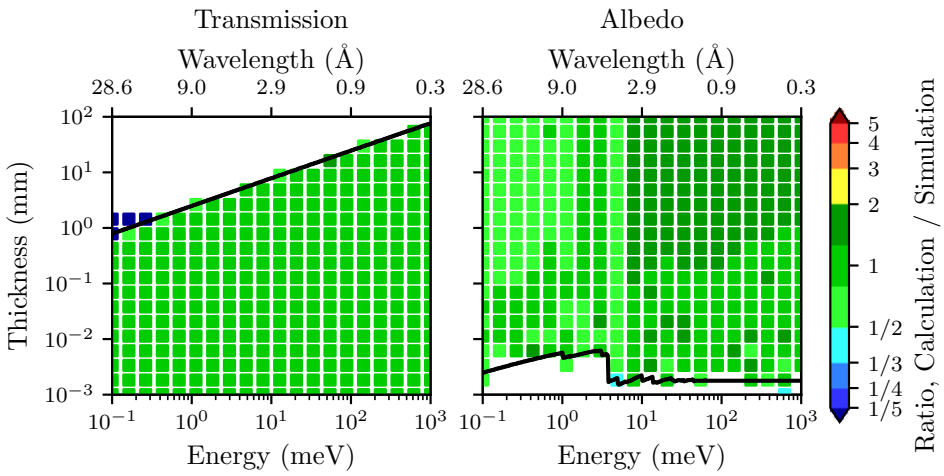

Figure A.15: Boral (90 wt% Al + 10 wt% $^{\text{nat}}B_4C$), a two-dimensional comparison between calculation and simulation. The transmission and albedo comparisons are shown in the left and right plots, respectively. The comparison is done for all combinations of 20 energies and 20 thicknesses evenly spread across the energy and thickness region under investigation. The colour shows the ratio between calculation and simulation. To only display data with a low statistical uncertainty, simulation values below 10^{-5} are not included in the analysis. The calculated iso-lines for 10^{-5} probability is presented in black for transmission and albedo in the left and right plot, respectively.

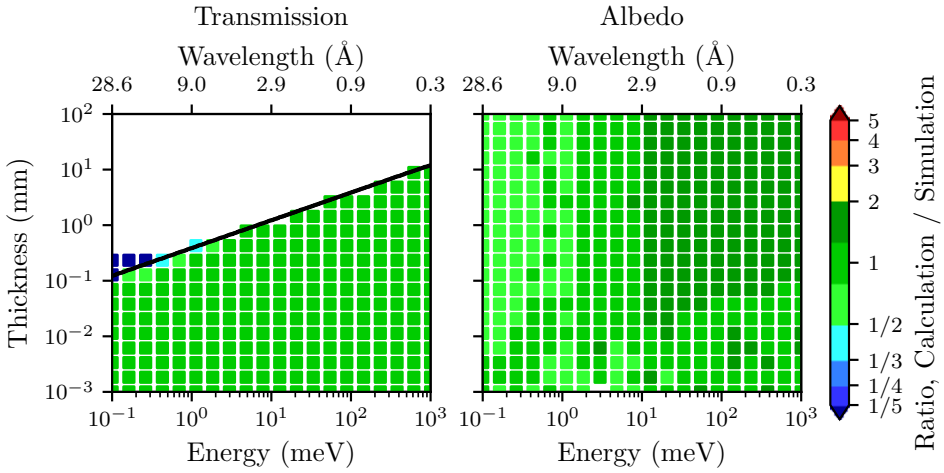

Figure A.16: Boral (33 wt% Al + 67 wt% $^{\text{nat}}B_4C$), a two-dimensional comparison between calculation and simulation. The transmission and albedo comparisons are shown in the left and right plots, respectively. The comparison is done for all combinations of 20 energies and 20 thicknesses evenly spread across the energy and thickness region under investigation. The colour shows the ratio between calculation and simulation. To only display data with a low statistical uncertainty, simulation values below 10^{-5} are not included in the analysis. The calculated iso-lines for 10^{-5} probability are presented in black for transmission in the left plot.

Appendix B

Shielding performance plots

Figures B.1 to B.13 show the performance of each material in terms of neutron transmission and albedo, as described in the main text. In the figures, the probability iso-lines for $P_{transmission}$ (blue) and $P^2_{transmission} \cdot \frac{1}{2}$ (red) are shown as a function energy and thickness for three different probabilities: 10^{-2}, 10^{-3} and 10^{-4}. Additionally, the albedo saturation thicknesses are shown as a function of energy, together with the corresponding albedo saturation level for each energy. Note that the albedo saturation level is colour coded according to the colour bar.

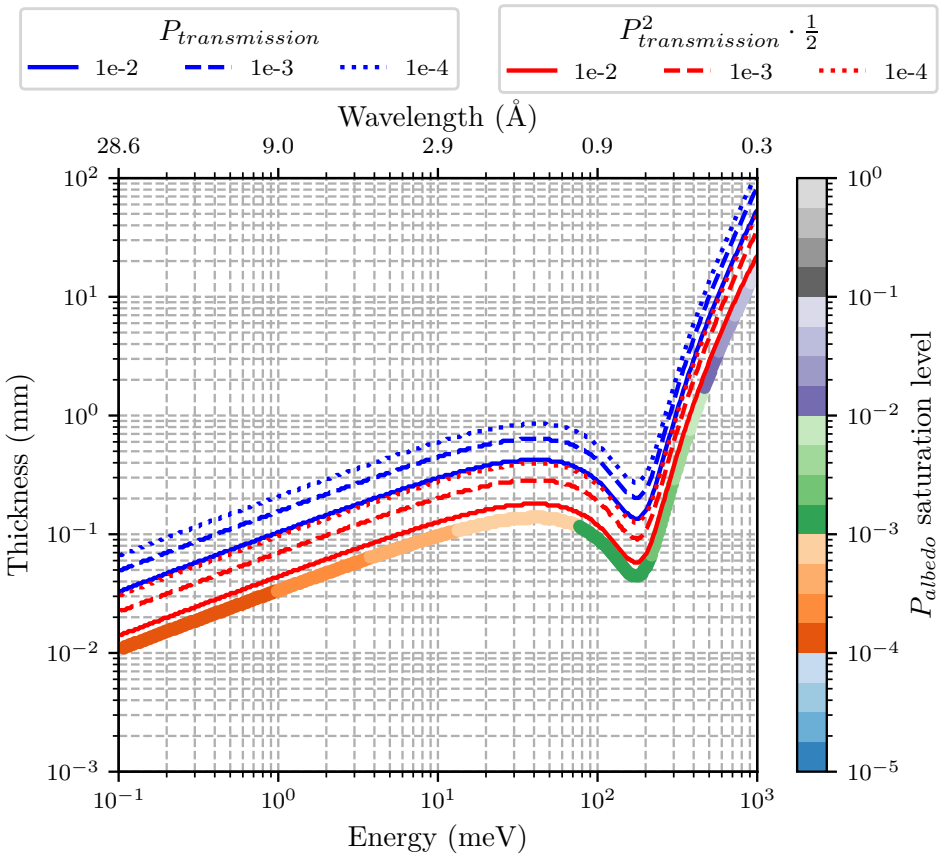

Figure B.1: Cadmium, material properties needed for shielding investigation. The probability iso-lines for $P_{transmission}$ (blue) and $P^2_{transmission} \cdot \frac{1}{2}$ (red) are shown as a function of thickness and energy for three different probabilities: 10^{-2}, 10^{-3} and 10^{-4}. Additionally, the albedo saturation thicknesses are shown as a function of energy, where the colour indicates the albedo saturation level.

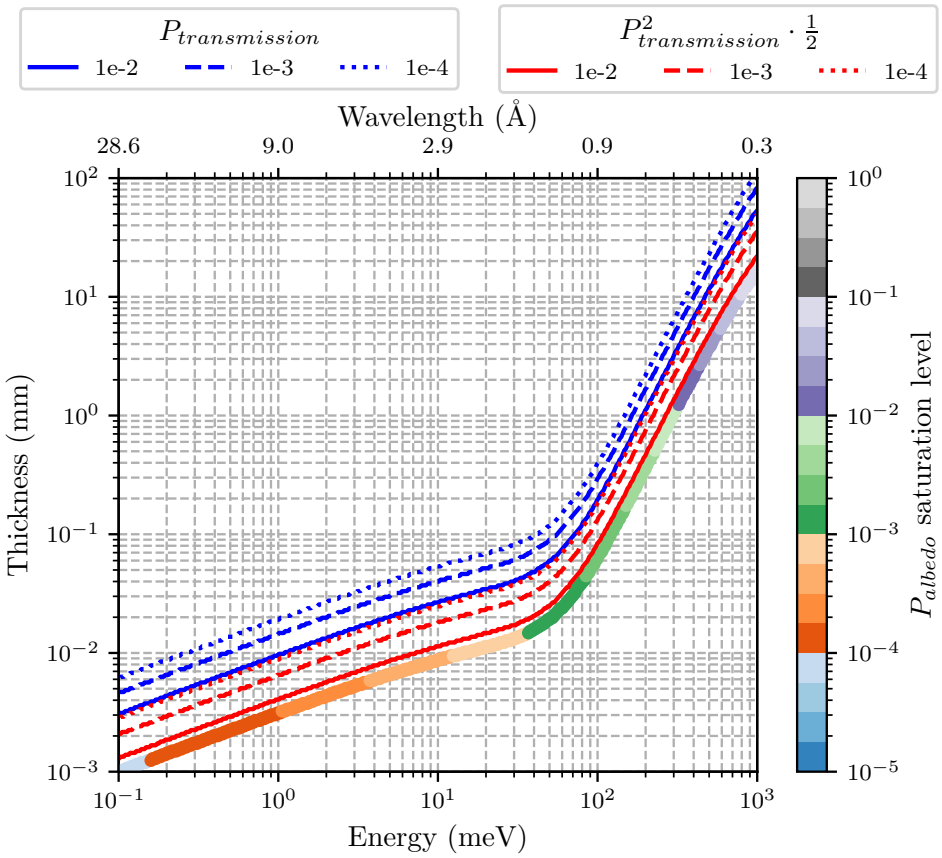

Figure B.2: $^{nat}Gd_2O_3$, material properties needed for shielding investigation. The probability iso-lines for $P_{transmission}$ (blue) and $P^2_{transmission} \cdot \frac{1}{2}$ (red) are shown as a function of thickness and energy for three different probabilities: 10^{-2}, 10^{-3} and 10^{-4}. Additionally, the albedo saturation thicknesses are shown as a function of energy, where the colour indicates the albedo saturation level.

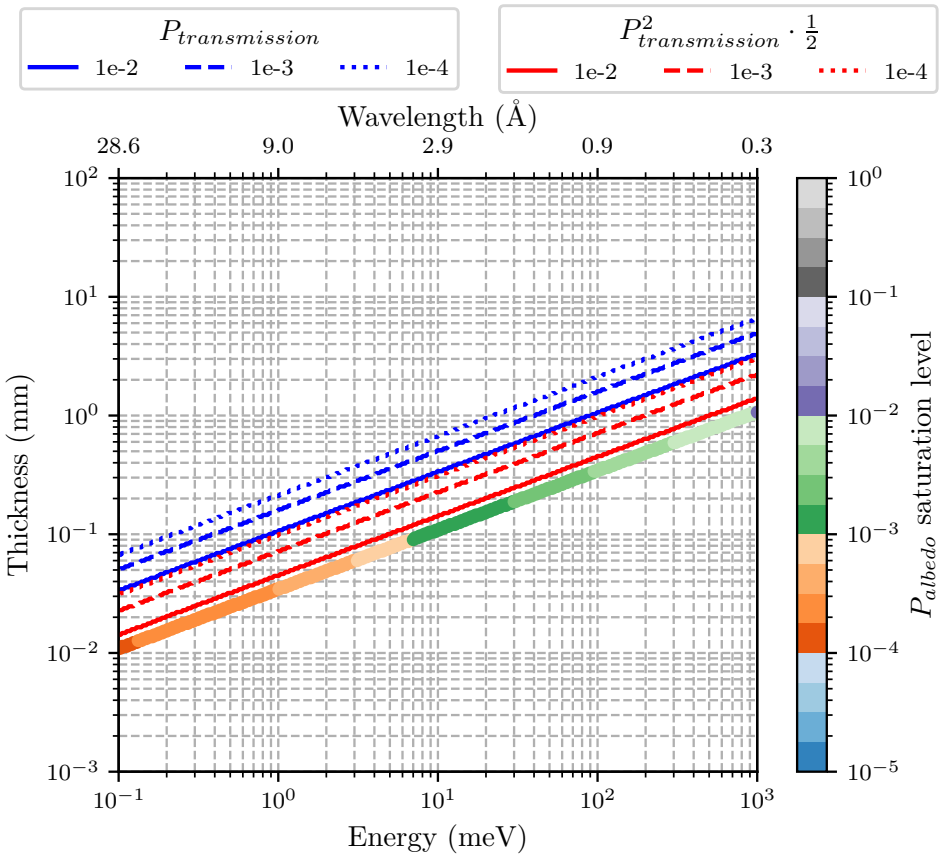

Figure B.3: $^{nat}B_4C$, material properties needed for shielding investigation. The probability iso-lines for $P_{transmission}$ (blue) and $P^2_{transmission} \cdot \frac{1}{2}$ (red) are shown as a function of thickness and energy for three different probabilities: 10^{-2}, 10^{-3} and 10^{-4}. Additionally, the albedo saturation thicknesses are shown as a function of energy, where the colour indicates the albedo saturation level.

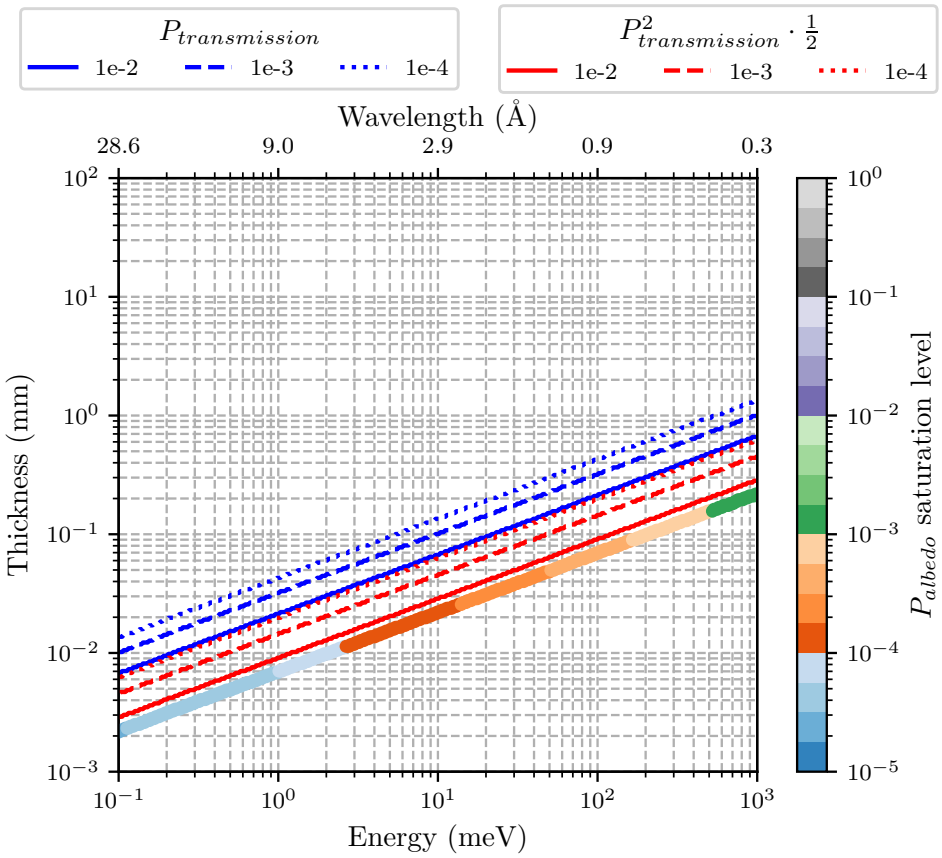

Figure B.4: B_4C ($^{10}B/B$: 99 at%), material properties needed for shielding investigation. The probability iso-lines for $P_{transmission}$ (blue) and $P^2_{transmission} \cdot \frac{1}{2}$ (red) are shown as a function of thickness and energy for three different probabilities: 10^{-2}, 10^{-3} and 10^{-4}. Additionally, the albedo saturation thicknesses are shown as a function of energy, where the colour indicates the albedo saturation level.

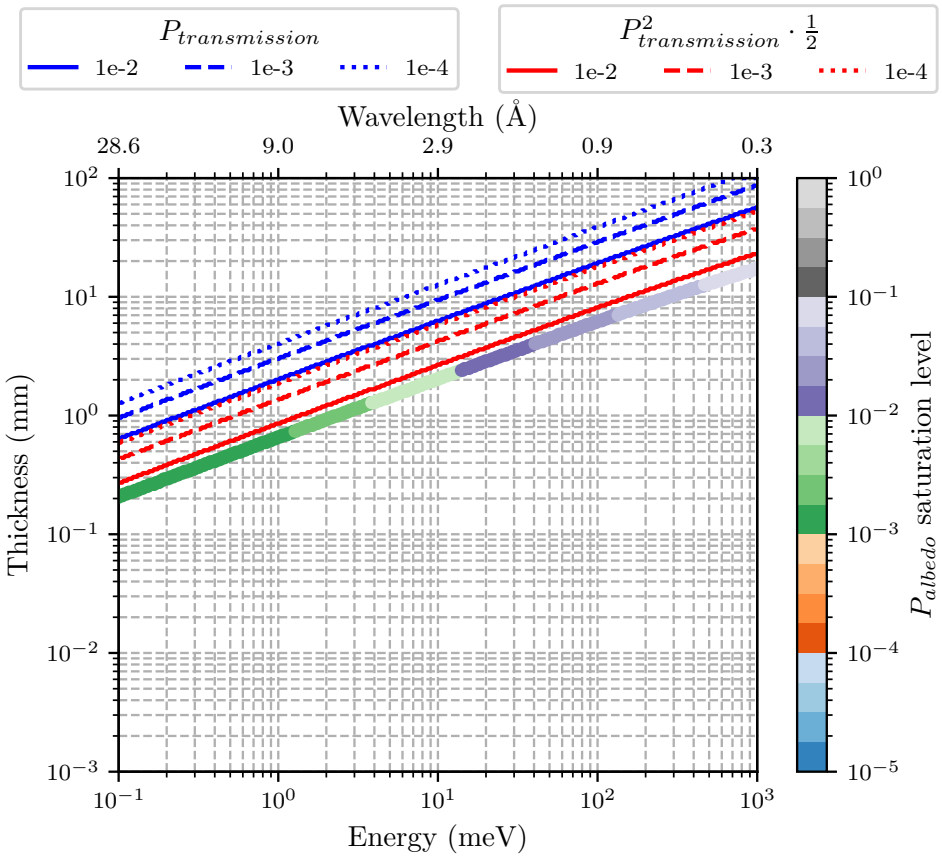

Figure B.5: ^{nat}LiF, material properties needed for shielding investigation. The probability iso-lines for $P_{transmission}$ (blue) and $P^2_{transmission} \cdot \frac{1}{2}$ (red) are shown as a function of thickness and energy for three different probabilities: 10^{-2}, 10^{-3} and 10^{-4}. Additionally, the albedo saturation thicknesses are shown as a function of energy, where the colour indicates the albedo saturation level.

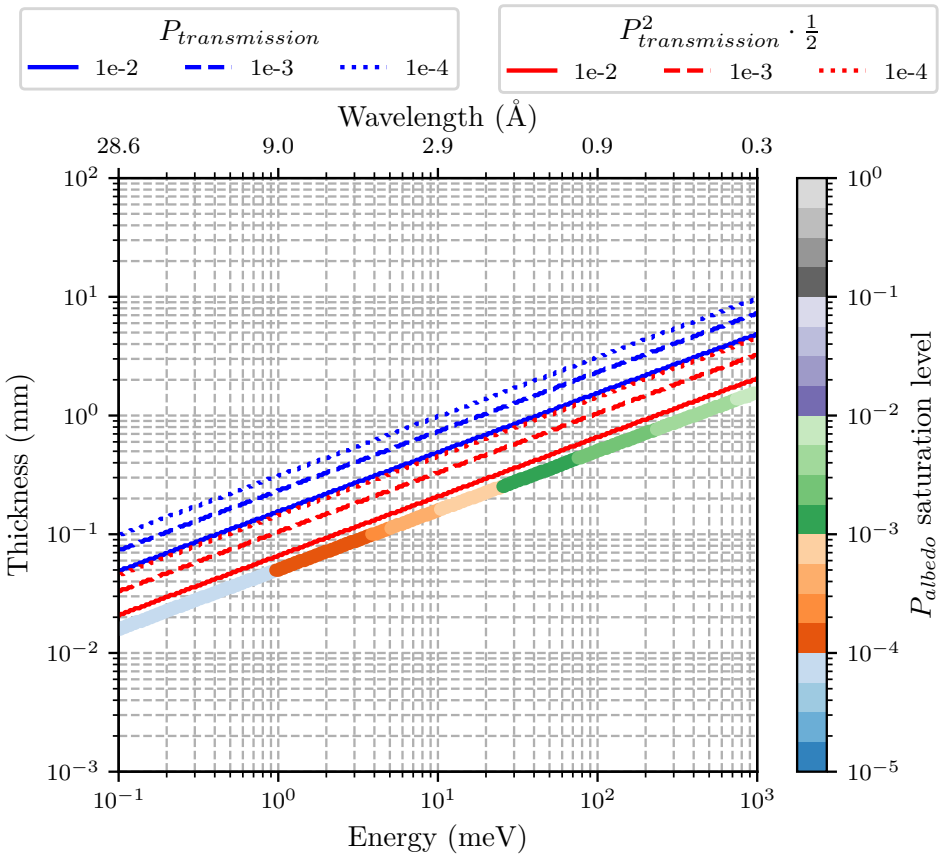

Figure B.6: LiF (^{6}Li/Li: 99 at%), material properties needed for shielding investigation. The probability iso-lines for $P_{transmission}$ (blue) and $P^2_{transmission} \cdot \frac{1}{2}$ (red) are shown as a function of thickness and energy for three different probabilities: 10^{-2}, 10^{-3} and 10^{-4}. Additionally, the albedo saturation thicknesses are shown as a function of energy, where the colour indicates the albedo saturation level.

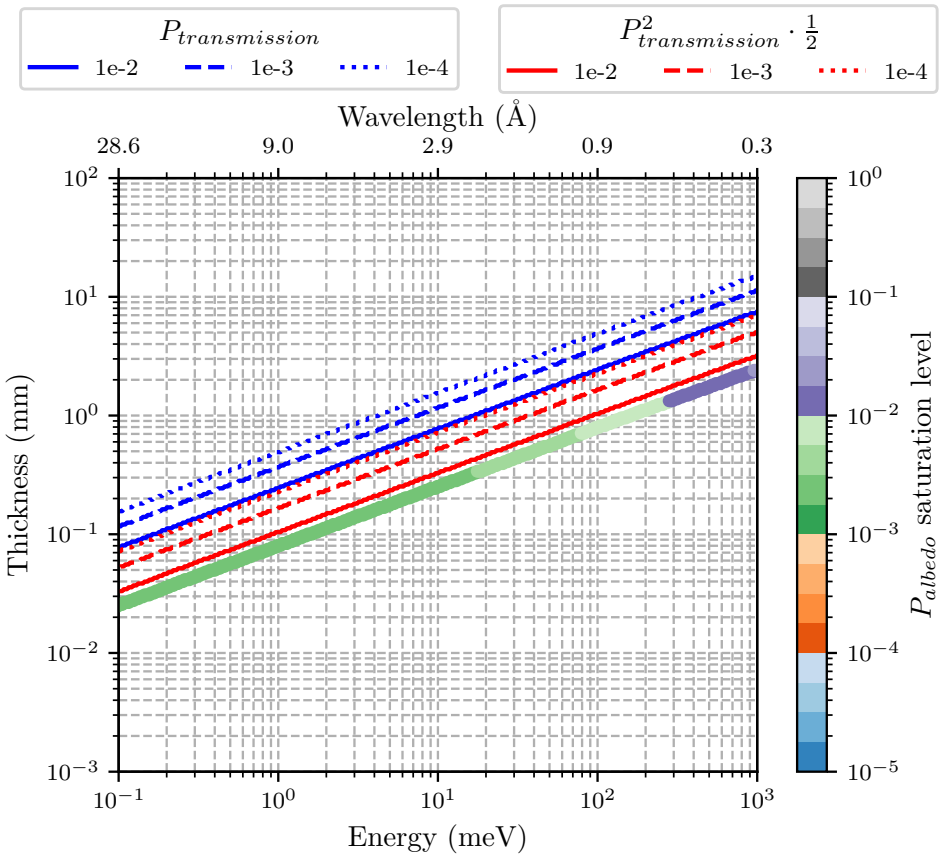

Figure B.7: MirroBor, material properties needed for shielding investigation. The probability iso-lines for $P_{transmission}$ (blue) and $P^2_{transmission} \cdot \frac{1}{2}$ (red) are shown as a function of thickness and energy for three different probabilities: 10^{-2}, 10^{-3} and 10^{-4}. Additionally, the albedo saturation thicknesses are shown as a function of energy, where the colour indicates the albedo saturation level.

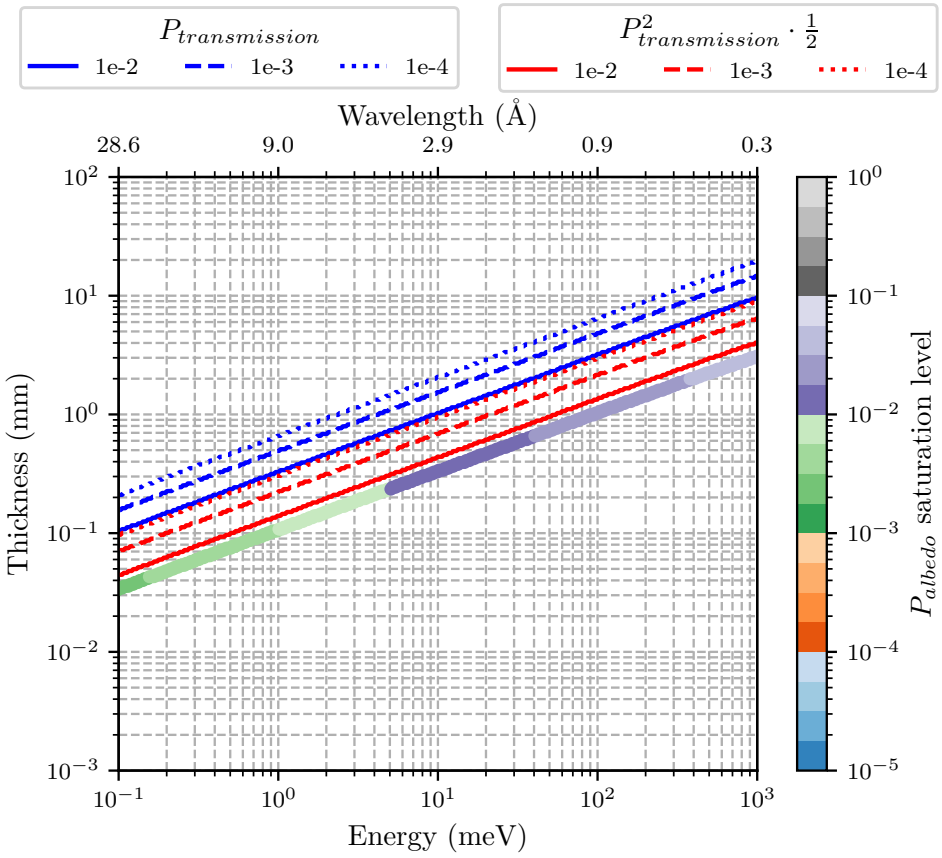

Figure B.8: Epoxy-$^{nat}B_4C$ (50 wt% epoxy + 50 wt% $^{nat}B_4C$), material properties needed for shielding investigation. The probability iso-lines for $P_{transmission}$ (blue) and $P^2_{transmission} \cdot \frac{1}{2}$ (red) are shown as a function of thickness and energy for three different probabilities: 10^{-2}, 10^{-3} and 10^{-4}. Additionally, the albedo saturation thicknesses are shown as a function of energy, where the colour indicates the albedo saturation level.

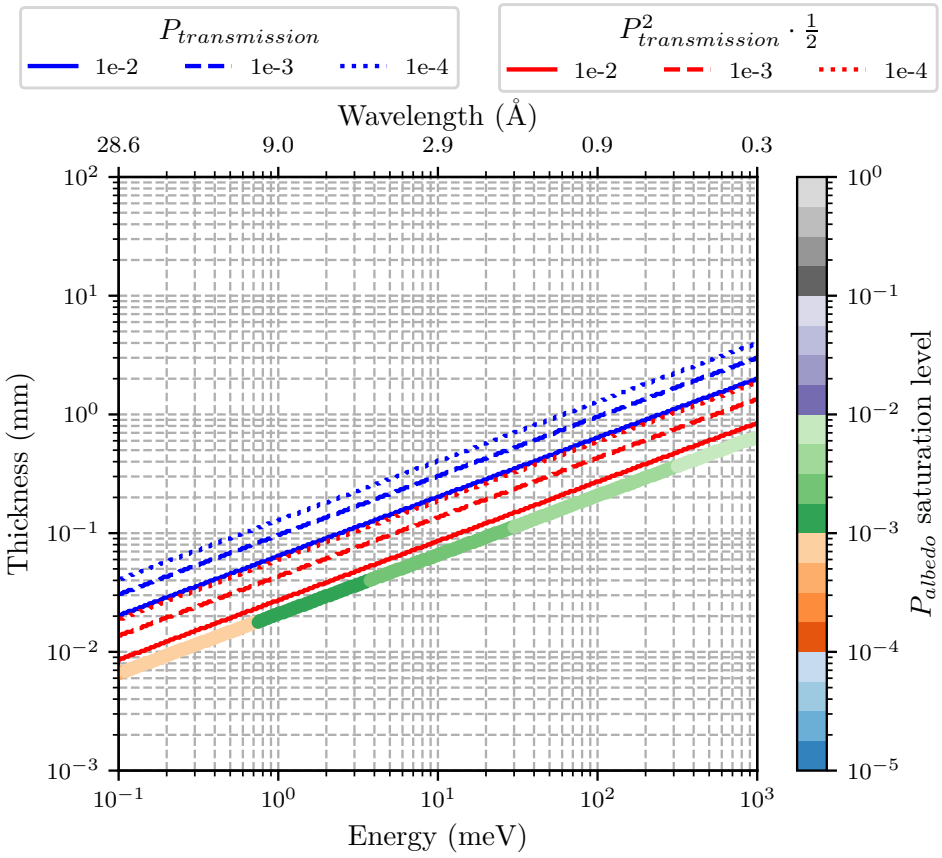

Figure B.9: Epoxy-B_4C, $^{10}B/B$: 99 at% (50 wt% epoxy + 50 wt% B_4C), material properties needed for shielding investigation. The probability iso-lines for $P_{transmission}$ (blue) and $P^2_{transmission} \cdot \frac{1}{2}$ (red) are shown as a function of thickness and energy for three different probabilities: 10^{-2}, 10^{-3} and 10^{-4}. Additionally, the albedo saturation thicknesses are shown as a function of energy, where the colour indicates the albedo saturation level.

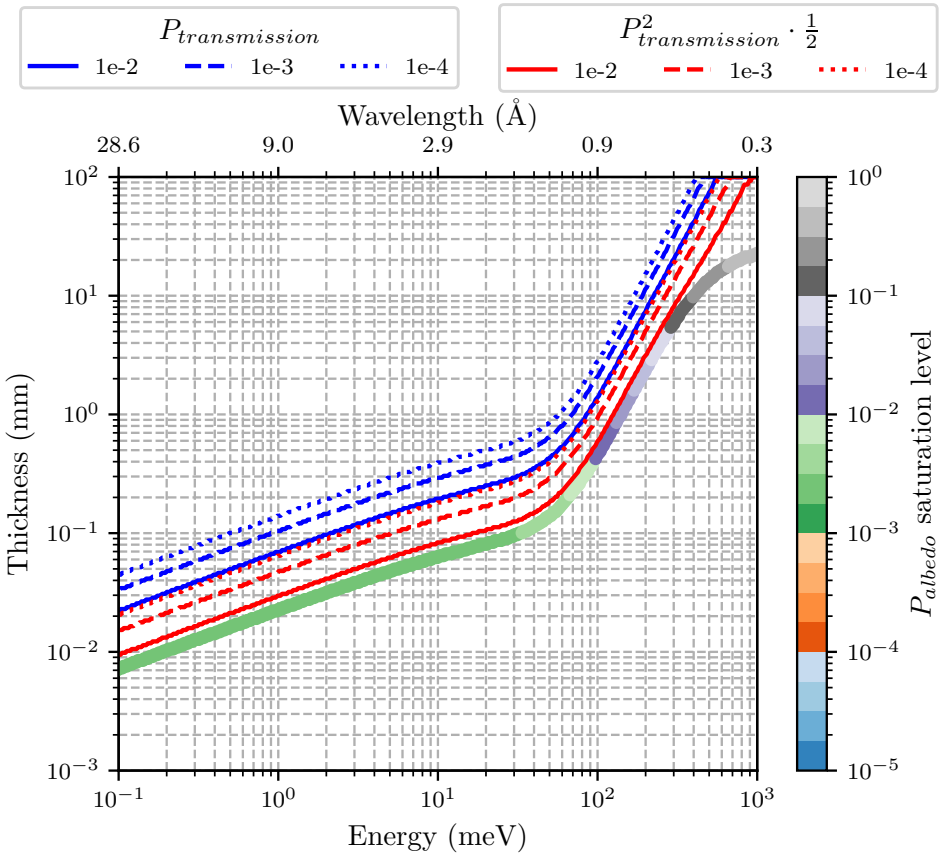

Figure B.10: Epoxy-$^{nat}Gd_2O_3$ (50 wt% epoxy + 50 wt% Gd_2O_3), material properties needed for shielding investigation. The probability iso-lines for $P_{transmission}$ (blue) and $P^2_{transmission} \cdot \frac{1}{2}$ (red) are shown as a function of thickness and energy for three different probabilities: 10^{-2}, 10^{-3} and 10^{-4}. Additionally, the albedo saturation thicknesses are shown as a function of energy, where the colour indicates the albedo saturation level.

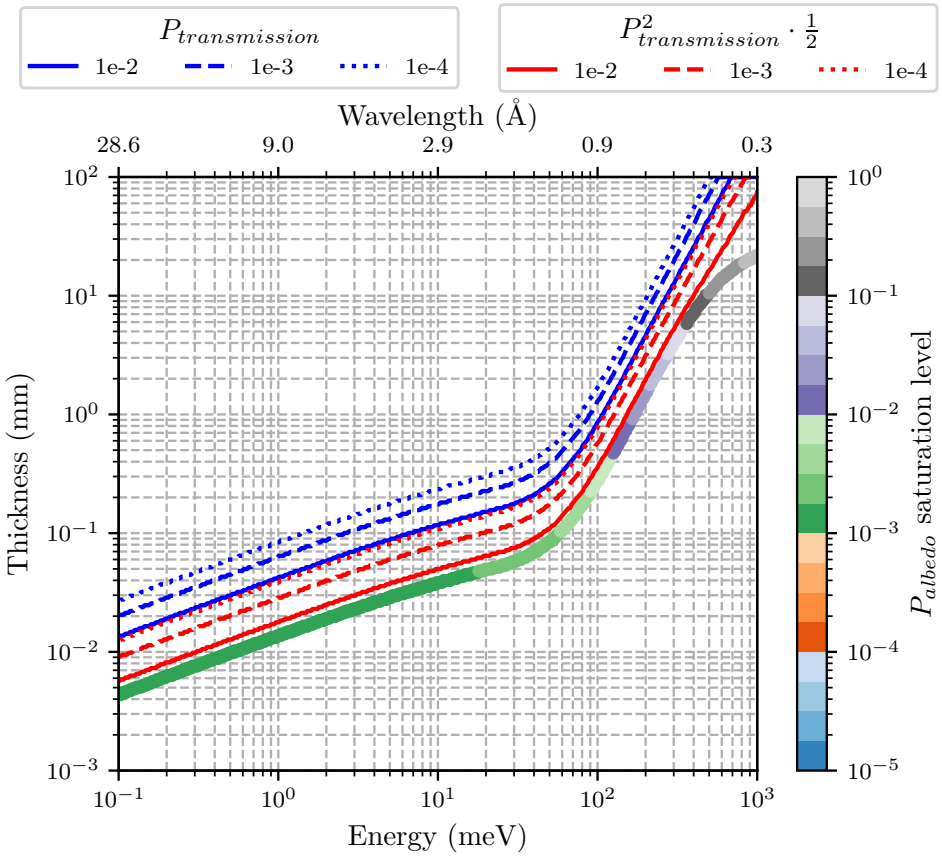

Figure B.11: Epoxy-$^{nat}Gd_2O_3$ (35 wt% epoxy + 65 wt% Gd_2O_3), material properties needed for shielding investigation. The probability iso-lines for $P_{transmission}$ (blue) and $P^2_{transmission} \cdot \frac{1}{2}$ (red) are shown as a function of thickness and energy for three different probabilities: 10^{-2}, 10^{-3} and 10^{-4}. Additionally, the albedo saturation thicknesses are shown as a function of energy, where the colour indicates the albedo saturation level.

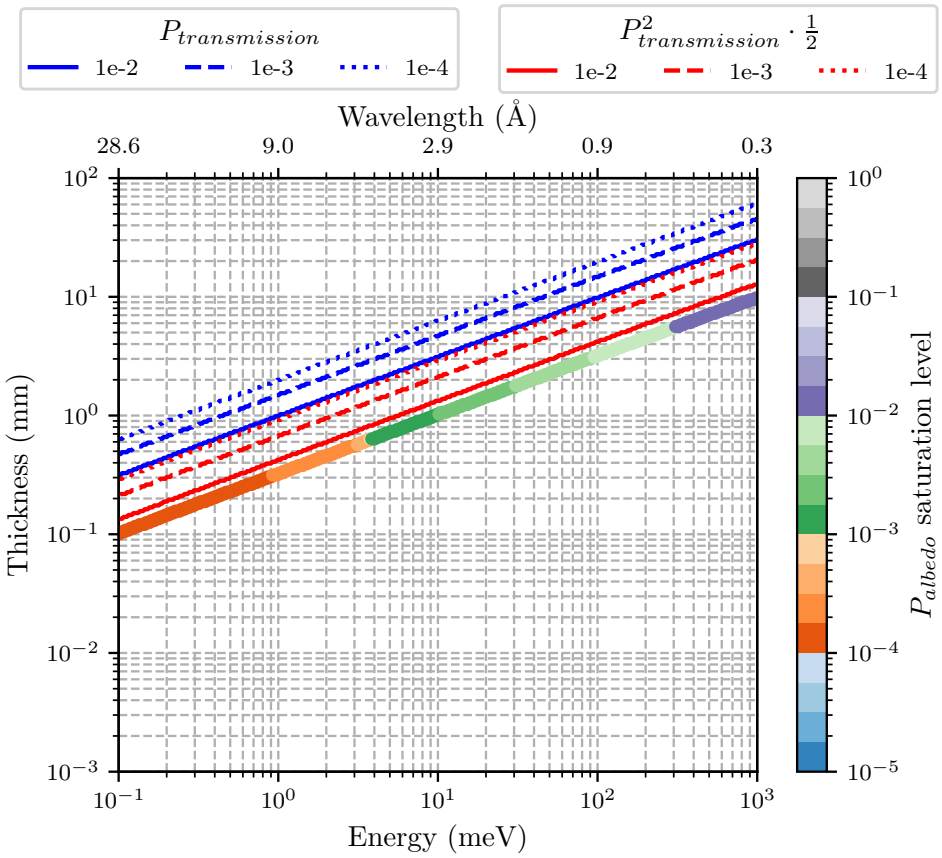

Figure B.12: Boral (90 wt% Al + 10 wt% $^{nat}B_4C$), material properties needed for shielding investigation. The probability iso-lines for $P_{transmission}$ (blue) and $P^2_{transmission} \cdot \frac{1}{2}$ (red) are shown as a function of thickness and energy for three different probabilities: 10^{-2}, 10^{-3} and 10^{-4}. Additionally, the albedo saturation thicknesses are shown as a function of energy, where the colour indicates the albedo saturation level.

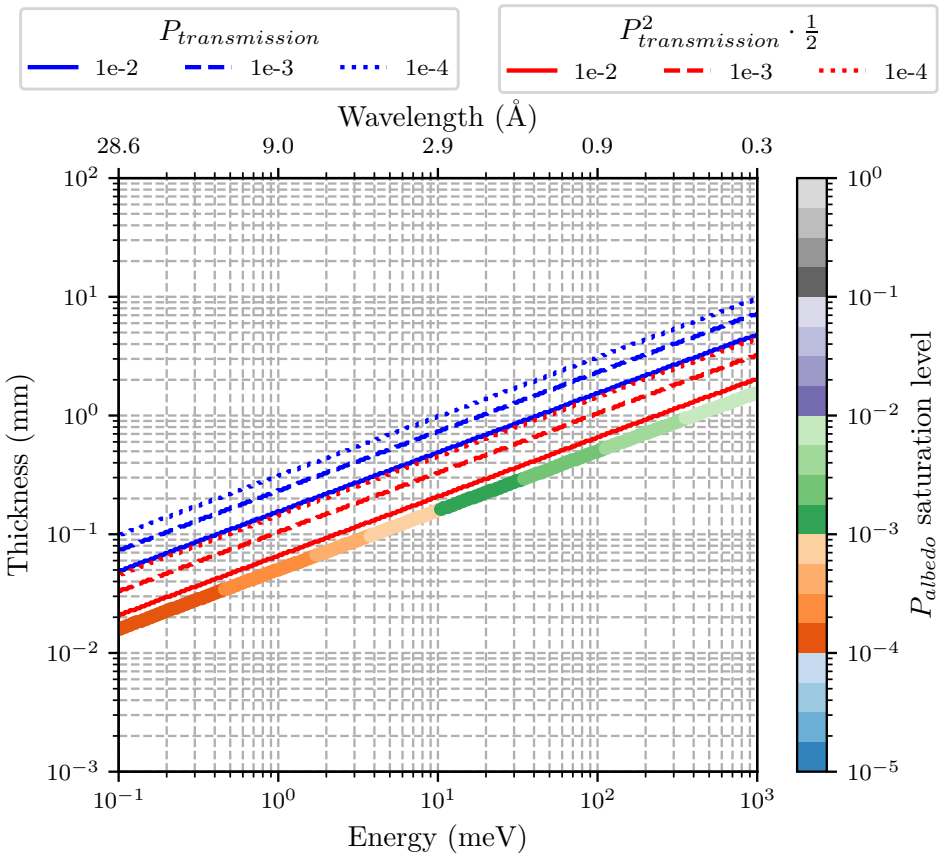

Figure B.13: Boral (33 wt% Al + 67 wt% $^{\text{nat}}B_4C$), material properties needed for shielding investigation. The probability iso-lines for $P_{transmission}$ (blue) and $P^2_{transmission} \cdot \frac{1}{2}$ (red) are shown as a function of thickness and energy for three different probabilities: 10^{-2}, 10^{-3} and 10^{-4}. Additionally, the albedo saturation thicknesses are shown as a function of energy, where the colour indicates the albedo saturation level.

Bibliography

[1] Guerard, B. and Buffet, J. C. Patent EP 2 363 876, Priority Date 2 March 2010

[2] Höglund, C., *et al.*: B4C thin films for neutron detection. Journal of Applied Physics **111**(10), 104908 (2012). doi:10.1063/1.4718573

[3] Correa, J.: 10B4C Multi-Grid as an alternative to 3He for Large Area Neutron Detectors. PhD thesis, University of Zaragoza and Institut Laue-Langevin (2012). https://zaguan.unizar.es/record/89632#

[4] Bigault, T., *et al.*: 10B multi-grid proportional gas counters for large area thermal neutron detectors. Neutron News **23**(4), 20–25 (2012). doi:10.1080/10448632.2012.725329

[5] Guérard, B., *et al.*: 10B multi-grid proportional gas counters for large area thermal neutron detectors. Nuclear Instruments and Methods in Physics Research Section A: Accelerators, Spectrometers, Detectors and Associated Equipment **720**, 116–121 (2013). doi:10.1016/j.nima.2012.12.021

[6] Khaplanov, A., Piscitelli, F., Buffet, J.-C., Clergeau, J.-F., Correa, J., van Esch, P., Ferraton, M., Guerard, B., Hall-Wilton, R.: Investigation of gamma-ray sensitivity of neutron detectors based on thin converter films. Journal of Instrumentation **8**(10), 10025–10025 (2013). doi:10.1088/1748-0221/8/10/p10025

[7] Khaplanov, A., *et al.*: In-beam test of the Boron-10 Multi-Grid neutron detector at the IN6 time-of-flight spectrometer at the ILL. Journal of Physics: Conference Series **528**, 012040 (2014). doi:10.1088/1742-6596/528/1/012040

[8] Khaplanov, A., *et al.*: Investigation of background in large-area neutron detectors due to alpha emission from impurities in aluminium. Journal of Instrumentation **10**(10), 10019–10019 (2015). doi:10.1088/1748-0221/10/10/p10019

[9] Khaplanov, A., *et al.*: Multi-Grid detector for neutron spectroscopy: results obtained on time-of-flight spectrometer CNCS. Journal of Instrumentation **12**(04), 04030–04030 (2017). doi:10.1088/1748-0221/12/04/p04030

[10] ILL. `https://www.ill.eu/`. Accessed: 2023-02-16

[11] European Spallation Source. `https://europeanspallationsource.se/`. Accessed: 2022-09-01

[12] Garoby, R., *et al.*: The european spallation source design. Physica Scripta **93**(1), 014001 (2017). doi:10.1088/1402-4896/aa9bff

[13] Peggs, S., *et al.*: ESS Technical Design Report [ESS-2013-0001]. Technical report, European Spallation Source (April 2013). `https://backend.orbit.dtu.dk/ws/portalfiles/portal/110641459/TDR_final.pdf`

[14] Zeitelhack, K.: Search for alternative techniques to helium-3 based detectors for neutron scattering applications. Neutron News **23** (2012). doi:10.1080/10448632.2012.725325

[15] Messi, F., *et al.*: (2020). The Neutron-Tagging Facility at Lund University (IAEA-TECDOC–1935). International Atomic Energy Agency (IAEA)

[16] Spallation Neutron Source. `https://neutrons.ornl.gov/sns`. Accessed: 2022-10-06

[17] Helmholtz-Zentrum Berlin. `https://www.helmholtz.de/en/`. Accessed: 2023-02-08

[18] ISIS neutron and muon source. `https://www.isis.stfc.ac.uk/Pages/home.aspx`. Accessed: 2022-10-06

[19] Carpenter, J.M., Loong, C.-K.: Elements of Slow-neutron Scattering. Cambridge University Press, University Printing House, Cambridge CB2 8BS, United Kingdom (2015). ISBN 978-0-521-85781-9

[20] Dianoux, A.-J., Lander, G.: Neutron Data Booklet. Old City Publishing Group, Old City Publishing, 628 North Second Street, Philadelphia, PA 19123 USA (2003)

[21] Willis, B.T.M., Carlile, C.J.: Experimental Neutron Scattering. Oxford University Press, Great Clarendon Street, Oxford, OX2 6DP, United Kingdom (2009). ISBN 978-0-19-851970-6

[22] Squires, G.L.: Introduction to the Theory of Thermal Neutron Scattering, 3rd edn. Cambridge University Press, The Edinburgh Building, Cambridge CB2 8RU, United Kingdom (2012). doi:10.1017/CBO9781139107808

[23] Dian, E.: Optimisation of signal-to-background ratio for thermal neutron detectors. PhD thesis, Budapest University of Technology and Economics (2019). `https://jinst.sissa.it/jinst/theses/2020_JINST_TH_001.jsp`

[24] The McClellan Nuclear Research Center - Neutron Imaging Overview. `https://mnrc.ucdavis.edu/neutron-radiography`. Accessed: 2023-04-05

[25] Mistonov, A.A., Dubitskiy, I.S., Shishkin, I.S., Grigoryeva, N.A., Heinemann, A., Sapoletova, N.A., Valkovskiy, G.A., Grigoriev, S.V.: Magnetic structure of the inverse opal-like structures: Small angle neutron diffraction and micromagnetic simulations. Journal of Magnetism and Magnetic Materials **477**, 99–108 (2019). doi:10.1016/j.jmmm.2019.01.016

[26] Klyushina, E.S., Lake, B., Islam, A.T.M.N., Park, J.T., Schneidewind, A., Guidi, T., Goremychkin, E.A., Klemke, B., Månsson, M.: Investigation of the spin-1 honeycomb antiferromagnet $BaNi_2V_2O_8$ with easy-plane anisotropy. Phys. Rev. B **96**, 214428 (2017). doi:10.1103/PhysRevB.96.214428

[27] Piscitelli, F.: Boron-10 layers, neutron reflectometry and thermal neutron gaseous detectors. PhD thesis, Institut Laue-Langevin and University of Perugia (2014). `https://jinst.sissa.it/jinst/theses/2021_JINST_TH_001.jsp`

[28] Andersen, K.H., Carlile, C.J.: A proposal for a next generation european neutron source. Journal of Physics: Conference Series **746**(1), 012030 (2016). doi:10.1088/1742-6596/746/1/012030

[29] Arch Daily. `https://www.archdaily.com/977421/european-spallation-source-buro-happold-plus-henning-larsen-plus-cobe`. Accessed: 2023-01-17

[30] Eshraqi, M., *et al.*: The ESS Linac. In: Proc. 5th International Particle Accelerator Conference (IPAC'14), Dresden, Germany, June 15-20, 2014. International Particle Accelerator Conference, pp. 3320–3322. JACoW, Geneva, Switzerland (2014). doi:10.18429/JACoW-IPAC2014-THPME043. `http://jacow.org/ipac2014/papers/thpme043.pdf`

[31] Zenklusen, A., Jurns, J., Arnold, P., Quack, H.: ESS Target Moderator Cryogenic Plant : Process Design. Vortrag gehalten auf European Cryogenic Days

2017, Karlsruhe, Germany, 13th - 15th September 2017. 37.06.02; LK 01 (2017). doi:10.5445/IR/1000075556

[32] Zanini, L., Batkov, K., Klinkby, E., Mezei, F., Schönfeldt, T., Takibayev, A.: The neutron moderators for the european spallation source. Journal of Physics: Conference Series **1021**(1), 012066 (2018). doi:10.1088/1742-6596/1021/1/012066

[33] Mezei, F. Novel polarized neutron devices: supermirror and spin component amplifier. Communications on Physics (London), 1(3), 81-85. (1976).

[34] Bentley, P.M., Hall-Wilton, R., Cooper-Jensen, C.P., Cherkashyna, N., Kanaki, K., Schanzer, C., Schneider, M., Böni, P.: Self-shielding copper substrate neutron supermirror guides. Journal of Physics Communications **5**(5), 055009 (2021). doi:10.1088/2399-6528/abfae3

[35] Dunning, J.R., Pegram, G.B., Fink, G.A., Mitchell, D.P., Segrè, E.: Velocity of slow neutrons by mechanical velocity selector. Phys. Rev. **48**, 704–704 (1935). doi:10.1103/PhysRev.48.704

[36] Issa, F., Khaplanov, A., Hall-Wilton, R., Llamas, I., Riktor, M.D., Brattheim, S.R., Perrey, H.: Characterization of thermal neutron beam monitors. Phys. Rev. Accel. Beams **20**, 092801 (2017). doi:10.1103/PhysRevAccelBeams.20.092801

[37] Maulerova, V., *et al.*: First neutron data recorded at the v20 test instrument utilizing prototype chopper systems and beam monitors planned for ESS. EPL (Europhysics Letters) **128**(5), 52001 (2020). doi:10.1209/0295-5075/128/52001

[38] Vergara, L., *et al.*: Evaluation of a method for time-of-flight, wavelength and neutron flight path calibration for neutron scattering instruments by means of a mini-chopper and standard neutron monitors. Journal of Instrumentation **18**(04), 04012 (2023). doi:10.1088/1748-0221/18/04/P04012

[39] CSPEC. `https://europeanspallationsource.se/instruments/cspec`. Accessed: 2022-09-06

[40] Deen, P.P., Longeville, S., Lohstroh, W., Moreira, F., Fabrèges, G., Loaiza, L., Noferini, D.: CSPEC: The cold chopper spectrometer of the ESS, a detailed overview prior to commissioning. Review of Scientific Instruments **92**(10), 105104 (2021). doi:10.1063/5.0059907

[41] Andersen, K.H., *et al.*: The instrument suite of the european spallation source. Nuclear Instruments and Methods in Physics Research Section A: Accelera-

tors, Spectrometers, Detectors and Associated Equipment **957**, 163402 (2020). doi:10.1016/j.nima.2020.163402

[42] T-REX. `https://europeanspallationsource.se/instruments/t-rex`. Accessed: 2022-09-06

[43] T-REX: A Time-of-flight Reciprocal space Explorer, ESS Instrument Construction Proposal. `https://indico.esss.lu.se/event/739/attachments/5717/7971/t-rex_proposal.pdf`. Accessed: 2023-04-05

[44] Babcock, E., Salhi, Z., Pistel, P., Simeoni, G., Ioffe, A.: Magic-PASTIS for XYZ polarization analysis using SEOP polarized ^{3}He gas. Journal of Physics: Conference Series **528**, 012018 (2014). doi:10.1088/1742-6596/528/1/012018

[45] Knoll, G.F.: Radiation Detection and Measurement; 3rd Ed. Wiley, New York, NY (2000)

[46] Sauli, F.: Principles of operation of multiwire proportional and drift chambers. Technical report, Geneva (1977). doi:10.5170/CERN-1977-009. CERN, Geneva, 1975 - 1976

[47] Sauli, F.: Gaseous Radiation Detectors: Fundamentals and Applications. Cambridge Monographs on Particle Physics, Nuclear Physics and Cosmology. Cambridge University Press, University Printing House, Cambridge CB2 8BS, United Kingdom (2014). doi:10.1017/CBO9781107337701

[48] Ramo, S.: Currents induced by electron motion. Proceedings of the IRE **27**(9), 584–585 (1939). doi:10.1109/JRPROC.1939.228757

[49] Shockley, W.: Currents to conductors induced by a moving point charge. Journal of Applied Physics **9**(10), 635–636 (1938). doi:10.1063/1.1710367

[50] Piscitelli, F., Esch, P.V.: Analytical modeling of thin film neutron converters and its application to thermal neutron gas detectors. Journal of Instrumentation **8**(04), P04020 (2013). doi:10.1088/1748-0221/8/04/P04020

[51] Carmona Basañez, A., Kanaki, K., Piscitelli, F.: DECal, a Python tool for the efficiency calculation of thermal neutron detectors based on thin-film converters. arXiv: 1801.07124, Github: `https://github.com/DetectorEfficiencyCalculator/dg_efficiencyCalculator` (2018)

[52] Schmidt, S., *et al.*: Low-temperature growth of boron carbide coatings by direct current magnetron sputtering and high-power impulse magnetron sputtering. Journal of Materials Science **51**(23), 10418–10428 (2016). doi:10.1007/s10853-016-0262-4

[53] iROC TECH. https://www.iroctech.com/. Accessed: 2023-04-05

[54] Boulby Underground Laboratory. https://www.ukri.org/about-us/stfc/locations/boulby-underground-laboratory/. Accessed: 2023-04-04

[55] MMR Multi-channel Readout. https://www.mesytec.com/products/datasheets/MMR_System.pdf. Accessed: 2022-09-21

[56] Granroth, G.E., Kolesnikov, A.I., Sherline, T.E., Clancy, J.P., Ross, K.A., Ruff, J.P.C., Gaulin, B.D., Nagler, S.E.: SEQUOIA: A newly operating chopper spectrometer at the SNS. Journal of Physics: Conference Series **251**, 012058 (2010). doi:10.1088/1742-6596/251/1/012058

[57] Bewley, R.I., Taylor, J.W., Bennington., S.M.: LET, a cold neutron multi-disk chopper spectrometer at ISIS. Nuclear Instruments and Methods in Physics Research Section A: Accelerators, Spectrometers, Detectors and Associated Equipment **637**(1), 128–134 (2011). doi:10.1016/j.nima.2011.01.173

[58] Mirrortron Radiation Shielding. https://mirrotron.com/en/products/radiation-shielding. Accessed: 2022-09-28

[59] VMMR-8 / 16. https://www.mesytec.com/products/datasheets/VMMR.pdf. Accessed: 2022-09-21

[60] mvme - mesytec VME Data Acquisition. https://www.mesytec.com/downloads/mvme/mvme.pdf. Accessed: 2022-09-21

[61] Kolya, S., *et al.*: BrightnESS Deliverable D4.1: Integration plan for detector readout (2015). doi: https://doi.org/10.17199/BRIGHTNESS.D4.1

[62] Pfeiffer, D., *et al.*: Rate-capability of the VMM3a front-end in the RD51 Scalable Readout System. Nuclear Instruments and Methods in Physics Research Section A: Accelerators, Spectrometers, Detectors and Associated Equipment **1031**, 166548 (2022). doi:10.1016/j.nima.2022.166548

[63] Höglund, C., *et al.*: Stability of 10B4C thin films under neutron radiation. Radiation Physics and Chemistry **113**, 14–19 (2015). doi:10.1016/j.radphyschem.2015.04.006

[64] Lai, C.-C., Boyd, R., Svensson, P.-O., Höglund, C., Robinson, L., Birch, J., Hall-Wilton, R.: Effect of substrate roughness and material selection on the microstructure of sputtering deposited boron carbide thin films. Surface and Coatings Technology **433**, 128160 (2022). doi:10.1016/j.surfcoat.2022.128160

[65] Dian, E., Kanaki, K., Ehlers, G., Hall-Wilton, R.J., Khaplanov, A., Kittelmann, T., Zagyvai, P.: Scattered neutron background in thermal neutron detectors. Nuclear Instruments and Methods in Physics Research Section A: Accelerators, Spectrometers, Detectors and Associated Equipment **902**, 173–183 (2018). doi:10.1016/j.nima.2018.04.055

[66] Dian, E., Kanaki, K., Khaplanov, A., Kittelmann, T., Zagyvai, P., Hall-Wilton, R.: Suppression of intrinsic neutron background in the Multi-Grid detector. Journal of Instrumentation **14**(01), P01021–01021 (2019). doi:10.1088/1748-0221/14/01/p01021

[67] Mauri, G.: Development and characterization of detectors for large area application in neutron scattering and small area application in neutron reflectometry. PhD thesis, Università degli studi perugia (2019). https://arxiv.org/abs/1905.12311

[68] Dian, E., Kanaki, K., Hall-Wilton, R.J., Zagyvai, P., Czifrus, S.: Neutron activation and prompt gamma intensity in Ar/CO2-filled neutron detectors at the european spallation source. Applied Radiation and Isotopes **128**, 275–286 (2017). doi:10.1016/j.apradiso.2017.06.003

[69] Khaplanov, A., *et al.*: Characterization of the boron-based Multi-Grid detector on the thermal neutron spectrometer SEQUOIA at the SNS. Unpublished internal note

[70] Stone, M.B., Crow, L., Fanelli, V.R., Niedziela, J.L.: Characterization of shielding materials used in neutron scattering instrumentation. Nuclear Instruments and Methods in Physics Research Section A: Accelerators, Spectrometers, Detectors and Associated Equipment **946**, 162708 (2019). doi:10.1016/j.nima.2019.162708

[71] Agostinelli, S., *et al.*: Geant4—a simulation toolkit. Nuclear Instruments and Methods in Physics Research Section A: Accelerators, Spectrometers, Detectors and Associated Equipment **506**(3), 250–303 (2003). doi:10.1016/S0168-9002(03)01368-8

[72] Allison, J., *et al.*: Recent developments in Geant4. Nuclear Instruments and Methods in Physics Research Section A: Accelerators, Spectrometers, Detectors and Associated Equipment **835**, 186–225 (2016). doi:10.1016/j.nima.2016.06.125

[73] Allison, J., *et al.*: Geant4 developments and applications. IEEE Transactions on Nuclear Science **53**(1), 270–278 (2006). doi:10.1109/TNS.2006.869826

[74] Kittelmann, T., *et al.*: Geant4 based simulations for novel neutron detector development. J. Phys: Conf. Ser. **513**, 022017 (2014). doi:10.1088/1742-6596/513/2/022017

[75] Kanaki, K., *et al.*: Simulation tools for detector and instrument design. Physica B: Condensed Matter **551**, 386–389 (2018). doi:10.1016/j.physb.2018.03.025

[76] Kittelmann, T., Cai, X.-X.: Elastic neutron scattering models for NCrystal. Computer Physics Communications **267**, 108082 (2021). doi:10.1016/j.cpc.2021.108082

[77] Cai, X.-X., Kittelmann, T.: NCrystal: A library for thermal neutron transport. Computer Physics Communications **246**, 106851 (2020). doi:10.1016/j.cpc.2019.07.015

[78] Backis, A., *et al.*: General considerations for effective thermal neutron shielding in detector applications. EPJ Techniques and Instrumentation **9** Article: 8 (2022). doi:10.1140/epjti/s40485-022-00083-0

[79] Backis, A.: General considerations for effective thermal neutron shielding in detector applications - Analysis & Data (2022). doi:10.5281/zenodo.6117346

[80] 3M™ Advanced Metal Matrix Composite. https://www.3m.com/3M/en_US/p/d/b5005056390/. Accessed: 2022-02-14

[81] CERN. https://www.home.cern/. Accessed: 2023-02-08

[82] Geant4. https://geant4.web.cern.ch/. Accessed: 2023-02-08

[83] dgcode. https://github.com/mctools/dgcode. Accessed: 2023-02-08

[84] Woracek, R., Hofmann, T., Bulat, M., Sales, M., Habicht, K., Andersen, K., Strobl, M.: The test beamline of the European Spallation Source – Instrumentation development and wavelength frame multiplication. Nuclear Instruments and Methods in Physics Research Section A: Accelerators, Spectrometers, Detectors and Associated Equipment **839** (2016) 102-116. doi:10.1016/j.nima.2016.09.034

[85] Strobl, M., Bulat, M., Habicht, K.: The wavelength frame multiplication chopper system for the ESS test beamline at the BER II reactor—A concept study of a fundamental ESS instrument principle. Nuclear Instruments and Methods in Physics Research Section A: Accelerators, Spectrometers, Detectors and Associated Equipment **705**, 74–84 (2013). doi:10.1016/j.nima.2012.11.190

[86] Krohn, H.: The research reactor BER II at the Helmholtz-Center Berlin. Internationale Zeitschrift fuer Kernenergie **58**, 611–612 (2012)

[87] Backis, A., *et al.*: Time- and energy-resolved effects in the boron-10 based multi-grid and helium-3 based thermal neutron detectors. Measurement Science and Technology **32**(3), 035903 (2020). doi:10.1088/1361-6501/abc63e

[88] Enlighten Research Data. `https://researchdata.gla.ac.uk/1085/`. Accessed: 2023-04-05. doi:10.5525/gla.researchdata.1085

[89] Eurisys Mesures, Product reference: Neutron beam monitor MNH10/4.2F. `https://www.mirion.com` (1996)

[90] Förster, D.F., *et al.*: Lightweight fast rotating Fermi-chopper, proof of principle for a scalable array chopper. Nuclear Instruments and Methods in Physics Research Section A: Accelerators, Spectrometers, Detectors and Associated Equipment **908**, 298–308 (2018). doi:10.1016/j.nima.2018.07.051

[91] Maulerova, V., *et al.*: Vanadium-based neutron beam monitor. Phys. Rev. Accel. Beams **23**, 072901 (2020). doi: 10.1103/PhysRevAccelBeams.23.072901

[92] Issa, F., Khaplanov, A., Hall-Wilton, R., Llamas, I., Dalseth Riktor, M., Brattheim, S.R., Perrey, H.: Characterization of thermal neutron beam monitors. Phys. Rev. Accel. Beams **20**, 092801 (2017). doi: 10.1103/PhysRevAccelBeams.20.092801

[93] Mirion Technologies. `https://www.mirion.com`. Accessed: 2020-08-20

[94] GE Reuter Stokes, RS-P4-0810-227, He3 Proportional Counter. `https://www.bakerhughesds.com/measurement-sensing/radiation-measurement/neutron-scattering` (2013)

[95] FAST ComTec GmbH, MCA4, 4 Input Multichannel Analyzer 2 Input Multichannel Scaler, User Manual. `https://www.fastcomtec.com/ftp/manuals/mca4doc.pdf`. Accessed: 2020-03-18

[96] Pfeiffer, D., *et al.*: First measurements with new high-resolution gadolinium-GEM neutron detectors. Journal of Instrumentation **11**(05), P05011–05011 (2016). doi:10.1088/1748-0221/11/05/p05011

[97] Piscitelli, F.: Calibration of He-3 tubes for ESS: Tube RS p4 0810 227 and Tube RS P4 0810 220 (IFE). unpublished (2014)

[98] Buffet, J.C., Correa, J., Van Esch, P., Guérard, B., Khaplanov, A., Piscitelli, F.: Study of a 10B-based multi-blade detector for neutron scattering science. In: 2012 IEEE Nuclear Science Symposium and Medical Imaging Conference Record (NSS/MIC), pp. 171–175 (2012). doi:10.1109/NSSMIC.2012.6551086

[99] Wahlén, R.: Constructing and commissioning of a Multi-Grid neutron detector prototype for the European Spallation Source. Student Paper (2022). `https://lup.lub.lu.se/student-papers/search/publication/9100956`

[100] Utgård. `https://europeanspallationsource.se/workshops-facilities`. Accessed: 2023-05-02

[101] Sears, V.F., Svensson, E.C., Powell, B.M.: Phonon density of states in vanadium. Canadian Journal of Physics **73**(11-12), 726–734 (1995). doi:10.1139/p95-107

[102] Arai, M.: Simple Vanadium Phonon and Background Calculation. Internal ESS Analysis Report, Document number: [ESS-4925294] (2023)

[103] McStas. `https://www.mcstas.org/`. Accessed: 2023-04-04

[104] Kanaki, K., *et al.*: Statistical energy determination in neutron detector systems for neutron scattering science. In: 2013 IEEE Nuclear Science Symposium and Medical Imaging Conference (2013 NSS/MIC), pp. 1–6 (2013). doi:10.1109/NSSMIC.2013.6829644

[105] Pastukhov, V.: Order restricted inference over countable preordered sets. Statistical aspects of neutron detection. PhD thesis, Lund University (2018). `https://lup.lub.lu.se/search/files/50644484/Thesis.pdf`